eman ta zabal zazu
Universidad del País Vasco
Euskal Herriko Unibertsitatea

Spin-to-charge current conversion in systems with spin-orbit coupling

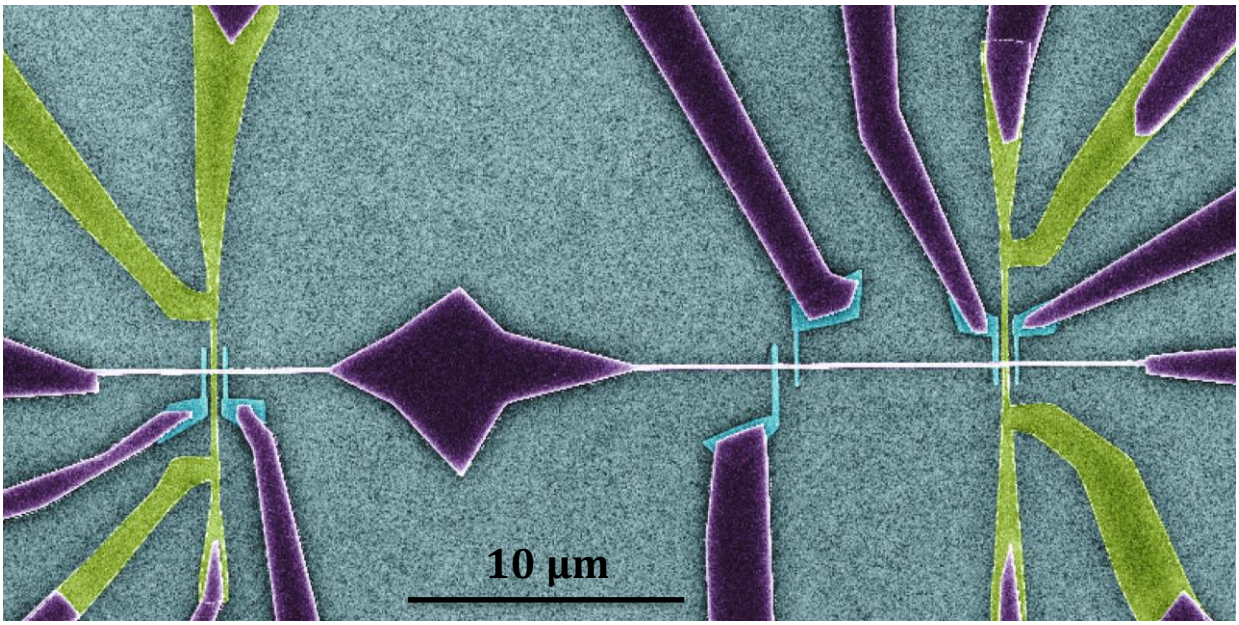

Edurne Sagasta Urrutia

PhD Thesis

Supervisors: Prof. Fèlix Casanova and Prof. Luis E. Hueso

2019


CIC
nanoGUNE
nanoscience cooperative research center

Naturaren izaera ulertzeko aurkikuntzak
etengabe eta beharbada amaigabeak dira,
gizakiaren adimen kognitibora mugatuak.
Tantaz tanta eratzen da erreka,
pausoz pauso bidea.
Hemen pertsonalki eta profesionalki
lau urte aberasgarri eta interesgarriren uzta,
spintronikaren kuriositatez ereindako hazitik bildutakoa.
Ikertzaile entregatu askoren hartuemanaz sortutakoa.
Eskerrik sakonenak denari,
guzti hau bizitzea posible egiteagatik.
Aurrera.

The discoveries to understand the behaviour of nature
are nonstopping and probably endless,
limited to the human cognitive capacity.
Drop by drop is a river formed,
step by step the way.
Here is the fruit of four personally and professionally
enriching and interesting years,
collected from the seeded curiosity in spintronics.
Created through the interaction with many dedicated scientists.
My deepest gratitude to every-all
for making this life experience possible.
Go ahead.

Laburpena

Spintronika, elektroiaren kargaz gain, spinaren askatasun gradua erabiltzen duen elektronikaren alorra da. Spina elektroiaren momentu angeluar intrintsekoa da, norabide jakin batean bi balio har ditzakena: goranzko spina eta beheranzko spina. Spinak garraiatu egin daitezke material ezberdinetan zehar, spin korronteen bidez. Hauek norantza bateko spin gehiago dituzten korronteak dira. Spin korronteez baliatuz, gaur egungo zirkuitu integratuen funtzio berak erdiestea da erronka, baina honetarako beharrezkoa den energia murriztuz.

Gaurko gailuen oinarrizko elementua transistorea da. Elementu honek zirkuituko elektroien karga korrontea kontrolatzen du. Azken urteotako transistorearen hobekuntzek eta tamainaren etengabeko miniaturizazioak zirkuitu integratua osatzen duten transistore kopurua bi urtero bikoiztea eragin du, Moore-ren legeak ondo deskribatzen duen moduan. Honek konputagailuen potentzia eta ahalmenaren hobekuntza ekarri du. Hala ere, tamainaren txikiagotze hau limite batera iristen ari da, non efektu atomikoek garrantzia hartu eta energia disipazioa ere nabarmen egiten den. Hau dela eta, elektronika konbentzionaletik haratago doan informazioa prozesatzeko teknologia berriak beharrezko bihurtu dira eta spintronika da hautagaietako bat.

Spinaren bi egoerak, goranzko spina eta beherazko spina, 0 eta 1 bit binarioak errepresentatzeko erabili daitezke. Era berean, material ferromagnetikoen (ingelesez *ferromagnetic*, FM) magnetizazioa erabili daiteke aipaturiko bit binarioak adierazteko. Material FM-ek norantza bateko spinentzat egoera libre gehiago dituzte eta ondorioz magnetizazio neto bat, hau da, norantza bateko spinen populazio handiago bat dute. Modu honetan, 0 eta 1 bit binarioak errepresentatzeko gai izanik, memoria elementu izateaz gain, spin aldagaia logika egiteko erabili daiteke. Hau guztia gauzatzeko, beharrezkoa da spin korronteak sortu, manipulatu eta detektatzea, ondoren, spinaren jokaeraren eta bere egoeraren kontrola izateko. Beste era batera esanda, gailu spintronikoak funtzionarazteko spin egoeren gainean *idatzi* eta *irakurri* operazioak burutzeko gai izan behar gara.

Memoria magnetikoak irakurtzea oso erraza da gaur egun

magnetoerresistentzia erraldoia erabiliz (ingelesez *giant magnetoresistance*, GMR). 1988an aurkitutako propietate hau dela eta, elementu FM baten magnetizazioa ezagutzea posible da, bigarren elementu FM baten magnetizazioa finkoa izanik, bien arteko egoera paralelo eta antiparaleloen arteko erresistentzia diferentzia oso handia delako. Aurkikuntza hau dela medio, 2007an Albert Fert-ek eta Peter Grünberg-ek Nobel saria jaso zuten eta spintronikako alorrak ikaragarrizko bultzada jasan zuen. Gaur egun merkatuan aurki ditzakegun disko gogor magnetikoen irakurgailuek (ingelesez *hard disk drive*) eta ausazko sarbidedun memoria magnetikoek (ingelesez *magnetic random access memory*) GMR-a dute oinarri.

Irakurketa operazioa arrunta izanik, gaurko erronka idazketa operazioa era eraginkor batean burutzea da. Teknika ezberdinak daude idazketarako, karga korronteek sortutako eremu magnetikoak erabiltzea edota elementu FM-tik spin polarizatutako korronteak pasaraztea, esaterako. Hauetaz gain, efizientzia eta tamaina aldetik onuragarria den teknika berri bat karga-spin korronte konbertsioak erabiltzea da. Karga korronte batetik sortzen den spin korrontea material FM-ra sartzean datza, bere egoera magnetikoa aldaraziko duena. Karga-spin korronte konbertsioak spin-orbita akoplamendu (ingelesez *spin-orbit coupling*, SOC) sendoa duten elementu ez-magnetikoetan (ingelesez *non-magnetic*, NM) gertatzen dira, eta beraz, material NM bat memoria elementu den material FM-ari atxikitzen zaio.

SOC-a elektroiaren spin eta momentu orbitalaren arteko elkarrekintzari dagokio. Interakzio hau spinean oinarritutako efektu berri askoren jatorria da, spin orbitronika alorrean jorratzen direnak. Aplikaziotarako garrantzitsuenetarikoak diren efektuak spin-karga korronte konbertsioak eragiten dituztenak dira, spin korronteak sortu edota detektatzeko erabili daitezkeelako. Horietako fenomeno batzuk, spin Hall efektua (ingelesez *spin Hall effect*, SHE) eta Edelstein efektua dira. Hauek, bereziki, memoria magnetikoak idazteko prozesuan erabili daitezke eta ondorioz, efektu hauen oinarrizko mekanismoak aztertzea interesgarria da, konbertsio efizientziak nola handitu daitezkeen adierazi dezaketelako. Tesi honen izenburuak dioen moduan, lan honetan spin-karga korronte konbertsioak aztertu dira SOC sendoa duten sistemetan.

Tesiaren lehen atalean, SHE-a aztertu da bi metal astunetan: Pt-an eta Ta-an. Metal astunak izateagatik, SOC sendoa dute, eta ondorioz, material hauek SHE handia erakusten dute, neurtutako seinale elektrikoak beste material batzuenekin konparatuz handiak izanik. SHE-ak karga korrontetik abiatuz, spin korronte puruak sortzeko aukera eskaintzen du. Spin korronte puru bat norantza ezberdineko spinak aurkako aldeetara mugitzean sortzen diren korronteak dira. SHE-an, aplikatutako karga korrontea osatzen duten goranzko eta beheranzko spinak aurkako norabidean desbideratzen dira, SOC-agatik, eta spin korronte

puru bat sortarazten dute norabide transbertsalean. Mekanismo intrintseko edo estrintsekoengatik gertatzen da desbideraketa hau. Intrintsekoaren kasuan, SOC-a materialaren banda elektronikoen menpekoa da eta estrintsekoan, aldiz, ezpurutasunek sortutako SOC efektiboa nabaritzen dute higitzen ari diren elektroiek. Spin-karga korronte konbertsio efizientzia spin Hall angeluak, θ_{SH}, ematen du, sortutako spin korronte puru eta aplikatutako karga korrontearen arteko zatiketak. Teknika ugari erabili dira metal astunetan SHE-a aztertzeko. Hala ere, talde ezberdinek lortutako θ_{SH}-ren balioen artean dispertsio handia dago, eta emaitza asko ez datoz bat. Horretaz gain, ez dago argi ea mekanismo intrintseko edo estrintsekoek dominatzen duten SHE-a metal hauetan.

Gailentzen den mekanismoa identifikatzeko eta θ_{SH} nola handitu aurkitzeko helburuekin, SHE-a Pt eta Ta-an aztertu da spin balbula lateraletan (ingelesez *lateral spin valve*, LSV) oinarritutako spin absortzio (ingelesez *spin absorption*, SA) gailuak erabiliz. LSV-ak bi elektrodo FM eta spin kanal NM batez osatuak daude, azken honek bi elektrodoak lotzen dituelarik. Bi elektrodo FM-ak, gure kasuan Py ($Ni_{81}Fe_{19}$)-z eginak, spin korronteak sortzeko eta detektatzeko erabili ditugu, hauen spin populazio ez-orekatua aprobetxatuz. Sortutako spin korrontea material NM-an txertatzen da, hau da, spin kanalean, gure kasuan Cu-z egina izango dena. Cu-ak spin difusio luzera, elektroia bere spina aldatu gabe difunditu daitekeen luzera karakteristikoa, luzea dauka, 1000 nm ingurukoa 10 K-etan, beraz spin kanalaren luzera tamaina horretakoa izango da gehienez. Bi elektrodo FM-en artean Pt edo Ta-zkoa den beste barra nanometriko bat gehitzen dugu. Azken honek spin kanalean doan spin korrontearen zati bat xurgatuko du (hemendik dator gailuaren SA izena) eta bere SOC sendoagatik, karga korronte bihurtuko du xurgatutako spin korrontea. Spin-karga korronte konbertsio honi alderantzizko SHE-a deritzo (ingelesez *inverse spin Hall effect*, ISHE). SA gailu hauek, metal pisutsuaren spin difusio luzera neurtzea ahalbidetzeaz gain, θ_{SH} kuantifikatzeko ere balio dute. ISHE-a tenperaturaren baitan aztertuz, metal bakoitzean SHE-aren zein mekanismo nagusitzen den frogatzen da. Tenperatura bakoitzari metalaren erresistibitate jakin bat dagokionez, ρ_{xx}, erresistibitatearen menpe egiten da ondoren analisia. Tian eta lankideek 2009an ekuazio fenomenologiko bat proposatu zuten Hall efektu anomaloa (ingelesez *anomalous Hall effect*, AHE) metalaren erresistibitateaz erlazionatzen zuena, mekanismo intrintseko eta estrintsekoak kontsideratuz. AHE-a metal FM-etan gertatzen da eta SHE-aren jatorri bera duela onartzen da, hau da, bi efektuak SOC-ean oinarritutako mekanismo berdinengatik gertatzen direla uste da, ekuazio fenomenologikoa bi fenomenoentzat baliagarria izanik. Proposatutako ekuazio honetan, SHE-ari lotutako erresistibitate transbertsala, ρ_{SH}, eta metalaren erresistibitatea erlazionatzen dira, ikus Ek. 1, $\rho_{\mathrm{SH}} = \theta_{\mathrm{SH}}\rho_{\mathrm{xx}}$ izanik.

$$-\rho_{\mathrm{SH}} = \sigma_{\mathrm{SH}}^{\mathrm{int}}\rho_{\mathrm{xx}}^{2} + \alpha_{\mathrm{SH}}^{\mathrm{ss}}\rho_{\mathrm{xx,0}} + \sigma_{\mathrm{SH}}^{\mathrm{sj}}\rho_{\mathrm{xx,0}}^{2}, \tag{1}$$

non $\rho_{xx,0}$ metalaren tenperatura baxuko erresistibitatea den. Lehen gaia mekanismo intrintsekoari dagokio, eta bigarren eta hirugarrena mekanismo estrintsekoei (ingelesez *skew scattering* eta *side jump* deiturikoak, hurrenez hurren). σ_{SH}^{int} spin Hall eroankortasun intrintsekoa da, α_{SH}^{ss} *skew scattering* mekanismoari dagokion spin Hall angelua eta σ_{SH}^{sj} *side jump* mekanismoari dagokion spin Hall eroankortasuna. Mekanismo bakoitzari dagokion pisua lortzeko, neurtutako datu esperimentalak (ρ_{SH}) Ek. 1-era doitzen dira, aipatutako azken hiru parametroak kuantifikatzeko hain zuzen ere.

Pt-aren kasuan, aztertutako erresistibitate tarte osoan, $\sim 7 - 70$ $\mu\Omega$cm, bi erregimen ezberdin identifikatu ditugu. Erresistibitate handiena duen Pt-an, mekanismo intrintsekoa nagusitzen dela frogatu dugu eta eroankortasun handieneko Pt-an, aldiz, *skew scattering* mekanismo estrintsekoa. AHE-an mekanismo intrintsekoa gailentzen den erregimenetik mekanismo estrintsekoa nagusitzen den erregimenerako bilakaera analogoa esperimentalki lehenago frogatu zen arren, bilakaera hau estreinakoz ikusi dugu SHE-an. $\sigma_{SH}^{int} = 1600 \pm 150(\hbar/e)$ $\Omega^{-1}\text{cm}^{-1}$ balio konstantea lortu dugu aztertutako Pt guztietarako, hau da, erresistibitatearekiko independentea den balioa lortu da. Ta-ari dagokionez, mekanismo intrintsekoa gailentzen dela ondorioztatu dugu aztertutako erresistibitate tarte osoan, $\sim 300 - 648$ $\mu\Omega$cm. $\sigma_{SH}^{int} = -820 \pm 120(\hbar/e)$ $\Omega^{-1}\text{cm}^{-1}$ balioa lortu dugu, Pt-arena baino txikiagoa eta aurkako zeinukoa. Zeinu aldaketa esperotakoa da, teorikoki frogatua baitago $5d$ orbitalaren betetze mailaren araberakoa dela zeinua. Bi metal pisutsuen kasuan, mekanismo intrintsekoak dominatzen duenean, θ_{SH} metalaren erresistibitatearekiko linealki proportzionala dela egiaztatu dugu esperimentalki: $\theta_{SH} = \sigma_{SH}^{int}\rho_{xx}$. Aurkikuntza hau garrantzitsua da, honen ondorioz Pt eta Ta-an karga-spin korronte konbertsio efizientzia handitzeko bidea erakusten dugulako.

Dena den, Pt/Cu eta Ta/Cu heteroegituretan metal pisutsuaren erresistibitatea handituz gero, θ_{SH} handitzeaz gain, spin-karga korronte konbertsioari dagokion boltaia txikiaraziko duen efektu bat (ingelesez *shunting* deritzona) handiagotzen dela ohartu gara. *Shunting* efektuan, Cu-aren erresistibitate baxua dela eta (metal pisutsuarenaz erkatuz), metal pisutsuan ISHE-agatik sortutako karga korrontearen zati bat Cu-ra itzultzen da, neurtutako boltaia txikiaraziz. Efektu hau ekiditeko, spin kanalaren erresistibitatea handitzea komeni da. Hori dela eta, grafenoan oinarritutako LSV-ak eraiki ditugu, grafenoaren gainazal erresistentzia Cu-arena baino handiagoa delako. Gainera, grafenoak Cu-aren besteko spin difusio luzera luzea dauka, tenperatura handitzean txikiagotzen ez dena, Cu-arenaz alderatuz. ISHE-a, beraz, Pt/grafeno heteroegituran neurtu dugu tenperatura ezberdinetan. Ingurugiro tenperaturan lortu dugun seinalea Pt/Cu heteroegituran lortutakoa baino ia bi magnitude ordena altuagoa da, *shunting* efektua erabat deuseztatu

delarik sistema berri honetan.

SHE-a, material NM-etan gertatzeaz gain, material FM-etan ere existitzen da. Karga korronte bat material FM batean aplikatzen denean, goranzko spinak eta beheranzko spinak kontrako alderantz desbideratzen dira eta SHE-az lotutako spin korronte purua edo spin akumulazio transbertsala sortzeaz gain, karga akumulazio transbertsal bat ere agertzen da. Azken honi, AHE-a deritzo. Karga pilaketa neto hau material FM-ko goranzko eta beheranzko spinen arteko kantitate desberdinengatik gertatzen da. Aurrez esan bezela, bi efektuek jatorri bera dute, SOC-a, eta biak mekanismo berdinengatik gertatzen direla onartzen da, hau da, efektu intrintseko eta estrintseko berdinengatik. Honetaz gain, bi efektuak material FM-aren spin polarizazioaren bidez erlazionatzen direla uste da. Hala ere, azken baieztapen hau ez da egiaztatua izan.

Tesiaren bigarren atalean, SHE-a eta AHE-a $3d$ elementu FM-etan aztertu da; Fe, Co, Py eta Ni-ean hain zuzen ere. SHE-a neurtzeko SA teknika LSV-etan erabili da eta AHE-aren kasuan, Hall barrak erabili dira. Fenomeno bakoitzaren kasuan, mekanismo bakoitzak (intrintseko edo estrintsekoak) daukan pisua neurtu da eta argi ikusi da goian aipaturiko erlazio sinplea ez dela orokorra. Aztertutako $3d$ elementu FM guztietan, $\sim$ 150 K-etatik aurrera, SHE-aren tenperaturarekiko menpekotasuna sakona da, kasu gehienetan zeinu aldaketa gertatzen delarik. Joera hau ez da ageri SHE-a material NM-etan aztertu dugunean (Pt eta Ta-an), mendekotasun ahulago bat lortu baita metal hauetan. AHE-aren kasuan ere, tenperaturarekiko menpekotasuna askoz ahulagoa da material FM guztietan eta ez da zeinu aldaketarik ageri. Emaitza hauetan oinarrituz, $3d$ elementu FM-en SHE-an, AHE-an presente ez dagoen mekanismo gehigarri bat dagoela ondorioztatu dugu. Posible izango litzatekeen mekanismo bat elektroi-magnoi arteko interakzioek eragindako desbideraketa da, SHE-ari soilik eragingo liokeelarik. Dena den, azken mekanismo honen existentzia frogatzeke geratzen da, aurrerago egiteko lan bat izanik.

Jakina da spin-karga korronte konbertsioak ez direla soilik materialen bolumenean gertatzen, bi geruza finen artean, interfasean, eta gainazaletan ere jazotzen dira. Bi/Ag, Bi/Cu, Bi_2O_3/Cu eta $LaAlO_3$/$SrTiO_3$ sistemetan, besteak beste, neurtu dira spin-karga korronte konbertsioak. Hauetan Rashba motako SOC-a ageri da, Edelstein efektua eragiten duena. Honetaz gain, teorikoki frogatua izan da inbertsio simetria hautsita duten sistemetan SOC erraldoiak ageri direla eta hauek bolumenean spin-karga korronte konbertsioak eragiten dituztela. Ab-initio kalkulu teorikoek erakutsi dute Fe/Au eta Py/Pt sistemetan, spin-karga korronteen konbertsio eraginkorrak gertatzen direla interfasetik gertu. Emaitza hauek abiapuntutzat hartuz, material FM-aren gainean beste geruza bat gehitzeak AHE-an aldaketarik eragin dezakeen aztertzea erabaki dugu. Co-an gertatzen den AHE-a nola aldatzen den aztertu da material FM honi Bi_2O_3-zko

geruza bat gainean jartzen zaionean. Bi_2O_3 material aproposa da azterketa hau egiteko, isolatzailea izanik aplikatuko dugun korronte guztia Co-tik pasako delako eta bestalde, jada egiaztatu delako Rashba akoplamendu handia dagoela Bi_2O_3/Cu sisteman. Co-ak Cu-aren lan-funtzio antzekoa izanik, antzeko Rashba akoplamendua izatea espero da.

Emaitzek argi erakusten dute Co-aren AHE-a % 37-raino alda daitekeela Bi_2O_3 geruza gainean jartzen bazaio. Azterketa sakonagoa egiteko, Co-aren lodiera ezberdineko laginak fabrikatu dira. Alde batetik Co soilik daukan erreferentziako laginak eta bestetik, Co/Bi_2O_3 bigeruzak eginez. Lodieraren menpeko emaitzek adierazten dute Bi_2O_3 geruzaren eragina nabarmenagoa dela Co-aren lodiera finen kasuetan. Hori dela eta, Bi_2O_3 eta Co-aren arteko mugan, interfasean, oinarritutako AHE-aren mekanismo bat dagoela ondorioztatu dugu.

Laburbilduz, tesi honetan spin-karga korronte konbertsioak aztertu dira esperimentalki SOC-a duten material ezberdinetan, eta hauek eragiten dituzten mekanismoak identifikatuz eta kuantifikatuz, konbertsioen eraginkortasuna handitzeko bidea erakutsi da. Lortutako emaitzak SOC-ean oinarritutako gailu teknologikoen bilakaerarako garrantzitsuak direla uste dugu. Memoria magnetikoen idazketa prosezuan eta Intel-ek aurten proposatutako spin-orbitan oinarritutako gailu logikoan aplikatu daiteke tesi honetako ekarpena.

Abstract

Spintronics is the field of electronics aiming at exploiting, apart from the charge, the spin degree of freedom of the electron. It is an alternative approach to the conventional electronics, a technology which only employs the charge of the electron for representing, transporting and storing information. The dimension of the transistors in today's electronic circuits, being the building block that controls the charge flow in a circuit, is already reaching the minimum possible size. At these nanometric scales, quantum effects and energy dissipation are prominent, which threatens further development of present charge-based circuits to keep up with Moore´s law. Alternatively, the spin of the electron, its intrinsic angular momentum, can be used as a state variable in computing, *i.e.* as a physical quantity that stores and transmits the logic state. The electron spin along a particular axis can take two possible values: *up* ($\hbar/2$) and *down* ($-\hbar/2$). The two spin states can be used to represent binary data in a non-volatile way and spin currents can be used to control this state, by read and write operations.

The discovery of giant magnetoresistance (GMR) in 1988 paved the way to reading the state of a magnetic memory, made of a ferromagnetic (FM) material, which has a net magnetization due to a major population of one of the spin states. In GMR, the resistance value changes significantly between a parallel and antiparallel configuration of the FM memory element with respect to a FM reference. This is the basic principle of the magnetic read heads and magnetic random access memories that we can find today in the market. One of the current challenges is how to write the magnetic state in an efficient way in the FM memory element. One approach is to use Oersted fields that are generated by electric currents. Another method is to use spin-transfer torques, which can modify the magnetization of a FM element when a spin-polarized current is injected. A more recent option that is gaining interest due to a favorable scalability and efficiency is the spin-orbit torque. It allows to electrically write a magnetic memory element by employing a non-magnetic (NM) material with spin-orbit coupling (SOC) adjacent to the FM element. Due to the SOC, the charge current injected in the NM conductor creates a transverse spin current, which exerts a torque that is able to switch the magnetization of the memory element.

SOC is a relativistic effect that couples the spin and the orbital momentum of electrons and is the origin of many novel phenomena that are studied in the emerging field of spin orbitronics. Some effects, particularly relevant for applications, are the conversions between charge currents and spin currents, as they can be used for spin current generation or detection. Some of the spin-orbit-based effects that result in a charge-to-spin current conversion are the spin Hall effect (SHE) and the Edelstein effect. They are indeed the phenomena that give rise to spin-orbit torques. The reciprocal effects, inverse spin Hall effect (ISHE) and inverse Edelstein effect, give rise to a spin-to-charge current conversion (SCC). The SHE occurs in the bulk of materials with strong SOC, such as heavy metals, Pt, Ta and W. When a charge current is injected in such a system, SOC deflects spin-up and spin-down electrons in opposite direction, giving rise to a transverse pure spin current. The asymmetric deflection of spin-up and spin-down electrons occurs due to different mechanisms: intrinsic, if the SOC is inherent to the electronic bands of the metal, or extrinsic, if the electrons feel the effective SOC coming from the impurities that are present in the host material. The SCC efficiency is given by the spin Hall angle, θ_{SH}. Many techniques have been used to study the SHE in these materials, although there is a large dispersion of θ_{SH} values among groups and techniques. On top of this, it is not clear which mechanism dominates the SHE in heavy metals, which is relevant to know in order to unveil the path to optimize the conversion efficiency.

In the first part of the thesis, we study the SHE in Pt and Ta using the spin absorption technique in Py/Cu lateral spin valves (LSVs). LSVs consist of two FM electrodes, made of Py ($Ni_{81}Fe_{19}$), that allow us to electrically inject and detect pure spin currents in a NM channel, made of Cu, where the pure spin current diffuses. In between the two FM electrodes, we add a nanowire made of Pt or Ta, that will absorb part of the spin current flowing in the NM channel. Due to the ISHE, SCC will occur in the heavy metal. The device allows us to quantify both the spin diffusion length of the heavy metal, *i.e.* how far the electron can diffuse without changing its spin orientation, and θ_{SH}. We are able to extract the weight of each mechanism using the phenomenological equation proposed by Tian *et al.* for the anomalous Hall effect (AHE), which is the analogous phenomenon to the SHE occurring in FM materials. It is generally assumed that the SHE and AHE share the same origin, SOC, and are driven by the same intrinsic and extrinsic mechanisms.

In case of Pt, we observe two different regimes when analyzing the results of the ISHE measurements: whereas at the clean metal limit regime the extrinsic mechanism governs the SHE, the intrinsic mechanism becomes dominant in the moderately dirty regime. A similar crossover has been observed in the AHE of different FM conductors, but it has never been demonstrated experimentally in

any spin Hall system before. We obtain a constant intrinsic spin Hall conductivity for all the studied resistivity range: $\sigma_{SH}^{int} = 1600 \pm 150(\hbar/e)\ \Omega^{-1}\text{cm}^{-1}$, which is in good agreement with theoretical reports. In Ta, we evidence that the intrinsic mechanism dominates the SHE in all the studied resistivity range and we obtain a constant value of $\sigma_{SH}^{int} = -820 \pm 120(\hbar/e)\ \Omega^{-1}\text{cm}^{-1}$. In the moderately dirty regime, there is a linear increase of θ_{SH} with the resistivity of the metal (ρ_{xx}) in both systems: $\theta_{SH} \approx \sigma_{SH}^{int}\rho_{xx}$. This shows a clear path to enhance the SCC efficiency. Interestingly, our experimental results evidence that the variation of the Pt resistivity among different groups is one of the main reasons for the spread of θ_{SH} values in literature.

In the Pt/Cu or Ta/Cu heterostructures where we measure the ISHE, we observe that higher resistivities of the heavy metals, apart from resulting in larger θ_{SH}, also cause a larger shunting. Due to this effect, part of the ISHE-generated charge current in the heavy metal flows back into the low-resistive Cu, reducing the measured output voltage. In other words, when the resistivity of the heavy metal is increased, the enhancement of the output voltage originated from the increase of θ_{SH} is counterbalanced by the enhancement of the shunting effect. In order to overcome this issue, we propose a LSV with a NM channel made of graphene, which has larger sheet resistance and superior spin transport properties as compared to Cu. We study the SCC in a Pt/graphene heterostructure and we observe an enhancement of the output signal of almost two orders of magnitude at room temperature, with respect to the metallic cases. This result is a consequence of the long and temperature independent spin diffusion length of graphene (contrary to the one of Cu that decreases when temperature increases), the enhancement of the resistivity and θ_{SH} of Pt with temperature and negligible shunting by the graphene.

Heavy metals are not the only type of materials where the SHE occurs. The SHE is also present in FM metals and it is appealing to focus our study on this type of materials, especially from a fundamental viewpoint. Due to the unbalanced spin population of FM materials, when a charge current is injected, the deflection of spin-up and spin-down electrons gives rise not only to the transverse spin current related to the SHE, but also to a transverse charge current, associated to the AHE. Since both effects have the same origin, it has been commonly accepted that both are driven by the same intrinsic and extrinsic mechanisms. In addition, it has been generally assumed that both effects are related by the current spin polarization of the FM element. However, it has not been experimentally verified if this simple relation is general, and therefore valid for all the FM conductors and all the mechanisms.

In the second part of the thesis, we focus on the AHE and SHE occurring in $3d$ FM metals. Using the spin absorption technique in LSVs and Hall bars, we

measure the ISHE and AHE, respectively, in Fe, Co, Py and Ni. We extract the weight of each mechanism that gives rise to the SHE and AHE and we evidence that the aforementioned simple relation is not generally fulfilled. The temperature dependence of the ISHE in all the studied 3*d* FM elements shows a interesting common feature: a strong temperature dependence above $\sim$ 150 K including a sign change in most of the cases. However, this tendency is dramatically different from the temperature dependence obtained for both the AHE in 3*d* FM metals and SHE in Pt and Ta. The obtained results suggest that there is an additional mechanism present only in the SHE of FM elements, which would explain the strong temperature dependence. A possible scenario could be the presence of an asymmetric spin-dependent scattering in the spin-flip processes induced by the electron-magnon interactions.

Finally, we focus on studying whether an interfacial mechanism can arise in the AHE of a 3*d* FM metal when a capping layer is added on top. It is now well known that SCCs not only occur in bulk but also at surface and interfaces where the inversion symmetry is broken. For instance, giant SCCs have been obtained by ab-initio calculations near Py/Pt and Fe/Au interfaces. In this framework, we study whether a Bi_2O_3 capping layer deposited on top of Co modifies the AHE of Co. Bi_2O_3 is an ideal material as it is an insulator and large Rashba effect can be expected at Co/Bi_2O_3 interface. By comparing the obtained AHE signals in the bilayer system and Co reference samples, we obtain an up to 37% variation in the AHE of Co. This variation decreases when the Co layer becomes thicker, pointing to the interfacial origin of the additional mechanism in the AHE. This opens the path to tune the AHE by interface modification, which could be useful to implement in the SHE as well.

Contents

Chapter 1

Introduction and state-of-the-art

The electron is an elementary particle defined by its fundamental properties: mass, charge and spin. The charge of the electron is employed in conventional electronics for representing, manipulating, transporting and storing information. The invention of the transistor triggered the development of electronic devices, as the basic operation of transistors is to control, turning on and off, the charge flow in electronic circuits. The continuous miniaturization and improvement of transistors has allowed to increase the amount of components in the integrated circuits as described by Moore´s law in 1975, leading to higher operation capacity, lower power consumption per transistor and better computing efficiency. However, the shrinking of these electronic building blocks is reaching atomic limits, which unavoidably affect the performance of the devices. Quantum effects are present at these scales, which can result in leakages, and also Joule heating becomes prominent due to the enhancement of the current density, inducing energy dissipation. Energy waste in electronic devices is becoming a sensitive issue considering the broad use of them in industry, services and as personal gadgets, being incompatible with the current demands to sustain the industrial growth, integrate the Internet of Things technology and more generally, with the increase of energy consumption in our planet. For this reason, introduction of alternative information processing technologies based in new physics, unconventional materials and structures becomes paramount.

1.1 Spintronics

Spintronics, also known as spin-electronics, is a field that exploits, apart from the charge, the spin degree of freedom of electrons. The spin is the intrinsic angular momentum of electrons, which is a quantum property of elementary particles and has an associated magnetic moment. For an electron, the component of the

angular momentum along a particular axis can take two values; $\hbar/2$ or $-\hbar/2$, which are known as "spin-up" and "spin-down" states, being $\hbar$ the reduced Planck constant [1].

The spin of the electron is the main source of the magnetism in ferromagnetic (FM) materials, as the associated magnetic moment is larger than the one of the nucleus of an atom. The magnetization of FM materials is originated from the excess of spin-up or spin-down electrons in the system. Ferromagnets play a relevant role in spintronics, but also the non-magnetic (NM) materials, where the population of spin-up and spin-down electrons is balanced. A major goal of spintronics is to understand and control the behavior of spin currents in each of these materials and combine them to form a plausible spin-only circuit where spin-logic and magnetic memory are integrated.

The spin can be used as a state variable in computing, *i.e.* a physical quantity that can store and transmit the logic state [2]. Regarding the memory, the two spin states associated to a net magnetization in the FM memory element can be used to represent binary data in a non-volatile way. Even if the power to the device is switched off, the magnetization conserves its state. This is how magnetic hard drivers or magnetic random access memories (MRAMs) work. However, in current computing, the logic operation is performed in a separate part, the microprocessor. By using spin currents to bring out information stored in the FM elements, logic operations could be performed in the same circuit, increasing the speed and lowering the power consumption [3, 4]. Due to these characteristics, spintronics is complementary to the conventional electronics that aims continuing Moore´s law beyond silicon-based, complementary metal-oxide-semiconductor (CMOS), technology.

1.1.1 From the discovery to applications

The influence of the spin in electronic transport can be traced back to 1857, with the discovery of the anisotropic magnetoresistance (AMR). Magnetoresistance refers to the change of the resistance with a change of the external magnetic field, $\vec{H}$. In AMR, the resistance of a FM metal changes for different relative orientations between the injected current and its magnetization, which is modified by $\vec{H}$. However, it was not until 1980s, with the discovery of several spin-dependent transport phenomena, that the spintronics field emerged.

In 1985 Johnson and Silsbee were able to inject electrically spin-polarized electrons from a FM metal to a NM metal, where they evidenced spin relaxation and spin precession around a magnetic field [5]. Three years later, the giant magnetoresistance (GMR) was discovered by Albert Fert [6] and Peter Grünberg

[7], who were awarded the Nobel Prize in Physics in 2007 due to this finding.

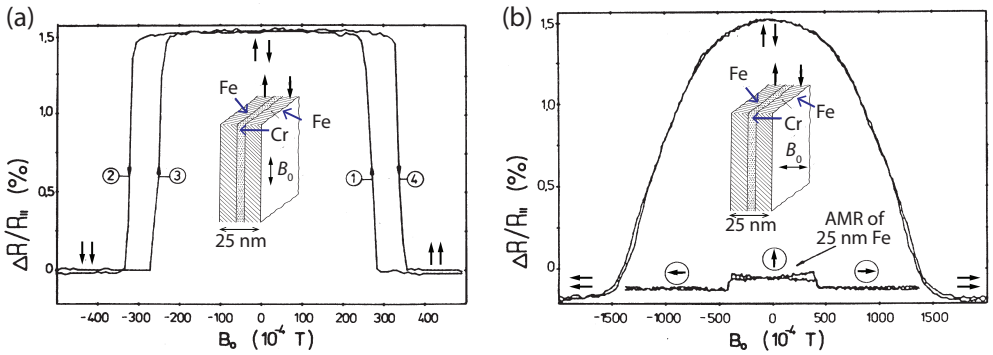

Figure 1.1: **Giant magnetoresistance. First observation of the GMR in Fe(12 nm)/Cr(1 nm)/Fe(12 nm) structure by Grünberg *et al.* [7].** (a) Magnetoresistance *vs.* magnetic field applied in plane, along the easy axis. Inset: Sketch of the 25nm thick Fe/Cr/Fe stack and orientation of the magnetic field. At B_0=0 T the exchange coupling of the Fe layers across the Cr is antiferromagnetic. (b) Magnetoresistance *vs.* magnetic field applied along the hard axis. The curve below shows the AMR measured in 25nm Fe film, with the same thickness as the Fe/Cr/Fe structure. Inset: Sketch of the 25nm thick Fe/Cr/Fe stack and orientation of the magnetic field. Figure adapted from Ref. [7].

They alternated a few-nm-thick FM and NM conducting layers and observed that, depending on the relative magnetization orientation of the FM layers, which directly depended on the applied magnetic field, the resistance of the system changed, see Fig. 1.1(a) for Fe(12 nm)/Cr(1 nm)/Fe(12 nm). This difference in resistance is caused by the accessible states that an electron with a given spin finds when traveling from one FM layer to the next one, passing through the NM middle layer. In case of parallel (antiparallel) alignment of the FM elements, the number of available states in the second FM element is larger (smaller), resulting in a smaller (higher) resistance state. Therefore, by measuring the resistance, the parallel and antiparallel configurations are distinguishable, making the FM/NM/FM spin valve useful as a memory element. Importantly, what converts the discovery in a potential breakthrough for applications is that the magnetoresistance in GMR can be as high as 50%, when extra FM/NM/FM layers are added in the multistack and the measurements are done at low temperatures [6]. On the contrary, the magnitude of AMR in alloys like NiFe or NiCo is of a few percent at room temperature but it is generally smaller in most ferromagnets [8] (compare the GMR and AMR curves in Fig. 1.1(b)), which explains the origin of the name *giant* for GMR.

The finding of GMR was the spark that caused an increase in the interest and brought intense work in the study of devices based on spin transport. This is why its discovery is considered to be the birth of *spintronics*. GMR was rapidly transferred into applications and to the market, such as read heads for hard disk

drivers, which allowed higher density of magnetic recording, non-volatile solid state memory approaches or magnetic field sensors.

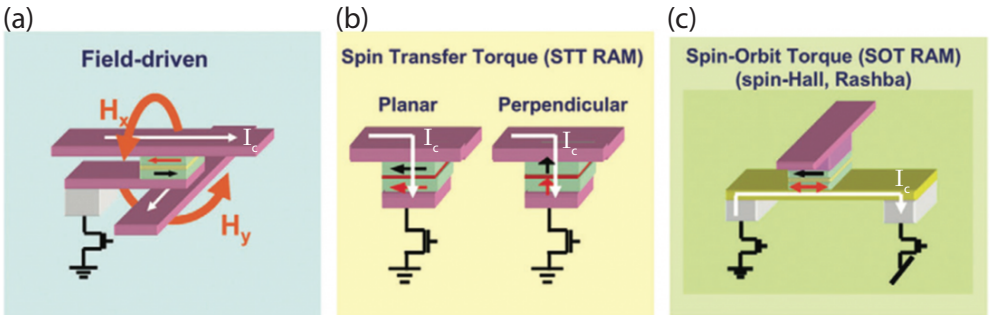

Figure 1.2: **Different writing techniques in MRAM building blocks based on MTJ.** (a) Field-driven writing. (b) Spin transfer torque writing. (c) Spin-orbit torque writing. Red (black) arrow indicates the magnetization of the free (pinned) layer. Figure adapted from Ref. [9].

By substituting the nanometer-thick NM conducting layer by a insulating layer, magnetic tunnel junctions (MTJ) were fabricated, where it was possible to observe the tunnel magnetoresistance (TMR) [10]. The working principle of this device is similar to GMR, but instead of the diffusive transport of the spin through a NM layer, the spin is preserved during the tunneling through the insulating material and reaches the second FM layer where the available states will depend on the spin orientation. With the optimization of the MTJ using AlO_x [11] and MgO [12] as the insulating layers, the magnetoresistance improved up to 70% and 604% at room temperature, respectively. MRAMs are composed of MTJ arrays, where each MTJ represents a non-volatile memory bit, and the parallel and antiparallel states of a MTJ, *i.e.* the two possible resistance states, correspond to 0 and 1 binary values. Each MTJ contains a free FM layer with a switchable magnetization and another FM layer with pinned magnetization due to an antiferromagnetic exchange coupling.

Figure 1.2 shows different building blocks of MRAM memories based on MTJs. In all cases, the reading of the magnetic bits is realized by measuring the resistance value of the MTJ after passing a relatively low charge current through the stack. However, the remaining challenge is how to write the magnetic bits, *i.e.* how to switch the magnetization of the free layer, in an efficient way. The first approach was to use the Oersted field created by charge currents, see Fig. 1.2(a). The main drawback of this technique is the obstacle for downscaling, given the difficulty to localize the generated magnetic field and the requirement for larger currents to switch the magnetization when the bit size is reduced [13]. Spin-transfer torque (STT) is an alternative method for writing. This phenomenon was predicted in 1996 by Slonczewski [14] and Berger [15] and results in the modification of the magnetization of a FM element when a spin-polarized current is injected. In case

of the MTJ in the MRAM, when a charge current is applied through the MTJ, as shown in Fig. 1.2(b), the first FM layer of the MTJ acts as a spin polarizer, hence the flowing charge current will be spin polarized. This spin-polarized current will tunnel through the insulating layer, transferring the angular momentum to the second FM layer of the MTJ and generating a torque that switches the magnetization. It is a more local technique, offering better scalability, with a lower power consumption and it is already applied in commercial STT-MRAMs [16]. The major disadvantage is that the relatively large charge current in the small area of the junction turns out to be harmful to MTJ, for instance high temperatures can be reached which lead to the loss of the antiferromagnetic exchange coupling [17].

There is a novel approach, known as spin-orbit torque (SOT) [18], to electrically write magnetic memory elements by employing a NM material with strong spin-orbit coupling (SOC). In this case, a charge current flows in a NM metal adjacent to the free layer of the MTJ, see Fig. 1.2(c), and this charge current is converted into a transverse spin current which exerts a torque, named SOT, that is able to switch the magnetization of the free layer. Since, in SOT-based MRAM, charge currents for writing do not flow through the MTJ, the device shows a major robustness. SOT is not commercially used yet, but it is seriously considered. Toshiba Corporation launched a proposal in 2018 where they combined SOT with voltage controlled magnetic anisotropy to write magnetic memories with reduced currents [19]. SOT requires efficient charge-to-spin conversions which are originated due to the SOC in the bulk of the NM metal or at the interface between the free layer of the MTJ and the NM material.

Although the initial commercial impact of spintronics was mostly linked to information storage, currently efforts are focused on obtaining logic functionalities in devices. The integration of non-volatile memory and spin-logic operations can give rise to innovative architectures which can pave the way to better memory and logic interconnections and more efficient and faster operations than in the current CMOS technology [20, 21]. Recently, several proposals of spin-based logic have been published. The first proposal by Dery and coworkers has a "magnetologic gate" as a building block consisting of a spin channel (made of a semiconductor or graphene) contacted by five FM electrodes, where the information is stored in their magnetization [3]. Two electrodes define the input, other two the operation and the last one is used to read out. The logic operation is performed by mixture and diffusion of spin currents and magnetization states are written via STT with charge currents. The "all-spin logic" proposal by Behin-Aein *et al.* is similar: the information is stored in nanomagnets and the main difference with the previous one is that even the STT is performed with pure spin currents [4]. Different prototypes of spin transistors can also be found in literature, based on different

novel spintronic materials, from two-dimensional electron gases (2DEGs) [22] to two-dimensional (2D) layered materials [23], where the spin current flowing in NM channels is controlled by gate voltages. In addition, Manipatruni *et al.,* from Intel Corporation have proposed a magneto-electric spin-orbit (MESO) logic device [24]. In the latter, information is stored in a FM material which can be written via magneto-electric coupling and the reading is done by spin-to-charge current conversion (SCC). These spin-based logic proposals are under development and demand to overcome certain fundamental and technological challenges for the implementation of such devices. Namely, a recently published review that contains the list of challenges for the realization of the MESO device [2] included the enhancement of the efficiency of SCCs, as it occurs with SOT technique. This will be addressed in this thesis by studying the main effects and mechanisms that give rise to these SCCs.

Although in less than four decades the field of spintronics has evolved significantly, unveiling novel spin-based effects and transferring them to applications, there is still much progress to be done, both from the fundamental and engineering point of view, in order to witness the integration of spin-based logic and memory devices in current electronic circuits.

1.1.2 Spin currents and spin relaxation in metals

An essential ingredient in spintronics is the transport of spin information, which is carried out by spin currents via conduction electrons in conducting materials or by magnons in FM conductors or insulators. In this thesis we employ conduction electrons to transport spins. We can distinguish between a *pure spin current*, a flow of spin angular momentum without a net charge flow, and a *spin-polarized current*, a flow of both charge and spin angular momentum. The former is achieved in a configuration where the same amount of spin-up and spin-down electrons are moving in the opposite direction. In the following, we will describe the nature of spin currents in FM materials and NM materials, and the spin relaxation mechanisms which prevent pure spin current flow indefinitely.

Spin currents in FM materials

FM materials have non-zero magnetization, even in the absence of magnetic field [1]. The main responsible for this spontaneous magnetization in the ferromagnets is the exchange interaction, which energetically favors the parallel alignment of the electrons' spins. This is revealed in the electronic bands with a shift in energy of the spin-sub bands, known as exchange energy, E_{ex}, which is determined by the energy difference between antiparallel and parallel spin configurations. Roughly speaking, the condition for ferromagnetism to arise is that E_{ex} has to be larger

than the gain on kinetic energy associated to the parallel spin configuration. In case of $3d$ FM transition metals, $3d$ spin-up and spin-down sub-bands are shifted with respect to each other, see Fig. 1.3, resulting in different density of states for spin-up and spin-down electrons in each energy level. These spin sub-bands are not completely filled for Fe ($Z = 26$), Co ($Z = 27$) and Ni ($Z = 28$) and, therefore, an excess of spin-up or spin-down electrons is present in the system, which gives rise to the ferromagnetism of these elements. In contrast, Cu ($Z = 29$), just having one more electron, fills up completely both $3d$ spin sub-bands and, thus, it does not show ferromagnetism.

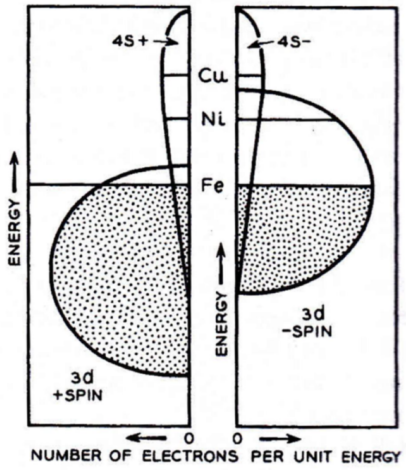

Figure 1.3: **Sketch of the density of states and indicators of Fermi level for Fe, Ni and Cu.** Three horizontal lines indicate the Fermi level of each material. In case of Fe and Ni, the density of states at the Fermi level is different for spin-up and spin-down electrons and for Cu it is equal. Figure adapted from Ref. [25].

Whereas the overall unbalanced spin population gives rise to the spontaneous magnetization in a ferromagnet, it is the unbalanced density of states at the Fermi level ($N_{\uparrow}(E_{\mathrm{F}}) \neq N_{\downarrow}(E_{\mathrm{F}})$, see the different length of the horizontal line for $3d$+spin and $3d-$spin in Fe and Ni in Fig. 1.3) that gives rise to the spin-dependent transport, as transport in metals occurs at the Fermi level. Therefore, transport processes for spin-up and spin-down electrons are different in ferromagnets: the Fermi velocities ($v_{\mathrm{F}\uparrow} \neq v_{\mathrm{F}\downarrow}$), as well as the mean free paths ($\lambda_{\mathrm{e}\uparrow} \neq \lambda_{\mathrm{e}\downarrow}$), leading to different conductivities:

$$\sigma_{\uparrow,\downarrow} = \frac{1}{3} N_{\uparrow,\downarrow}(E_{\mathrm{F}}) e^2 v_{\mathrm{F}\uparrow,\downarrow} \lambda_{\mathrm{e},\uparrow,\downarrow}, \tag{1.1}$$

where e is the charge of the electron.

Consequently, the conduction in a FM metal can be interpreted as two independent and parallel channels, one with spin-up electrons and the other with spin-down electrons flowing. This "two-channel model" was proposed by Mott in 1936 [26]. The total charge current, I_{c}, is the addition of the current of each

channel, $I_c = I_\uparrow + I_\downarrow$, and the spin current is the subtraction, $I_s = I_\uparrow - I_\downarrow$, which transports angular momentum. In a FM metal, the usual I_c is accompanied by I_s, since $\sigma_\uparrow$ and $\sigma_\downarrow$ are unequal and $I_\uparrow$ and $I_\downarrow$ do not cancel out. This leads to the creation of a *spin-polarized current*. We can thus define the current spin polarization, α_{FM}, as:

$$\alpha_{FM} = \frac{\sigma_\uparrow - \sigma_\downarrow}{\sigma_\uparrow + \sigma_\downarrow}. \tag{1.2}$$

The finite α_{FM} of ferromagnets makes them suitable to be used as a source of spin currents. Let us highlight that the electrons dominating the transport are the ones with the highest conductivity and these are not necessarily the electrons with the majority spin defining the magnetization [27].

Spin currents in NM materials

Since the density of states for spin-up and spin-down electrons at the Fermi level are equivalent in a NM material, see the case of Cu in Fig. 1.3, $N_\uparrow(E_F) = N_\downarrow(E_F)$, then $\sigma_\uparrow = \sigma_\downarrow$. This symmetry prevents the presence of a spontaneous spin-polarized current in NM elements and, hence, different techniques have been developed to inject a spin imbalance in such materials. In the following section (Section 1.1.3) we will focus on the spin injection methods in NM metals either using FM materials or exploiting different phenomena occurring in NM elements that give rise to spin currents.

Spin relaxation

In contrast to charge currents, spin currents are not conservative. Conduction electrons interact with their environment and find different ways to relax their spin, *i.e.* to bring an unbalanced population of spin states into equilibrium. This relaxation occurs due to the SOC which is the interaction between the spin and orbital momentum of electrons. There are several spin relaxation mechanisms based on the SOC.

The Elliott-Yafet (EY) mechanism is governing in conductors with spacial inversion symmetry in the absence of magnetic impurities. The spin of the electron in these elements interacts with the local electric field generated by the lattice ions (phonons), non-periodic impurities or crystal grain boundaries, resulting in a spin-flip scattering, see Fig. 1.4(a). The spin relaxation time τ_s, the characteristic time during which the electron conserves its spin, is proportional to the momentum relaxation time τ. τ is the characteristic time during which the electron conserves its momentum, an indication of how often it scatters, and it is defined as $3/(\rho_{NM} N(E_F) e^2 v_F^2)$, where ρ_{NM} is the resistivity of the NM metal. The proportionality between both terms, $\tau_s \propto \tau$, can be understood

as the spin flipping has certain probability to occur during a scattering event. This relaxation mechanism dominates in light metals with weak SOC, such as Cu [28, 29], Ag [30–32] and Al [29] and also in some heavy metals with strong SOC, such as in polycrystalline Pt [33] and Ta [34].

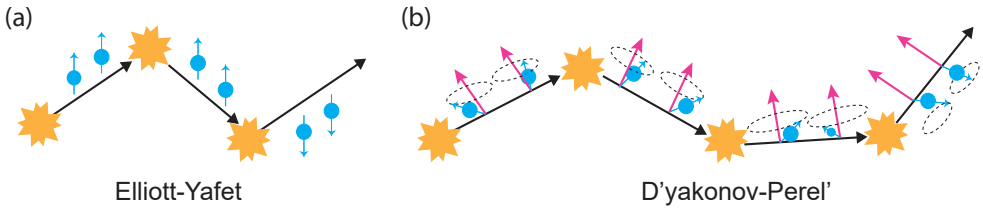

Figure 1.4: **Spin relaxation mechanisms.** Sketch of (a) Elliott-Yafet mechanism and (b) D'yakonov-Perel' mechanism. Yellow stars represent momentum scattering events and the pink arrows show the orientation of the effective magnetic field that the electrons feel and spins precess around.

On the contrary, the spin relaxation due to D'yakonov-Perel' (DP) mechanism arises in conductors that lack spatial inversion symmetry. The spin-up and spin-down energy levels in the conduction bands are split, generating a momentum-dependent effective magnetic field, which leads to spin precession and, hence, spin relaxation. When the electron scatters, its velocity is modified and so does the effective magnetic field, thus the precession will start again but along a different axis, see Fig. 1.4(b). The smaller the momentum relaxation time is, the less time the spin has to change its direction by precession around the magnetic field, which makes the spin relaxation time longer. Then, $\tau_s \propto 1/\tau$. DP mechanism dominates in III-V semiconductors, such as GaAs [35, 36] which has zincblende structure characterized by bulk inversion asymmetry. In surface or interfaces, where the spacial inversion symmetry is broken, DP mechanism becomes also dominant. This is the case for thin epitaxial films of Pt and Ta [33, 34].

The transport of spin information should be realized in materials with weak spin relaxation. We define the spin diffusion length, λ_s, as the characteristic distance at which the polarization of the diffusive spin current decays. λ_s is related to τ_s as $\lambda_s = \sqrt{D\tau_s}$, where $D = 1/(\rho_{NM} N(E_F) e^2)$ is the diffusion coefficient.

Generally, λ_s is larger than the mean free path λ_e, which is the characteristic length where the electron conserves its momentum. Therefore, light metals with high conductivity (i.e. long λ_e) are useful as spin transporters in spintronic devices. The metals with longest λ_s are Cu, Ag and Al [37], where precisely EY dominates the spin relaxation mechanism. In this case, $\lambda_s \propto 1/\rho_{NM}$ is fulfilled given the linear relation between τ and τ_s, and the definition of D and τ. Considering that the length scales for λ_s in these materials are hundreds of nm, spintronic devices, namely the channels where the spin is transported, should be of these dimensions.

1.1.3 Techniques for spin injection and detection in metals

Three basic capabilities are required in a spintronic device for a successful performance. First of all, spins should be injected in the transport channel. Then, the spin information should be transported and manipulated during the transport. Finally, the output spin current has to be detected. In the previous section, we summarized the relaxation mechanisms that take place during the transport of spin currents and we identified the light NM elements as the most convenient ones for this task. Now we will summarize the different techniques for spin injection and detection in NM metals.

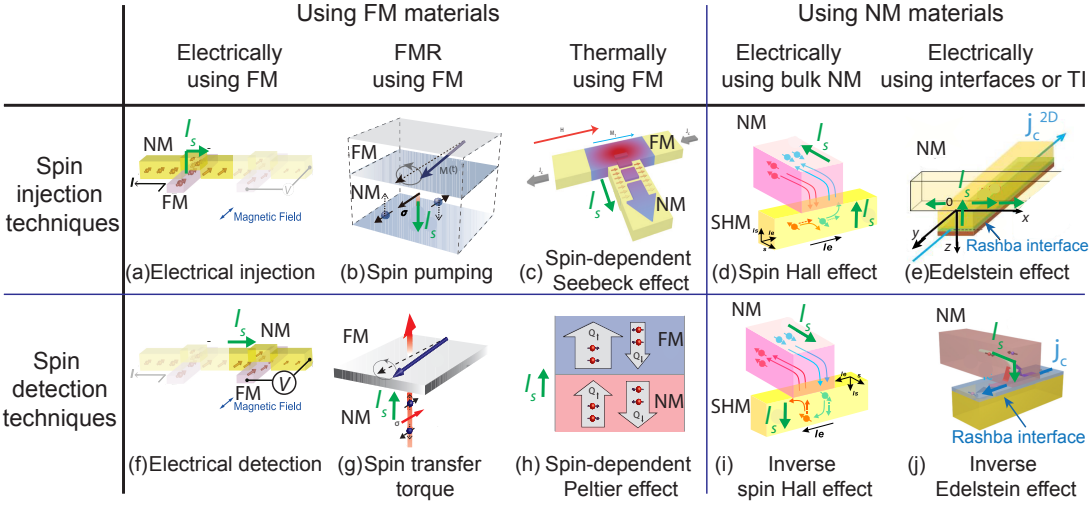

Figure 1.5: **Spin injection and detection techniques in NM metals.** (a) Electrical injection using FM materials. Figure adapted from Ref. [38]. (b) SP technique to inject spin currents. Figure adapted from Ref. [39]. (c) Thermal spin injection via spin-dependent Seebeck effect. Figure adapted from Ref. [40]. (d) Electrical spin injection via spin Hall effect occurring in a SHM. Figure adapted from Ref. [41]. (e) Electrical spin injection via Edelstein effect. Figure adapted from Ref. [42]. (f) Electrical detection using FM materials. Figure adapted from Ref. [38]. (g) Spin transfer torque technique to detect spin currents. Figure adapted from Ref. [43]. (h) Thermal spin detection via spin-dependent Peltier effect. Figure adapted from Ref. [44]. (i) Electrical spin detection via inverse spin Hall effect. Figure adapted from Ref. [41]. (j) Electrical spin detection via inverse Edelstein effect. Figure adapted from Ref. [45]. (a)-(c) and (f)-(h) require FM materials, and (d), (e), (i) and (j) do not.

The classical approach to generate spin currents in NM metals is by using FM materials that intrinsically have different amount of spin-up and spin-down electrons. There are different techniques that employ FM elements for spin injection into NM materials. One of the methods is the electrical injection [5], see Fig. 1.5(a). In a very simple picture, when there is a flow of charge current

from a ferromagnet into a NM material, which are in direct contact, the excess of spin-up electrons is accumulated at the interface and diffuses as a spin current in the NM element. This technique, which will be explained more in detail in the next chapter, offers the possibility of integration with conventional electronics. Spin pumping (SP) is another widely used method for spin injection based on the magnetization dynamics of ferromagnets [46]. When the magnetization of the FM element is precessing in ferromagnetic resonance (FMR), there is angular momentum transfer from the precessing local spins to the conduction electrons of the adjacent NM metal, see Fig. 1.5(b), thus, a spin current is generated here. The spin-dependent Seebeck effect is a thermal spin injection method that employs also ferromagnets. A temperature gradient in a FM metal generates a spin current, see Fig. 1.5(c), driven by the different Seebeck coefficient for spin-up and spin-down electrons in this type of material [40]. An alternative thermal spin injection technique, which is not limited only to FM metals but also exists for FM insulators, is the spin Seebeck effect. It is a collective effect where a temperature gradient in the ferromagnet generates a spin current, parallel to the temperature gradient, which is transported via magnons and injected into the adjacent NM material as electron spin current [47, 48].

Spin injection techniques without the need of FM materials are also being widely explored. The spin Hall effect (SHE) is a phenomenon where a charge current is converted into a transverse pure spin current in a spin Hall metal (SHM), *i.e.*, a NM metal with strong bulk SOC [49,50], see Fig. 1.5(d), which can diffuse to an adjacent NM material. The Edelstein effect (EE) [51], which occurs in 2D systems such as Rashba interfaces and surfaces of topological insulators (TI), gives rise to a net spin density when a charge current is injected, see Fig. 1.5(e). This spin imbalance can diffuse, leading to a spin current in the NM material, which is placed on one side of the Rashba interface or adjacent to the TI.

In order to detect spin currents, the reciprocal phenomena of the spin generation techniques are typically used. The electrical detection is based on measuring the spin voltage that corresponds to the spin accumulation in the FM/NM interface [5], as represented in Fig. 1.5(f). The reciprocal effect of the SP is the spin transfer torque, see Fig. 1.5(g), where an injected spin-polarized current into a FM element generates a torque in its magnetization, which can be detected by different approaches [43,52,53]. Thermal spin detection is realized via the spin-dependent Peltier effect [44], which results in a net heat current generated from the interface into the FM metal given that heat currents are different for majority and minority carriers, see Fig. 1.5(h). In case of the detection via spin Peltier effect, the temperature modulation generated via spin currents injected from a metal into a FM insulator can be detected using a thermopile [54]. The generated magnon current in the FM insulator interacts with phonons and the

magnetic fluctuations are the responsible of modulating the phonon temperature that is detectable.

Among the detection techniques without the need of ferromagnets, we find the inverse spin Hall effect (ISHE) [49, 50], represented in Fig. 1.5(i) and the inverse Edelstein effect (IEE) [51,55], shown in Fig. 1.5(j), where from a spin current and spin density, respectively, a measurable charge current is generated.

The aforementioned spin injection and detection techniques that do not require FM elements rely on different phenomena that are originated due to SOC and lead to spin-to-charge conversions. The opportunity they offer to generate and detect electrically a spin current in NM materials establishes them as promising effects for applications in spintronics. These phenomena are part of the emergent field of spin orbitronics.

1.2 Spin orbitronics

Spin orbitronics is a novel direction in spintronics that exploits the coupling between the orbital and spin degree of freedom, known as SOC, and offers a plausible opportunity to control magnetism electrically. Fundamentally, SOC is a relativistic effect in which the magnetic moment of a traveling particle in an electric field couples to an effective magnetic field that notices in its rest frame, in the absence of any externally applied magnetic field. A general expression to define an effective spin-orbit Hamiltonian is the following [56]:

$$\hat{H}_{\mathrm{SO}} = -\eta_{\mathrm{SO}}(\vec{p} \times \vec{\nabla} V) \cdot \vec{\sigma}, \tag{1.3}$$

where $\eta_{\mathrm{SO}} = \frac{\hbar}{4m_0^2c^2}$, being m_0 the mass of the electron and c the speed of light. $\vec{\sigma}$ is the vector of Pauli matrices, V is the potential acting on the electron and $\vec{p}$ the momentum operator.

Comparing to the Hamiltonian that describes the Zeeman effect $\hat{H}_{\mathrm{Z}} = g\mu\vec{B}\cdot\vec{\sigma}$, we can deduce that $-(\eta_{\mathrm{SO}}/g)\mu(\vec{p}\times\vec{\nabla}V)$ is the effective magnetic field the electron is coupling to and is influencing its behavior and trajectory. In other words, the Zeeman interaction between the electron spin and the magnetic field, $\vec{B}$, is analogous to the coupling of the electronic spin and momentum degrees of freedom [57]. SOC splits degenerate spin sub-bands, modifying the electronic band structure, and induces novel spin-dependent transport phenomena.

In a solid, the potential V acting on the electron is composed by several contributions: i) the periodic potential related to the lattice and ii) a non-periodic one ascribed to the impurities, boundaries and external applied fields [56]. SOC is also present in systems with structural inversion asymmetry, such as in metallic

surfaces and interfaces. Therefore, the SOC can have different origins and will result in different spin-dependent transport phenomena [57, 58].

Among the key spin-orbit phenomena are the anomalous Hall effect (AHE), the SHE and EE. The AHE and SHE are widely studied transport phenomena that are driven by the bulk SOC. The EE is a consequence of the SOC present in 2D systems with spin-momentum locking, such as surface states of TIs and Rashba interfaces. These phenomena give rise to SCCs that will be studied in this thesis. In the following, we will give a detailed description of these effects.

1.2.1 Anomalous Hall effect

The ordinary Hall effect (OHE), discovered by E. H. Hall in 1879, was well understood as a result of the Lorentz force deflecting the charge carriers under the application of an external out-of-plane magnetic field, H_z, in metals and semiconductors [59], see Fig. 1.6(a). Thereby a transverse voltage (perpendicular to the charge current and magnetic field) and, thus, a transverse resistivity, ρ_{xy}, was measurable in these systems. This transverse resistivity originated from the OHE is proportional to the applied magnetic field:

$$\rho_{xy} = R_0 H_z, \tag{1.4}$$

where $R_0 = -1/(n_c e)$ is the Hall coefficient, a material dependent constant whose sign depends on the type of carrier (electron or hole) and the magnitude on the density of carriers, n_c. When E. H. Hall tried to measure his recently discovered effect in FM materials, it turned out that the measured Hall resistivity included an additional contribution even at $H = 0$, the so-called AHE [60]. Although the AHE and OHE contributions sum up in the measured transverse voltage in a FM conductor, contrary to the OHE, no magnetic field is required for the AHE. The following phenomenological equation, which considered the OHE and AHE, was proposed by Smith and Sears in 1929 [61]:

$$\rho_{xy} = \rho_{OH} + \rho_{AH} = R_0 H_z + R_1 \mu_0 M, \tag{1.5}$$

where R_1 is the anomalous Hall coefficient, μ_0 the vacuum permeability and M the out-of-plane magnetization of the FM conductor. The equation indeed highlights that the AHE depends on the magnetization of the FM material rather than on the applied magnetic field. Even if the equation was successful to describe the AHE in many FM materials, it did not offer a microscopic interpretation of the effect.

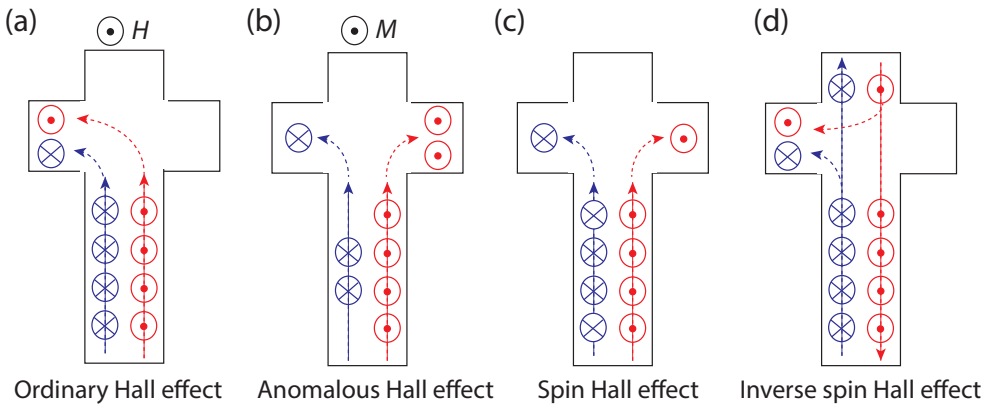

Figure 1.6: **Different Hall effects.** Sketches of the (a) ordinary Hall effect, (b) anomalous Hall effect, (c) spin Hall effect and (d) inverse spin Hall effect. Red (blue) circles containing a dot (cross) represent spin-up (spin-down) electrons.

The relation between longitudinal resistivity and conductivity, σ_{xx} is:

$$\rho_{xx} = \sigma_{xx}^{-1} \tag{1.6}$$

and for transverse resistivity and conductivity we have:

$$\rho_{\mathrm{xy}} = -\frac{\sigma_{\mathrm{xy}}}{\sigma_{\mathrm{xy}}^2 + \sigma_{\mathrm{xx}}^2} \approx -\frac{\sigma_{\mathrm{xy}}}{\sigma_{\mathrm{xx}}^2} = \sigma_{\mathrm{xy}}\rho_{\mathrm{xx}}^2. \tag{1.7}$$

Note that $\rho_{\mathrm{xy}} = -\rho_{\mathrm{yx}}$. In this thesis, the anomalous Hall parameters are given in xy, *i.e.* $\rho_{\mathrm{AH}} \equiv \rho_{\mathrm{xy,AH}}$ and $\sigma_{\mathrm{AH}} \equiv \sigma_{\mathrm{xy,AH}}$.

The anomalous Hall angle, θ_{AH}, relates ρ_{AH} with ρ_{xx} and the anomalous Hall conductivity, σ_{AH}, with σ_{xx}:

$$\theta_{\mathrm{AH}} = -\frac{\rho_{\mathrm{AH}}}{\rho_{\mathrm{xx}}} = \frac{\sigma_{\mathrm{AH}}}{\sigma_{\mathrm{xx}}}. \tag{1.8}$$

Anomalous Hall effect mechanisms

It took more than 70 years to establish the SOC as the driving force of the AHE. When a charge current is injected in a longitudinal direction in a FM conductor, SOC acts as an effective magnetic field that deflects the spin-up and spin-down electrons in opposite direction, see Fig. 1.6(b). The difference between $\sigma_{\uparrow}$ and $\sigma_{\downarrow}$, which can be illustrated as different amount of spin-up and spin-down conduction electrons, gives rise to a transverse charge accumulation, which can be measured as a transverse voltage drop. Note that the injected current, spin polarization and the generated transverse charge accumulation are mutually perpendicular. There are different mechanisms that contribute to the AHE:

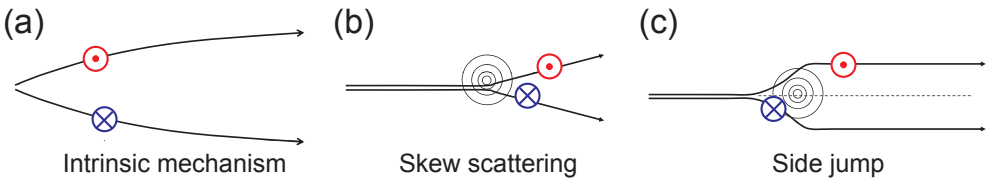

Figure 1.7: **Anomalous Hall effect mechanisms.** Sketches of the (a) intrinsic mechanism, (b) skew scattering and (c) side jump. Red (blue) circles containing a dot (cross) represent spin-up (spin-down) electrons and the black concentric circles are the equipotential lines induced by the impurities. Figure adapted from Ref. [62].

- **Intrinsic mechanism**

  Karplus and Luttinger (1954) were the first authors in pointing out that the AHE was related to SOC which could create a transverse velocity in between scattering events [63], see Fig. 1.7(a). Nowadays, this mechanism is identified as the intrinsic mechanism of the AHE, which relies on the band structure of the metal and is described by the Berry curvature. From the latter, the intrinsic anomalous Hall conductivity, $\sigma_{\mathrm{AH}}^{\mathrm{int}}$, can be calculated [64], a constant value linked to the band structure of each metal. From Eq. 1.7, $\rho_{\mathrm{AH}} = \sigma_{\mathrm{AH}}^{\mathrm{int}}\rho_{\mathrm{xx}}^2$ dependence is obtained.

- **Extrinsic mechanisms: skew scattering and side jump**

  Some years later, skew-scattering and side-jump mechanisms were proposed by Smit in 1958 [65] and Berger in 1970 [66], respectively. In these cases, the transverse displacement is generated during the scattering with impurities and are thus extrinsic mechanisms. Skew scattering contribution arises due to spin-dependent scattering caused by effective SOC of impurities in the lattice, see Fig. 1.7(b). The corresponding ρ_{AH} shows linear dependence with the residual resistivity, $\rho_{\mathrm{xx,0}}$: $\rho_{\mathrm{AH}} = \alpha_{\mathrm{AH}}^{\mathrm{ss}}\rho_{\mathrm{xx,0}}$, being $\alpha_{\mathrm{AH}}^{\mathrm{ss}}$ the skew-scattering angle. Namely, the residual resistivity of a metal is its resistivity at low temperatures, which is originated from the scattering of the electrons at impurities, and it is independent of temperature. Side-jump scattering results in a deflection of the electron velocity in opposite direction for the different spin states due to the opposite electric field they experience when approaching an impurity, see Fig. 1.7(c). ρ_{AH} corresponding to this mechanism is proportional to $\rho_{\mathrm{xx,0}}^2$, being the proportionality constant the anomalous Hall conductivity related to side-jump contribution, $\sigma_{\mathrm{AH}}^{\mathrm{sj}}$.

The total AHE occurring in a FM conductor will be a combination of the different mechanisms occurring simultaneously. We arrive to the following general equation, which was proposed by Tian *et al.* in 2009 [67], where the three mentioned contributions are considered:

$$-\rho_{\mathrm{AH}} = \alpha_{\mathrm{AH}}^{\mathrm{ss}}\rho_{\mathrm{xx,0}} + \sigma_{\mathrm{AH}}^{\mathrm{int}}\rho_{\mathrm{xx}}^2 + \sigma_{\mathrm{AH}}^{\mathrm{sj}}\rho_{\mathrm{xx,0}}^2. \tag{1.9}$$

Following Eq. 1.7, Eq. 1.9 can be rewritten in terms of conductivities as:

$$\sigma_{\mathrm{AH}} = \alpha_{\mathrm{AH}}^{\mathrm{ss}} \sigma_{\mathrm{xx},0}^{-1} \sigma_{\mathrm{xx}}^{2} + \sigma_{\mathrm{AH}}^{\mathrm{int}} + \sigma_{\mathrm{AH}}^{\mathrm{sj}} \sigma_{\mathrm{xx},0}^{-2} \sigma_{\mathrm{xx}}^{2}. \tag{1.10}$$

Resistivity or conductivity dependent studies are adequate to unveil the weight of each mechanism of the AHE and determine which one dominates. The transition of the AHE from the moderately dirty regime, where the intrinsic mechanism is governing, to a superclean metal regime, where the extrinsic effects are dominating, has been observed in several FM conductors, such as in Fe(001) shown in Fig. 1.8 [68, 69]. In the dirty limit, a $\sigma_{\mathrm{xy}} \propto \sigma_{\mathrm{xx}}^{n}$ dependence has been observed, being $n = 1.66$, a scaling behavior that is consistent with other FM compounds in this regime [70].

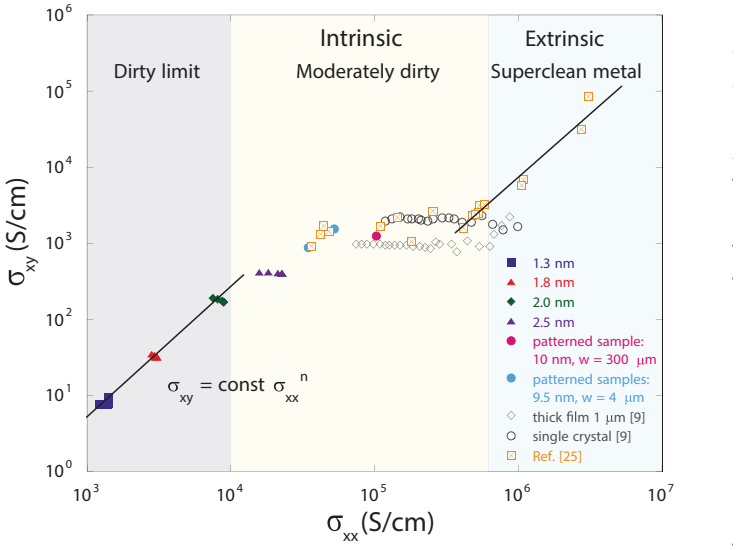

Figure 1.8: **Different regimes of the AHE in Fe(001).** Anomalous Hall conductivity *vs.* longitudinal conductivity of Fe (001). Three regimes are distinguished. In the dirty limit $\sigma_{\mathrm{xy}} \propto \sigma_{\mathrm{xx}}^{n}$, being $n = 1.66$, dependence has been found. In the moderately dirty regime the intrinsic mechanism governs and $\sigma_{\mathrm{xy}} = \sigma_{\mathrm{AH}}^{\mathrm{int}}$ is a constant value. In the superclean regime, the extrinsic mechanism dominates. Figure adapted from Ref. [68].

Six years later, a multivariable scaling law for the AHE was proposed by Hou *et al.* [71]:

$$-\rho_{\mathrm{AH}} = \alpha_{\mathrm{AH}}^{\mathrm{ss}} \rho_{\mathrm{xx},0} + \beta_{\mathrm{AH}}^{0} \rho_{\mathrm{xx},0}^{2} + \gamma_{\mathrm{AH}} \rho_{\mathrm{xx},0} \rho_{\mathrm{xx,T}} + \beta_{\mathrm{AH}}^{1} \rho_{\mathrm{xx,T}}^{2}, \tag{1.11}$$

where $\rho_{\mathrm{xx,T}} (= \rho_{\mathrm{xx}} - \rho_{\mathrm{xx},0})$ is the resistivity induced by phonons. In this expression, the side-jump terms due to static (impurities or grain boundaries) and dynamic (phonons) scattering sources as well as the intrinsic contribution are entangled in β_{AH}^{0}, γ_{AH} and β_{AH}^{1} parameters in a complex manner. Nevertheless, the effect

of the intrinsic contribution is most strongly reflected in the β^1_{AH} term. Equation 1.11 can be rewritten in terms of conductivities as:

$$\sigma_{\mathrm{AH}} = \alpha^{\mathrm{ss}}_{\mathrm{AH}}\sigma^{-1}_{\mathrm{xx},0}\sigma^{2}_{\mathrm{xx}} + \beta^{1}_{\mathrm{AH}} + (\beta^{0}_{\mathrm{AH}} - \beta^{1}_{\mathrm{AH}})\sigma^{-2}_{\mathrm{xx},0}\sigma^{2}_{\mathrm{xx}} + (\gamma - 2\beta^{1}_{\mathrm{AH}})(\sigma^{-1}_{\mathrm{xx},0}\sigma_{\mathrm{xx}} - \sigma^{-2}_{\mathrm{xx},0}\sigma^{2}_{\mathrm{xx}}). \tag{1.12}$$

The first three terms on the right hand side of Eq. 1.12 have the same form as Eq. 1.10. The last term, is negligible at low temperature limit (where $\sigma_{\mathrm{xx},0} \simeq \sigma_{\mathrm{xx}}$) and high temperature limit in case of high purity metals ($\sigma_{\mathrm{xx},0} \gg \sigma_{\mathrm{xx}}$). Therefore, it is in the intermediate temperature regime where this last term takes relevance [71].

1.2.2 Spin Hall effect

Once SOC was ascribed as the origin of the AHE in ferromagnets, it was concluded that SOC should also result in spin-up and spin-down deflections in NM materials. By 1971, D'yakonov and Perel' had already predicted that the SOC would convert charge currents into transverse spin currents and vice versa [72]. However, Hirsch, who was the responsible for its resurgence, introduced the term 'spin Hall effect' in 1999 for this phenomenon [73].

In a NM material, the density of states for spin-up and spin-down electrons are equal, as well as the corresponding conductivities (see Section 1.1.2) and, hence, any flowing charge current will be unpolarized. When a charge current is injected in a NM conductor with strong SOC, opposite spins are deflected in the opposite direction due to the same mechanisms that give rise to the AHE in the FM materials, generating a transverse spin accumulation, see Fig. 1.6(c). Whereas the AHE results in a transverse charge imbalance, the SHE is associated to a transverse spin accumulation without a charge imbalance, which makes the effect more difficult to measure. The gradient of this spin accumulation gives rise to a diffusive pure spin current. Note that the injected charge current, the spin polarization and the generated pure spin current are mutually perpendicular. It is important to remark that both the AHE and the SHE exist in the absence of external magnetic fields.

Since the SHE results in the conversion of a charge current into a pure spin current, it can be used as a pure spin current generation technique, see Fig. 1.5(d). The reciprocal phenomenon of the SHE, ISHE, converts pure spin current into transverse charge current, see Fig. 1.6(d), and relies on the same mechanisms as the SHE. Hence, it can be used as a spin current detection method, see Fig. 1.5(i) .

The spin Hall angle, θ_{SH}, determines the efficiency of the SCC, *i.e.* how much

pure spin current density, $\vec{j_s}$, has been generated for a given charge current density, $\vec{j_c}$, and can be expressed as:

$$\vec{j_s} = \left[\frac{\hbar}{e}\right]\theta_{SH}\vec{j_c} \times \vec{s} \qquad \text{for SHE} \tag{1.13}$$

$$\vec{j_c} = \left[\frac{e}{\hbar}\right]\theta_{ISH}\vec{j_s} \times \vec{s} \qquad \text{for ISHE,} \tag{1.14}$$

where $\vec{s}$ is the spin polarization. $\theta_{SH} = \theta_{ISH}$ due to Onsager reciprocity [41]. In analogy to θ_{AH}, θ_{SH} can be also written in terms of the spin Hall resistivity, ρ_{SH}, and the spin Hall conductivity, σ_{SH} *:

$$\theta_{SH} = -\frac{\rho_{SH}}{\rho_{xx}} = \frac{\sigma_{SH}}{\sigma_{xx}}. \tag{1.15}$$

In this thesis, the spin Hall parameters will be given in xy, *i.e.* $\rho_{SH} \equiv \rho_{xy,SH}$ and $\sigma_{SH} \equiv \sigma_{xy,SH}$.

Spin Hall effect mechanisms

It is commonly accepted that the SHE and AHE share the same origin, *i.e.* both rely on the same mechanisms [49, 76]. Therefore, it is reasonable to employ the phenomenological equation of ρ_{AH}, Eq. 2.27, for ρ_{SH}:

$$-\rho_{SH} = \sigma_{SH}^{int}\rho_{xx}^2 + \alpha_{SH}^{ss}\rho_{xx,0} + \sigma_{SH}^{sj}\rho_{xx,0}^2. \tag{1.16}$$

Here σ_{SH}^{int} is the intrinsic spin Hall conductivity, α_{SH}^{ss} is the skew-scattering angle and σ_{SH}^{sj} is the spin Hall conductivity related to side jump. This equation was first successfully used in a study of the SHE in Pt and Au in our group in collaboration with Dr. Martin Gradhand [77]. As we will demonstrate in Chapters 4 and 5, the experimental results on the SHE of Pt and Ta are consistently explained with this equation and allows us to quantify the weight of each mechanism.

Theoretically, the intrinsic and extrinsic contributions have been separately quantified for different systems. Tanaka *et al.* reported σ_{SH}^{int} values for different $4d$ and $5d$ transition metals as shown in Fig. 1.9(a), obtaining the largest value for Pt [78]. There is a sign change in σ_{SH}^{int} when the electron number in the outermost shell $n = n_s + n_d$ (being n_o the number of electrons in the o orbital) increases. Gradhand and coworkers analyzed the skew-scattering mechanism in dilute alloys and proposed the ones with the largest θ_{SH} [79], see Fig. 1.9(b). Interestingly, they are the ones which combine a light metal with a heavy element, such as Ag(Bi),

*In this thesis σ_{SH} is defined in units of $\hbar/e$. We use this notation following Ref. [74], in order to have consistency with AHE measurements, other SHE measurements, and theoretical expressions. In some other works, σ_{SH} is defined in units of $\hbar/(2e)$ or $\theta_{SH} = 2\frac{\sigma_{SH}}{\sigma_{xx}}$. Therefore, θ_{SH} is double than in our case. A discussion can be found in the Supplemental Material of Ref. [75].

Cu(Bi) and Au(C). Since the SOC in solids is influenced by the nuclei, it was reasoned that the presence of heavy metals gives rise to a larger SHE [56] and this is in agreement with theoretical predictions for both intrinsic and extrinsic mechanisms.

Experimentally, the largest values of θ_{SH} have been obtained in heavy metals, such as Pt, Ta and W, or light materials with heavy impurities, such as Cu_xBi_{1-x} [80] or Cu_xIr_{1-x} [81], see Table 1.1, as it was predicted theoretically.

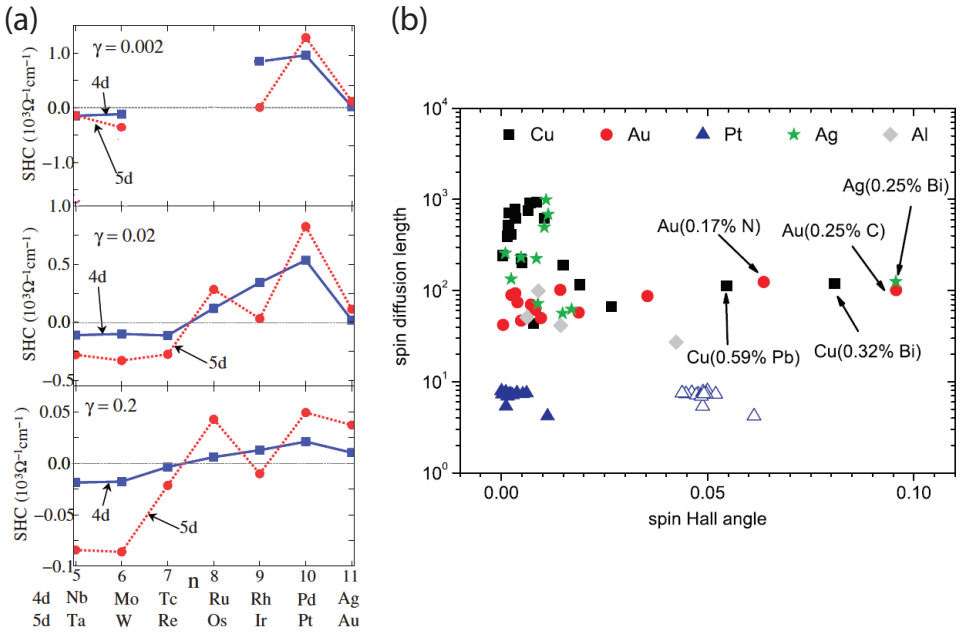

Figure 1.9: **Theoretical calculations of spin Hall parameters corresponding to intrinsic and extrinsic SHE mechanisms.** (a) Intrinsic spin Hall conductivity *vs.* electron number in the outermost shell for different $4d$ and $5d$ transition metals. Three different panels correspond to different resistivity regimes of the metals (the resistivity increases from top to bottom). Figure taken from Ref. [78]. (b) Spin diffusion length (in nm) *vs.* skew-scattering angle for different diluted alloys with different host materials. Figure taken from Ref. [79].

SHE measurement techniques

Although the spin accumulation generated by the SHE is not straightforward to measure, different techniques have been developed. The first SHE measurement was performed in films of semiconductor GaAs by optical means by Kato *et al.* in 2004 [97]. They extracted the position dependent spin density in GaAs using the magneto-optical Kerr effect (MOKE) and observed the opposite spin accumulation in the edges of the semiconductor induced by the SHE when a charge current was applied in the longitudinal direction, see Fig. 1.10(a). The ISHE was soon detected in metals. Saitoh *et al.* injected a pure spin current

Table 1.1: Spin Hall angle values* found in literature for different transition metals with different resistivity and measured using different techniques (SA: Spin absorption, SP: spin pumping, ST-FMR: spin-torque ferromagnetic resonance, LSSE: longitudinal spin Seebeck effect, MO: magneto-optical detection). β-Ta and β-W refer to the β-phase of the material. *θ_{SH} values are normalized by considering σ_{SH} in units of $(\hbar/e)$ and the definition of θ_{SH} given by Eq. 1.15.

Material	$\rho_{xx}(\mu\Omega cm)$	θ_{SH} (%)*	Technique	Ref.
β-Ta	185	-5.5	ST-FMR	[82]
	190	-7.5	ST-FMR	[83]
	200	-3 ± 1	SP	[84]
	350	≈ -0.5	LSSE	[85]
	133-1250	≈ -1.0	SP	[86]
	180	≈ -2.0	SP	[87]
	130-400	-0.3 ± 0.05	SP	[88]
β-W	170	-17 ± 3	ST-FMR	[89]
Pt	$12.5 - 18$	$0.44 - 0.9$	SA	[90]
	12.4	2.1 ± 0.5	SA	[74]
	16-27	4 ± 1	MO	[75]
	17.9 ± 0.2	5.6 ± 1.0	SP	[91]
	20	7.6	ST-FMR	[52]
	15	8.0 ± 0.5	ST-FMR	[92]
Au	3.62	0.21 ± 0.07	SA	[77]
	4.0	1.4 ± 0.4	SA	[93]
Nb	91	-0.87 ± 0.20	SA	[74]
Mo	35.7	-0.80 ± 0.18	SA	[74]
Pd	45.5	1.2 ± 0.4	SA	[74]
Cu_xBi_{1-x}	≈ 10	-11	SA	[80]
Cu_xIr_{1-x}	≈ 10	2.1 ± 0.6	SA	[81]
Cu_xPb_{1-x}	5.4	-13 ± 3	SA	[93]
$Cu_{72}Pt_{28}$	~ 50	5.4	ST-FMR	[94]
Ag_xBi_{1-x}	6.8	-2.3 ± 0.6	SA	[93]
Au_xTa_{1-x}	85	50	SP	[95]
Au_xW_{1-x}	90	15	SP&SA	[95]
Au_xPt_{1-x}	~ 50	$20 - 30$	SP	[96]

via SP in Pt, which was converted into a charge current due to the ISHE and measured the corresponding voltage drop in 2006 [46], see Fig. 1.10(b). In the same year, Valenzuela and Tinkham measured the ISHE in Al using a lateral spin valve (LSV) [98], which consists of a CoFe spin injector with Al_2O_3 tunnel barriers and Al spin channel. A pure spin current was electrically injected from CoFe into Al with out-of-plane spin polarization and the spin-up and spin-down electrons were deflected in opposite directions as a consequence of ISHE, giving rise to a transverse voltage drop, V, see Fig. 1.10(c).

The reciprocity between the SHE and ISHE was confirmed by Kimura *et al.* [41] in 2007 using the spin absorption technique in LSVs, see Fig. 1.10(d). This all-electrical technique will be detailed in the following chapter as it is the method employed in this thesis. In 2011, Liu *et al.* were able to evidence SHE via spin-torque ferromagnetic resonance (ST-FMR) in a $Ni_{81}Fe_{19}$/Pt bilayer [52]. The torque, resulting from the spin current that was generated due to the SHE when an alternating charge current was injected into the bilayer, induced a magnetization precession which led to an oscillatory AMR, see Fig. 1.10(e). From the measured dc voltage, originated from the oscillation of the bilayer resistance due to the AMR of the FM element and injected alternating charge current, they were able to quantify the SHE. The magnetization precession can also be analyzed by harmonic Hall measurements, which is a more recent technique to measure and quantify the SHE [99].

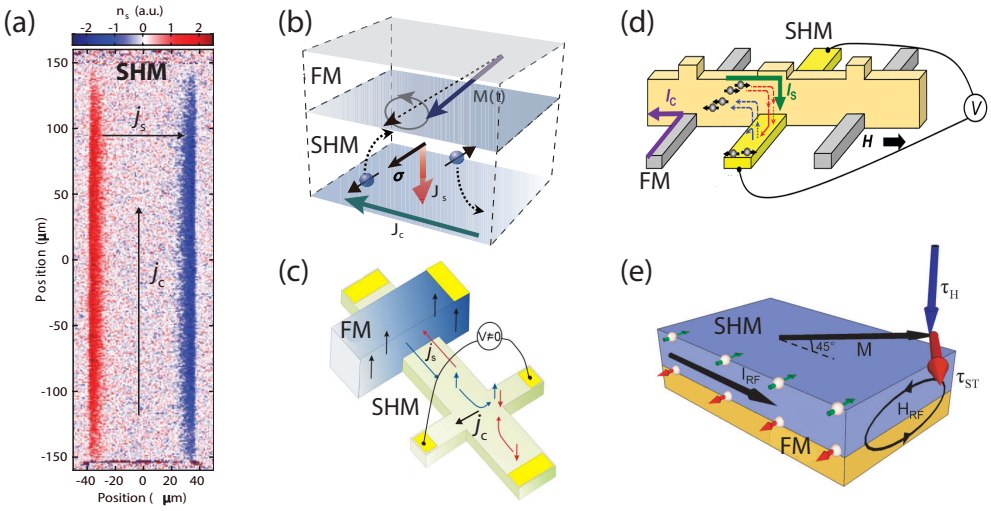

Figure 1.10: **Different techniques to measure the SHE.** (a) Optical method. Figure adapted from Ref. [97]. (b) SP technique. Figure taken from Ref. [39]. (c) LSV using a SHM with a relatively long λ_s, of hundreds of nm, as a channel. Figure taken from Ref. [100]. (d) Spin absorption technique in a LSV containing a SHM with short λ_s, from a few to tens of nm. Figure adapted from Ref. [101]. (e) ST-FMR technique. Figure taken from Ref. [83].

Table 1.1 evidences that there is a significant spread in the θ_{SH} value of a

same material among different groups and techniques. Given the complexity and peculiarity of each technique, each one has unavoidable systematic misestimations or spurious effects which makes the direct comparison among different results difficult. However, a general agreement and consensus is desired in the community in order to attain a complete fundamental understanding of the phenomenon, estimate the weight of each mechanism and open the path to efficient SCCs for spintronic applications.

1.2.3 Edelstein effect

Recently, spin-to-charge conversions occurring in 2D systems (two-dimensional electron gases, 2D materials, surfaces or interfaces) are also taking relevance in the field of spin orbitronics. The EE is the phenomenon that results in a net spin density, δs, when a charge current is injected in a system with spin-momentum locking [51]. Here, we will describe two systems where EE is occurring: Rashba interfaces and TIs.

Rashba SOC arises in systems with lack of inversion symmetry, such as surfaces or interfaces, where an electric field along the normal direction of the surface or interface is present. The coupling of the spin of conducting electrons to this electric field, or the effective magnetic field that they feel in their frame, is known as Rashba SOC. The Rashba Hamiltonian describes the interaction between the momentum and spin:

$$\hat{H}_{\mathrm{SO,R}} = \alpha_{\mathrm{R}}(\hat{z} \times \vec{k}) \cdot \vec{\sigma}, \tag{1.17}$$

where $\vec{k}$ is the wavenumber of carriers ($\hbar\vec{k}$ is the momentum), $\hat{z}$ is the direction normal to the interface, and α_{R} is the Rashba coefficient, proportional to the strength of the electric field and SOC. This interaction results in an opposite shift in the parabolic energy bands for spin-up and spin-down electrons, as indicated by the blue and red dashed arrows in Fig. 1.11(a). Here the effective magnetic field can be written as $\vec{B}(k) = 2\alpha_{\mathrm{R}}\hat{z} \times \vec{k}$ [56], which is perpendicular to $\vec{k}$, and therefore, it will cause the spins to align perpendicular to the momentum. This is clearly observed in the Fermi contours shown in Fig. 1.11(a).

In case of three-dimensional TIs, a similar single Fermi contour is obtained although its origin is totally different. The SOC in this type of system is strong enough to induce an inversion between $s - p$ bands with a gap in between that is ascribed to the insulating bulk of the system. In addition, extra bands arise corresponding to surface states with linear energy-momentum dispersion, describing a Dirac cone nearby the Fermi level, see Fig. 1.11(b). These specific energy bands are characteristic of TIs: the bulk of the system is insulator, whereas

the surface states are metallic. At the Fermi level, we find the helical contour of the Dirac cone where the spins point perpendicular to the momentum, as shown in Fig. 1.11(b).

The Fermi contours of Rashba interfaces and of the Dirac cone of TIs have a common feature: the spin-momentum locking, *i.e.* spin of the carriers are locked orthogonal to their momentum. Due to this especial characteristic, the systems own the capability for spin-to-charge conversion. If a charge current is injected along y direction in the Rashba system, which is equivalent to give momentum to the electrons $\Delta k_{\mathrm{y}} > 0$, both Fermi contours shift to the right side, which results in a net spin density ($\delta s_{\uparrow} \neq \delta s_{\downarrow}$), see Fig. 1.11(c). This effect, which was predicted theoretically by Edelstein for 2DEGs, is known as the Edelstein effect [51]. Although the induced spin density in each Fermi contour is opposite, they do not cancel out due to the larger δs in the outer contour. In case of the TI, since they are characterized by a single Fermi contour, the generated δs is more effective.

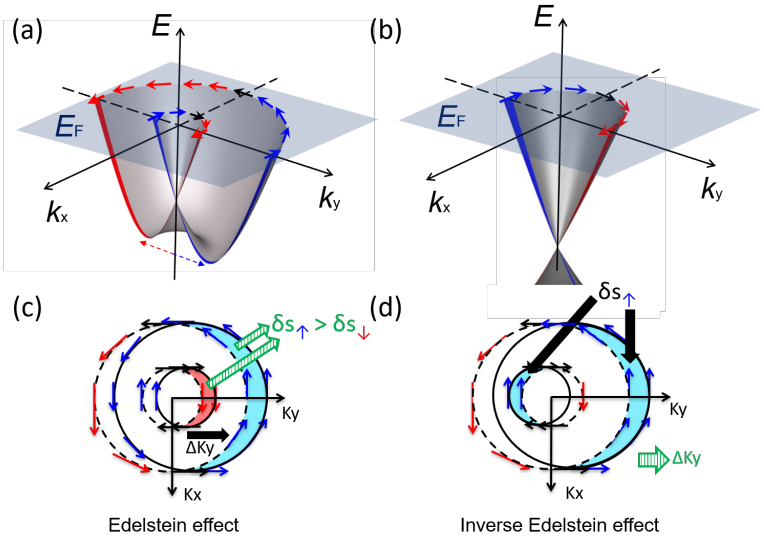

Figure 1.11: **The Edelstein effect and inverse Edelstein effect occurring in Rashba interfaces and topological insulators.** (a) Sketch of the splitting of spin sub-bands in a Rashba system with the spin texture at the Fermi energy. (b) Sketch of Dirac cone of a TI with the spin texture at the Fermi energy. (c) Representation of the EE in the Fermi contours of a Rashba system. When a charge current is injected in y direction, Fermi contours are displaced Δk_y in the same direction, giving rise to uncompensated spin densities $\delta s_{\uparrow} \neq \delta s_{\downarrow}$. (d) Representation of the IEE in the Fermi contours of a Rashba system. When a finite spin density is injected in the system, the Fermi contours are shifted in opposite y direction, giving rise to a net charge current in this direction.

In the reciprocal effect, the IEE, the injection of an imbalanced spin density in a Rashba system shifts the Fermi contours in opposite directions and an effective Δk_{y} is generated, giving rise to a net charge current, see Fig. 1.11(d). In the TI

system, equivalently, the single Fermi contour is shifted but without a partial cancellation of the effect.

EE has been observed in several Rashba interfaces, such as Bi/Ag [55], Bi/Cu [45], Bi_2O_3/Cu [102] and $LaAlO_3/SrTiO_3$ [103], and in TIs, such as α-Sn [104] and $(Bi_{1-x}Sb_x)_2Te_3$ [105].

1.3 This thesis

This thesis is based on the experimental study of SCC phenomena that rely on SOC. The aim of this fundamental study is to understand the mechanisms that give rise to these phenomena and find routes to enhance their efficiencies. The results are divided in two main parts. In the first part (Chapters 4, 5 and 6), we focus on the SHE occurring in heavy metals and in the second part (Chapters 7 and 8), we study the AHE and the SHE in different 3*d* FM systems. The manuscript is divided into 9 chapters in total.

Chapter 1 is a general introduction to spintronics and spin orbitronics. Most relevant discoveries and applications of the field are included and the main concepts and phenomena that are essential in this thesis are also described, such as the AHE and SHE.

Chapter 2 explains the principles of spin injection, accumulation, transport and detection of spin currents and presents the spintronic devices used in this thesis: LSVs and Hall bars. The functionality of each device is described together with the equations to quantify the spin transport and spin-to-charge conversion parameters.

Chapter 3 introduces the experimental techniques used in the fabrication and characterization of the spintronic devices employed in this thesis and details the specific recipes for their fabrication.

In **Chapter 4** and **Chapter 5**, the study of the SHE in Pt and Ta is presented, respectively. **Chapter 6** explores a spin-to-charge current converter based on a Pt/graphene heterostructure.

Chapter 7 is focused on the study of the relation between SHE and AHE in the 3*d* FM metals.

Chapter 8 investigates a novel interfacial contribution to the AHE of Co, induced by an oxide capping layer of Bi_2O_3.

Chapter 9 collects the final conclusions and the future perspectives.

Chapter 2

Spintronic devices

In this chapter, we introduce the spintronic devices that will be employed in this thesis: lateral spin valves (LSVs) and Hall bars (HBs). Firstly, we explain how spin currents are injected, accumulated, transported and detected in LSVs. We also describe the method to extract the spin injection and transport parameters: the current spin polarization of a ferromagnetic (FM) conductor, α_{FM}, and the spin diffusion length, λ_{s}, which have been defined in Chapter 1. Then, we focus on the spin absorption technique that allows us to characterize the short λ_{s} of some metals. This technique is also useful to study spin-to-charge current conversions (SCC), such as the spin Hall effect (SHE) or the Edelstein effect (EE). This is covered in the last part of the LSVs section where we explain how to extract the spin Hall parameters. The HB device is presented in the last part of this chapter. We describe how to measure the anomalous Hall effect (AHE) and how to extract the anomalous Hall parameters using this type of device.

2.1 Lateral spin valves

A spin valve is the most basic spintronic device used to study spin-dependent transport in metals and semiconductors. The first approaches and first technological successes of spintronics were related to vertical spin valves which consist of a FM and non-magnetic (NM) multilayered structures where the electrons flow perpendicular to the layers. Giant magnetoresistance was observed for instance on such a device [6, 7], see Fig. 1.1. Spin-polarized currents flow in these type of devices, preferentially in short distances, and there is no chance to generate pure spin currents.

LSVs are a second generation of spintronic devices where pure spin currents can be generated, transported, manipulated and detected. This is realized in a

nonlocal configuration, *i.e.* the current excitation path and the voltage path are spatially separated. As pure spin currents do not contain net charge current, spurious effects, such as anisotropic magnetoresistance (AMR) [106], are avoided in this type of devices. They consist of two FM electrodes bridged by a NM channel which is perpendicular to them, see Fig. 2.1(a). The first FM electrode (FM1) acts as a spin injector, a pure spin current is transported along the NM channel and the second FM electrode (FM2) is the spin detector. In LSVs, pure spin currents flow to longer distances than in vertical devices and they can be manipulated during the transport using gate voltages or magnetic fields.

2.1.1 Spin injection, accumulation, transport and detection

First of all, we introduce the concept of the electrochemical potential, because its gradient is the driving force for electron transport. The electrochemical potential, μ, is the sum of the chemical potential, μ_{ch}, defined as the energy needed to add one electron in the system, and the electric potential energy eV, being e the charge of the electron and V the electric potential that the electron is feeling. Thus, $\mu = \mu_{\mathrm{ch}} - eV$.

When there is an excess of electrons, with small deviations from equilibrium ($\Delta\mu_{\mathrm{ch}} \ll E_{\mathrm{F}}$), the chemical potential equals the excess electron density, n, divided by the density of states at Fermi energy, $N(E_{\mathrm{F}})$: $\mu_{\mathrm{ch}} = n/N(E_{\mathrm{F}})$. When the system is under an electric field, $\vec{E}$, electrons also posses electric potential energy. When μ varies in space, electrons tend to move to the region with lowest μ. This variation in μ might be originated by the spatial variation in the particle density ($\vec{\nabla}\mu_{\mathrm{ch}} \propto \vec{\nabla}n$), which leads to particle diffusion, or due to an electric field ($\vec{E} = -\vec{\nabla}V$), which results in a particle drift. The charge current density generated by the variation of the electrochemical potential is given by:

$$\vec{j}_{\mathrm{c}} = \frac{\sigma}{e}\vec{\nabla}\mu, \tag{2.1}$$

where σ is the electrical conductivity. Considering the two channel model introduced by Mott, see Section 1.1.2, Eq. 2.1 is also applied to the electrochemical potentials associated to spin-up and spin-down electrons ($\mu_{\uparrow,\downarrow}$):

$$\vec{j}_{\uparrow,\downarrow} = \frac{\sigma_{\uparrow,\downarrow}}{e}\vec{\nabla}\mu_{\uparrow,\downarrow}, \tag{2.2}$$

where $j_{\uparrow}$ ($j_{\downarrow}$) and $\sigma_{\uparrow}$ ($\sigma_{\downarrow}$) are the electron current density and conductivity of spin-up (spin-down) electrons, respectively. The sum of the two current densities results in the charge current density $\vec{j}_{\mathrm{c}} = \vec{j}_{\uparrow} + \vec{j}_{\downarrow}$ and the subtraction defines the spin current density $\vec{j}_{\mathrm{s}} = \vec{j}_{\uparrow} - \vec{j}_{\downarrow}$.

Spin injection and accumulation

When a charge current is applied in a FM material, there will be simultaneously a spin current due to the different conductivities of spin-up and spin-down electrons, see Section 1.1.2. Therefore, when a charge current, I_c, is driven from the FM1 to the NM channel (as indicated in Fig. 2.1(a)), where the conductivities for opposite spin orientations remain the same, electrons with a preferred spin orientation will accumulate at the interface, *i.e.* there will be a splitting of $\mu_\uparrow$ and $\mu_\downarrow$ as shown in Figs. 2.1(b) and 2.1(c). Namely, the spin accumulation is quantified by the magnitude of the splitting: $\mu_s = \mu_\uparrow - \mu_\downarrow$, which is tagged with an arrow in Figs. 2.1(b) and 2.1(c), and has the maximum value at the FM/NM interface. Importantly, the average of the spin-up and spin-down electrochemical potential away from the interface, $\mu_{ECP} = (\mu_\uparrow + \mu_\downarrow)/2$, is discontinuous at the FM/NM interface. The magnitude of the discontinuity is given by $\Delta\mu$, which in case of transparent FM/NM interfaces is related to the spin accumulation by:

$$\mu_s = \frac{2\Delta\mu}{\alpha_{FM}}. \tag{2.3}$$

In case of tunneling interfaces, instead of α_{FM}, the spin polarization of the interface, α_I, is relevant and it should be replaced in Eq. 2.3.

Additionally, on the right side of the LSV, there is no charge current flow (μ_{ECP} is constant), but a diffusion of a pure spin current due to the gradient of $\mu_\uparrow$ and $\mu_\downarrow$. Therefore, there is a decoupling between the charge current, that will flow to the left side, and the pure spin current, that will flow to the right side of the NM channel.

Spin transport

The generated spin accumulation at the FM/NM interface decays with the distance in the NM channel following the one-dimensional spin-dependent diffusion equation developed by Valet and Fert [107]:

$$D\frac{\partial^2\mu_s}{\partial^2 x} = \frac{\mu_s}{\tau_s^{NM}}, \tag{2.4}$$

where D is the diffusion coefficient and τ_s^{NM} the spin relaxation time of the NM material, which are related to the spin diffusion length as $\lambda_s^{NM} = \sqrt{D\tau_s^{NM}}$, see Section 1.1.2. The diffusive regime is considered given larger dimensions of the LSVs (hundreds of nanometers) as compared to the electron mean free path (tens of nanometers in polycrystalline metals [108]), λ_e, defined in Section 1.1.2. The criteria for the one-dimensional equation application is uniform interfacial spin current over the FM/NM contact area and over the thickness of NM channel, t_{NM}, which translates into $\lambda_s^{NM} \gg t_{NM}, w_{FM}, w_{NM}$, being w_{FM} and w_{NM} the widths

of the FM electrode and NM channel, respectively (see Fig. 2.1(a)). These are experimentally fulfilled when using light metals with long λ_s^{NM}, such as Cu, Ag, and Al. The solution of this equation has the following general form:

$$\mu_s = \mu_+ e^{-x/\lambda_s^{NM}} + \mu_- e^{x/\lambda_s^{NM}}, \tag{2.5}$$

where μ_+ and μ_- are coefficients to be defined from boundary conditions (continuity of charge and spin currents in space).

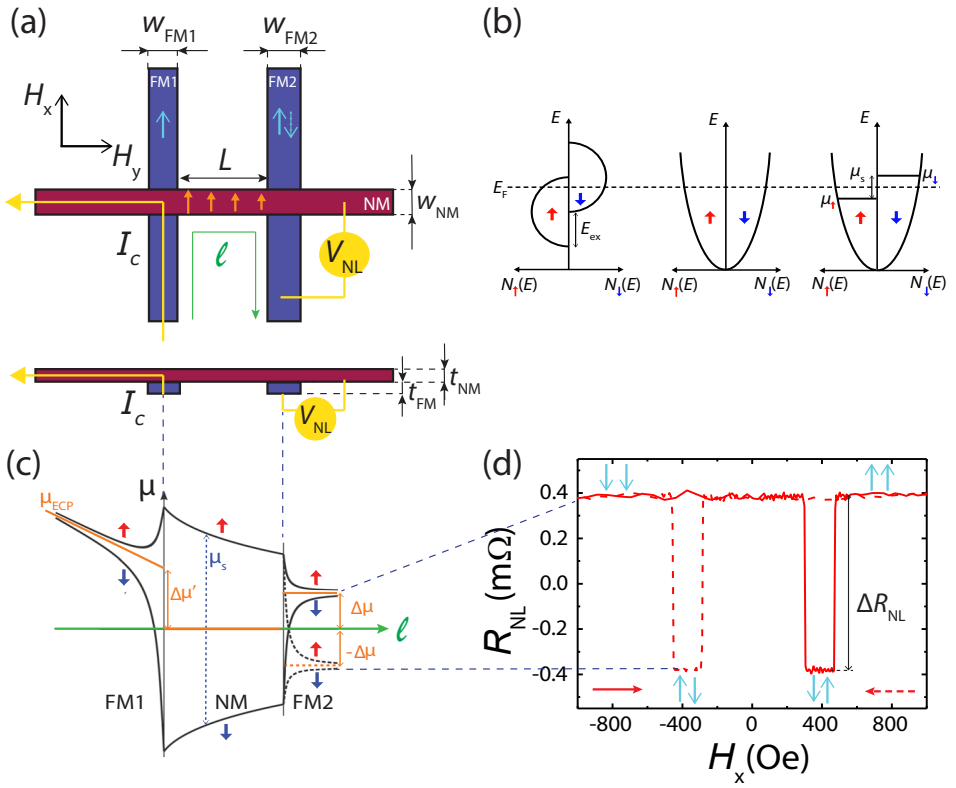

Figure 2.1: **Nonlocal measurement of spin accumulation in a LSV.** (a) Sketch of a LSV that consists of two FM electrodes (FM1 and FM2) bridged by a NM channel. The magnetization of FM1 and FM2 is represented by a light blue arrow. The solid (dashed) arrow in FM2 gives rise to the parallel (antiparallel) magnetization configuration of the FM electrodes. Orange arrows represent the spins diffusing through the NM channel. The nonlocal measurement configuration is shown. (b) Schematic representation of the density of states of spin sub-bands for a $3d$ orbital in a FM metal (left) and s orbital in a NM metal without (middle) and with (right) spin accumulation. (c) Sketch of the spatial dependence of the electrochemical potential in the LSV along the ℓ line in case of transparent FM/NM interfaces. Black solid (dashed) line is a representation of the spin-up, indicated by a red arrow, and spin-down, indicated by a blue arrow, chemical potentials where FM electrodes have a parallel (antiparallel) magnetization configuration. (d) Nonlocal resistance measured in a Py/Cu LSV at 10 K using the configuration shown in (a). Blue vertical arrows indicate the parallel or antiparallel configuration of the FM electrodes. The red solid (dashed) line and horizontal arrow indicate the sweeping direction of the magnetic field. The spin signal (ΔR_{NL}) is tagged.

Spin detection

In order to detect the pure spin current that is flowing in the NM channel, a second FM electrode is placed at a certain distance from the FM injector, close enough so that the spin splitting μ_s is still large enough to be detected. In the second FM/NM interface μ_{ECP} is also discontinuous, $\Delta\mu$, due to the spin imbalance present at this interface. This $\Delta\mu$ generates a voltage, $V_s = \Delta\mu/e$, which is measurable with a voltmeter. The sign of $\Delta\mu$ depends on the relative orientation between the two FM electrodes as shown in Fig. 2.1(c). The solution of Eq. 2.4 with the boundary conditions of continuity of charge and spin currents gives rise to the following V_s [109]:

$$V_s = \pm 2 I_c R_s^{NM} e^{-L/\lambda_s^{NM}} \frac{\hat{P}_1 \hat{P}_2}{r_1 r_2 - e^{-2L/\lambda_s^{NM}}}, \tag{2.6}$$

$$r_k = 2Q_{Ik} + 2Q_k + 1, \tag{2.7}$$

$$\hat{P}_k = \alpha_{Ik} Q_{Ik} + \alpha_k Q_k, \tag{2.8}$$

where $\pm$ corresponds to the parallel/antiparallel configuration of the FM electrodes. $Q_{Ik} = \frac{1}{1-(\alpha_{Ik})^2}\frac{R_{Ik}}{R_s^{NM}}$ and $Q_k = \frac{1}{1-(\alpha_k)^2}\frac{R_s^k}{R_s^{NM}}$. $k = 1, 2$ refers to FM1 and FM2, respectively. Table 2.1 names the quantities used in the equations.

The spin resistance is defined as

$$R_s = \rho\lambda_s/A, \tag{2.9}$$

where A is the cross-sectional area through which the spin current flows and ρ is the longitudinal resistivity of the metal [38]. In case of the NM channel, the cross sectional area at which the pure spin current flows is $A = w_{NM} t_{NM}$. In case of the FM electrode, due to its short λ_s, $A = w_{NM} w_{FM}$. Therefore, $R_s^{NM} = \frac{\lambda_s^{NM}\rho_{NM}}{w_{NM} t_{NM}}$ and $R_s^{FM} = \frac{\lambda_s^{FM}\rho_{FM}}{w_{FM} w_{NM}}$. The spin resistance represents the opposition of a material to the flow of spin current. Namely, the materials with lowest spin resistance will be the best spin absorbers, as spins prefer to relax on a material with low spin resistance.

As mentioned, the $\pm$ sign in Eq. 2.6 corresponds to the parallel and antiparallel configurations of the FM electrodes. In order to obtain these configurations, we design FM1 to be wider than FM2 so that the electrodes switch their magnetization direction, along the easy axis, at different magnetic fields. Figure 2.1(d) shows the nonlocal resistance measured in a Permalloy (Py, $Ni_{81}Fe_{19}$)/Cu LSV as a function of external magnetic field applied along the easy axis of the FM electrodes. By sweeping the magnetic field from negative to positive values (red solid line in Fig. 2.1(d)) and vice versa (red dashed line in Fig. 2.1(d)), we are able to observe both parallel ($\downarrow\downarrow, \uparrow\uparrow$) and antiparallel ($\downarrow\uparrow, \uparrow\downarrow$) configurations, as indicated by the blue arrows in Fig. 2.1(d).

Table 2.1: Relevant quantities of Eqs. 2.6, 2.7 and 2.8.

Symbol	Definition
$R_{\rm s}^{\rm NM}$	Spin resistance of NM
$R_{\rm s}^{k}$	Spin resistance of FM (k=1≡ FM1, k=2≡ FM2)
$\lambda_{\rm s}^{\rm NM}$	Spin diffusion length of NM
α_k	Spin polarization of the FM (k=1≡ FM1, k=2≡ FM2)
$\alpha_{{\rm I}k}$	FM/NM interface spin polarization (k=1≡ FM1/NM, k=2≡ FM2/NM)
$R_{{\rm I}k}$	FM/NM interface resistance (k=1≡ FM1/NM, k=2≡ FM2/NM)
L	FM interelectrode distance

The nonlocal resistance, $R_{\rm NL}$, is not a conventional resistance but the measured voltage normalized by the injected current, $I_{\rm c}$:

$$R_{\rm NL} = \frac{V_{\rm s}}{I_{\rm c}}. \tag{2.10}$$

To eliminate possible baselines, we define the spin signal ($\Delta R_{\rm NL}$) as the difference between $R_{\rm NL}$ at the parallel and at the antiparallel state, as tagged in Fig. 2.1(d). This value is twice the value of $R_{\rm NL}$, and is proportional to the spin accumulation reaching the detector:

$$\Delta R_{\rm NL} = 4R_{\rm s}^{\rm NM} e^{-L/\lambda_{\rm s}^{\rm NM}} \frac{\hat{P}_1 \hat{P}_2}{r_1 r_2 - e^{-2L/\lambda_{\rm s}^{\rm NM}}}. \tag{2.11}$$

In order to extract $\Delta R_{\rm NL}$ from the measured data (Fig. 2.1(d)), two linear fits are realized, one considering $R_{\rm NL}$ values at parallel configuration and the other with $R_{\rm NL}$ values at antiparallel configuration. From the difference between the intercepts obtained in the two fittings, we extract $\Delta R_{\rm NL}$. The corresponding error is calculated from the error propagation, taking into account the error of the intercept obtained in the fitting.

- For the case where the FM/NM interface resistances dominate the injection and detection ($R_{{\rm I}k} \gg R_{\rm s}^{k}, R_{\rm s}^{\rm NM}$) and interface spin polarization is the same for the injector and detector ($\alpha_{\rm I1} = \alpha_{\rm I2} = \alpha_{\rm I}$), Eq. 2.11 simplifies to:

$$\Delta R_{\rm NL} = R_{\rm s}^{\rm NM} \alpha_{\rm I}^2 e^{-L/\lambda_{\rm s}^{\rm NM}}. \tag{2.12}$$

- For the limiting case where both FM/NM junctions are electrically transparent ($R_{{\rm I}k} \ll R_{\rm s}^{k}, R_{\rm s}^{\rm NM}$) and both FM electrodes are equivalent

($\alpha_1 = \alpha_2 = \alpha_{\mathrm{FM}}$ and $Q_1 = Q_2 = Q_{\mathrm{FM}}$), Eq. 2.11 simplifies to:

$$\Delta R_{\mathrm{NL}} = 4R_{\mathrm{s}}^{\mathrm{NM}}\alpha_{\mathrm{FM}}^2 \frac{1}{\left[2+\frac{1}{Q_{\mathrm{FM}}}\right]^2 e^{L/\lambda_{\mathrm{s}}^{\mathrm{NM}}} - \left[\frac{1}{Q_{\mathrm{FM}}}\right]^2 e^{-L/\lambda_{\mathrm{s}}^{\mathrm{NM}}}}. \tag{2.13}$$

Equation 2.13 gives the possibility to extract $\lambda_{\mathrm{s}}^{\mathrm{NM}}$ and α_{FM} by measuring the spin signal for LSVs with different interelectrode lengths L and fitting the extracted data to the equation. The errors of the extracted parameters are coming from the fitting.

L must be of the order of $\lambda_{\mathrm{s}}^{\mathrm{NM}}$, because if it is much longer the spin accumulation vanishes. Taking into account that the lateral resolution of the current nanofabrication techniques are of the order of tens of nanometers, this technique is useful to extract $\lambda_{\mathrm{s}}^{\mathrm{NM}}$ of light NM metals such as Al, Cu or Ag, which are characterized by $\lambda_{\mathrm{s}}^{\mathrm{NM}}$ of hundreds of nm. On the contrary, materials that have $\lambda_{\mathrm{s}}^{\mathrm{NM}}$ of few nanometers, such as heavy metals or some FM metals, cannot be used as spin channels in standard LSVs. For these cases, there is an alternative approach to extract the short $\lambda_{\mathrm{s}}^{\mathrm{NM}}$: the spin absorption technique.

2.1.2 Spin absorption

The spin absorption method is based on introducing an additional wire, made of the material to study (MS) whose spin diffusion length, $\lambda_{\mathrm{s}}^{\mathrm{MS}}$, is to be known, between the two FM electrodes of the LSV, see Fig. 2.2(a). Two LSVs are fabricated; one containing the additional wire, usually in centered in between the FM electrodes, and the other one without the wire, being the latter the reference one. When the pure spin current is flowing through the NM channel containing the middle wire, part of the spin current is absorbed by the MS wire, resulting in a smaller detected spin signal in FM2 (see the comparison between the absorbed blue signal and the reference red signal in Fig. 2.2(b)). The detected nonlocal spin absorption signal is given by:

$$\Delta R_{\mathrm{NL}}^{\mathrm{abs}} = 4R_{\mathrm{s}}^{\mathrm{NM}}\hat{P}_1\hat{P}_2 \frac{(r_3-1)e^{-L/\lambda_{\mathrm{s}}^{\mathrm{NM}}}}{r_1r_2(r_3-Q_{\mathrm{I3}}) - r_1(1+Q_{\mathrm{I3}})e^{-2(L-l)/\lambda_{\mathrm{s}}^{\mathrm{NM}}} - r_2(1-Q_{\mathrm{I3}})e^{-2l/\lambda_{\mathrm{s}}^{\mathrm{NM}}} - (r_3-Q_{\mathrm{I3}})e^{-2L/\lambda_{\mathrm{s}}^{\mathrm{NM}}} + 2e^{-2L/\lambda_{\mathrm{s}}^{\mathrm{NM}}}}, \tag{2.14}$$

where l is the distance between the FM1 and MS, as shown in Fig. 2.2(a). r_3 corresponds to MS and is defined by Eq. 2.7. R_{I3} and α_{I3} refer to the MS/NM interface. MS is usually a NM material with strong SOC, being the spin polarization of the MS, α_3, and α_{I3} equal to 0. However, not to lose generality and be able to apply the equation when MS is FM, we keep α_3 and α_{I3} in the expression. Note that Eq. 2.11 is regained from Eq. 2.14 when considering $R_{\mathrm{s}}^3, R_{\mathrm{I3}} \to \infty$, *i.e.*, no effect of the MS on the LSV.

The spin resistance of MS, $R_s^3 \equiv R_s^{MS}$, when MS is a NM heavy metal with short λ_s^{MS} (of few nanometers), is defined by the following expression [74]:

$$R_s^{MS} = \frac{\rho_{MS}\lambda_s^{MS}}{w_{NM}w_{MS}\tanh\left(\frac{t_{MS}}{\lambda_s^{MS}}\right)}, \tag{2.15}$$

being ρ_{MS}, w_{MS} and t_{MS} the resistivity, width and thickness of the middle wire. The hyperbolic tangent in Eq. 2.15 is coming from the fact that the spin current is zero at the surface of the MS that is opposite to the one in contact with the NM channel.

In order to extract ΔR_{NL}^{abs} from the measured data (Fig. 2.2(b)) and the corresponding error, the same procedure as the one described to obtain ΔR_{NL} in the previous section is used.

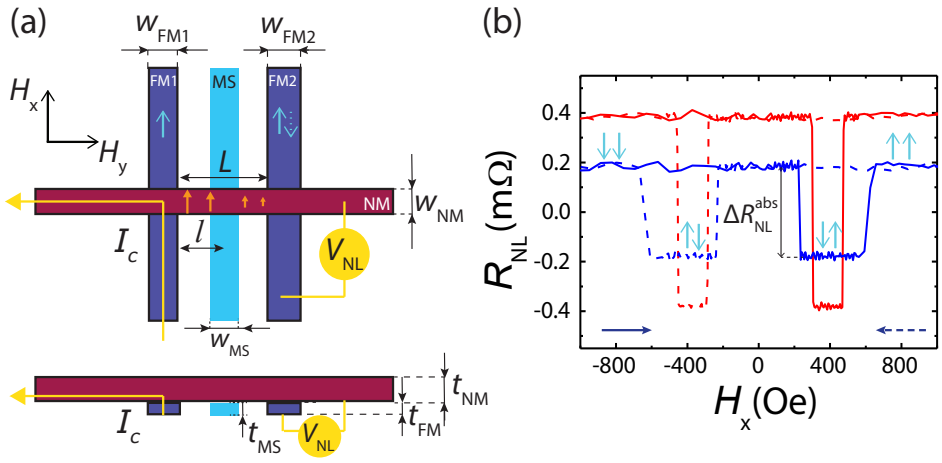

Figure 2.2: **Nonlocal measurement of spin absorption in a LSV.** (a) Sketch of a LSV with a spin absorber in between the two FM electrodes. The magnetization of FM1 and FM2 are represented by light blue arrows. The solid (dashed) arrow in FM2 gives rise to the parallel (antiparallel) magnetization configuration of the FM electrodes. Orange arrows represent the spins diffusing through the NM channel. The nonlocal measurement configuration is shown. (b) Nonlocal resistance measured at 10 K in a Py/Cu LSV with a Ta middle wire as spin absorber (blue line) in comparison to the reference Py/Cu LSV without the middle wire (red line). Blue vertical arrows indicate the parallel or antiparallel configuration of the FM electrodes. The blue solid (dashed) line and horizontal arrow indicate the sweeping direction of the magnetic field. The spin absorption signal (ΔR_{NL}^{abs}) is tagged.

- For the case where i) FM/NM interface resistances dominate the injection and detection ($R_{I1,2} \gg R_s^{1,2}$), ii) interface spin polarization is the same for the injector and detector ($\alpha_{I1} = \alpha_{I2} = \alpha_I$), iii) MS/NM interface resistance and the spin resistance of the middle wire are smaller than the spin resistance of the spin channel ($R_{I3}, R_s^3 \ll R_s^{NM}$) and iv) $L = 2l$, Eq.

2.14 can be simplified to:

$$\Delta R_{\mathrm{NL}}^{\mathrm{abs}} = 8R_{\mathrm{s}}^{\mathrm{NM}} Q_{\mathrm{I1}} Q_{\mathrm{I2}} \alpha_{\mathrm{I}}^2 \frac{(Q_{\mathrm{I3}} + Q_3) e^{-L/\lambda_{\mathrm{s}}^{\mathrm{NM}}}}{(2Q_{\mathrm{I1}}+1)(2Q_{\mathrm{I2}}+1) - 2(Q_{\mathrm{I1}}+Q_{\mathrm{I2}}+1)e^{-L/\lambda_{\mathrm{s}}^{\mathrm{NM}}} + e^{-2L/\lambda_{\mathrm{s}}^{\mathrm{NM}}}}. \tag{2.16}$$

The general procedure to extract $\lambda_{\mathrm{s}}^{\mathrm{MS}}$ with the spin absorption technique is based on comparing the spin signals obtained in the LSV that contains the middle MS wire with the reference LSV without the MS, having both devices the same L and equivalent FM and NM electrodes. The ratio between both spin signals, η, is given by:

$$\eta = \frac{\Delta R_{\mathrm{NL}}^{\mathrm{abs}}}{\Delta R_{\mathrm{NL}}} = \frac{(r_1 r_2 - e^{-2L/\lambda_{\mathrm{s}}^{\mathrm{NM}}})(r_3 - 1)}{r_1 r_2 (r_3 - Q_{\mathrm{I3}}) - r_1(1+Q_{\mathrm{I3}})e^{-2(L-l)/\lambda_{\mathrm{s}}^{\mathrm{NM}}} - r_2(1-Q_{\mathrm{I3}})e^{-2l/\lambda_{\mathrm{s}}^{\mathrm{NM}}} - (r_3 - Q_{\mathrm{I3}})e^{-2L/\lambda_{\mathrm{s}}^{\mathrm{NM}}} + 2e^{-2L/\lambda_{\mathrm{s}}^{\mathrm{NM}}}}. \tag{2.17}$$

- For the limiting case where both FM/NM junctions are electrically transparent ($R_{\mathrm{I}k} \ll R_{\mathrm{s}}^k, R_{\mathrm{s}}^{\mathrm{NM}}$), the NM/MS junction is transparent ($R_{\mathrm{I3}} \ll R_{\mathrm{s}}^{\mathrm{NM}}$) and both FM electrodes are equivalent ($\alpha_1 = \alpha_2 = \alpha_{\mathrm{FM}}$ and $Q_1 = Q_2 = Q_{\mathrm{FM}}$), Eq. 2.17 simplifies to:

$$\eta = \frac{2Q_{\mathrm{MS}}[2Q_{\mathrm{FM}} e^{L/\lambda_{\mathrm{s}}^{\mathrm{NM}}} + 2Q_{\mathrm{FM}}^2 e^{L/\lambda_{\mathrm{s}}^{\mathrm{NM}}} + \sinh(L/\lambda_{\mathrm{s}}^{\mathrm{NM}})]}{B}, \tag{2.18}$$

where

$$B = \cosh\left(\frac{L}{\lambda_{\mathrm{s}}^{\mathrm{NM}}}\right) - \cosh\left(\frac{L-2l}{\lambda_{\mathrm{s}}^{\mathrm{NM}}}\right) + 2Q_{\mathrm{FM}}\sinh\left(\frac{l}{\lambda_{\mathrm{s}}^{\mathrm{NM}}}\right)e^{(L-l)/\lambda_{\mathrm{s}}^{\mathrm{NM}}} + 2Q_{\mathrm{MS}}\sinh\left(\frac{L}{\lambda_{\mathrm{s}}^{\mathrm{NM}}}\right)$$
$$+4Q_{\mathrm{FM}}Q_{\mathrm{MS}}e^{L/\lambda_{\mathrm{s}}^{\mathrm{NM}}} + 2Q_{\mathrm{FM}}\sinh\left(\frac{L-l}{\lambda_{\mathrm{s}}^{\mathrm{NM}}}\right)e^{l/\lambda_{\mathrm{s}}^{\mathrm{NM}}} + 2Q_{\mathrm{FM}}^2 e^{L/\lambda_{\mathrm{s}}^{\mathrm{NM}}} + 4Q_{\mathrm{FM}}^2 Q_{\mathrm{MS}} e^{L/\lambda_{\mathrm{s}}^{\mathrm{NM}}}, \tag{2.19}$$

and $Q_{\mathrm{MS}} \equiv Q_3 \equiv R_{\mathrm{s}}^{\mathrm{MS}}/R_{\mathrm{s}}^{\mathrm{NM}}$. In case that MS is a FM material, we use the expression of Q_{FM}.

$\lambda_{\mathrm{s}}^{\mathrm{MS}}$ is thus extracted by substituting the rest of the parameters, that are previously quantified, in the corresponding expression of η (or $\Delta R_{\mathrm{NL}}^{\mathrm{abs}}$). The error of $\lambda_{\mathrm{s}}^{\mathrm{MS}}$ is calculated from the propagation of errors of the parameters included in these equations. The 1D spin diffusion model employed in this section is valid as long as w_{MS} is smaller than $\lambda_{\mathrm{s}}^{\mathrm{NM}}$. If this condition is not fulfilled, the spin accumulation profile under the absorber should be taken into account, as explained and detailed by Laczkowski *et al.* to avoid misestimations when extracting $\lambda_{\mathrm{s}}^{\mathrm{MS}}$ values [110].

2.1.3 Spin-to-charge current conversion

In the previous section we showed how a middle wire with low enough spin resistance can absorb part of the pure spin current flowing in the spin channel of the LSV. If this middle wire is characterized by a strong bulk SOC, *i.e.*, if MS is a spin Hall metal (SHM), the pure spin current absorbed can be converted into a measurable charge current due to the inverse spin Hall effect (ISHE), making the SCC experimentally observable and measurable in this device.

Spin-to-charge current conversions due to SHE and ISHE

Figure 2.3(a) shows how the spin current absorbed by the middle wire, MS, being the spin polarization pointing along the NM channel, is converted into a measurable charge current along the MS wire, $I_c^{'}$, fulfilling the symmetries of the ISHE: the absorbed spin current, spin polarization and the generated charge current are mutually perpendicular.

The ISHE measurement configuration using a LSV is shown in Fig. 2.3(b). A pure spin current is injected electrically into the NM channel by applying a charge current, I_c, to FM1 with the spin polarization pointing along the NM wire due to the orientation of the magnetic field, H_y. The pure spin current flows along the NM channel and it is partially absorbed by the MS, as shown in Fig. 2.3(a). The charge current generated along the MS wire ($I_c^{'}$) is detected as a voltage drop, V_{ISHE}. Normalizing the measured voltage drop by the injected current, we define the ISHE resistance, $R_{\mathrm{ISHE}} = V_{\mathrm{ISHE}}/I_c$. If we reverse the magnetic field, the spins injected into the NM channel will point in the opposite direction, and therefore, they will be deflected to the other side in the MS wire, giving rise to the opposite R_{ISHE}, see the green line in Fig. 2.3(c).

The difference between the two saturated R_{ISHE} values is twice the ISHE signal: $2\Delta R_{\mathrm{ISHE}}$. As we observe in Fig. 2.3(c), the saturation fields of R_{ISHE} (top panel) coincides perfectly with the saturation fields of the longitudinal resistance, R_{xx}, (bottom panel) measured in the FM1 injector using two point measurement configuration. The observed variation of R_{xx} with the orientation of $\vec{H}$ is ascribed to AMR. Above $|H_y| \sim 2500$ Oe, the magnetization of the FM1 is saturated in y direction, hence the ISHE resistance also saturates. In order to extract this value from the measured data (Fig. 2.3 (c) top panel), the average of the saturated R_{ISHE} values at positive H and the average of the saturated R_{ISHE} values at negative H is calculated, being the error the standard deviation. $2\Delta R_{\mathrm{ISHE}}$ will be the difference between the averages and the corresponding error is extracted from error propagation.

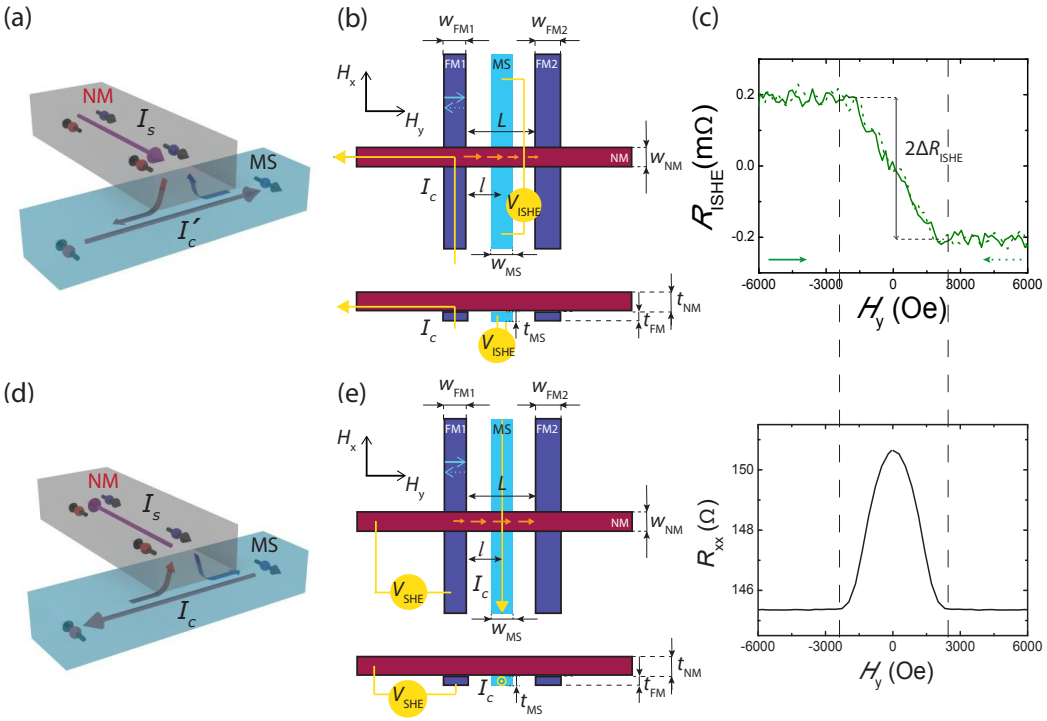

Figure 2.3: **Nonlocal measurement of the ISHE and SHE in a LSV using the spin absorption technique.** (a) Sketch of the spin absorption from the NM channel into the MS and SCC due to ISHE occurring in the MS. (b) Sketch of a LSV with a spin absorber in between the two FMs. The magnetization of FM1 is represented by a solid (dashed) light blue arrow indicating that the magnetization switches during the measurement. Orange arrows represent the spins diffusing through the NM channel. Nonlocal configuration for the ISHE resistance measurement is shown. (c) Top panel: measured ISHE resistance as a function of the applied magnetic field in a Py/Cu LSV with Ta middle wire at 10 K. The green solid (dashed) line and horizontal arrow indicate the sweeping direction of the magnetic field. The ISHE signal ($2\Delta R_{\mathrm{ISHE}}$) is tagged. Bottom panel: longitudinal resistance measurement as a function of the external magnetic field realized in the FM injector. Dashed black vertical lines from the top to the bottom panel are a guide to the eye indicating that the saturation fields match. (d) Sketch of the spin injection from the MS into the NM channel due to the SHE occurring in the MS. (e) Same sketch of the LSV as in (b) but showing the nonlocal configuration for the SHE resistance measurement.

The relation between the experimentally measured ΔR_{ISHE} and the spin Hall resistivity, ρ_{SH}, is given by [74]:

$$\rho_{\mathrm{SH}} = -\frac{w_{\mathrm{MS}}}{x_{\mathrm{MS,NM}}}\left(\frac{I_{\mathrm{c}}}{\bar{I}_{\mathrm{s}}}\right)\Delta R_{\mathrm{ISHE}}, \tag{2.20}$$

where $x_{\mathrm{MS,NM}}$ is the shunting factor that takes into account the current in the MS that is shunted through the NM channel. Given the smaller resistivity of the NM spin channel as compared to the one of the MS wire, $\rho_{\mathrm{MS}} > \rho_{\mathrm{NM}}$, the charge current generated along the MS wire due to the ISHE ($I_{\mathrm{c}}^{'}$) partially flows back into

the NM channel, giving rise to an effectively smaller output voltage. This issue is considered in the equation via the shunting factor, which is very sensitive to the geometry of the device and relevant to avoid underestimations in ρ_{SH} and θ_{SH}. $\bar{I}_{\mathrm{s}}$ is the effective spin current injected vertically into the MS wire that contributes to the ISHE, because the spin current at the MS/NM interface $I_{\mathrm{s}}(z=0)$ is diluted into the MS thickness. To calculate $\bar{I}_{\mathrm{s}}$, the spin current injected into the MS wire is integrated and then divided by the thickness:

$$\frac{\bar{I}_{\mathrm{s}}}{I_{\mathrm{c}}} = \frac{\int_0^{t_{\mathrm{MS}}} I_{\mathrm{s}}(z)dz}{t_{\mathrm{MS}} I_{\mathrm{c}}} = \frac{\lambda_{\mathrm{s}}^{\mathrm{MS}}\left(1-e^{-\frac{t_{\mathrm{MS}}}{\lambda_{\mathrm{s}}^{\mathrm{MS}}}}\right)^2}{t_{\mathrm{MS}}\left(1-e^{-\frac{2t_{\mathrm{MS}}}{\lambda_{\mathrm{s}}^{\mathrm{MS}}}}\right)} \frac{I_{\mathrm{s}}(z=0)}{I_{\mathrm{c}}}. \tag{2.21}$$

This equation highlights the relevance of $\lambda_{\mathrm{s}}^{\mathrm{MS}}$ in the quantification of the spin Hall parameters (ρ_{SH} and θ_{SH}), considering that $\lambda_{\mathrm{s}}^{\mathrm{MS}}$ is proportional to $\bar{I}_{\mathrm{s}}/I_{\mathrm{c}}$ as shown by the prefactor. $I_{\mathrm{s}}(z=0)$ is given by the following equation:

$$\frac{I_{\mathrm{s}}(z=0)}{I_{\mathrm{c}}} = \frac{2\hat{P}_1\left[r_2(1-Q_{\mathrm{I3}})e^{-l/\lambda_{\mathrm{s}}^{\mathrm{NM}}} - (1+Q_{\mathrm{I3}})e^{-(2L-l)/\lambda_{\mathrm{s}}^{\mathrm{NM}}}\right]}{r_1 r_2(r_3-Q_{\mathrm{I3}}) - r_1(1+Q_{\mathrm{I3}})e^{-2(L-l)/\lambda_{\mathrm{s}}^{\mathrm{NM}}} - r_2(1-Q_{\mathrm{I3}})e^{-2l/\lambda_{\mathrm{s}}^{\mathrm{NM}}} - (r_3-Q_{\mathrm{I3}})e^{-2L/\lambda_{\mathrm{s}}^{\mathrm{NM}}} + 2e^{-2L/\lambda_{\mathrm{s}}^{\mathrm{NM}}}}. \tag{2.22}$$

- For the case where i) FM/NM interface resistances dominate ($R_{\mathrm{I1,2}} \gg R_{\mathrm{s}}^{1,2}$), ii) interface spin polarization is the same for the injector and detector ($\alpha_{\mathrm{I1}} = \alpha_{\mathrm{I2}} = \alpha_{\mathrm{I}}$), iii) MS/NM interface resistance and the spin resistance of the middle wire are smaller than the spin resistance of the NM channel $R_{\mathrm{I3}}, R_{\mathrm{s}}^3 \ll R_{\mathrm{s}}^{\mathrm{NM}}$ and iv) $L = 2l$, Eq. 2.22 simplifies to:

$$\frac{I_{\mathrm{s}}(z=0)}{I_{\mathrm{c}}} = \frac{2\alpha_{\mathrm{I}} Q_{\mathrm{I1}}\left[(2Q_{\mathrm{I2}}+1)e^{\frac{L}{2\lambda_{\mathrm{s}}^{\mathrm{NM}}}} - e^{-\frac{L}{2\lambda_{\mathrm{s}}^{\mathrm{NM}}}}\right]}{(2Q_{\mathrm{I1}}+1)(2Q_{\mathrm{I2}}+1)e^{L/\lambda_{\mathrm{s}}^{\mathrm{NM}}} - 2(Q_{\mathrm{I1}}+Q_{\mathrm{I2}}+1) + e^{-L/\lambda_{\mathrm{s}}^{\mathrm{NM}}}}. \tag{2.23}$$

- For the limiting case where both FM/NM junctions are electrically transparent ($R_{\mathrm{I1}}, R_{\mathrm{I2}} \ll R_{\mathrm{s}}^{\mathrm{NM}}$), the NM/MS junction is transparent ($R_{\mathrm{I3}} \ll R_{\mathrm{s}}^{\mathrm{NM}}$) and both FM electrodes are equivalent ($\alpha_1 = \alpha_2 = \alpha_{\mathrm{FM}}$ and $Q_1 = Q_2 = Q_{\mathrm{FM}}$), Eq. 2.22 simplifies to:

$$\frac{I_{\mathrm{s}}(z=0)}{I_{\mathrm{c}}} = \frac{2\alpha_{\mathrm{FM}}[Q_{\mathrm{FM}}\sinh(\frac{L-l}{\lambda_{\mathrm{NM}}}) + Q_{\mathrm{FM}}^2 e^{\frac{L-l}{\lambda_{\mathrm{NM}}}}]}{B}. \tag{2.24}$$

where B is given by Eq. 2.19.

ρ_{SH} (and the rest of spin Hall parameters that can be calculated considering their relation, see Eq. 1.15) is extracted using the equations presented in this

section, as the other parameters included in the equations can be previously quantified and, thus, substituted in the equations. The errors of the obtained spin Hall parameters are calculated from error propagation.

As mentioned, λ_s^{MS} plays an important role for the correct quantification of the spin Hall parameters, given its presence in the prefactor of Eq. 2.21. Importantly, we are able to extract it precisely from the spin absorption experiment described in the previous section. Indeed, this is one of the major advantages of the spin absorption technique, in contrast to the rest of the methods to measure and quantify the SHE (described in Section 1.2.2): it enables to quantitatively derive both the λ_s^{MS} and ρ_{SH} (or θ_{SH}) of the MS using the very same device.

LSVs containing the MS middle wire also allow us to observe the direct SHE. In this case, a charge current, I_c, is injected along the MS, which is converted into a pure spin current in the transverse direction that will flow in the NM channel, as shown in Fig. 2.3(d). This pure spin current reaches the FM detector where a voltage V_{SHE} is detected using the measurement configuration shown in Fig. 2.3(e). Normalizing V_{SHE} by I_c, we define the SHE resistance R_{SHE}. If we reverse the magnetic field, the magnetization of the detector is inverted, giving rise to the opposite V_{SHE} (and R_{SHE}). The difference between the R_{SHE} values at saturated magnetization of the FM detector is twice the SHE signal: $2\Delta R_{SHE}$. ΔR_{SHE} obtained in this measurement should be the same as ΔR_{ISHE} due to the Onsager reciprocity [111]. The reciprocity between ISHE and SHE was first confirmed in Ref. [41] using this technique.

To sum up, the spin absorption technique allows us to quantify unambiguously the spin-dependent transport parameters and SCC parameters of the very same material. Therefore, LSVs with a middle wire are a unique and promising platform to study novel materials with short λ_s and sizeable SCC, unveiling their mechanisms and efficiencies.

2.2 Hall bars

HB is a standard device widely employed in electronics and spintronics. It consist of a rectangular shaped solid with lateral contacts where longitudinal and transverse resistances are readily measured, see Figs. 2.4(a) and 2.4(b). Generally, a charge current, I_c, is injected along the main channel and the voltage drop is measured in the longitudinal direction, V_{xx}, or transverse direction, V_{xy}, see Fig. 2.4(a). The width of the contacts are much smaller than the length L between the contacts to avoid current spreading.

The longitudinal resistivity, ρ_{xx}, is related to the longitudinal resistance $R_{xx} =$

V_{xx}/I_c by geometrical factors:

$$\rho_{xx} = R_{xx} wt/L, \tag{2.25}$$

where w and t are the width and thickness of the metal, as shown in Figs. 2.4(a) and 2.4(b), respectively. In order to extract accurately the longitudinal resistivity of the material, R_{xx} is measured along different L. By fitting R_{xx} *vs.* L, ρ_{xx} can be extracted.

Regarding the transverse resistance measurement, the voltage probes are placed perpendicular to the current path, and $R_{xy} = V_{xy}/I_c$ is obtained. The transverse resistivity, ρ_{xy}, is related to R_{xy} as:

$$\rho_{xy} = R_{xy} t. \tag{2.26}$$

Different effects can contribute to ρ_{xy}, such as the ordinary Hall effect (OHE) and the AHE when the magnetization is out of plane, see Section 1.2.1, or the planar Hall effect (PHE), *i.e.* transverse contribution of AMR, when the magnetization is in plane [112]. Next, we explain how to quantify the AHE from a transverse measurement.

2.2.1 Anomalous Hall effect

The AHE is readily measured using HBs. A charge current is injected in the longitudinal direction of the HB. The AHE deflects the spin-up and spin-down electrons in opposite direction so that a transverse charge accumulation is generated as shown in Fig. 2.4(b) and it is detected as a voltage drop. Although the AHE is present in the system without the need of an external magnetic field, we sweep the magnetic field in order to change the magnetization of the ferromagnet and be able to quantify this effect. We apply the magnetic field out of plane so that the spins point in this direction and the symmetries of the AHE are fulfilled: injected charge current direction, spin polarization and electric field direction generated by the charge accumulation are mutually perpendicular.

The obtained measurement curve is shown in Fig. 2.4(c) top panel. When the material is NM, we only observe a linear dependence of the R_{xy} as a function of H_z, ascribed to the OHE. However, in the FM case, the linear dependence is only observed at high magnetic fields, where the magnetization is saturated out of plane and thus, the contribution of the AHE is constant. The saturation of the magnetization is confirmed by measuring R_{xx} using four-point measurement configuration, see Fig. 2.4(c) bottom panel. When the magnetization is saturated R_{xx} is constant, as the relative orientation between the magnetization and applied current does not change. The latter effect is ascribed to AMR and effectively, the

saturation fields in the AMR and transverse measurement coincide. At lower magnetic fields, we observe the rotation of the magnetization, as R_{xx} changes when the relative orientation between the injected current and magnetization changes.

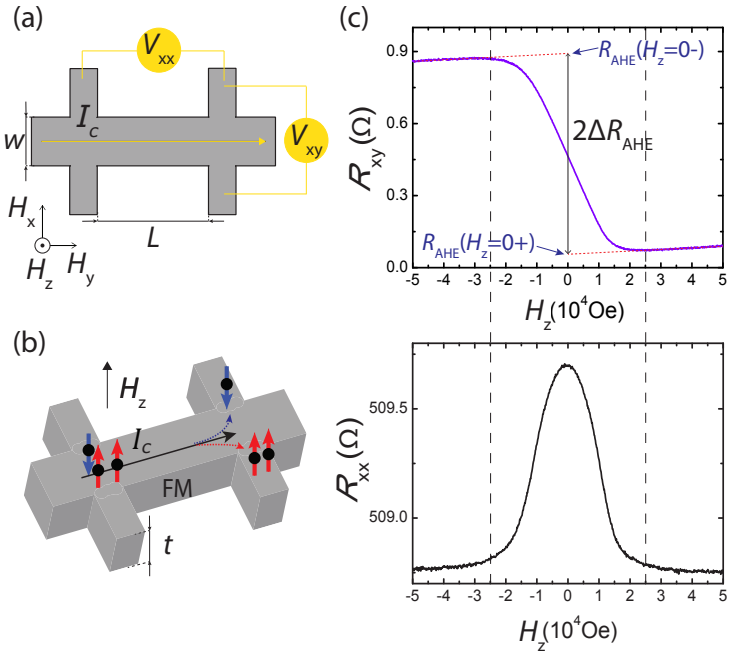

Figure 2.4: **Anomalous Hall effect measurement in a Hall bar.** (a) Top view of a Hall bar. Longitudinal and transverse measurement configuration are shown. (b) Sketch of the AHE occurring in a FM conductor. (c) Top panel: measured transverse resistance as a function of the applied magnetic field in Co at 10 K. Red dashed lines are linear curves fitted to high magnetic field data. The AHE signal ($2\Delta R_{\mathrm{AHE}}$) is tagged. Bottom panel: longitudinal resistance as a function of the external out-of-plane magnetic field measured using four-point configuration in Co at 10 K. Dashed black vertical lines from the top to the bottom panel are a guide to the eye indicating that the saturation fields match.

The significant jump observed in the transverse resistance below the saturation fields is precisely the signature of the AHE. It can be quantified as $2\Delta R_{\mathrm{AHE}}$. To extract this value, we fit the data at high positive and negative magnetic fields to two linear functions, see the red dashed lines in top panel of Fig. 2.4(c). From the intercept of the fittings at high positive and high negative magnetic fields, we extract $R_{\mathrm{AHE}}(H_z = 0+)$ and $R_{\mathrm{AHE}}(H_z = 0-)$, respectively. The difference between the two values is twice the AHE signal, $2\Delta R_{\mathrm{AHE}} = R_{\mathrm{AHE}}(H_z = 0+) - R_{\mathrm{AHE}}(H_z = 0-)$. From ΔR_{AHE} we obtain the anomalous Hall resistivity, ρ_{AH}:

$$\rho_{\mathrm{AH}} = \Delta R_{\mathrm{AHE}} t, \tag{2.27}$$

being t the thickness of the FM conductor. The error of ΔR_{AHE} is calculated from the error propagation, considering the errors of the intercepts given by the

fitting. The error of ρ_{AH} is calculated from the error of ΔR_{AHE} and t, which is measured by X-ray reflectivity.

Chapter 3

Experimental techniques

In this chapter, we explain how we fabricate and characterize the spintronic devices used in this thesis: the lateral spin valves (LSVs) and the Hall bars (HBs). Although both devices share the same fabrication techniques, the recipes and number of fabrication steps are different, given the difference in the structure and design of the devices.

3.1 Fabrication techniques

Two of the basic procedures for the fabrication of nanostructures are the lift-off procedure and the etching procedure, which are sketched in Figs. 3.1(a) and 3.1(b), respectively. They consist of several steps. In the lift-off procedure, firstly, a lithography process is carried out, which includes the spin coating of the resist (i, in Fig. 3.1(a)), exposure of the resist (ii, in Fig. 3.1(a)), either by electron-beam (e-beam) lithography or photolithography, and developing to remove the resist that has been exposed (iii, in Fig. 3.1(a)). Secondly, a material deposition is performed (iv, in Fig. 3.1(a)), via sputtering, e-beam evaporation or thermal evaporation. Finally, in the lift-off process (v, in Fig. 3.1(a)), the resist that remains in the substrate and the material that is on top are removed. In the etching procedure the same techniques are employed but a different order is followed. Firstly, the deposition of the material is performed (i, in Fig. 3.1(b)), then the lithography is realized: the spin coating of the resist (ii, in Fig. 3.1(b)), exposure of the resist (iii, in Fig. 3.1(b)), and developing (iv, in Fig. 3.1(b)). Later, an etching process, via ion milling, reactive ion etching, plasma etching, chemical etching, *etc.* is carried out to remove the parts that are uncovered by resist (iv, in Fig. 3.1(b)) and, finally, the resist that remains on top of the patterned material is removed (v, in Fig. 3.1(b)). Generally, Ar-ion milling is commonly performed in certain samples for cleaning the interfaces and remove the resist left overs and

surface oxides. To fabricate the complete device, these two general procedures are repeated as many times as required, depending on the design of the device. Hereafter, each of the aforementioned fabrication steps will be explained and the different lithography techniques and thin film deposition methods will be detailed.

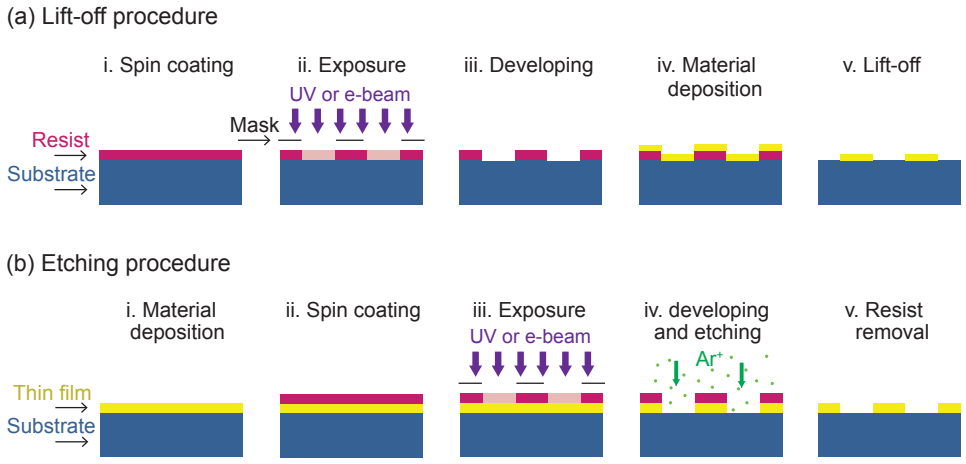

Figure 3.1: **General procedures for nanofabrication.** (a) Lift-off procedure and (b) etching procedure. The name refers to the technique employed to remove part of the material in the thin film so that the desired nanostructure is obtained on the substrate. Each procedure is based on several steps that are sketched and named.

3.1.1 Cleaning of the substrates

The very first step in the fabrication of devices is the cleaning of the substrates. The devices are build on clean substrates SiO_2(150nm)/doped-Si of 10mm×10mm or 5mm×5mm area. First, we immerse the substrate in acetone with ultrasounds for 5 minutes and subsequently, for another 5 minutes in isopropanol with ultrasounds. Later, we sink the substrate in water for several minutes and dry it in a hot plate at temperatures higher than 100 °C to evaporate the last water drops.

3.1.2 Lithography

Lithography is the basic technique for electronic circuits patterning, which consists of three steps: spin coating, exposure and developing of the resist.

Spin coating

Spin coating of a ultra-violet (UV) light sensitive or e-beam sensitive resist is realized on top of the clean substrate. The spin coating of the resist is done at certain speed, acceleration and time to achieve the optimized thickness of

the resist. After the spin coating, the sample is baked in order to remove the solvent present in the resist. In some cases, a double layer (DL) of resists is used, performing two consecutive spin coatings. Each resist layer has different characteristics: different molecular weight and concentration in the solvent. Generally, the bottom layer has a lower molecular weight, so that it is more sensitive to the e-beam. Consequently, after the exposure, the resist near the substrate is more developed forming an undercut, which helps to perform the lift-off process. Depending on the dimensions of the design and the required resolution, either photolithography or e-beam lithography is employed for the exposure and the appropriate resist is selected. The resists employed in this thesis are:

- S1818: Photosensitive resist.
- PMMA: E-beam sensitive resist, poly(methyl methacrylate). PMMAs with different molecular weight and anisole (A) concentration have been used. The higher the molecular weight, the less sensitive to the e-beam. The higher the anisole concentration, the thicker the resist.
  - PMMA 495 A4: 495K molecular weight, hence more sensitive to the e-beam than the following one. It generates an undercut that makes the lift-off easier. Diluted in anisole at 4% concentration.
  - PMMA 950 A2: 950K molecular weight, thus less sensitive to the e-beam than the previous one. Diluted in anisole at 2% concentration.
- ZEP 520 A7: E-beam sensitive resist. 57K molecular weight, diluted in anisole. Higher sensitivity and etch durability than PMMA [113].

Exposure

In the exposure step, the resist will be exposed to UV light or e-beam and consequently, the chains of the exposed polymer are broken to smaller more soluble fragments. This is the case for resists that are used in this thesis, which are positive resists. In a negative resist, the exposed part becomes extremely difficult to dissolve, more than the areas that were unexposed. It is important to perform a dose-test the first time we are using a new type of resist or substrate, to confirm the amount of energy we need to give to the system to modify the bondings of the exposed part of the resist.

- **Photolithography**

  Photolithography is based on the exposure of a photosensitive resist by employing UV light. Masks containing the desired design are used, which

allow light to pass in certain areas and, thus, only expose part of the resist that is on top of the substrate, transferring the desired pattern to the resist. The design in the mask consists of opaque and clear features. The opaque part is made of a Cr layer on a glass, which is the transparent part. The wavelength employed in the mask aligner system from *EV Group* is 365 nm and the smallest fabricated patterns are 5 μm, even if the resolution could be slightly better if the system is properly aligned and optimized (∼1 μm). One of the advantages in photolithography is the fast exposure time, because a large area, *i.e.* a full wafer, is exposed at the same time. The relevant parameters to consider in this method are the irradiated power and dose or time of irradiation, in order to provide enough energy to the resist to modify its properties.

- **e-beam lithography**

  It consists of exposing an e-beam-sensitive resist by employing a highly focused e-beam. The major advantages of this technique are the good resolution, of around 10 nm in the two e-beam lithography systems by *Raith* used in this work, and that no masks are necessary. The design is created in the software provided by the company and is editable. The main disadvantage is that the e-beam needs to scan all the area to be exposed (in fact, the sample holder or stage is the one that moves), making the exposure a time-demanding task. The required time also for adjusting the beam and perform the write field (WF) alignments makes the whole patterning process slower than in photolithography. The relevant parameters to consider in this method are the acceleration voltage of the electron beam, the aperture, WF and dose. The acceleration voltage determines the energy of the electrons reaching the stage where the sample is placed and, together with the aperture, determines the current of the e-beam. The WF is the area that will be exposed by just deflecting the e-beam, being the stage fixed. The smaller the WF is, the better resolution can be attained. WF alignment procedures are relevant in order to have good alignments between two adjacent patterned areas, avoiding stitching errors, and overlays (aligning a pattern to a previous one). The dose determines the amount of charge per unit area that reaches the sample, which will vary depending on the resist.

Developing

After the exposure, the resist is developed by rinsing the sample in the developer. In this process, the positive resist that has been exposed (*i.e.,* fragmented) is dissolved. When using negative resist, the non-exposed resist is removed in the developing process and the exposed part of the resist remains on top of the substrate. The pattern is now transferred into the resist.

3.1.3 Thin film deposition and lift-off

On top of the patterned resist, a thin film is deposited. There are different methods for deposition. Depending on the material one needs to grow, dimensions of the patterned nanostructures and the type of device, one or another technique is recommended. In this thesis, we use several physical vapor deposition techniques, where the material goes from condensed phase to vapor phase and is deposited in the substrate in condensed phase. This is realized in chambers with ultra-high vacuum (UHV), where usually the pressures during deposition, P_{dep} are in the order of $\sim 10^{-8}$ mbar. To attain this, first the sample is loaded in a pre-chamber and once the vacuum is good enough, it is transferred to the main chamber, where the base pressure, P_{base}, *i.e.* the pressure of the chamber before the deposition, is lower than P_{dep}. In order to calibrate the thickness of the thin films, X-ray reflectivity (XRR), see Section 3.3.2, is employed and also a quartz crystal monitor is placed in the chamber close to the sample in order to monitor the real-time thickness and deposition rate.

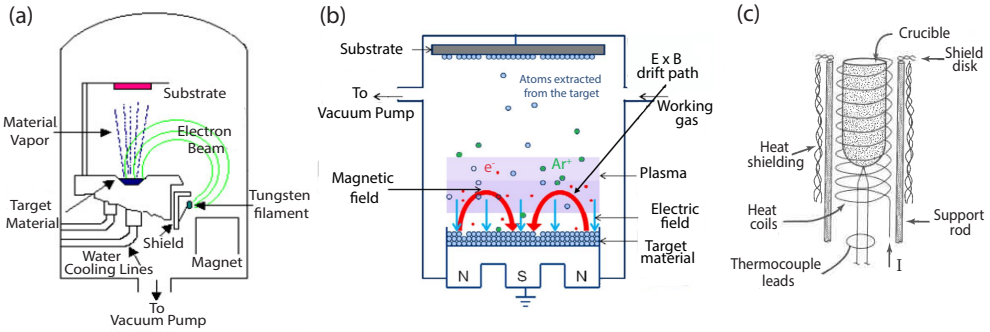

Figure 3.2: **Physical vapor deposition techniques.** (a) e-beam evaporation. (b) Sputtering. (c) Thermal evaporation. Figures adapted from Refs. [114], [115] and [116], respectively.

- **e-beam evaporation**

  In the e-beam evaporation, high-energy electrons are used to evaporate the material to be deposited. Electrons are thermionically emitted by applying current to a hot filament, usually made of W, and accelerated into the source material or target that will be evaporated by applying a voltage, $V_{\text{e-beam}}$. By using magnetic fields, the e-beam current, $I_{\text{e-beam}}$, is focused to the material of interest, see Fig. 3.2(a). The electrons reaching the source material have enough energy to evaporate any material, the local temperature is increased above the boiling point in order to start evaporating. High temperature metals can be evaporated, because we are not limited by the melting point of the heater element as it is the case in the thermal evaporation. In this thesis, an UHV system by *CreaTec* is used to e-beam evaporate metals. It

also contains effusion cells for thermal evaporation. Such a system provides clean and high purity layers due to the low P_{base} ($\sim 10^{-9}$ mbar).

- **Sputtering**

  Sputter-erosion is a source of vapor for thin film deposition attained by bombarding the target, which consists of the material to be sputtered, by energetic particles such as ions. The chamber is filled by an inert gas, Ar in our case, at low pressures and plasma containing Ar ions, Ar^+, is created. These Ar ions are accelerated into the target using a bias potential, see Fig. 3.2(b). When the ions hit the target with larger energy than the binding energy of the target atoms, the latter are extracted from the target generating a vapor in the chamber that will deposit in all surfaces, including our substrate. In this work, an UHV Magnetron Sputtering system by *AJA* that contains seven targets has been used. In magnetron sputtering, magnetic fields are used to increase the plasma density and attain higher deposition rates.

- **Thermal evaporation**

  Thermal evaporation is based on heating with electrical currents, by Joule effect, the effusion cell or crucible where the source material has been placed, see Fig. 3.2(c). By passing currents around the cell, the heat dissipated by the resistance is used to increase the temperature of the material inside the cell. It is also known as Joule heating evaporation. An UHV system by *CreaTec* has been used.

Lift-off

Once the thin film has been deposited, using any of the techniques, the sample is rinsed in a solvent ('remover'). The remover dissolves the resist and, therefore, removes the material that was on top. Hereby, the substrate containing the structure with the desired design is obtained.

3.1.4 Ar-ion milling

Ar-ion milling is a purely physical process employed for cleaning the surfaces or etching away material on a substrate. It is based on bombarding Ar ions almost perpendicular to the sample. In order to achieve that, Ar ions are accelerated to create a beam, which impacts with high energy on the sample etching away the material. The relevant parameters are the voltage and current of the ion beam, V_{beam} and I_{beam} respectively, acceleration voltage, V_{acc}, to accelerate the Ar plasma against the surface, the angle between the sample plane and Ar-ion beam, ϕ, and

the process time or eating rate. In this work, an Ar-ion miller equipment from *4Wave* has been used.

3.1.5 Mechanical exfoliation

In Chapter 6, we use a LSV based on a graphene spin channel. The narrow flake graphene is obtained by mechanical exfoliation of natural graphite. This is possible due to the weak van der Waals interaction between the layers that form the graphite, compared to the covalent bonds between the C atoms inside a layer. Nitto tape (Nitto SPV 224P) is used for the exfoliation process, which is realized several times until the proper amount of material is obtained on the tape. This can be estimated by eye or by optical microscopy. Then, the material on the tape is transferred to a 300-nm-thick SiO_2 on doped Si substrate by pressing the tape against the substrate using a rubber, right after heating the samples in a hot plate at 100 °C. The thickness of the transferred flakes are identified using its optical contrast [117]. This task has been carried out by Dr. W. Yan.

3.2 Specific fabrication recipes

Once the general procedures for the fabrication of nanodevices and the main lithography and thin film deposition methods have been introduced, we focus on the specific recipes that have been used in the fabrication of our spintronic nanodevices. The devices employed in this thesis have been fabricated in a clean room with a classification of ISO 5 (class 100), ISO 6 (class 1000), and ISO 7 (class 10000), where the contamination, the number of particles per cubit meter at a specific particle size, is controlled. All the fabrication equipment mentioned in the previous section is found in this clean room. Next, the detailed recipes for the fabrication of our nanodevices, LSVs and HBs, are given.

3.2.1 Metallic lateral spin valves for spin absorption technique

The fabrication of the metallic LSVs with a middle wire made of the material to study (MS), shown in Fig. 3.1(a), consist of four consecutive lift-off procedures, where in each one a lithography, metal deposition and lift-off is performed:

1. Macroscopic golden paths
2. FM electrodes
3. Middle wire, MS
4. Spin channel.

Table 3.1: Detailed fabrication recipe of metallic LSVs for spin absorption technique.

Steps	Parameters(↓)|Procedures(→)	1. Macroscopic paths	2. FM electrodes	3. Middle wire, MS	4. Spin channel
Spin coating	Resist	S1818	ZEP	DL PMMA (495 A4 and 950 A2)	DL PMMA (495 A4 and 950 A2)
	Speed (acceleration)	4000 rpm (1000 rpm/s)	2500 rpm (1000 rpm/s)	4000 rpm (1000 rpm/s)	4000 rpm (1000 rpm/s)
	Time	60 sec	60 sec	60 sec	60 sec
	Baking (time)	115 °C (1 min)	180 °C (5 min)	180 °C (5 min)	180 °C (5 min)
Exposure	Technique	Photolithography	e-beam lithography	e-beam lithography	e-beam lithography
	Exposure characteristics	Power= 18 mW/cm^2 Dose= 150 mJ/cm^2	Acceleration V = 10 kV Aperture= 10 µm WF= 100 × 100 µm^2 Dose= 50 µC/cm^2	Acceleration V = 10 kV Aperture= 10 µm WF= 100 × 100 µm^2 Dose= 130 µC/cm^2	Acceleration V = 10 kV Aperture= 10 µm WF= 100 × 100 µm^2 Dose= 150 µC/cm^2
Developing	Developer (time)	MK-319 (30 sec)	ZED (30 sec)	MIBK:IPA (1:3) (30 sec)	MIBK:IPA (1:3) (30 sec)
	Rinse	Water	Isopropanol	Isopropanol	Isopropanol
Metal deposition	Metal(thickness)	Ti/Au (4 nm/40 nm) *in situ*	Py (30 nm)	(A) Pt (20 nm) or Ta (10, 20 nm) (B) Fe, Co, Py or Ni (20 nm)	Ar-ion milling * +Cu (100 nm) *(conditions in text)
	Technique	e-beam evaporation	e-beam evaporation	(A) Sputtering (B) e-beam evaporation	Thermal evaporation
	Deposition characteristics	P_{base}=1.5 × 10^{-8} mbar P_{dep}=2.8 × 10^{-8} mbar $I_{e\text{-}beam}$ = 38/36 mA $V_{e\text{-}beam}$ = 8/10 kV Rate=0.86/1.36 Å/s	P_{base}=4.8 × 10^{-9} mbar P_{dep}=3.3 × 10^{-8} mbar $I_{e\text{-}beam}$ = 44 mA $V_{e\text{-}beam}$ = 10 kV Rate=0.8 Å/s	(A) Check Table 3.2 (B) Check Table 3.3	P_{base}=8.0 × 10^{-9} mbar P_{dep}=1.8 × 10^{-8} mbar T_{Cu} = 1300 °C Rate=1.5 Å/s
Lift-off	Remover (time)	Acetone (Overnight)	ZD MAC (1-2 hours)	Acetone (Overnight)	Acetone (Overnight)
	Rinse	Isopropanol	Acetone	Isopropanol	Isopropanol

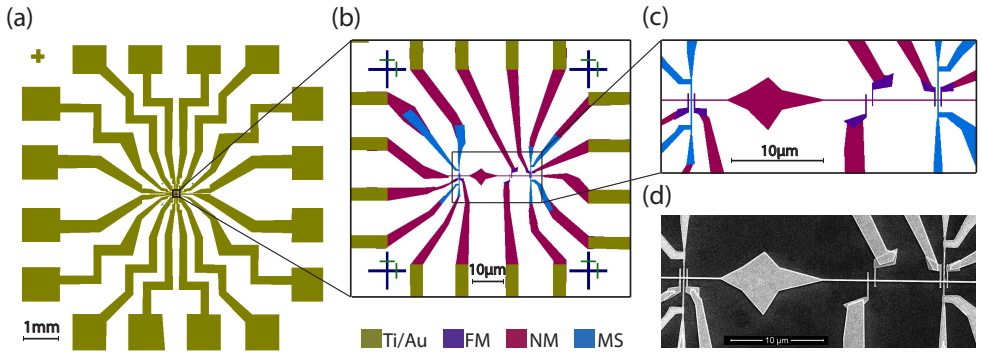

Figure 3.3: **Design and SEM of a sample containing metallic LSVs with a middle wire for spin absorption.** (a) Macroscopic golden paths. (b) Central part of the sample that consist of three LSVs with the FM electrodes (purple), middle wire with the MS in the two LSVs of the edges (blue) and the spin channel made of a NM material (dark-pink). (c) Zoom in of (b). (d) SEM image of the real device.

Figure 3.3(a) shows the macroscopic design of a sample, where only the macroscopic golden paths that are fabricated in the first lift-off procedure are visible. 4 nm of Ti are deposited before Au for better adhesion of the metal to the substrate. LSVs are placed in the central part of the sample, as shown in Fig. 3.3(b) and with a zoom in Fig. 3.3(c). The FM electrodes of the LSVs, purple electrodes in the design of Fig. 3.3, are made of Py ($Ni_{81}Fe_{19}$) and are fabricated in the second procedure. The middle wire, blue electrodes in the design of Fig. 3.3, is made of the MS (Pt, Ta, Fe, Co, Py or Ni) and fabricated in the third procedure. In the fourth procedure, the Cu spin channel, pink electrodes in the design of Fig. 3.3, is fabricated. Before the Cu evaporation, an Ar-ion milling step is carried out to clean the surface of the FM electrodes and middle wire and remove the possible resist left-overs. This is realized by applying $V_{\text{beam}} = 300$ V and $I_{\text{beam}} = 50$ mA for the ion-beam at $V_{\text{acc}} = 50$ V of acceleration voltage and bombarding Ar ions almost perpendicular to the sample ($\phi = 260°$) for 30 sec. The proper alignment between the different overlays is crucial in this multiple-step fabrication, and the blue crosses shown in Fig. 3.3(b) are used for this alignment process. The scanning electron microscopy (SEM) image of the real sample is shown in Fig. 3.3(d). The specific fabrication parameters of each of the procedures are gathered in Table 3.1.

For nanometric accuracy in metal deposition and Ar-ion milling, previous calibration of deposition and milling rates is needed. For a proper calibration of the rate in a deposition technique, a thin film is first deposited, the thickness is measured by XRR and the quartz crystal monitor is adjusted accordingly. In case of the Ar-ion milling, the milling rate is extracted after the deposition of the material in several samples, performing Ar-ion milling processes with different duration for each of them and estimating by XRR the amount of material that has been etched.

Table 3.2: Sputtering conditions of Pt and Ta.

Parameters(↓)|Metal(→)	Pt	Ta
Power (W)	40 / 80	20
Ar Pressure (Torr)	3×10^{-3}	1.5×10^{-3}
P_{base}(Torr)	$10^{-7} - 10^{-8}$	8×10^{-8}
Temperature	Room temperature	Room temperature
Rate (Å/s)	0.6 / 1.3	1.6

Table 3.3: e-beam evaporation conditions for Fe, Co Py and Ni.

Metal(→) Parameters(↓)	Fe	Co	Py	Ni
P_{base}(Torr)	6×10^{-8}	6×10^{-8}	$1 - 5 \times 10^{-9}$	3×10^{-9}
P_{dep}(Torr)	$\sim 10^{-8}$	$\sim 10^{-8}$	$\sim 10^{-8}$	$\sim 10^{-8}$
$I_{e\text{-}beam}$(mA)	60-70	80-90	80-100	120
$V_{e\text{-}beam}$(kV)	3.8	3.8	3.8	3.8
Rate (Å/s)	0.6-0.7	0.6-0.7	0.6-0.7	0.6-0.7
T_{Sample}(°C)	3-5	3	5-6	8-9

3.2.2 Graphene-based lateral spin valves for spin absorption technique

The fabrication of the graphene-based LSVs with middle wire consist of three procedures:

1. Exfoliation of a graphene flake, following the description of Section 3.1.5.
2. Fabrication of the middle wire, following the lift-off procedure described in '*3. Middle wire, MS*' column in Table 3.1. In our case MS is Pt, hence the sputtering conditions shown in Table 3.2 (specifically the conditions of Power = 40 W) are used.
3. Fabrication of the FM electrodes with their respective interfacial barriers, following a lift-off procedure. The spin coating, exposure and developing conditions are the same as the ones in '*3. Middle wire, MS*' column in Table 3.1, except a larger dose in the exposure (dose=175 $\mu C/cm^2$). A larger dose is used to further remove the possible resist left-overs, because an ion-milling process is avoided during this fabrication not to damage the graphene flake. The metal deposition consists on the e-beam evaporation

of 6 Åof Ti (using Ti conditions shown in '*Metal deposition*' line in '*1. Macroscopic paths*' column in Table 3.1) and 35-nm-thick Co at $P_{\text{base}} = 2 \times 10^{-10}$, $P_{\text{dep}} = 4 \times 10^{-9}$, $I_{\text{e-beam}}$ =44 mA, $V_{\text{e-beam}}$ =8 kV, with a rate =0.8 Å/s.

3.2.3 Hall bars

HBs employed in this thesis are fabricated using different procedures. The fabrication of the HBs made of Fe, Co, Py or Ni used in Chapter 7 follows lift-off procedure, shown in Fig. 3.1(a), and the fabrication of Co and Co/Bi_2O_3 HBs in Chapter 8 follows the etching procedure, shown in Fig. 3.1(b). The main reason for different procedures is the difficulty of the lift-off step in the lift-off procedure in the fabrication of Co/Bi_2O_3 HBs. Except for the 3*d* FM-HBs that are included in the middle wire of LSVs (see Fig. 7.1(b)), photolithography is used with S1818 resist for the 3*d* FM-HBs and Co/Bi_2O_3 HBs fabrication. Opposite masks are used for each case: in the former, the H-shape of the HB is transparent and the rest opaque, and in the latter, only the H-shape is opaque. The former are fabricated following the steps of '*1. Macroscopic paths*' column in Table 3.1 but using the e-beam evaporation conditions for 3*d* FMs shown in Table 3.3. The specific fabrication parameters of the HB made of Co and Co/Bi_2O_3 are gathered in Table 3.4. In case of Co/Bi_2O_3, the deposition of Co and Bi_2O_3 is done *in situ* in a evaporation system by *Kurt J. Lesker Company*.

Table 3.4: Detailed fabrication recipe of Co and Co/Bi_2O_3 Hall bars.

Steps	Parameters	1. Hall bar
Metal deposition	Metal(thickness)	Co (15 nm) / Bi_2O_3 (20 nm)
	Technique	e-beam evaporation
	Deposition characteristics	P_{base} =2.4×10^{-7} mbar / 3.6 × 10^{-7} mbar P_{dep} =9×10^{-7} mbar / 2 × 10^{-6} mbar $I_{e\text{-}beam}$ = 29 mA/2 mA $V_{e\text{-}beam}$ = 8.0 kV/3.1 kV Rate = 0.5 Å/s / 0.1 Å/s
Spin coating	Resist	S1818
	Speed (acceleration)	4000 rpm (1000 rpm/s)
	Time	60 sec
	Baking (time)	115 °C (1 min)
Exposure	Technique	Photolithography
	Exposure characteristics	Power = 18 mW/cm^2 Dose = 150 mJ/cm^2
Developing	Developer (time)	MK-319 (30 sec)
	Rinse	Water
Ar-ion milling	Conditions	V_{beam} = 300 V I_{beam} = 50 mA V_{acc} = 300 V ϕ = 260 ° Milling-rate = 0.17 Å/s / 1.1 Å/s
Lift-off	Remover	Acetone
	Time	Overnight
	Rinse	Isopropanol

3.3 Characterization techniques

Once the samples are fabricated, we proceed with the characterization. As the effects studied in this thesis give rise to low-resistance signals ($\sim$ mΩ or smaller), we use a electrical equipment setup prepared for this kind of measurements. The electrical measurements are done at different temperatures (T) applying external magnetic fields ($\vec{H}$). We measure the thickness of the metallic layers via XRR. The crystallographic structure of some of the metals is extracted by X-ray diffraction (XRD) or transmission electron microscopy (TEM). SEM is employed to measure the dimensions of the electrodes in the devices.

3.3.1 Electrical measurements

Electrical measurements are carried out in the Physical Property Measurement System (PPMS) developed by *Quantum Design*. The sample, device under test (DUT), is glued and wired to a chip carrier (called 'puck'), see Fig. 3.4(a), using eight contacts. The wiring is realized by a wire-bonder or by indium pressing. The puck is fixed in the rotator, see Fig. 3.4(b), and introduced in the liquid helium cryostat, see Fig. 3.4(c). By using a switchboard, we select the current and voltage probes, which are connected to the electrical measurement setup. The system allows to vary T from 2 K to 400 K and change H from -9 T to 9 T employing a superconducting coil. With the help of the rotator, the sample can be oriented in different angles with respect to $\vec{H}$. Therefore, phenomena occurring under different orientations of $\vec{H}$ and their evolution with T can be analyzed.

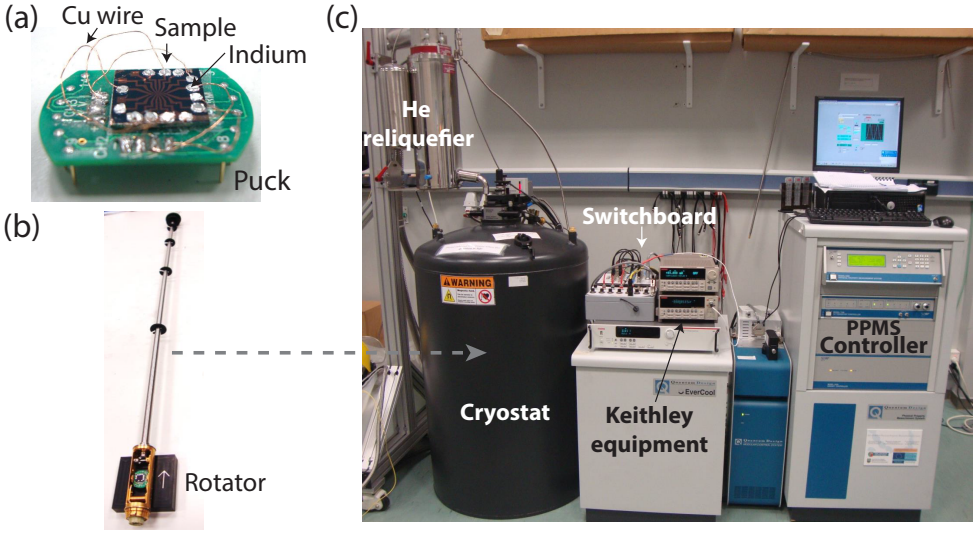

Figure 3.4: **Physical Property Measurement System.** (a) Sample connected to the puck using Cu wires and indium. (b) The rotator where the puck is placed to be introduced into the cryostat. (c) The PPMS equipment.

Current is applied to the sample by a Keithley 6221 current source and voltage is measured by a Keithley 2182A nanovoltmeter, using four terminals as shown in Fig. 3.5(a). The measurements are realized using a "DC reversal" (DC = direct current) technique, also known as delta mode. This method allows us to remove thermoelectric effects (either constant or linear with time) and to reduce noise. Hence, it is a suitable technique for low-resistance measurements. Delta mode consists of injecting alternated positive and negative currents, see Fig. 3.5(b), and measuring the voltage each time that the polarity of the current is changed (such as V_{M1}, V_{M2}, V_{M3} in Fig. 3.5(b)). The voltages V_{M1}, V_{M2}, V_{M3} contain, apart from the voltage drop coming form the DUT (V_{DUT}), a constant thermal voltage offset (V_{EMF}) and a linearly changing thermoelectric voltage (δV):

$$V_{M1} = V_{DUT} + V_{EMF}, \tag{3.1}$$

$$V_{M2} = -V_{DUT} + V_{EMF} + \delta V, \tag{3.2}$$

$$V_{M3} = V_{DUT} + V_{EMF} + 2\delta V \tag{3.3}$$

In order to isolate the voltage corresponding to DUT the following calculation is performed:

$$V_A = \frac{V_{M1} - V_{M2}}{2} = V_{DUT} - \frac{\delta V}{2}, \tag{3.4}$$

$$V_B = \frac{V_{M3} - V_{M2}}{2} = V_{DUT} + \frac{\delta V}{2}, \tag{3.5}$$

$$V_{Final} = \frac{V_A + V_B}{2} = V_{DUT}. \tag{3.6}$$

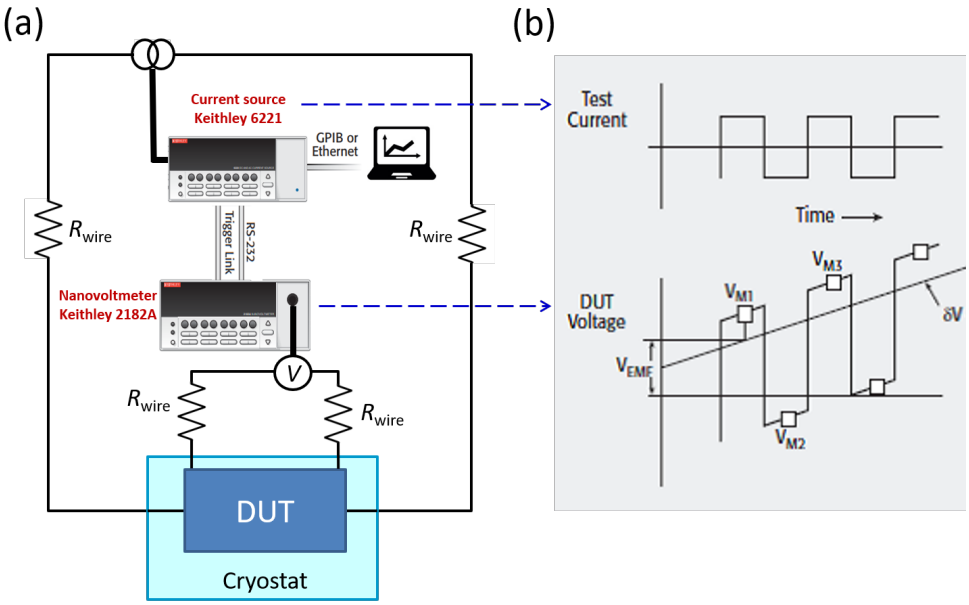

Figure 3.5: **Measurement configuration using Keithley current source and nanovoltmeter.** (a) Electrical measurement setup to measure DUT. (b) Injected current by the current source and measured voltage drop, in delta mode configuration.

To further improve the signal-to-noise ratio the voltage can be measured more times. In our measurements, 64 counts are generally used. The resistance, R, value is obtained by $R = V_{\mathrm{Final}}/I_{\mathrm{c}}$, being I_{c} the current applied to the sample. Generally, we measure R as a function of the applied magnetic field, $R(H)$ or temperature $R(T)$, by repeating the procedure to extract R for each value of H or T, respectively.

In the measurements carried out in the laboratory of Prof. Otani in the Institute of Solid State Physics of the University of Tokyo, instead of the delta mode, the equivalent lock-in technique was used, where alternating currents (AC) are applied. This method is based on measuring an AC voltage coming from the sample whose frequency is known. By using a reference signal of the same frequency and a known amplitude and phase, it is possible to obtain the amplitude and phase of the AC voltage from the multiplication of both signals and the use of a low pass filter. Any signal whose frequency differs from the reference one, is filtered out and will not affect the measurement. In our measurements, the frequency of 173 Hz is used.

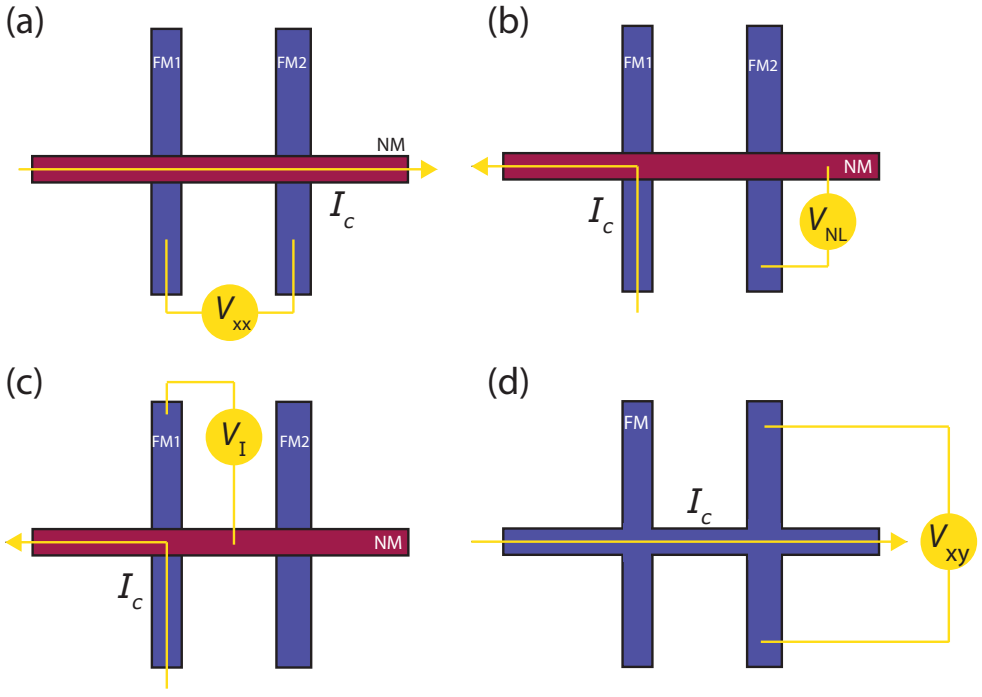

Figure 3.6: **Measurement configurations used in this thesis.** (a) Longitudinal resistance measurement using four-point measurement configuration. (b) Nonlocal measurement. (c) Interface resistance measurement. (d) Transverse resistance measurement.

In the LSVs or HBs used in this thesis, four-point measurement configuration is used to measure the longitudinal resistances, as shown in Fig. 3.6(a). In this configuration, current-carrying and voltage-sensing electrodes are separated

and consequently, contact or wire resistances (such as R_{wire} in Fig. 3.5(a)) are eliminated from the voltage drop that the nanovoltmeter will measure. This is one of the advantages of using four-point measurement, in contrast to two-point measurement, and it is indispensable to perform precise low-resistance measurements in the DUT. Figure 3.6(b) shows the nonlocal measurement configuration used in LSVs to extract spin signals. We refer as nonlocal, because the current excitation path and the voltage path are separated spatially. The interface resistances are measured in the configuration shown in Fig. 3.6(c) and the transverse resistance in the one of Fig. 3.6(d).

3.3.2 X-ray reflectivity and diffraction

XRR measurements have been used to quantify the thickness and XRD, or grazing incidence XRD (GI-XRD), experiments to extract the structure and grain sizes of the same thin films. The thin films are grown together with the actual sample by adding a substrate (150 nm SiO_2/doped-Si 10mm×10mm size) in each thin film that is deposited. The X-ray equipment *X'Pert PRO* by *PANalytical* used in this work is shown in Fig. 3.7(a). It is based on an X-ray tube for the X-ray generation, a precise goniometer and a detector with Medipix2 solid state pixel detector technology. The sample is placed on the sample stage above a silicon piece, which reduces the background.

As crystals consists of regularly spaced atoms, the interaction of the incident X-rays with the crystal gives rise to scattered X-rays that interfere constructively and destructively in concrete spatial directions. The spatial variation of the intensity forms a diffraction pattern that contains information of the crystallographic structure of the material. Bragg´s law describes the condition for the constructive interference:

$$n\lambda = 2d\sin(\theta) \tag{3.7}$$

where n is an integer, λ is the wavelength of the incident wave, d is the distance between adjacent atomic planes and θ is the scattering angle, see the inset of Fig. 3.7(a). $\lambda = 0.154$ nm, corresponding to Cu K_α radiation as the anode material used for X-ray generation is made of Cu.

We obtain the diffraction spectrum by collecting the intensity at the detector by scanning θ angle. We observe intensity peaks at particular θ angles, see Fig. 3.7(b), that we can associate to a distance between atomic planes using Eq. 3.7. Generally, the diffraction spectrum is compared to database to identify the crystallographic phase or phases present in the sample. The width of the peak gives information of the grain sizes, the narrower the peak the larger the grain size. We have used GI-XRD technique for the structural characterization of thin

polycrystalline films, by fixing the incident wave angle at $< 1°$and scanning θ.

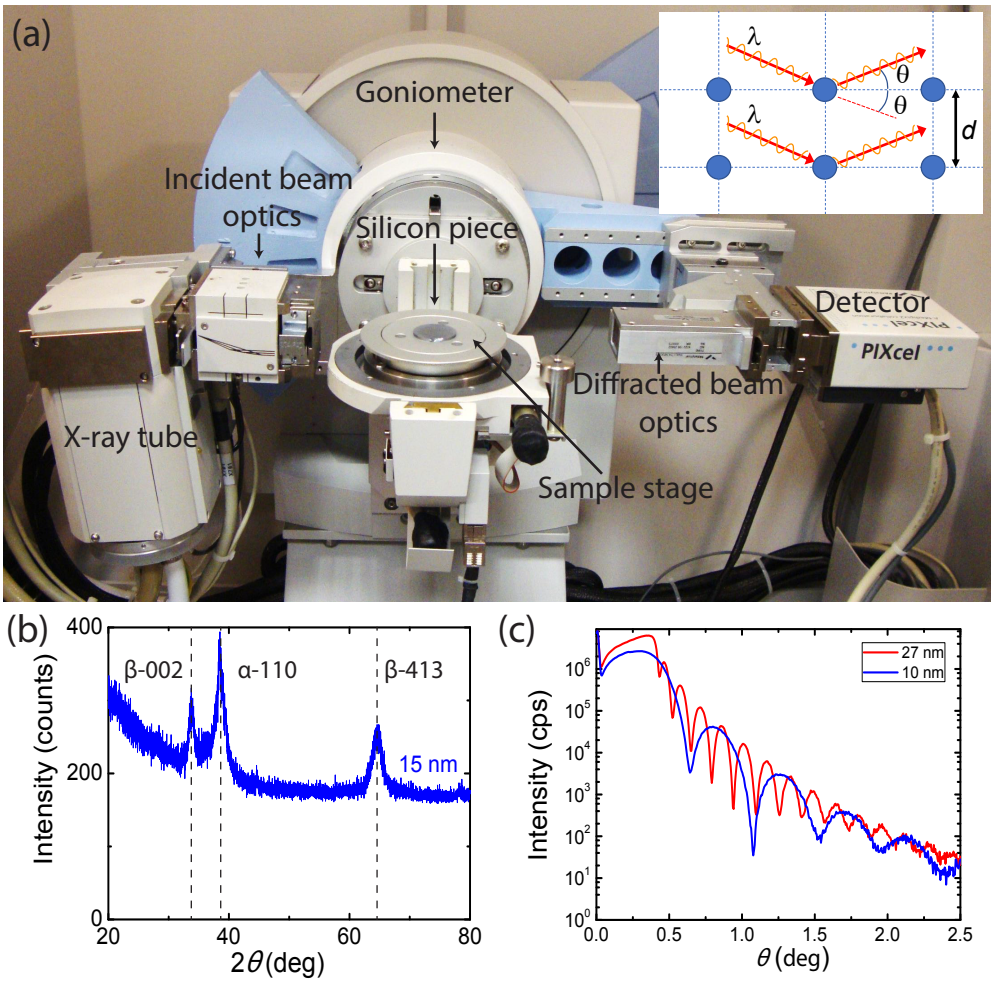

Figure 3.7: **X-ray reflectivity and diffraction measurements.** (a) X-ray equipment. Inset: schematic of the scattering of X-rays in the crystallographic structure . (b) X-ray diffraction pattern of 15-nm-thick Ta thin film. Phase and indexed peaks are tagged. (c) Kiessig fringes of 27-nm and 10-nm-thick Py thin films.

In the reflectivity measurement X-ray incident beam angle and detection angle have the same grazing incidence value during the scan. The interference is generated from the reflected X-rays at the top and bottom surface of the thin film, giving rise to the Kiessig fringes in the measured intensity. From the periodicity of these fringes, the thickness of the material is calculated. Figure 3.7(c) shows the reflectivity data extracted from a 27-nm and 10-nm-thick Py thin films. The thinner the thin film is the broader the fringes are.

3.3.3 Electron microscopy

Scanning electron microscopy

SEM is used to measure the dimensions, lengths and widths, of the fabricated nanodevices with nanometric resolution. SEM is a microscopy technique that by focusing a high energy beam of electrons onto a surface of a sample is able to obtain a high resolution image that contains information about the topography and composition of the sample. The sample is scanned point by point and the secondary electrons or backscattered electrons that are coming from the interaction of the incident electrons with the sample surface are detected. By superposing the information obtained from each individual point the whole image is formed. In this work, the environmental SEM *Quanta FEG 250* from *FEI company* and the e-beam lithography systems by *Raith* have been used.

Transmission electron microscopy

TEM has been used to identify the crystallographic phase and grain sizes of thin films. In this microscopy technique, an image of the sample is formed by detecting the beam of electrons that is transmitted through it. The sample is usually a thin section or lamella. TEM images shown in Chapter 5 are taken by Prof. A. Chuvilin and the sample preparation using the standard focused ion beam (FIB) protocol [118] is carried out by Dr. C. Tollan. Titan 60-300 electron microscope by *FEI Co.*, equipped with an imaging Cs corrector, was used.

Results. Part I

The spin Hall effect in heavy metals: mechanisms and optimization of devices

Chapter 4

The spin Hall effect in Pt

Pt is the prototypical spin Hall metal. The spin Hall effect (SHE) has been studied in Pt by using many different techniques, such as spin pumping [46], spin-torque ferromagnetic resonance (ST-FMR) [52], spin absorption [41,74,90] and by optical methods [75], see some of the techniques in Fig. 1.10. Despite of the broad use of Pt as spin Hall metal, there are relevant open questions that need to be addressed in order to understand the basics of the phenomenon that takes place in this heavy metal and exploit it for plausible applications. On the one hand, the spin Hall angle of Pt, $\theta_{\mathrm{SH}}^{\mathrm{Pt}}$, obtained from different groups and techniques has a large dispersion as shown in Table 1.1 and there is a lack of understanding of why this happens. On the other hand, a systematic experimental study of the different mechanisms contributing to the SHE for relevant materials is lacking. In other words, there are no robust experimental evidences of which mechanism dominates the SHE in Pt. Finding routes to maximize the SHE is not possible as long as it remains unclear whether the dominant mechanism in a material is intrinsic or extrinsic.

In this chapter, we experimentally study the inverse spin Hall effect (ISHE) in Pt with a broad range of longitudinal resistivities, ρ_{Pt}, by using the spin absorption technique in lateral spin valves (LSVs). We first characterize the spin diffusion length of Pt, $\lambda_{\mathrm{s}}^{\mathrm{Pt}}$, as a function of ρ_{Pt}, which plays a relevant role in the SHE phenomenon. We later measure the ISHE in the very same LSVs as a function of temperature and extract the weight of each mechanism of the SHE. We unveil the leading mechanisms of the SHE in Pt and show a route to enhance $\theta_{\mathrm{SH}}^{\mathrm{Pt}}$.

4.1 Characteristics of the samples

Eight devices (E1−E4, S1−S4) were fabricated on top of SiO_2(150nm)/Si substrates by using multiple-step e-beam lithography, subsequent metal deposition and lift-off, as detailed in Section 3.2.1 and Table 3.1. Each device contains two Py($Ni_{81}Fe_{19}$)/Cu LSVs, both with the same Py interelectrode distance $L \sim 630$ nm, but one of them with a Pt wire in between the electrodes as shown in Fig. 4.1(a).

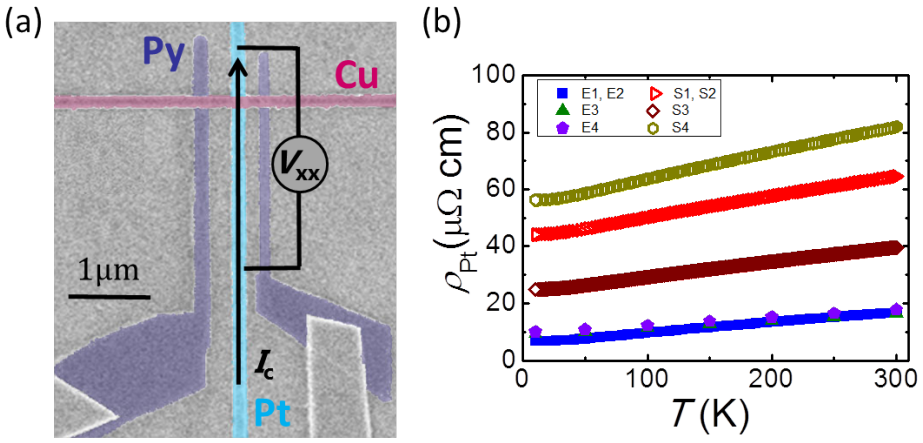

Figure 4.1: **Pt resistivity measurement in the middle wire of the LSV.** (a) Scanning electron microscopy (SEM) image of a Py/Cu LSV with a Pt wire between the two Py electrodes. Four-point measurement configuration is shown to measure the longitudinal resistance of the Pt wire. (b) Longitudinal resistivity of Pt as a function of temperature for the different devices measured at $I_c = 10$ µA in the configuration shown in (a).

First, each pair of Py electrodes was patterned with different widths, w_{FM1} ∼100 nm and w_{FM2} ∼170 nm, in order to obtain different switching magnetic fields, and 35 nm of Py were e-beam evaporated. During the second step, a ∼130-nm-wide and 20-nm-thick Pt was deposited by e-beam evaporation (base pressure $\leq 10^{-8}$ Torr, rate 0.1 − 2.0 Å/s, substrate temperature 5−7 °C) in half of the devices (E1−E4) and by magnetron sputtering (base pressure from 10^{-7} to 10^{-8} Torr, power 80 W, Ar pressure 3×10^{-3} Torr, rate 1.3 Å/s, substrate temperature 25 °C) in the other half (S1−S4). The different Pt wires cover a broad range of resistivities, with the evaporated ones having a smaller residual resistivity, $\rho_{Pt,0}$, due to the larger grain sizes than the sputtered ones, see Fig. 4.1(b) and Table 4.1. In the third lithography step, a ∼150-nm-wide channel was patterned and 100-nm-thick Cu was thermally evaporated. In order to have highly transparent Py/Cu and Pt/Cu interfaces, the surfaces of the Py and Pt wires were cleaned via Ar-ion milling before the Cu deposition. Transparent interfaces were confirmed by measuring the interface resistances using the configuration shown

in Fig. 3.6(c). All longitudinal resistivity and nonlocal transport measurements were carried out using a "dc reversal" technique, see Section 3.3.1, in a liquid-He cryostat, applying an external magnetic field, $\vec{H}$, and varying temperature, T.

4.2 Spin diffusion length of Pt

First we characterize λ_s^{Pt} of the Pt middle wire in the LSV, using the spin absorption technique described in Section 2.1.2. The accurate quantification of λ_s^{Pt} is relevant in order to extract later precise spin-to-charge current conversion (SCC) parameters.

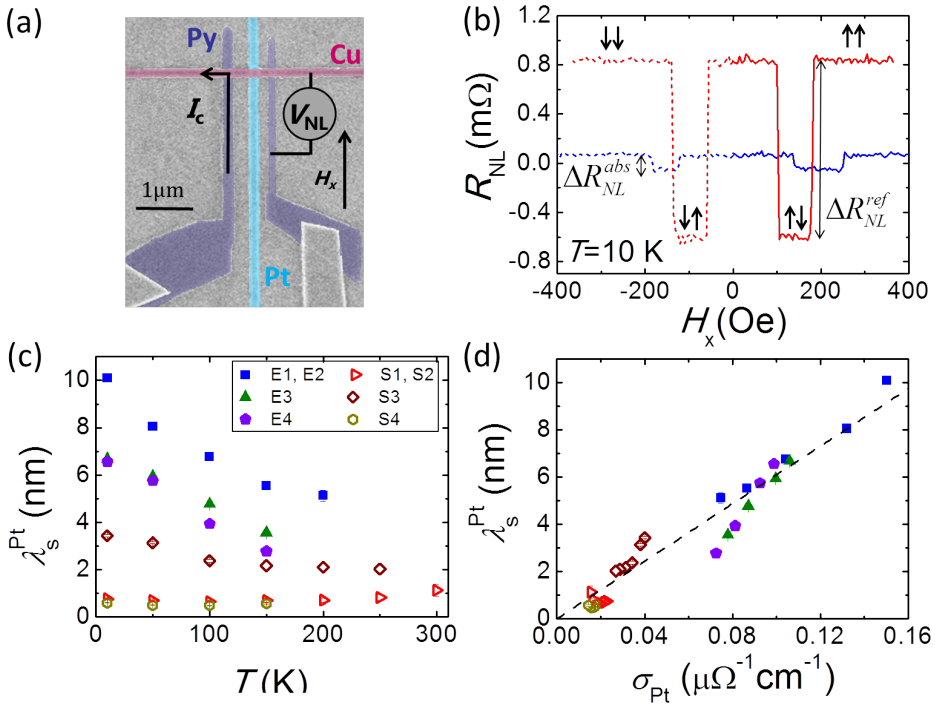

Figure 4.2: **Characterization of the spin diffusion length of Pt using LSVs with a Pt middle wire.** (a) SEM image of a Py/Cu LSV with a Pt middle wire between the two Py electrodes. The nonlocal measurement configuration and the direction of the applied magnetic field (H_x) is shown. (b) Nonlocal resistance as a function of H_x measured at $I_c = 100$ μA and 10 K in device S2 using the configuration shown in (a) for a Py/Cu LSV with (blue line) and without (red line) a Pt wire in between the Py electrodes. The solid (dashed) line corresponds to the increasing (decreasing) magnetic field. The reference spin signal (ΔR_{NL}^{ref}) and the spin signal with Pt absorption (ΔR_{NL}^{abs}) are tagged. (c) Spin diffusion length of Pt as a function of temperature for all devices. (d) Spin diffusion length of Pt as a function of longitudinal conductivity for all devices. The black dashed line is a linear fitting of the experimental data. Since devices E1 and E2 (S1 and S2) were fabricated in the same chip, Pt was evaporated (sputtered) in the same deposition, hence it is assumed that E1 and E2 (S1 and S2) have the same ρ_{Pt} and λ_s^{Pt}.

Figure 4.2(a) shows the nonlocal measurement configuration with the external magnetic field applied in the easy axis of the ferromagnetic (FM) electrodes, H_x. Using this configuration, the signals shown in Fig. 4.2(b) have been obtained for reference Py/Cu LSV (red line) and Py/Cu LSV with Pt middle wire (blue line). In the latter, the obtained spin signal, ΔR_{NL}^{abs}, is smaller than the reference spin signal, ΔR_{NL}^{ref}, due to the spin absorption of Pt. From the ratio of two spin signals, which is given by Eq. 2.18, we can extract λ_s^{Pt}. The rest of the parameters used in Eq. 2.18 are known. The widths and lengths are measured by SEM and the thicknesses by X-ray reflectivity (XRR). The resistivities of the Cu channel and Py electrodes are measured in the same device using the four-point configuration as shown in Fig. 4.1(a) for Pt. The current spin polarization of Py, α_{Py}, and the spin diffusion length of Cu and Py, λ_s^{Cu} and λ_s^{Py} respectively, were previously quantified in our group by Villamor *et al.* [28,119]. By repeating the measurement shown in Fig. 4.2(b) at different temperatures and in all devices, λ_s^{Pt} as a function of temperature is obtained for all devices, see Fig. 4.2(c) and Table 4.1.

Table 4.1: **Charge transport, spin transport and spin Hall parameters of the different Pt devices.** Residual resistivity ($\rho_{Pt,0}$), spin diffusion length (λ_s^{Pt}) and spin Hall angle (θ_{SH}^{Pt}) of Pt wires of each device at 10 K are listed. Intrinsic spin Hall conductivity (σ_{SH}^{int}) and skew-scattering angle (α_{SH}^{ss}) extracted from the individual fittings of each device are included. The calculated shunting factor $x_{Pt,Cu}$ at 10 K for each device is also added.

Device	$\rho_{Pt,0}$ ($\mu\Omega$cm)	λ_s^{Pt} (nm)	θ_{SH}^{Pt} (%)	σ_{SH}^{int} ($(\hbar/e)\Omega^{-1}$cm^{-1})	α_{SH}^{ss} (%)	$x_{Pt,Cu}$
E1	6.66	10.1 ± 0.1	2.1 ± 0.7	1480 ± 110	1.2 ± 0.2	0.228
E2	6.66	10.1 ± 0.1	1.7 ± 0.4	1780 ± 95	0.7 ± 0.2	0.228
E3	9.42	6.7 ± 0.1	2.2 ± 0.2	1750 ± 360	0.4 ± 0.5	0.285
E4	10.12	6.5 ± 0.1	2.2 ± 0.3	1910 ± 700	0.1 ± 0.9	0.285
S1	44.19	0.75 ± 0.03	8.5 ± 1.3	1525 ± 220	2.1 ± 1.3	0.156
S2	44.19	0.75 ± 0.03	7.4 ± 0.7	1280 ± 140	2.0 ± 0.9	0.156
S3	24.96	3.43 ± 0.05	5.3 ± 0.6	1435 ± 390	1.9 ± 1.3	0.086
S4	56.25	0.59 ± 0.01	10.7 ± 1.0	1770 ± 760	1.6 ± 5.2	0.147

Combining Fig. 4.1(b) and Fig. 4.2(c), we plot λ_s^{Pt} as a function of the longitudinal conductivity of Pt ($\sigma_{Pt} = \rho_{Pt}^{-1}$) in Fig. 4.2(d). The linear dependence between λ_s^{Pt} and σ_{Pt} confirms that Elliott-Yafet, see Section 1.1.2, is the main spin relaxation mechanism in Pt. This result is compatible with other observations using other experimental techniques [92, 120]. From our data, we obtain a slope of $(0.61 \pm 0.02 \times 10^{-15}\ \Omega m^2)$, which is in excellent agreement with a theoretical prediction $(0.63 \pm 0.02 \times 10^{-15}\ \Omega m^2)$ from first principle scattering theory

combined with temperature-induced disorder [121].

4.3 The spin Hall effect in Pt

Next, we measure the ISHE in Pt using the spin absorption technique, described in Section 2.1.3, in the same eight devices by changing the measurement configuration to the one described in Fig. 4.3(a). Figure 4.3(b) shows the nonlocal resistance R_{ISHE} as a function of H_{y} measured in Pt as a result of the ISHE. We repeat this measurement at different temperatures and for the eight devices.

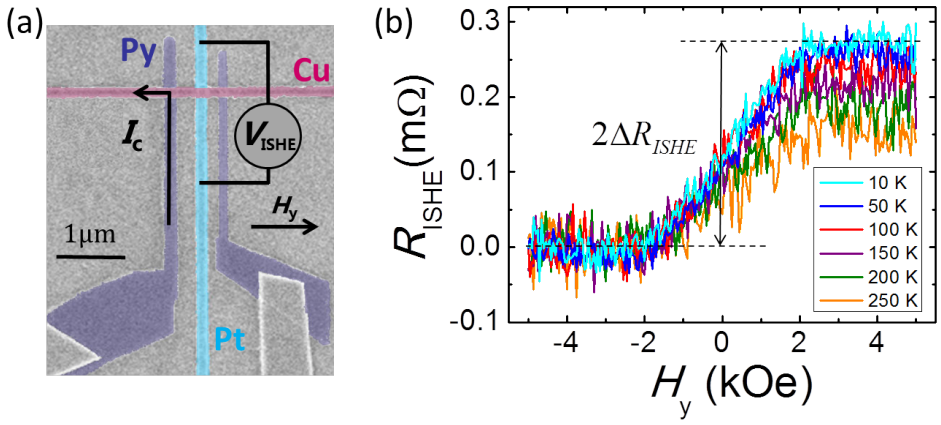

Figure 4.3: **Characterization of the ISHE in Pt using LSVs with a Pt middle wire.** (a) SEM image of a Py/Cu LSV with a Pt middle wire between the two Py electrodes used to measure ISHE. The nonlocal measurement configuration for the ISHE and the direction of the applied magnetic field (H_{y}) is shown. (b) ISHE resistance as a function of magnetic field measured in device S2 at $I_{\mathrm{c}} = 100$ μA and different temperatures in the configuration shown in (a). The curves have been shifted for clarity. The ISHE signal ($2\Delta R_{\mathrm{ISHE}}$) for 10 K is tagged.

Considering the measured ΔR_{ISHE} and employing Eqs. 2.20, 2.21 and 2.24, we calculate the spin Hall resistivity, $\rho_{\mathrm{SH}} \equiv \rho_{\mathrm{xy,SH}}$, for each temperature for all devices. We substitute in these equations the geometrical factors measured by SEM, the thicknesses measured by XRR, the resistivities of Cu, Pt and Py measured in the same device using four-point configuration as shown in Fig. 4.1(a) for Pt, $\lambda_{\mathrm{s}}^{\mathrm{Cu}}$, $\lambda_{\mathrm{s}}^{\mathrm{Py}}$ and α_{Py} that were previously determined in our group by Villamor *et al.* [28, 119] and, importantly, $\lambda_{\mathrm{s}}^{\mathrm{Pt}}$ that was extracted in the previous section. $\lambda_{\mathrm{s}}^{\mathrm{Pt}}$ has an important weight in the prefactor of Eq. 2.21, as it describes for how long the spins diffuse in Pt and the SCC will only take place in this length. Another relevant parameter is the shunting factor, $x_{\mathrm{Pt,Cu}}$, introduced in Section 2.1.3, that was calculated by SPINFLOW 3D software [80] by Dr. Y. Omori. For this calculation, the exact w_{Cu}, w_{Pt}, ρ_{Cu} and ρ_{Pt} values of the devices were considered, as the parameter depends strongly on them.

As we measured the temperature dependence of ρ_{Pt}, see Fig. 4.1(b), we can now relate ρ_{SH} with ρ_{Pt}. By plotting $-\rho_{\mathrm{SH}}$ against ρ_{Pt}^2 we are able to fit the data of each device to an individual linear function. Following Eq. 1.16, the slope corresponds to the intrinsic contribution, namely the intrinsic spin Hall conductivity, $\sigma_{\mathrm{SH}}^{\mathrm{int}}$, and the intercept divided by $\rho_{\mathrm{Pt},0}$ defines the skew-scattering angle, $\alpha_{\mathrm{SH}}^{\mathrm{ss}}$. As the side-jump contribution arises only in materials with high impurity concentrations [50, 122, 123], this contribution is negligible in out high purity Pt. Figure 4.4 shows the data for all devices and the corresponding linear fits for each device. The values extracted from the individual fits for each device, *i.e.* $\sigma_{\mathrm{SH}}^{\mathrm{int}}$ and $\alpha_{\mathrm{SH}}^{\mathrm{ss}}$, are collected in Table 4.1.

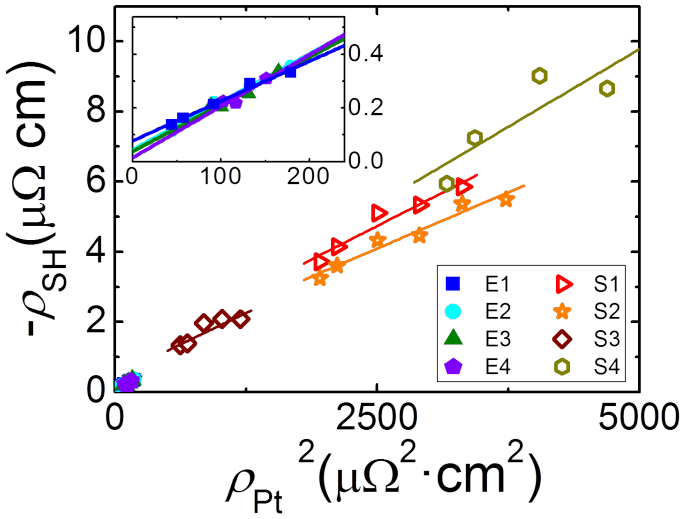

Figure 4.4: **Extraction of the spin Hall parameters to unveil the leading mechanism in the SHE of Pt.** Spin Hall resistivity as a function of the square of the longitudinal resistivity of Pt for all devices. Solid lines correspond to the individual fit of the data of each device to Eq. 1.16. Inset: Zoom of the previous plot at low resistivities, showing the data of the devices with evaporated Pt.

Interestingly, the data in Table 4.1 reveals that the extracted $\sigma_{\mathrm{SH}}^{\mathrm{int}}$ for all the devices are very close to each other, especially taking into account the different resistivities and $\theta_{\mathrm{SH}}^{\mathrm{Pt}}$ in each device. We obtain an average value of $\sigma_{\mathrm{SH}}^{\mathrm{int}} = 1600 \pm 150(\hbar/e)\ \Omega^{-1}\mathrm{cm}^{-1}$ for Pt, indicating that the intrinsic contribution of the spin Hall conductivity is a constant within a 10% dispersion. This experimental finding is in excellent agreement with theoretical values of $1300(\hbar/e)\ \Omega^{-1}\mathrm{cm}^{-1}$ [78] and $1600(\hbar/e)\ \Omega^{-1}\mathrm{cm}^{-1}$ [124] obtained with different approaches. The predicted decrease of $\sigma_{\mathrm{SH}}^{\mathrm{int}}$ of Pt at higher resistivities by Tanaka *et al.* [78] lies outside our studied range. A recent experimental study employing ST-FMR technique (see Fig. 1.10(e)) reports a lower bound of $\sigma_{\mathrm{SH}}^{\mathrm{int}} = 2950 \pm 100(\hbar/e)\ \Omega^{-1}\mathrm{cm}^{-1}$ for Pt [92], much higher than ours and theoretical predictions.

The skew-scattering angle yields similar values for all devices deposited

with the same technique, but slightly different for each deposition type. The observation is reasonable as this extrinsic contribution depends directly on the kind of defects in the Pt. Sputtered and evaporated Pt have different grain sizes and, moreover, the deposition in different chambers gives rise to the presence of different impurities, hence explaining the different skew-scattering contribution in each type of Pt.

As the extrinsic contribution, $\alpha_{\mathrm{SH}}^{\mathrm{ss}}$, is different for the evaporated and sputtered sample we cannot plot a universal curve for the SHE in Pt. Nevertheless, we can still plot $\theta_{\mathrm{SH}}^{\mathrm{Pt}}$ and the spin Hall conductivity, $\sigma_{\mathrm{SH}} = -\rho_{\mathrm{SH}}/\rho_{\mathrm{Pt}}^2$, as a function of σ_{Pt}, see Fig. 4.5 in order to compare the relative weight of the different contributions in analogy to the different scaling regimes obtained in the anomalous Hall effect (AHE) (see Fig. 1.8) [68, 69, 125].

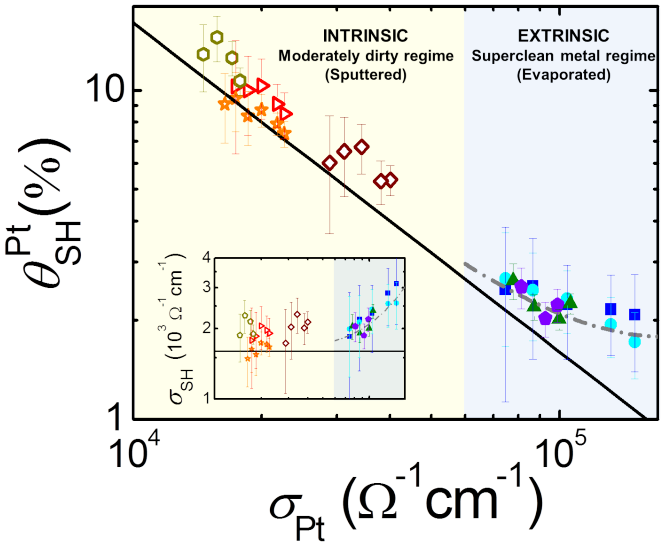

Figure 4.5: **Crossover between the moderately dirty and the superclean scaling regimes of the SHE in Pt.** Spin Hall angle as a function of the longitudinal conductivity of Pt of all devices. The regions with different scaling regimes are indicated. The black solid line corresponds to the intrinsic contribution of the spin Hall angle $\theta_{\mathrm{SH}}^{\mathrm{Pt,int}} = \sigma_{\mathrm{SH}}^{\mathrm{int}}/\sigma_{\mathrm{Pt}}$, using $\sigma_{\mathrm{SH}}^{\mathrm{int}} = 1600(\hbar/e)\ \Omega^{-1}\mathrm{cm}^{-1}$. The gray dashed line in the superclean region corresponds to the total spin Hall angle calculated with both intrinsic and skew-scattering contributions, using the average value $\alpha_{\mathrm{SH}}^{\mathrm{ss}} = 0.6\%$ obtained for this region. The symbols that represent each device are the same as in Fig. 4.4. Inset: same data plotted as spin Hall conductivity. The scale of the horizontal axis is the same as in the main panel.

$\theta_{\mathrm{SH}}^{\mathrm{Pt}}$ for evaporated and sputtered devices scale in a very different way with σ_{Pt}, as it can be seen in Fig. 4.5. $\theta_{\mathrm{SH}}^{\mathrm{Pt}}$ for sputtered devices, with highest resistivity, shows the same trend expected from the intrinsic contribution ($\theta_{\mathrm{SH}}^{\mathrm{Pt,int}} = \sigma_{\mathrm{SH}}^{\mathrm{int}}/\sigma_{\mathrm{Pt}}$, black solid line), and the total experimental $\theta_{\mathrm{SH}}^{\mathrm{Pt}}$ nearly merges into the intrinsic value (the small difference is given by the minor contribution of

the skew scattering). This region dominated by the intrinsic scaling regime thus corresponds to the moderately dirty region, similarly to what is observed in the AHE [68, 69]. In contrast, in the lower resistivity region, the intrinsic contribution cannot explain the values of the experimental data, even the trend. Nevertheless, by adding the corresponding extrinsic contribution for this region to the diminishing intrinsic one, we obtain the gray dashed line that matches perfectly with our data. This region is thus representing a clean metal, where the skew scattering dominates the scaling. Consequently, we observe the crossover from the intrinsic moderately dirty regime to the extrinsic superclean metal regime for the SHE, demonstrating a perfect correspondence with the AHE [68, 69, 125].

4.4 Conclusions

We experimentally obtain a general scaling of the SHE using Pt, which is analogous to the one observed for the AHE in FM conductors. We demonstrate that $\sigma_{\mathrm{SH}}^{\mathrm{int}}$ is constant in Pt with the value $1600 \pm 150(\hbar/e)\ \Omega^{-1}\mathrm{cm}^{-1}$ and this allows us to move from an intrinsic to an extrinsic regime when decreasing the resistivity from a moderately dirty to a clean metal. The obtained experimental results evidence that the variation of the Pt resistivity among different groups is one of the main reasons for the spread of $\theta_{\mathrm{SH}}^{\mathrm{Pt}}$ values in literature. Indeed, we are able to tune $\theta_{\mathrm{SH}}^{\mathrm{Pt}}$ from $\sim 2\%$ to $\sim 14\%$ by varying ρ_{Pt} from ~ 7 $\mu\Omega$cm to ~ 70 $\mu\Omega$cm, reproducing partially the dispersion in literature. A very important consequence is that we show a clear path to enhance $\theta_{\mathrm{SH}}^{\mathrm{Pt}}$ by simply increasing the resistivity of any material with a dominant intrinsic contribution to the SHE.

Regarding the spin transport properties of Pt, we confirmed that Elliott-Yafet is the main spin relaxation mechanism in Pt. $\lambda_{\mathrm{s}}^{\mathrm{Pt}}$ varies linearly with the longitudinal conductivity of the metal. This indicates that assuming a constant $\lambda_{\mathrm{s}}^{\mathrm{Pt}}$ value for a series of Pt samples characterized by different ρ_{Pt} implies an incorrect approximation, which is frequently done in literature, specially when thickness dependence studies are performed.

Chapter 5

The spin Hall effect in Ta

Ta exists in two different crystallographic phases: α-Ta and β-Ta. Whereas bulk Ta is α phase, β-Ta is a metastable phase mainly observed in sputter deposited thin films. The former is metallic and is characterized by a lower resistivity ($\rho_{\alpha\text{-Ta}} = 15 - 60$ $\mu\Omega$cm) than the latter ($\rho_{\beta\text{-Ta}} = 170 - 200$ $\mu\Omega$cm) [126, 127]. β-Ta has a negative temperature coefficient of resistance (TCR), *i.e.* $\rho_{\beta\text{-Ta}}$ decays with temperature [128]. Importantly, the crystallographic structure is different for each phase: α-Ta has a bcc crystal structure [127], and for β-Ta tetragonal, hexagonal and cubic candidates have been proposed [129]. Recent experimental works assign a tetragonal structure to β-Ta [86, 88]. In 2008, Tanaka *et al.* theoretically calculated the intrinsic spin Hall conductivity, $\sigma_{\text{SH}}^{\text{int}}$, for the $4d$ and $5d$ transition metals, obtaining at the high-resistive regime the largest values for Ta (α-Ta) and W [78], see Fig. 1.9(a). Four years later, Liu *et al.* found a giant spin Hall effect (SHE) in β-Ta, highlighting its suitability for spin-orbit based applications [83].

Since the experimental finding by Liu and coworkers, several groups have studied the SHE in β-Ta employing different techniques. As it occurs with Pt, discrepancies between the measured spin Hall angle of β-Ta, $\theta_{\text{SH}}^{\text{Ta}}$, among different groups and techniques are common, see Table 1.1. More importantly, experimental evidences of the weight of each mechanism that contributes to the SHE of Ta are lacking. This hides the path to enhance $\theta_{\text{SH}}^{\text{Ta}}$, which prevents the development of plausible and efficient spin-orbit based applications [2].

The proper characterization of the Ta-phase in the experimental samples is essential, in order to avoid the comparison between results obtained for different Ta phases, either experimentally or theoretically. As it was remarked in Section 1.2.1, the intrinsic contribution relies precisely on the band structure of the metal. Therefore, a different $\sigma_{\text{SH}}^{\text{int}}$ is expected for α-Ta and β-Ta [130], given their different crystallographic phases and, hence, their different electronic bands.

In this chapter, we experimentally study the inverse spin Hall effect (ISHE) in β-Ta in a wide range of resistivities employing the spin absorption technique in lateral spin valves (LSVs). We first realize the structural characterization of the Ta thin films to determine that we are studying the ISHE in β-Ta phase. Then, we extract the spin diffusion length of Ta, λ_s^{Ta}, which plays a relevant role in the spin-to-charge current conversion (SCC) phenomenon and, finally, we measure the ISHE and extract the weight of each mechanism. We unravel the dominating mechanism of the SHE in Ta and we are able to enhance θ_{SH}^{Ta}, achieving the largest conversion efficiency reported so far for a pure metal. The fabrication and the measurement of the devices of this work was carried out in the laboratory of Prof. Otani in the Institute of Solid State Physics of the University of Tokyo, where I completed an internship of three months.

5.1 Characteristics of the samples

Seven devices (D1-D7) were fabricated on top of SiO_2(150nm)/Si substrates. Multiple-step e-beam lithography, subsequent metal deposition and lift-off was done, as detailed in Section 3.2.1 and Table 3.1, although ZEP resist was employed for the patterning of the Ta wire and Py and Cu evaporation conditions were slightly different, as detailed below. Each device contains two Py($Ni_{81}Fe_{19}$)/Cu LSVs, both with the same Py interelectrode distance $L \sim 1000$ nm, but one of them includes a Ta wire in between the electrodes as shown in Fig. 5.1(a).

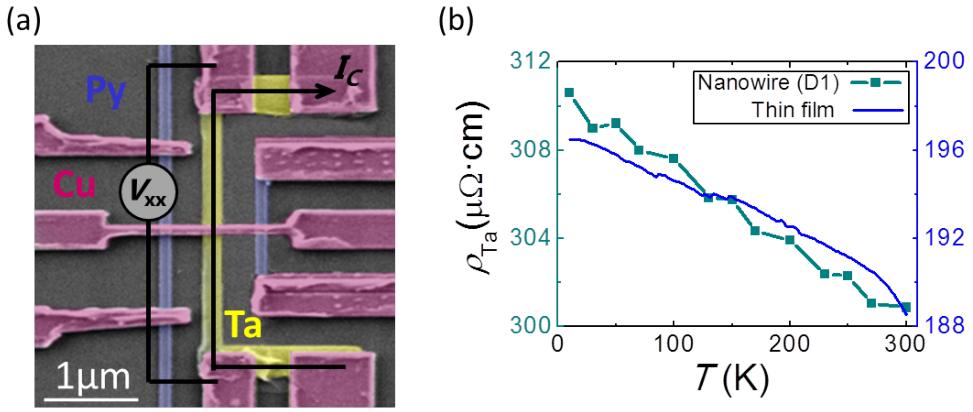

Figure 5.1: **Ta resistivity measurement in 15-nm-thick Ta middle wire of the LSV and 15-nm-thick Ta film.** (a) Scanning electron microscopy (SEM) image of a Py/Cu LSV with a Ta wire between the two Py electrodes. Four-point measurement configuration to measure the longitudinal resistance of the Ta wire is shown. (b) Longitudinal resistivity of Ta as a function of temperature of the 15-nm-thick Ta nanowire in D1 device (solid green squares) measured at $I_c = 0.2$ μA in the configuration shown in (a) and of a 15-nm-thick Ta film (blue solid line) grown in the same sputtering conditions as the D1 nanowire, measured by the Van der Pauw method at $I_c = 0.5$ mA. Green solid line is a guide to the eye.

First, 100-nm-wide Py electrodes were patterned with different shape to get different switching magnetic fields, with an interelectrode distance of 1 μm and 30 nm of Py were e-beam evaporated at 0.6 Å/s and 1.4×10^{-8} Torr. In the second step, the Ta electrode was patterned and 10 or 15 nm of Ta were sputtered at 1.6 Å/s, 20 W of power, 8×10^{-8} Torr of base pressure and 1.5×10^{-3} Torr of Ar pressure. The width and thickness of the Ta nanowires were modified in order to obtain different residual resistivities, $\rho_{\mathrm{Ta},0}$. In the third step, a 100-nm-wide channel was patterned and ∼100 nm of Cu were thermally evaporated at 3 Å/s and $1.2{\times}10^{-8}$ Torr. In order to remove the ∼2.4-nm-thick native oxide from the Ta wire, see Figs. 5.2(a) and 5.2(d), and achieve electrically transparent Ta/Cu and Py/Cu interfaces, the surfaces of Py and Ta were *in-situ* cleaned by Ar-ion milling before the Cu deposition. Transparent interfaces were confirmed by measuring the interface resistances using the configuration shown in Fig. 3.6(c). In this study, instead of the delta mode technique (described in Section 3.3.1), all transport measurements were carried out using the lock-in technique (173 Hz) in a ^{4}He flow cryostat, applying an external magnetic field, $\vec{H}$, and varying temperature, T.

The temperature dependence of ρ_{Ta} for the Ta nanowire in device D1 is plotted by the green solid squares in Fig. 5.1(b). It shows a negative TCR, as expected for β-Ta phase [128] and ρ_{Ta} varies slightly with the temperature, ∼3% from 10 K to 300 K, which is also characteristic of this phase. ρ_{Ta} of a 15-nm-thick Ta film measured by Van der Pauw method [131] is shown by the blue curve in Fig. 5.1(b). Interestingly, the obtained ρ_{Ta} values, 189−197 μΩcm in the temperature range of 10−300 K, are in very good agreement with the ones corresponding to β-Ta phase [126]. Although the ρ_{Ta} results point towards a β-Ta phase, we perform a detailed structural characterization, via X-ray diffraction (XRD) and electron diffraction (ED), to confirm which Ta phase is present in our samples.

Structural characterization

Structural characterization was performed in 10- and 15-nm-thick Ta films grown at the same conditions as the middle Ta wire in the LSVs using transmission electron microscopy (TEM) by Prof. Andrey Chuvilin. High-resolution TEM (HR-TEM) images were obtained at 300 kV at negative Cs imaging conditions [132]. The sample for TEM were fabricated by the standard focused ion beam (FIB) protocol [118] by Dr. Christopher Tollan.

Figures 5.2(a) and 5.2(d) show the HR-TEM image of a cross section of the 15-nm-thick and 10-nm-thick Ta film, respectively. The films are polycrystalline with seemingly random distribution of crystal orientations. As ED from such a thin and laterally extended structure is technically difficult to obtain, its mathematical analog was used instead: 2D fast Fourier transform (FFT) of a high resolution image, shown in Figs. 5.2(b) and 5.2(e) for 15-nm-thick and

10-nm-thick Ta, respectively.

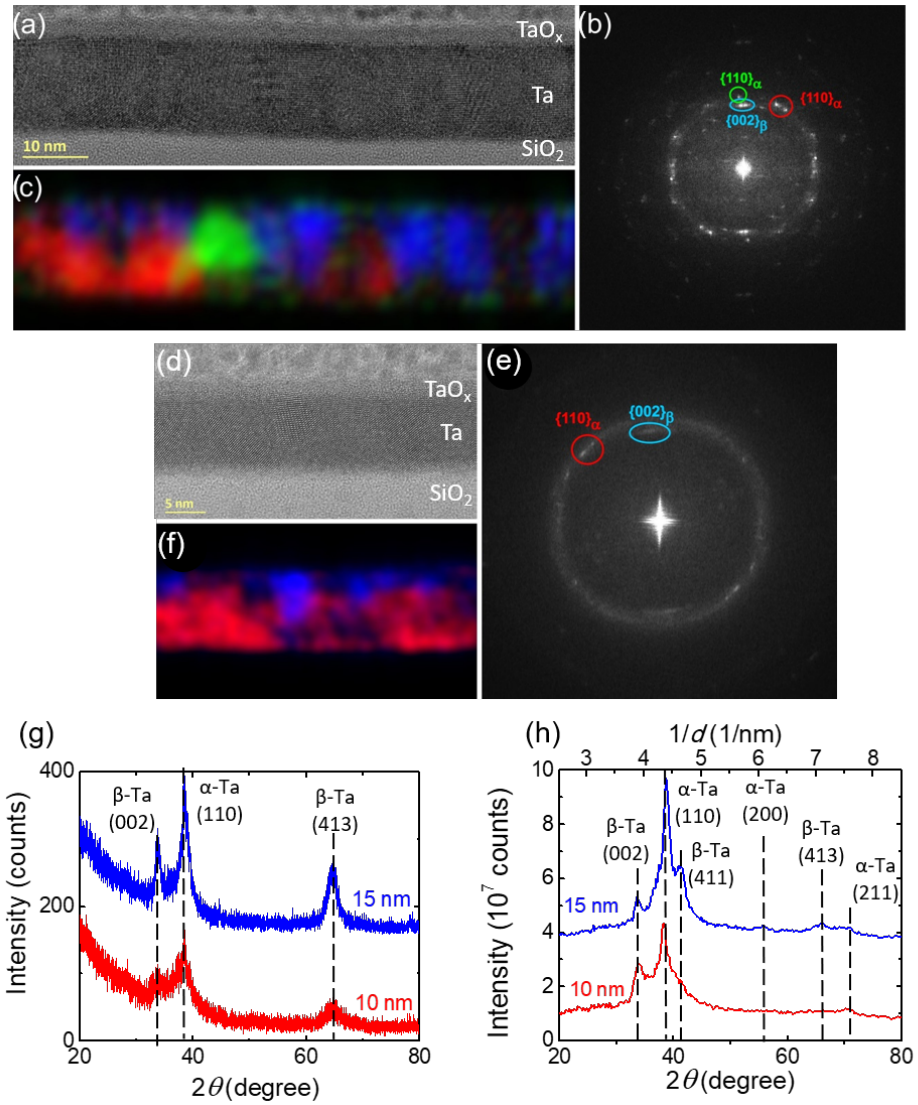

Figure 5.2: **Structural characterization of 10- and 15-nm-thick Ta films.** (a) and (d) High-resolution TEM image of a cross section of the 15-nm-thick and 10-nm-thick Ta films, respectively. (b) and (e) FFT pattern of the layer on (a) and (d), respectively. (c) and (f) Superposition of color-coded virtual dark-field images reconstructed from reflections marked on (b) and (e), respectively, showing distribution, size and shape of β-Ta and α-Ta nanocrystals in the layer. (g) GI-XRD 2θ scan for a grazing incidence angle of $\phi = 0.5°$ in 15- (blue line) and 10-nm-thick (red line) Ta films. The data of 15-nm-thick Ta has been shifted for clarity. (h) ED pattern obtained by TEM for 15-nm (blue line) and 10-nm-thick (red line) Ta thin films. The data of 15-nm-thick Ta has been shifted for clarity. d is the distance between adjacent atomic planes in the crystal, see Section 3.3.2.

The FFT pattern reveals the coexistence of two types of reflections: with the interatomic plane distance of $d \sim 0.26$ nm, that can be attributed to $\{002\}$ lattice planes of β-Ta (either tetragonal or hexagonal) and $d \sim 0.23$ nm, which can be

attributed to {110} lattice planes of cubic α-Ta. It is remarkable that although α-Ta nanocrystals have random orientations, *i.e.*, its reflections are uniformly distributed on the ring of the FFT pattern, the β-Ta phase shows a clear texture with the c axis normal to the surface.

Figures 5.2(c) and 5.2(f) combine virtual dark-field images, reconstructed from the reflections marked in Figs. 5.2(b) and 5.2(e), respectively, for 15-nm-thick and 10-nm-thick Ta. Green and red colors in Fig. 5.2(c) correspond to the same α-Ta phase but we distinguish the reflection from where they were reconstructed, as shown in Fig. 5.2(b). The β-Ta phase forms a continuous, yet heavily distorted, layer on top of α-Ta nanocrystals in both Ta thicknesses. This last observation is relevant, as the spin current arriving to the Ta via Cu spin transport channel will be absorbed by the top part of Ta, thus mainly by β-Ta. Due to short $\lambda_{\mathrm{s}}^{\mathrm{Ta}}$, as we will see in the next section, the SCC will take place here. Grazing incidence XRD (GI-XRD) confirms the coexistence of α-Ta and β-Ta phases in both films, see Fig. 5.2(g), which is in good agreement with the ED result, shown in Fig. 5.2(h).

5.2 Spin diffusion length of Ta

In order to extract $\lambda_{\mathrm{s}}^{\mathrm{Ta}}$, the spin absorption experiment is performed, as described in Section 2.1.2.

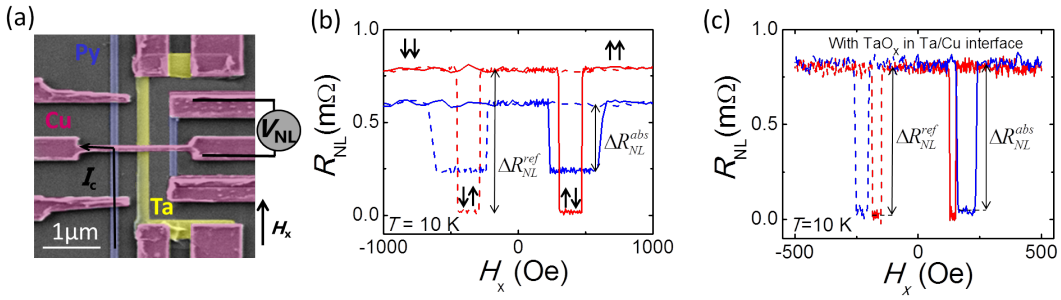

Figure 5.3: **Characterization of the spin diffusion length of Ta using LSVs with a Ta middle wire.** (a) SEM image of a Py/Cu LSV with a Ta middle wire between the two Py electrodes. The nonlocal measurement configuration and the direction of the applied magnetic field (H_{x}) is shown. (b) Nonlocal resistance as a function of H_{x} measured at $I_{\mathrm{c}} = 575$ μA and 10 K in device D1 using the configuration shown in (a) for a Py/Cu LSV with (blue line) and without (red line) a Ta wire in between the Py electrodes. The solid (dashed) line corresponds to the increasing (decreasing) magnetic field. The reference spin signal ($\Delta R_{\mathrm{NL}}^{\mathrm{ref}}$) and the spin signal with Ta absorption ($\Delta R_{\mathrm{NL}}^{\mathrm{abs}}$) are tagged. (c) Same measurement as in (b) but in a device where the Ar-ion milling and the Cu thermal evaporation were not done *in situ*, resulting on the presence of TaO_{x} at the Cu/Ta interface, which prevents spin absorption ($\Delta R_{\mathrm{NL}}^{\mathrm{ref}} = \Delta R_{\mathrm{NL}}^{\mathrm{abs}}$).

Figure 5.3(a) shows the nonlocal measurement configuration with the external

magnetic field applied in the easy axis of the ferromagnetic electrodes, H_x. Using this configuration, the spin signals shown in Fig. 5.3(b) have been obtained for reference Py/Cu LSV (red line) and Py/Cu LSV with Ta middle wire (blue line). In the latter, the obtained spin signal, ΔR_{NL}^{abs}, is smaller than the reference spin signal, ΔR_{NL}^{ref}. This indicates that the Ta is indeed absorbing part of the spin current that is flowing in the Cu channel. Interestingly, Fig. 5.3(c) shows the spin signals obtained in a reference (red line) and spin absorption (blue line) devices where the Ar-ion milling and Cu thermal evaporation were not done *in situ*. This is a control experiment evidencing that, if the TaO_x is not properly removed between the Cu and Ta interface, the Ta middle wire is not able to absorb any spin current and the reference spin signal equals the spin signal obtained for the LSV with the Ta middle wire.

From the ratio of the spin signals obtained in Fig. 5.3(b), λ_s^{Ta} is obtained by applying Eq. 2.18. Here we substitute the values of the lengths and widths that are measured by SEM, the thicknesses by X-ray reflectivity (XRR), the resistivities by four-point measurements, see Fig. 5.1(a) for the case of Ta. The current spin polarization of Py, α_{Py}, the spin diffusion length of Py, λ_s^{Py}, and the spin diffusion length of Cu, λ_s^{Cu}, were previously quantified by the Otani´s group [133,134]. We repeat this measurement and calculation in D1 as a function of temperature and for all the different devices (D2−D7) at 10 K. The obtained λ_s^{Ta} for each device at 10 K is shown in Table 5.1. We observe that λ_s^{Ta} is small for all devices, between 0.8 and 2.4 nm and has no clear tendency with ρ_{Ta}.

Table 5.1: **Charge transport, spin transport and spin Hall parameters of the different Ta nanowires.** Thickness (t_{Ta}), width (w_{Ta}), residual resistivity ($\rho_{Ta,0}$), spin diffusion length (λ_s^{Ta}) and spin Hall angle (θ_{SH}^{Ta}) of the Ta nanowires at 10 K are included. The calculated shunting factor $x_{Ta,Cu}$ values at 10 K are also added.

Device	t_{Ta} (nm)	w_{Ta} (nm)	$\rho_{Ta,0}$($\mu\Omega$cm)	λ_s^{Pt}(nm)	θ_{SH}^{Ta} (%)	$x_{Ta,Cu}$
D1	15	270	311	2.39 ± 0.03	-5.0 ± 0.3	0.095
D2	15	270	330	1.27 ± 0.02	-7.6 ± 0.6	0.096
D3	15	270	369	0.81 ± 0.02	-11.3 ± 0.9	0.102
D4	10	273	401	1.52 ± 0.05	-10 ± 1	0.041
D5	10	224	483	1.31 ± 0.02	-13.2 ± 0.9	0.045
D6	10	187	493	2.22 ± 0.06	-17 ± 1	0.041
D7	10	195	648	0.76 ± 0.03	-35 ± 3	0.039

5.3 The spin Hall effect in Ta

Once demonstrated that Ta absorbs part of the spin current flowing along the Cu channel, we measure the ISHE in Ta using the spin absorption technique as described in Section 2.1.3 . Using the configuration shown in Fig. 5.4(a), we measure the nonlocal resistance R_{ISHE}, originated due to the ISHE of Ta, as a function of H_{y}. The obtained curve for device D1 is plotted in Fig. 5.4(b). Note that the measured ΔR_{ISHE} in Ta is negative, *i.e.*, opposite to the one obtained in Pt (see Fig. 4.3(b)), which is expected because the d band is less than half filled in Ta ($5d^3 6s^2$) in contrast to Pt ($5d^9 6s^1$), where d band is more than half filled [74, 78]. We use Eqs. 2.20, 2.21 and 2.24 to extract the spin Hall resistivity, $\rho_{\mathrm{SH}} \equiv \rho_{\mathrm{xy,SH}}$. For this, we introduce the measured ΔR_{ISHE} value, the geometrical factors measured by SEM, the thicknesses measured by XRR, the resistivities of Cu, Ta and Py measured in the same device using four-point configuration as shown in Fig. 5.1(a) for Ta, and $\lambda_{\mathrm{s}}^{\mathrm{Cu}}$, $\lambda_{\mathrm{s}}^{\mathrm{Py}}$ and α_{Py} determined in Refs. [133, 134]. We also introduce the shunting factor, $x_{\mathrm{Ta,Cu}}$, that was calculated by SPINFLOW 3D software [80] by Dr. Y. Omori, considering w_{Cu}, w_{Ta}, ρ_{Cu} and ρ_{Ta} values of the devices and, importantly, $\lambda_{\mathrm{s}}^{\mathrm{Ta}}$ that was extracted in the previous section.

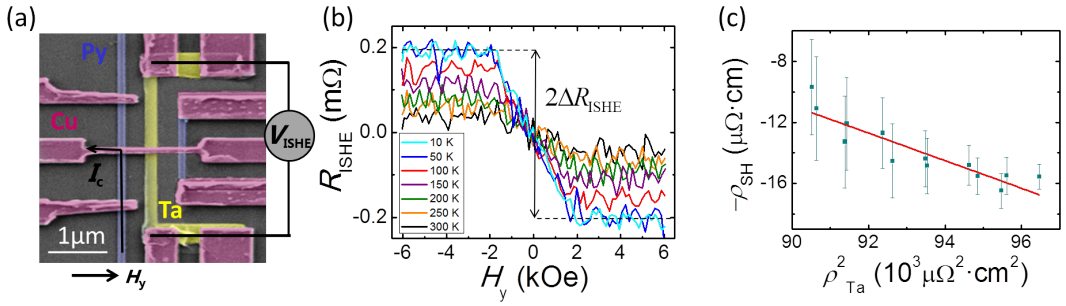

Figure 5.4: **Characterization of the ISHE in Ta as a function of temperature using a LSV with a Ta middle wire.** (a) SEM image of a Py/Cu LSV with a Ta middle wire between the two Py electrodes used to measure ISHE. The nonlocal measurement configuration for ISHE and the direction of the applied magnetic field (H_{y}) is shown. (b) ISHE resistance as a function of magnetic field measured at selected temperatures and $I_{\mathrm{c}} = 575$ μA in device D1 using the configuration shown in (a). The curves have been shifted for clarity. The ISHE signal ($2\Delta R_{\mathrm{ISHE}}$) for 10 K is tagged. (c) Spin Hall resistivity as a function of the square of the longitudinal resistivity of Ta for device D1. Red solid line is the fitting of the data to Eq. 1.16.

In Fig. 5.4(c), we plot $-\rho_{\mathrm{SH}}$ against ρ_{Ta}^2 obtained from device D1 and fit this data to a linear function. Following Eq. 1.16, the slope corresponds to $\sigma_{\mathrm{SH}}^{\mathrm{int}}$ and the intercept to the sum of the skew-scattering and side-jump contributions. We extract:

$$\sigma_{\mathrm{SH}}^{\mathrm{int}} = -910 \pm 130(\hbar/e)\ \Omega^{-1}\mathrm{cm}^{-1}$$

$$\sigma_{\mathrm{SH}}^{\mathrm{sj}}\rho_{\mathrm{Ta},0}^{2} + \alpha_{\mathrm{SH}}^{\mathrm{ss}}\rho_{\mathrm{Ta},0} = 71 \pm 12(e/\hbar)\ \mu\Omega\mathrm{cm},$$

where $\alpha_{\mathrm{SH}}^{\mathrm{ss}}$ is the skew-scattering angle and $\sigma_{\mathrm{SH}}^{\mathrm{sj}}$ is the spin Hall conductivity that corresponds to the side-jump contribution.

The variation of ρ_{Ta} with temperature is very small, around 3% as shown in Fig. 5.1(b), thus, the studied ρ_{Ta} range in device D1 is relatively short. The additional devices (D2−D7) containing Ta wires with different $\rho_{\mathrm{Ta},0}$, see Table 5.1, were fabricated in order to get a more complete study, covering a broader range of resistivities.

Next, we measured the ISHE for each device at 10 K, as shown in Fig. 5.5(a) for three selected devices that are characterized by different $\rho_{\mathrm{Ta},0}$. We observe that $|\Delta R_{\mathrm{ISHE}}|$ increases with $\rho_{\mathrm{Ta},0}$. This result is consistent for all the studied devices, as shown in the inset of Fig. 5.5(a). Using Eqs. 2.20, 2.21 and 2.24, we extract ρ_{SH} for each device (as we did for D1), which is plotted in Fig. 5.5(b) as a function of $\rho_{\mathrm{Ta},0}$. A clear increase of $|\rho_{\mathrm{SH}}|$ with $\rho_{\mathrm{Ta},0}$ is observed.

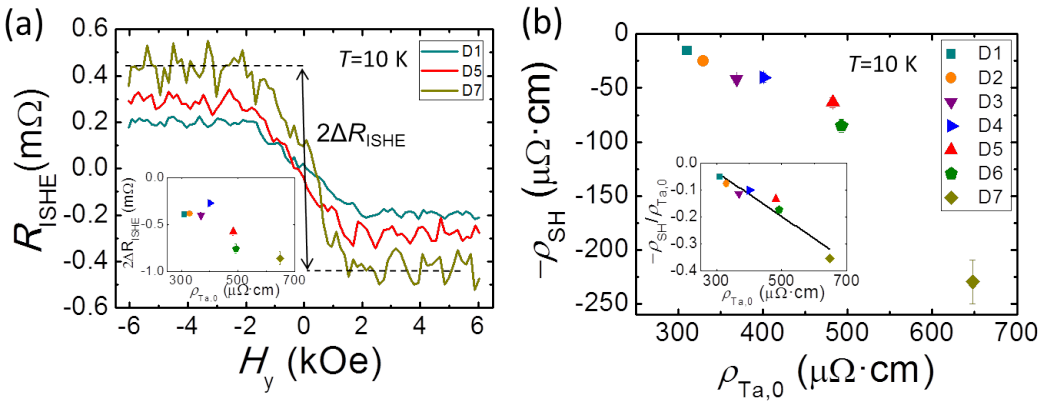

Figure 5.5: **Characterization of the ISHE in Ta at 10 K using LSVs with Ta middle wires with different residual resistivities.** (a) ISHE resistance *vs.* magnetic field at 10 K for selected devices measured using the configuration shown in Fig. 5.4(a). Inset: ISHE signal *vs.* residual resistivity of Ta for all devices at 10 K. The symbols that represent each device are the same as in (b). (b) Spin Hall resistivity *vs.* residual resistivity of Ta for all devices at 10 K. Inset: Ratio of the spin Hall resistivity and residual resistivity of Ta *vs.* residual resistivity of Ta for all devices at 10 K. Black solid line is the fitting of the data to Eq. 5.1 at low temperature.

At low temperatures, Eq. 1.16 can be rewritten as:

$$\frac{-\rho_{\mathrm{SH}}}{\rho_{\mathrm{Ta},0}} = (\sigma_{\mathrm{SH}}^{\mathrm{int}} + \sigma_{\mathrm{SH}}^{\mathrm{sj}})\rho_{\mathrm{Ta},0} + \alpha_{\mathrm{SH}}^{\mathrm{ss}}. \tag{5.1}$$

Using the experimental data at low temperatures of all devices, we can perform a linear fit of $\frac{-\rho_{\mathrm{SH}}}{\rho_{\mathrm{Ta},0}}$ against $\rho_{\mathrm{Ta},0}$, see the inset of Fig. 5.5(b), obtaining $(\sigma_{\mathrm{SH}}^{\mathrm{int}} + \sigma_{\mathrm{SH}}^{\mathrm{sj}})$ from the slope and $\alpha_{\mathrm{SH}}^{\mathrm{ss}}$ from the intercept. We extract from devices D1−D7:

$$\sigma_{\mathrm{SH}}^{\mathrm{int}} + \sigma_{\mathrm{SH}}^{\mathrm{sj}} = -820 \pm 120(\hbar/e)\ \Omega^{-1}\mathrm{cm}^{-1}$$
$$\alpha_{\mathrm{SH}}^{\mathrm{ss}} = 0.21 \pm 0.05.$$

The obtained $\sigma_{\mathrm{SH}}^{\mathrm{int}}$ from the previous fit in device D1 ($-910 \pm 130(\hbar/e)$ $\Omega^{-1}\mathrm{cm}^{-1}$) is compatible with $\sigma_{\mathrm{SH}}^{\mathrm{int}} + \sigma_{\mathrm{SH}}^{\mathrm{sj}} = -820 \pm 120(\hbar/e)\ \Omega^{-1}\mathrm{cm}^{-1}$ result obtained considering all devices. This indicates that $\sigma_{\mathrm{SH}}^{\mathrm{sj}}$ is negligible, which is expected in a pure metal [50, 122, 123]. Therefore, from the previous fit in device D1, we can consider $\alpha_{\mathrm{SH}}^{\mathrm{ss}}\rho_{\mathrm{Ta},0} = 71 \pm 12(e/\hbar)$ $\mu\Omega$cm, which leads to $\alpha_{\mathrm{SH}}^{\mathrm{ss}} = 0.23 \pm 0.04$. This skew-scattering angle is also consistent with the last result $\alpha_{\mathrm{SH}}^{\mathrm{ss}} = 0.21 \pm 0.05$ obtained using all devices at low temperature.

Considering that the upper part of the Ta wire, where the spin absorption from Cu occurs, is composed by β-Ta grains as concluded in the structural characterization, see Figs. 5.2(c) and 5.2(f), and that $\lambda_{\mathrm{s}}^{\mathrm{Ta}}$ is a few nanometers, see Table 5.1, we can safely consider that the SCC occurs in the upper β-Ta grains. Therefore, the obtained $\sigma_{\mathrm{SH}}^{\mathrm{int}} = -820 \pm 120(\hbar/e)\ \Omega^{-1}\mathrm{cm}^{-1}$ is dominated by β-Ta. In Ref. [85], they extract $-378(\hbar/e)\ \Omega^{-1}\mathrm{cm}^{-1}$ for clean β-Ta based on first principles and Berry curvature based spin transport calculations. In order to model disorder they exploit the supercell as well as the virtual crystal approximation but do not present results showing the variation of the Fermi energy for β-Ta. However, in a system such as β-Ta it can be expected that $\sigma_{\mathrm{SH}}^{\mathrm{int}}$ changes dramatically as a function of the Fermi energy as shown in Ref. [135] for β-W. Using Fig. 2 of Ref. [135] and assuming the virtual crystal approximation, going from β-W to β-Ta would reduce the Fermi energy by ≈ 1.3 eV and result in $\sigma_{\mathrm{SH}}^{\mathrm{int}}$ quantitatively close to the value identified in this work. A very recent work by Qiao *et al.* reports $-389(\hbar/e)\ \Omega^{-1}\mathrm{cm}^{-1}$ for β-Ta at Fermi energy and indeed they observe a strong variation of $\sigma_{\mathrm{SH}}^{\mathrm{int}}$ with the variation of the Fermi energy. For instance, they extract $-2055(\hbar/e)\ \Omega^{-1}\mathrm{cm}^{-1}$ at 1.238 eV above the Fermi energy [130]. The obtained $\alpha_{\mathrm{SH}}^{\mathrm{ss}} = 0.21 \pm 0.05$ in this work corresponds to a remarkable extrinsic contribution of $\theta_{\mathrm{SH}}^{\mathrm{Ta}} = 21\%$, independent of $\rho_{\mathrm{Ta},0}$. Nevertheless, due to the opposite signs of the intrinsic and extrinsic contributions and the high ρ_{Ta}, the skew scattering is counterbalanced by the intrinsic contribution, which becomes dominant.

We can compare the obtained $\theta_{\mathrm{SH}}^{\mathrm{Ta}}$ values with those found in literature using alternative techniques to measure the SHE, which are collected in Table 1.1. In general, we observe that we obtain larger $\theta_{\mathrm{SH}}^{\mathrm{Ta}}$ values, which can be ascribed to the higher resistivities achieved in our Ta nanostructures in combination with the predominance of the intrinsic mechanism in Ta.

5.4 Comparing the spin Hall effect in Pt and Ta

We now compare the ISHE results obtained for Ta samples and Pt samples in the previous chapter. Figure 5.6(a) shows the absolute value of θ_{SH} of Pt and Ta as a function of resistivity (ρ_{xx}). In Ta, we are able to increase linearly θ_{SH}^{Ta} up to $-35 \pm 3\%$ by simply increasing ρ_{Ta}. This is a clear indication of the dominance of the intrinsic mechanism in the SHE of Ta. We observe a similar linear tendency in the intrinsic regime of Pt, but with a larger slope as shown in Fig. 5.6(a), due to the larger σ_{SH}^{int} of Pt. However, as $\theta_{SH}^{int} = \sigma_{SH}^{int}\rho_{xx}$ is fulfilled in the intrinsic regime, due to the much larger resistivity of Ta, θ_{SH}^{Ta} can be as large as or even larger than θ_{SH}^{Pt}.

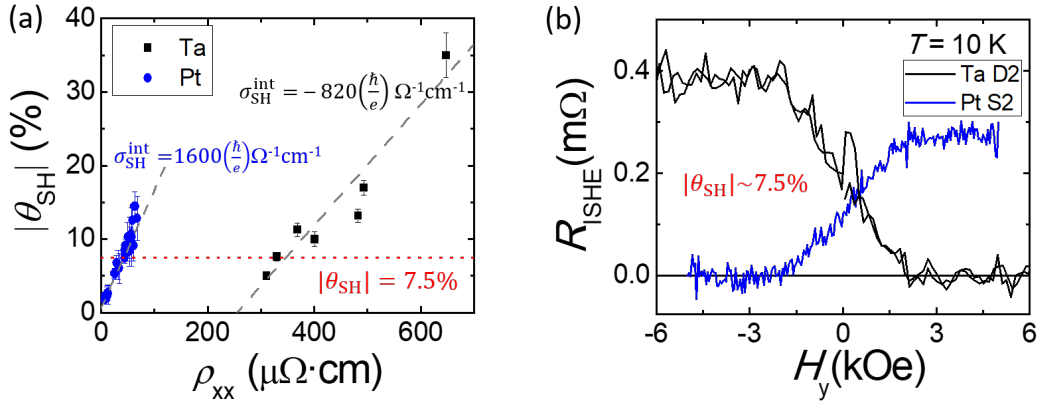

Figure 5.6: **Comparison of the spin Hall angles and output resistances in Pt and Ta**. (a) Longitudinal resistivity dependence of the absolute value of the spin Hall angle of Ta (black solid squares) and Pt (blue solid circles). The grey dashed lines are the curve $\theta_{SH} = \sigma_{SH}^{int}\rho_{xx} + \alpha_{SH}^{ss}$ obtained for Ta (Pt), with $\sigma_{SH}^{int} = -820(\hbar/e)$ $\Omega^{-1}cm^{-1}$ ($1600(\hbar/e)$ $\Omega^{-1}cm^{-1}$) and $\alpha_{SH}^{ss} = 21\%$ (0.6%, average value). Red dotted line is the constant $|\theta_{SH}| = 7.5\%$. (b) ISHE resistance as a function of magnetic field measured in D2 (Ta) device (black solid line) and S2 (Pt) device (blue solid line) at 10 K with the same $|\theta_{SH}| \sim 7.5\%$.

Evidence of the shunting effect

The shunting effect is present in the Cu/heavy metal heterostructure when realizing the ISHE experiment and influences the measured ISHE signal. This is clearly confirmed when comparing the output resistance signals of the ISHE, ΔR_{ISHE}, measured at Pt and Ta when both devices are characterized by the same SCC efficiency. If we consider two devices, one of Pt (S2) and one of Ta (D2), with a similar $|\theta_{SH}|$ of approximately 7.5% (see the red horizontal line in Fig. 5.6(a)), we observe that the corresponding resistivity of Ta (330 μΩcm) is larger than the one of Pt (44 μΩcm). Therefore, when making the ISHE measurement the voltage drop that will be measured in the spin-orbit metal is expected to be larger in Ta,

approximately one order of magnitude, due to the almost one order of magnitude larger Ta resistivity compared to the Pt one. However, if we observe the obtained results for these two devices in Fig. 5.6(b), we conclude that the difference in the output resistance is not so large. This is explained by the shunting effect: due to the small resistivity of the Cu channel, part of the charge current generated in the spin-orbit metal flows back into the Cu, reducing the measured signal. The shunting effect is larger in Ta than in Pt, due to the larger resistivity of Ta, which is in agreement with the shunting factor calculation ($x_{\mathrm{Ta,Cu}} = 0.096$, $x_{\mathrm{Pt,Cu}} = 0.156$). Therefore, in terms of output signals, increasing the resistivity of the heavy metal enhances the θ_{SH} which gives rise to a larger spin signal. However, this enhancement of the output voltage is partially counterbalanced by the shunting effect that is stronger when the resistivity of the spin-orbit metal is larger. This observation is also pointed out in Ref. [136].

5.5 Conclusions

We experimentally determine the intrinsic mechanism as the leading contribution of the SHE in highly resistive Ta. We extract $\sigma_{\mathrm{SH}}^{\mathrm{int}}$ for β-Ta to be $-820 \pm 120(\hbar/e)\ \Omega^{-1}\mathrm{cm}^{-1}$, which is constant in a broad range of resistivities. The predominance of the intrinsic mechanism reveals the path to increase $\theta_{\mathrm{SH}}^{\mathrm{Ta}}$: increasing the resistivity of the metal. With this approach, by measuring with the spin absorption technique, we can systematically vary $\theta_{\mathrm{SH}}^{\mathrm{Ta}}$ from $-5 \pm 0.3\%$ up to $-35 \pm 3\%$, achieving the largest conversion efficiency reported so far for a pure metal. This work unveils the intrinsic potential of Ta as a spin-to-charge-current-convertor, definitely appealing and promising for spin-orbit-based technological applications.

In the last part of the chapter, we compare the SHE results obtained in Ta and Pt. We evidence that in the intrinsic regime $\theta_{\mathrm{SH}}^{\mathrm{int}} = \sigma_{\mathrm{SH}}^{\mathrm{int}}\rho_{\mathrm{xx}}$ is fulfilled, being $\sigma_{\mathrm{SH}}^{\mathrm{int}}$ larger for Pt than for Ta. We also discuss the role of the shunting effect in the output signals that we obtain. The shunting effect is larger in Ta devices than in Pt ones, given the larger resistivity of Ta, and limits the output voltage. The final conclusion is that a larger resistivity of the spin Hall metal results in a larger θ_{SH}, which favors a major output signal, but is counterbalanced by a larger shunting effect that reduces the output signal.

Chapter 6

Enhanced spin-to-charge current conversion signal in a graphene/Pt heterostructure

Conversions between charge currents and spin currents that occur due to the spin Hall effect (SHE) and inverse SHE (ISHE) can be used for writing and reading operations in magnetic memories and spin-logic devices [2,83]. These applications require efficient spin-to-charge current conversions (SCC) and large output voltages. In Chapters 4 and 5, we focused on understanding the mechanisms of the SHE in Pt and Ta, respectively, that allowed us to find a path to enhance the spin Hall angle, θ_{SH}. We found that, by increasing the resistivity, ρ, of these two spin Hall metals (SHM), in the intrinsic regime, we were able to enhance linearly θ_{SH}, which is in turn proportional to the output voltage. However, we addressed the issue of the shunting effect in Section 5.4, which is enhanced when increasing ρ of the heavy metal and results in a reduction on the output voltage. Therefore, we concluded that simply increasing ρ of the SHM is not a straightforward method to increase the SCC output voltage.

In this chapter, we employ an alternative approach to enhance the SCC output voltages originated in the ISHE of Pt. Instead of modifying the properties of the SHM as we did in Chapters 4 and 5, here we replace the Cu spin channel, characterized by a low resistivity with a material with larger resistivity but with a similarly long spin diffusion length, λ_{s}. A promising material fulfilling these two requirements is graphene. By substituting the Cu spin channel in a lateral spin valve (LSV) by a graphene spin channel, we are able to overcome the shunting effect and exploit the long λ_{s} of graphene. We first characterize the spin transport properties of a reference graphene LSV. Then, we analyze the spin absorption by Pt in graphene. Finally, we study the SCC in a graphene/Pt heterostructure. We

experimentally demonstrate that, at room temperature, the SCC output signal in a graphene/Pt heterostructure is almost two orders of magnitude larger than those in metallic heterostructures.

6.1 Characteristics of the sample

We use LSVs that consist of ferromagnetic (FM) Co electrodes with their respective TiO_2 interfacial barriers for spin injection and detection in a graphene spin channel. Spin injection from the FM electrodes into the non-magnetic (NM) materials with high resistivity suffers from the conductivity mismatch problem [137], which avoids an efficient electrical injection of spins into the NM channel. This occurs when the spin resistance, defined in Eq. 2.9, of the NM material is larger than the one of the ferromagnet ($R_s^{NM} \gg R_s^{FM}$), as $\rho_{NM} \gg \rho_{FM}$ and $\lambda_s^{NM} \gg \lambda_s^{FM}$. This issue is solved by adding a resistive enough spin-dependent interface, which maintains the spin dependence of the wave-vector of the FM element, between the FM electrode and the NM channel [138]. If the resistance of the interface, R_I, fulfills $R_I \gg R_s^{NM}$, the injected current will be controlled by the spin-dependent resistance of the interface and an efficient spin injection will take place. In our case, Co electrodes with their respective TiO_2 interfacial barriers are placed on top of a graphene flake that is employed as a spin channel to transport spins. Some of the LSVs contain a Pt middle wire, as shown in Fig.6.1.

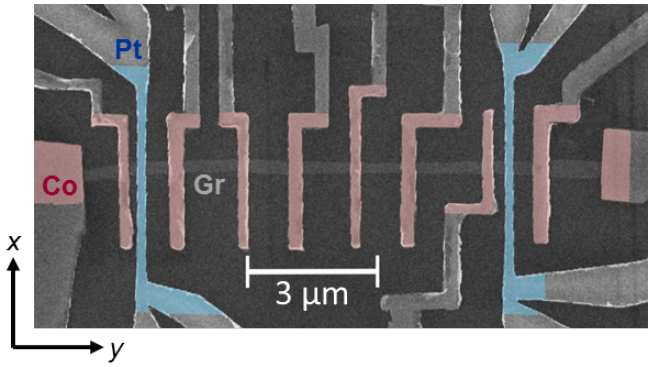

Figure 6.1: **Scanning electron microscopy (SEM) image of the sample.** The sample consists of several Co/TiO_2/graphene LSVs. Two of the LSV devices contain a Pt wire between the two FM electrodes.

The spin channel consists of a 250-nm-wide flake of trilayer graphene (with a sheet resistance of $R_{Gr}^{\blacksquare} = 1085\ \Omega$ and a carrier density $n_c \sim 8 \times 10^{11}$ cm^{-2} at 300 K) obtained via exfoliation [117], as explained in Section 3.1.5. The exfoliation of the graphene flake was done by Dr. W. Yan. The flake with the most convenient shape (long and narrow) was selected, regardless of the number of layers, as the excellent spin transport properties of graphene do not depend strongly on the

number of graphene layers [139]. The nanofabrication of the device, described in Section 3.2.2, follows two steps of e-beam lithography with electrode metal deposition and lift-off. For the 200-nm-wide Pt wires, 21 nm of Pt were sputtered at 0.6 Å/s using 40 W in 3 mTorr of Ar pressure. This deposition condition gives rise to very resistive Pt with $\rho_{\mathrm{Pt}} = 99$ (134) μΩcm at 50 (300) K and, therefore, a Pt with large spin Hall angle, $\theta_{\mathrm{SH}}^{\mathrm{Pt}} = 17.8{\pm}2.0$ (23.4±2.5)%. These $\theta_{\mathrm{SH}}^{\mathrm{Pt}}$ values have been calculated considering the intrinsic spin Hall conductivity and skew-scattering angle obtained in Chapter 4. The 35-nm-thick Co electrodes with different widths, between 150 and 350 nm to attain different switching magnetic fields, are deposited in an ultra-high vacuum chamber using e-beam evaporation on top of 6 Å of Ti after the natural oxidation of Ti in air. The presence of TiO_2 between the Co electrode and the graphene channel leads to Co/graphene interface resistances, R_{ICo}, between 10 and 42 kΩ. All longitudinal resistivity and nonlocal transport measurements were carried out using a "dc reversal" technique, see Section 3.3.1, in a liquid-He cryostat, applying an external magnetic field, $\vec{H}$, and varying temperature, T.

6.2 Spin transport properties of graphene

We first study the spin transport in a standard graphene LSV, as shown in Fig. 6.2(a). A spin-polarized current (I_{c}) is injected from a Co electrode into the graphene channel, creating a spin accumulation at the Co/graphene interface. This spin accumulation diffuses toward both sides of the graphene channel, creating a pure spin current (I_{s}) in the right side, which is detected by another Co electrode as a nonlocal voltage (V). The measured nonlocal resistance, $R_{\mathrm{NL}} = V/I_{\mathrm{c}}$, is high and low depending on the relative orientation of the magnetization of the two FM electrodes, see Fig. 6.2(b), which can be set by applying an in-plane magnetic field in the x direction, H_{x} (defined in Fig. 6.2(a)), due to the shape anisotropy of the electrodes. The difference between the two resistance states is defined as the spin signal, $\Delta R_{\mathrm{NL}}^{\mathrm{ref}}$. We obtain a spin signal of $\Delta R_{\mathrm{NL}}^{\mathrm{ref}} \sim 3\ \Omega$ owing to the large interface resistance given by good quality TiO_2.

In order to characterize the spin transport properties of the graphene-based LSV, we perform a Hanle measurement by applying H perpendicular to the injected spins. In this case, the diffusing spins precess around the magnetic field. The angle of rotation, φ, of the spin at a time τ with respect to its initial orientation is $\varphi = \omega_{\mathrm{L}}(H)\tau$, being $\omega_{\mathrm{L}}(H)$ the Larmor frequency, which is lineal to the magnetic field. When the spin reaches the detector, only the component parallel to the magnetization of the detector will be detected, giving rise to a cos $(\varphi(H))$ dependence in the detected R_{NL} signal, corresponding to the projection of

the spins along the magnetization of the FM detector. Apart from the precession, due to the distribution of the traveling times τ in the diffusive transport, not all the spins precess the same angle φ and there will be decoherence between spins, which will reduce spin accumulation. In particular, at high H the spin accumulation is totally suppressed due to spin decoherence. In addition, spin relaxation by spin-flip processes will occur, which also reduces the spin signal. A Hanle measurement allows us to quantify the spin polarization of the Co/graphene interface, α_{ICo}, and the spin diffusion length of graphene, $\lambda_{\mathrm{s}}^{\mathrm{Gr}}$.

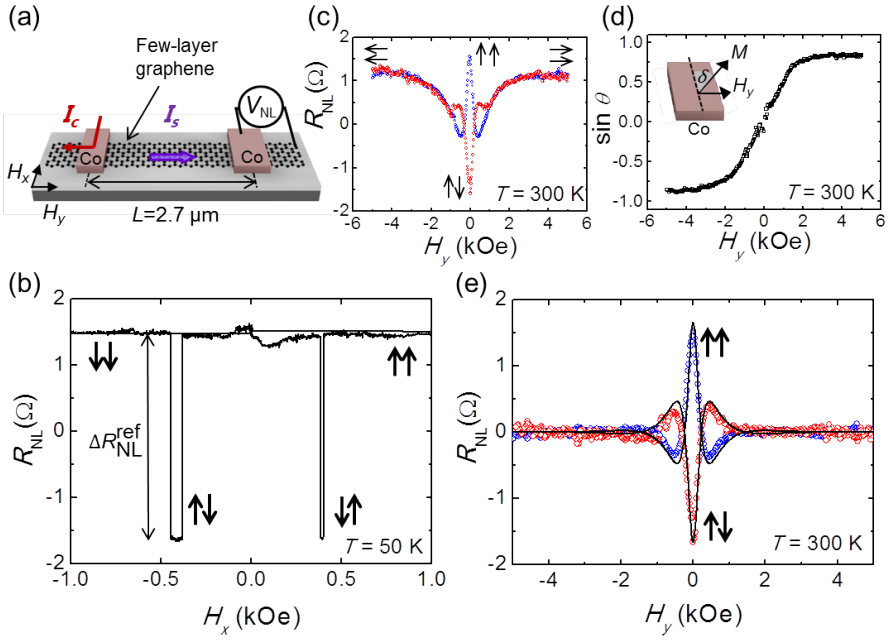

Figure 6.2: **Spin transport in a reference trilayer graphene lateral spin valve.** (a) Sketch of the measurement configuration and the directions of the applied magnetic field (H_{x} and H_{y}). (b) Nonlocal resistance as a function of H_{x} measured with $I_{\mathrm{c}} = 10$ μA at 50 K in the configuration shown in (a) and center-to-center Co electrode spacing $L = 2.7$μm. The spin signal $\Delta R_{\mathrm{NL}}^{\mathrm{ref}}$ has been tagged. (c) Hanle measurement, for which R_{NL} is measured in the same device as a function of H_{y} with $I_{\mathrm{c}} = 10$ μA at 300 K in the configuration shown in (a), while the injecting and detecting Co electrodes are in the parallel (blue circles) and antiparallel (red circles) initial magnetization configurations. (d) sin δ as a function of H_{y} extracted from data in (c). Inset: the magnetization direction of the Co electrode relative to x direction defines the angle δ. (e) Pure spin precession and decoherence data extracted from data in (c), where the contribution from the in-plane magnetization rotation of the electrodes under H_{y} is removed. Spin transport properties are extracted by fitting Hanle equation to the experimental data (black solid line). The black arrows in (b), (c) and (e) indicate the relative magnetization configuration of the Co electrodes.

Such a measurement starts at $H_{\mathrm{y}} = 0$, once the parallel (antiparallel) configuration of the FM electrodes in x direction has been established. Then, H is swept in y until the magnetization of the Co electrodes saturate in this direction. As the injected spins are oriented along the x direction and a perpendicular

in-plane magnetic field, H_y (defined in Fig. 6.2(a)), is applied, the spins precess around this field. The precession and decoherence of the spins cause the oscillation and decay of the signal, see Fig. 6.2(c). In addition, the effect of the rotation of the Co magnetizations with H_y tends to align the polarization of the injected spin current with the applied field, restoring the R_{NL} signal to its zero-field value when the Co electrodes reach parallel magnetizations along the y direction at high enough H_y. By the proper combination of the measured R_{NL} curves with an initial parallel (blue circles in Fig. 6.2(c)) and antiparallel (red circles in Fig. 6.2(c)) magnetization configuration of the electrodes in the x direction (see Supplementary Material in Section 6.6), we can obtain the rotation angle δ of the Co magnetization (Fig. 6.2(d)) and the pure spin precession and decoherence (Fig. 6.2(e)). The data in Fig. 6.2(e) can be fitted using the Hanle equation (see Supplementary Material in Section 6.6). The fitting allows us to extract:

$$\alpha_{ICo} = 0.068 \pm 0.001$$
$$\lambda_s^{Gr} = 1.20 \pm 0.02 \ \mu m.$$

Most importantly, the reference spin signals are independent of temperature (compare the amplitude of the signals in Fig. 6.2(b) at 50 K and Fig. 6.2(e) at 300 K), in agreement with the fact that λ_s^{Gr} and α_{ICo} are basically insensitive to temperature [139–142]. In contrast, λ_s of metallic channels such as Cu and Ag are significantly reduced with increasing temperature [28, 143].

6.3 Spin absorption by Pt in a graphene LSV

Once we have extracted the spin transport properties of graphene from a reference LSV, we now explore in the very same sample the spin absorption by Pt, following the procedure described in Section 2.1.2.

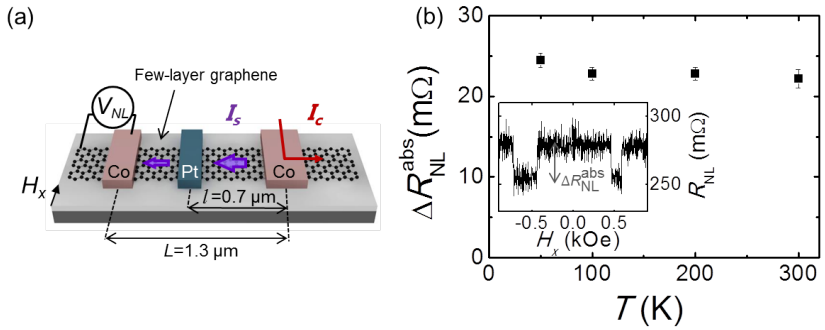

Figure 6.3: **Spin absorption by Pt in trilayer graphene lateral spin valve.** (a) Sketch of the measurement configuration and the direction of the applied magnetic field (H_x). (b) Spin signal after Pt absorption as a function of the temperature. Inset: nonlocal resistance as a function of H_x measured with $I_c = 10$ μA in the configuration shown in (a) and center-to-center Co electrode spacing $L = 1.3$ μm. The spin absorption signal ΔR_{NL}^{abs} is tagged, which corresponds to 50 K.

For this experiment, we use the nonlocal configuration shown in Fig. 6.3(a). The pure spin current that has been injected in graphene from one Co electrode is partially absorbed by the Pt wire present in the middle of the spin current path before reaching the detector. The spin signal we measure after absorption by Pt is $\Delta R_{\mathrm{NL}}^{\mathrm{abs}} \sim 25$ mΩ, more than two orders of magnitude smaller than expected without the presence of the middle Pt wire (compare inset of Fig. 6.3(b) with Fig. 6.2(b)). This result indicates that the Pt wire acts as an extremely efficient spin absorber. We observe that $\Delta R_{\mathrm{NL}}^{\mathrm{abs}}$ has weak temperature dependence as it occurs in the reference LSV, implying that the Pt wire absorbs similar amount of spins across the temperature range investigated, see Fig. 6.3(b).

6.4 Spin-to-charge current conversion in a graphene/Pt heterostructure

6.4.1 ISHE in a graphene/Pt heterostructure

After confirming that the Pt wire absorbs the spin current from graphene, and considering that Pt has a large $\theta_{\mathrm{SH}}^{\mathrm{Pt}}$, we measure the ISHE in the graphene/Pt heterostructure using the spin absorption technique, described in Section 2.1.3.

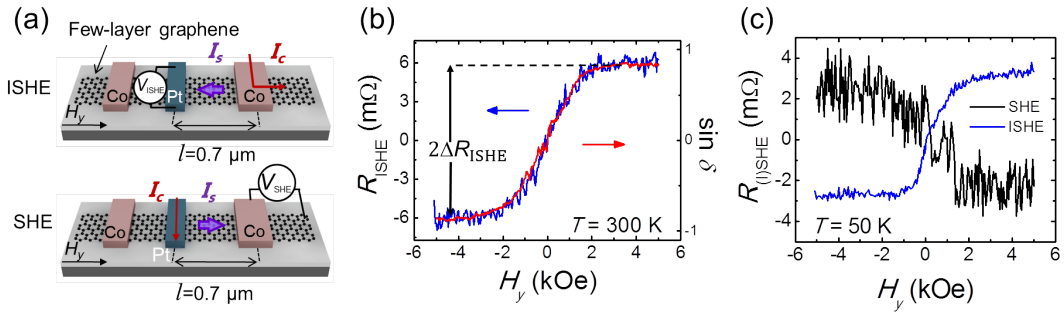

Figure 6.4: **SCC in a trilayer graphene/Pt heterostructure.** (a) Sketch of the ISHE (top) and the SHE (bottom) measurement configurations and the direction of the applied magnetic field (H_{y}). (b) ISHE resistance (blue solid line) as a function of H_{y} measured with $I_{\mathrm{c}} = 10$ μA at 300 K in the configuration shown in (a) top. The ISHE signal ($2\Delta R_{\mathrm{ISHE}}$) is tagged. A baseline signal of 6.5 mΩ, corresponding to the Ohmic contribution given by the van der Pauw currents spreading to the voltage detector, has been subtracted. For comparison, sin δ (red solid line) as a function of H_{y} extracted from the Hanle measurement is also shown. (c) The ISHE (blue solid line) and the SHE (black solid line) resistance as a function of H_{y} measured with $I_{\mathrm{c}} = 10$ μA at 50 K in the configuration sketched in (a) (top and bottom, respectively) with center-to-center Co-Pt electrode spacing of $l = 0.7$ μm, showing the reciprocity of the two effects. A baseline signal of 4 mΩ (7 mΩ), corresponding to the Ohmic contribution, has been subtracted from the ISHE (SHE) curve.

Employing the measurement configuration shown in Fig. 6.4(a) (top sketch), we measure the ISHE resistance at 300 K shown in Fig. 6.4(b) (blue line). According to the symmetry of the ISHE, the signal detected in the Pt wire should be proportional to sin δ [98], a value which has been extracted from the Hanle data (Fig. 6.2(d)). Indeed, we observe a perfect match when overlapping R_{ISHE} with sin δ as a function of H_{y} (Fig. 6.4(b)). This excellent match unambiguously confirms that the measured signal arises from SCC and demonstrates we can indeed electrically detect this spin current by using the ISHE of the Pt wire.

In order to rule out any spurious magnetoresistance effect in graphene as the origin of the observed ISHE signal, we fabricated a control device where we substitute the Pt wire by a Cu wire, a NM metal with weak spin-orbit coupling (SOC) and, therefore, no SCC signal is expected [80, 81].

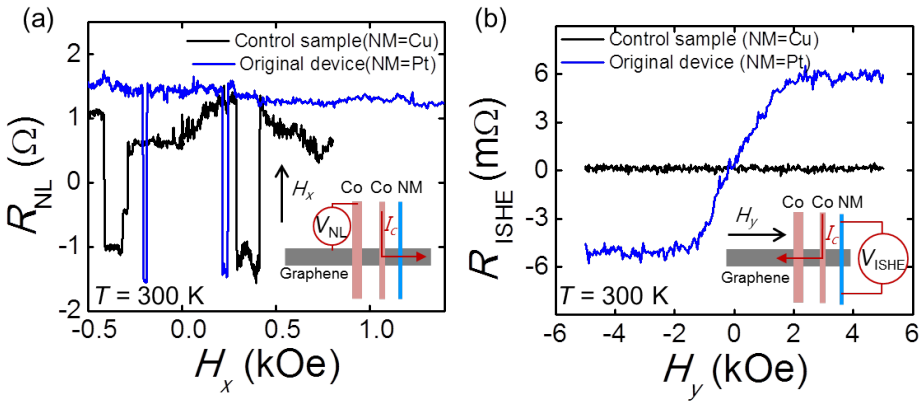

Figure 6.5: **Control experiment: comparison between the original device with Pt and a control device using graphene LSV and Cu wire.** (a) Nonlocal resistance as a function of the magnetic field using a reference spin valve next to the NM metal wire. Similar spin signal is obtained in both, the control device (NM=Cu, black solid line) and the original device (NM=Pt, blue solid line), at 300 K and applying $I_{\mathrm{c}} = 10$ μA in both systems, indicating that Co electrode next to Cu wire in the control device is as good spin injector as the one in the original device. Inset: Sketch of the measurement configuration including the direction of the applied magnetic field. (b) ISHE resistance as a function of the magnetic field measured in both, the control device (black solid line) and the original device (blue solid line), with $I_{\mathrm{c}} = 10$ μA and T =300 K in both measurements. Inset: Sketch of the measurement configuration including the direction of the applied magnetic field.

As the dimensions of the control device are very similar to the original graphene/Pt device, any spurious effect other than the ISHE signal, such as magnetoresistive effects arising from the stray fields created by the Co injector, should also be present in the control measurement.

First of all, we check that the Co electrode is of similar quality as in the original graphene/Pt sample by measuring a reference spin valve in a nonlocal

configuration at 300 K, see Fig. 6.5(a). The nice and clear nonlocal spin signal indicates that the Co electrode next to the Cu wire is an efficient spin injector.

Next, we measure the voltage drop across the Cu wire while using the Co electrode for spin injection at 300 K in the ISHE measurement configuration, see the inset in see Fig. 6.5(b). This measurement produces a flat nonlocal background much smaller than that of the ISHE signal measured in the original graphene/Pt device at the same T, indicating there is no spurious contribution to the ISHE signal (compare black and blue solid curves in Fig. 6.5(b)).

6.4.2 SHE in a graphene/Pt heterostructure

The ISHE experiment shows that the Pt electrode can electrically detect spins traveling in the graphene channel. Next, we demonstrate that a pure spin current can also be generated using the SHE of Pt and injected into graphene. Here, we pass a charge current I_c through the Pt wire as shown in Fig. 6.4(a) (bottom sketch). The transverse spin current generated in Pt (in out-of-plane direction) by the SHE has a spin polarization oriented along the y axis, and the spin accumulation in the graphene/Pt interface leads to spin injection into graphene. By employing now the Co electrode as a detector, we are able to measure the pure spin current reaching the Co electrode as a voltage, V, obtaining the corresponding SHE resistance, R_{SHE}, after normalizing V to I_c (black solid curve in Fig. 6.4(c)). We observe that $R_{\mathrm{SHE}}(H_y) = R_{\mathrm{ISHE}}(-H_y)$ by swapping the voltage and current probes with the same polarity, confirming the reciprocity between the ISHE and SHE in our experiment via the Onsager relation [41, 111]. This SHE measurement demonstrates that it is possible to generate pure spin currents in graphene using a NM SHM.

6.4.3 Superior performance of a graphene/Pt heterostructure

We have performed the ISHE experiment at different temperatures, as shown in Fig. 6.6(a). Interestingly, as the temperature is increased from 10 to 300 K, ΔR_{ISHE} increases from $\sim$ 5 mΩ to $\sim$ 11 mΩ, indicating that the SCC signal improves at higher temperatures. This increase of ΔR_{ISHE} with temperature is robust and reproducible among different samples, which are not shown for the sake of brevity. Our devices based on the few-layer graphene/Pt heterostructure show superior performance over devices using a metallic spin channel, such the ones employed in Chapters 4 and 5 or the ones reported in literature [74, 80, 81, 90, 136, 144], as summarized in Fig. 6.6(b). Two key aspects can be highlighted in this last plot. In the first place, $2\Delta R_{\mathrm{ISHE}}$ obtained in our devices is almost two

orders of magnitude larger at 300 K than in the ones containing metallic spin channels. In the second place, the output signal in a graphene/Pt heterostructure increases significantly with increasing temperature in contrast to the decreasing tendency found when using a metallic channel, see the inset of Fig. 6.6(b).

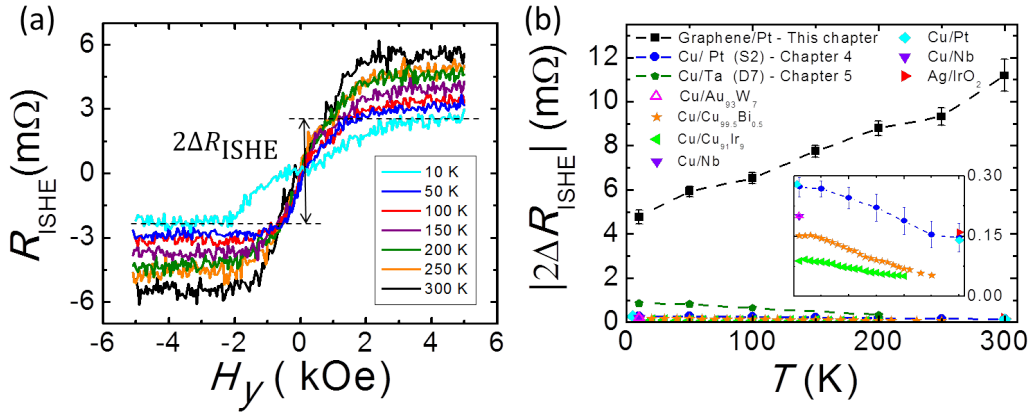

Figure 6.6: **Temperature dependence of the SCC signal in a trilayer graphene/Pt heterostructure.** (a) ISHE resistance as a function of H_y measured at different temperatures from 10 K to 300 K in the configuration shown in Fig.6.4(a) top. The ISHE signal ($2\Delta R_{ISHE}$) for 10 K is tagged. (b) Experimental values of the ISHE signal at different temperatures measured in the graphene/Pt heterostructure (black solid squares). Literature values of $2\Delta R_{ISHE}$ of various SHMs employing different metallic spin channels in LSVs are also included for comparison: Cu/Pt (Chapter 4, [90]), Cu/Ta (Chapter 5), $Cu/Au_{93}W_7$ [144], Ag/IrO_2 [136], $Cu/Cu_{99.5}Bi_{0.5}$ [80], Cu/Nb [74] and $Cu/Cu_{91}Ir_9$ [81]. Dashed solid lines are a guide for the eye. Inset: Zoom of the main plot showing the data of the devices with metallic spin channels. The scale of the horizontal axis is the same as in the main panel. Dashed solid lines are a guide for the eye.

6.4.4 Quantification of the spin transport and spin Hall parameters

Our experimental observations can be well explained by the standard one-dimensional spin diffusion model. The spin signal after absorption is given by the Eq. 2.14, but in our case we can use the simplified Eq. 2.16, considering i) dominance of the Co/graphene interface resistances, R_{ICo1} and R_{ICo2}, in the spin injection and detection ($R_{ICo1,2} \gg R_s^{Co1,2}$, being $R_s^{Co1,2}$ the spin resistance of Co injector,detector), ii) same interface spin polarization for the injector and detector ($\alpha_{ICo1} = \alpha_{ICo2} \equiv \alpha_{ICo}$), iii) smaller Pt/graphene interface resistance, R_{IPt}, and spin resistance of Pt, R_s^{Pt}, than the spin resistance of graphene, R_s^{Gr}, and iv) $L = 2l$. $R_s^{Gr} = \frac{R_{Gr}^{\blacksquare}\lambda_s^{Gr}}{w_{Gr}}$ and R_s^{Pt} is given by Eq. 2.15. The geometrical factors w_{Gr}, w_{Pt}, t_{Pt} and λ_s^{Pt} (which appear in Eq. 2.15) are the width of the graphene, width of Pt, thickness of Pt and spin diffusion length of Pt, respectively.

SCC signal ΔR_{ISHE} of the ISHE experiment can be isolated from Eq. 2.20 and written as a function of Pt and graphene parameters as:

$$\Delta R_{\mathrm{ISHE}} = -\frac{\theta_{\mathrm{SH}}^{\mathrm{Pt}} \rho_{\mathrm{Pt}} x_{\mathrm{Pt,Gr}}}{w_{\mathrm{Pt}}} \left(\frac{\bar{I}_{\mathrm{s}}}{I_{\mathrm{c}}} \right), \tag{6.1}$$

where $x_{\mathrm{Pt,Gr}}$ is the shunting factor between Pt and graphene. $(\bar{I}_{\mathrm{s}}/I_{\mathrm{c}})$ is given by Eqs. 2.21 and 2.23, as in this case also the TiO_2 interface resistance dominates the spin injection and $L = 2l$ can be considered.

For the calculation, we introduce into Eqs. 2.16, 6.1, 2.21 and 2.23 the experimental values of $\Delta R_{\mathrm{NL}}^{\mathrm{abs}}$ and ΔR_{ISHE}, the obtained α_{ICo} and $\lambda_{\mathrm{s}}^{\mathrm{Gr}}$ from the graphene reference LSV measurement, widths and lengths measured from SEM images, thicknesses via X-ray reflectivity (XRR), the value of ρ_{Pt}, which was measured experimentally, and $\theta_{\mathrm{SH}}^{\mathrm{Pt}}$, calculated by using the relation between $\theta_{\mathrm{SH}}^{\mathrm{Pt}}$ and ρ_{Pt} obtained in Chapter 4. We assume negligible current shunting into the graphene due to the much larger sheet resistance of graphene when compared to Pt at the junction area, $R_{\mathrm{Gr}}^{\blacksquare} = 1085\ \Omega$ *vs.* $\rho_{\mathrm{Pt}}/t_{\mathrm{Pt}} = 64\ \Omega$ at 300 K, which leads to $x_{\mathrm{Pt,Gr}} \sim 1$. We extract two very sensitive parameters at 300 K:

$$\lambda_{\mathrm{s}}^{\mathrm{Pt}} = 2.1 \pm 0.4 \text{ nm}$$
$$\mathrm{R}_{\mathrm{IPt}} = 8.4 \pm 0.4\ \Omega.$$

The obtained $\lambda_{\mathrm{s}}^{\mathrm{Pt}}$ is expected when considering the resistivity or conductivity of our Pt wire (see Fig. 4.2(d)). The small value of R_{IPt} facilitates strong spin absorption by Pt from graphene and is compatible with our direct measurement of the interface resistance. We measured directly R_{IPt} in the graphene/Pt cross-shaped junction using the configuration shown in Fig. 3.6(c). The measured values are negative, ranging from -8.5 Ω (10 K) to -13 Ω (300 K). This is an artifact which occurs when the resistance of the channel is of the order or higher than the interface resistance due to an inhomogeneous current distribution in this geometry, which is expected due to the large sheet resistance of graphene ($R_{\mathrm{Gr}}^{\blacksquare} = 1085\ \Omega \gg R_{\mathrm{I,Pt}} = 8.4\ \Omega$ at 300 K) [145, 146]. Using the same procedure, we extract $\lambda_{\mathrm{s}}^{\mathrm{Pt}} = 2.1 \pm 0.3$ nm and $R_{\mathrm{IPt}} = 10.6 \pm 0.4\ \Omega$ at 50 K. The good consistency of extracted values confirms that our assumption of $x_{\mathrm{Pt,Gr}} \sim 1$ is robust.

Having quantified accurately all the parameters in our system, we can confirm the origin of the observed large SCC and its strong temperature dependence. It mainly arises from four factors that appear in Eq. 6.1:

1. Superior spin transport properties of graphene ($\lambda_{\mathrm{s}}^{\mathrm{Gr}} \sim 1.2$ μm) and its temperature insensitivity. Graphene's exceptional ability to transport spins remains intact at room temperature, *i.e.*, the same amount of spin current

arrives to the Pt absorber at different temperatures. This is also due to the constant α_{ICo} at different temperatures. Both parameters are considered in $(\bar{I}_{\mathrm{s}}/I_{\mathrm{c}})$.

2. The efficiency of the conversion of Pt ($\theta_{\mathrm{SH}}^{\mathrm{Pt}}$) increases linearly with temperature from 17.8 ± 2.0 % at 50 K to 23.4 ± 2.5 % at 300 K. Although the amount of spin current to be converted remains the same, due to the first factor, larger efficiency gives rise to larger output signal.

3. ρ_{Pt} increases from 99 μΩcm at 50 K to 134 μΩcm at 300 K.

4. The negligible shunting of the charge current in Pt by graphene ($x_{\mathrm{Pt,Gr}} \sim 1$).

The enhancement of ΔR_{ISHE} with increasing temperature mainly benefits from the first three factors, which are constant $\lambda_{\mathrm{s}}^{\mathrm{Gr}}$ and α_{ICo}, and increasing $\theta_{\mathrm{SH}}^{\mathrm{Pt}}\rho_{\mathrm{Pt}}$ product as described in Eq. 6.1. In contrast, in metallic spin channels, $\lambda_{\mathrm{s}}^{\mathrm{NM}}$ decreases significantly with increasing temperature [28, 143] and so does the current spin polarization of the FM metal, α_{FM}, used as injector and detector, leading to reduced output voltage with the temperature. Our devices give much larger ΔR_{ISHE} than those using metallic spin channels mainly due to the first (long $\lambda_{\mathrm{s}}^{\mathrm{Gr}}$) and fourth (negligible shunting) factors. In traditional metallic LSV devices, the resistivity of the metallic channel is close or smaller than that of the SHM, thus $x_{\mathrm{SHM,NM}}$ are much lower, (0.010–0.285), see Table 4.1 or Table 5.1, a serious issue preventing large SCC pointed out in Ref. [136]. However, in our device with few-layer graphene/Pt heterostructure, $x_{\mathrm{Pt,\,Gr}} \sim 1$ is close to ideal and the use of more resistive graphene (single or bilayer) is not necessary, as $x_{\mathrm{Pt,Gr}}$ cannot be further increased. Further improvement to the SCC could be easily achieved by using high quality graphene devices, where almost two orders of magnitude enhancement of $\lambda_{\mathrm{s}}^{\mathrm{Gr}}$ is obtained [147, 148], or reducing the spin current dilution into the Pt wire by decreasing its thickness (as can be deduced from the prefactor in Eq. 2.21).

After the results of this chapter were published, Savero-Torres *et al.* reported a 100% of spin absorption in monolayer graphene/Pt heterostructure and observed also a two-order of magnitude enhancement of the spin Hall signal in comparison to the metallic counterparts, in agreement with our results [149].

On the application side, the combination of spin injection from one FM element where the non-volatile information is stored and subsequent SCC in a NM element is important for cascading in potential applications such as the spin-orbit logic proposed by Intel [24]. Additionally, substituting a FM element by a NM electrode overcomes the necessity of controlling the relative magnetic orientation of a second FM electrode when used as a detector. For instance, another potential application of our results would be in the spin-based magnetologic device proposed

by Dery *et al.*, where a graphene spin channel is connected with 5 FM electrodes for input, operation and reading out [3, 150]. If some of the FM electrodes in the magnetologic device can be substituted by a SHM, this would lead to the control of spin currents by charge current instead of the magnetization of the FM element, as well as to cascading output voltages from one logic element to the next.

6.4.5 Simultaneous spin injection and detection in graphene using Pt

The generation and detection of spin currents in graphene using simultaneously SHE and ISHE in Pt gives us the chance to achieve fully electrically controlled spintronic devices without the need of magnetic materials. We prepared several samples with adjacent Pt electrodes, as shown in Fig. 6.7(a) to study this possibility. Unfortunately, a very small signal ($\sim$ 0.01 mΩ) is expected, due to the conductivity mismatch of the two graphene/Pt contacts (instead of one contact only in the cases of spin detection with ISHE or spin injection with SHE, respectively). In order to observe a spin signal from the Ohmic baseline in the nonlocal measurement, a magnetic field of 7 kOe is rotated in plane. In the x direction, the dephasing of the Hanle precession would cancel the spin signal, while in the y direction (the same as the spin polarization), no Hanle effect would occur. A $\cos^2\psi$ (ψ is defined in Fig. 6.7(a)) dependence would be expected, with an amplitude corresponding to the spin signal. The noise of the measurement (0.1-0.2 mΩ) is larger than the expected signal and, therefore, cannot be observed, see Fig. 6.7(b).

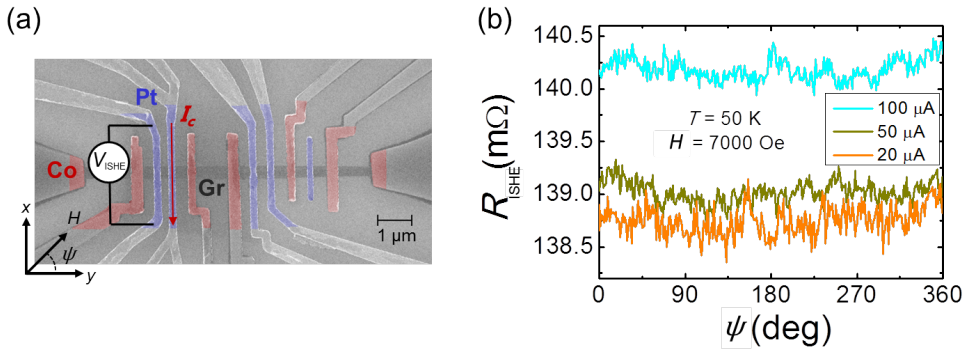

Figure 6.7: **Simultaneous spin injection and detection in a graphene channel using Pt wires.** (a) SEM image of a graphene/Pt lateral heterostructure with adjacent Pt electrodes in a trilayer graphene channel. Co electrodes with TiO_2 barrier placed adjacent to each Pt are used to confirm proper spin injection via SHE or detection via ISHE of the Pt wires. The measurement configuration shown allows full spin injection and detection using the Pt wires. (b) Nonlocal resistance as a function of the angle of the applied magnetic field, measured using the configuration shown in (a) at T=50 K and 7 kOe with different applied currents I_c.

These results show that a full spin injection and detection with Pt is not feasible at this stage due to the low efficiency for spin injection. The configuration of the SCC consists of a transparent interface through which spins can be absorbed or injected. Here the transport is diffusive and the impedance mismatch plays a role. But the transparent interface is necessary to allow for absorption of the pure spin current in the spin Hall material, which is then converted to a charge current that can be potentially utilized. Nevertheless, in our proof-of-principle device, we showed not only that there is spin injection to graphene using Pt, but also that the overall SCC of the whole device is more efficient than in conventional LSVs with metallic spin channels.

6.5 Conclusions

We electrically injected and detected pure spin currents in few-layer graphene by employing the SHE and ISHE of Pt, respectively. The extraordinary ability of graphene to transport spins, together with its relatively high resistance compared to Pt, results in the largest SCC signal reported so far. Most importantly, the largest conversion, which is two orders of magnitude larger than in devices employing metallic spin channels, occurs at room temperature. The fuse and perfect match of these two elements in a heterostructural device of graphene/Pt provides new plausible opportunities for future spin-orbit-based devices.

6.6 Supplementary Material

Spin transport properties of graphene

The spin transport properties of graphene are obtained from the fitting of the Hanle measurement. The decoherence of the spin during precession causes the decay of an oscillating signal, which can be fitted using the following equation [151]:

$$R_{\mathrm{NL}} = -2R_{\mathrm{s}}^{\mathrm{Gr}}\hat{P}_1\hat{P}_2\frac{C_{12}}{\det(\hat{X})}, \tag{6.2}$$

where $\hat{P}_k$ is defined in Eq. 2.8. C_{12} and $\hat{X}$ are defined as:

$$C_{12} = -\det\begin{pmatrix} \mathrm{Re}[\bar{\lambda}_{\mathrm{s},\omega}e^{-L/\tilde{\lambda}_{\mathrm{s},\omega}}] & -\mathrm{Im}[\bar{\lambda}_{\mathrm{s},\omega}e^{-L/\tilde{\lambda}_{\mathrm{s},\omega}}] & -\mathrm{Im}[\bar{\lambda}_{\mathrm{s},\omega}] \\ \mathrm{Im}[\bar{\lambda}_{\mathrm{s},\omega}] & r_{1\perp} + \mathrm{Re}[\bar{\lambda}_{\mathrm{s},\omega}] & \mathrm{Re}[\bar{\lambda}_{\mathrm{s},\omega}e^{-L/\tilde{\lambda}_{\mathrm{s},\omega}}] \\ \mathrm{Im}[\bar{\lambda}_{\mathrm{s},\omega}e^{-L/\tilde{\lambda}_{\mathrm{s},\omega}}] & \mathrm{Re}[\bar{\lambda}_{\mathrm{s},\omega}e^{-L/\tilde{\lambda}_{\mathrm{s},\omega}}] & r_{2\perp} + \mathrm{Re}[\bar{\lambda}_{\mathrm{s},\omega}] \end{pmatrix} \tag{6.3}$$

$$\hat{X} = \begin{pmatrix} r_{1\parallel} + \mathrm{Re}[\bar{\lambda}_{\mathrm{s},\omega}] & \mathrm{Re}[\bar{\lambda}_{\mathrm{s},\omega} e^{-L/\tilde{\lambda}_{\mathrm{s},\omega}}] & -\mathrm{Im}[\bar{\lambda}_{\mathrm{s},\omega}] & -\mathrm{Im}[\bar{\lambda}_{\mathrm{s},\omega} e^{-L/\tilde{\lambda}_{\mathrm{s},\omega}}] \\ \mathrm{Re}[\bar{\lambda}_{\mathrm{s},\omega} e^{-L/\tilde{\lambda}_{\mathrm{s},\omega}}] & r_{2\parallel} + \mathrm{Re}[\bar{\lambda}_{\mathrm{s},\omega}] & -\mathrm{Im}[\bar{\lambda}_{\mathrm{s},\omega} e^{-L/\tilde{\lambda}_{\mathrm{s},\omega}}] & -\mathrm{Im}[\bar{\lambda}_{\mathrm{s},\omega}] \\ \mathrm{Im}[\bar{\lambda}_{\mathrm{s},\omega}] & \mathrm{Im}[\bar{\lambda}_{\mathrm{s},\omega} e^{-L/\tilde{\lambda}_{\mathrm{s},\omega}}] & r_{1\perp} + \mathrm{Re}[\bar{\lambda}_{\mathrm{s},\omega}] & \mathrm{Re}[\bar{\lambda}_{\mathrm{s},\omega} e^{-L/\tilde{\lambda}_{\mathrm{s},\omega}}] \\ \mathrm{Im}[\bar{\lambda}_{\mathrm{s},\omega} e^{-L/\tilde{\lambda}_{\mathrm{s},\omega}}] & \mathrm{Im}[\bar{\lambda}_{\mathrm{s},\omega}] & \mathrm{Re}[\bar{\lambda}_{\mathrm{s},\omega} e^{-L/\tilde{\lambda}_{\mathrm{s},\omega}}] & r_{2\perp} + \mathrm{Re}[\bar{\lambda}_{\mathrm{s},\omega}] \end{pmatrix} \tag{6.4}$$

where $\bar{\lambda}_{\mathrm{s},\omega} = \tilde{\lambda}_{\mathrm{s},\omega}/\lambda_{\mathrm{s}}^{\mathrm{NM}}$ with $\tilde{\lambda}_{\mathrm{s},\omega} = \lambda_{\mathrm{s}}^{\mathrm{NM}}/\sqrt{1 + i\omega_{\mathrm{L}}\tau_{\mathrm{s}}}$, where τ_{s} is the spin relaxation time defined in Section 1.1.2. $r_{k\parallel} = r_k - 1$ and $r_{k\perp} = 1/(R_{\mathrm{s}}^{\mathrm{NM}} G_{Ik}^{\uparrow\downarrow})$, being $G_{Ik}^{\uparrow\downarrow}$ the spin mixing conductance. k=1,2 refers to the injection,detection electrode.

The Hanle measurement of the reference graphene LSV (Fig. 6.2(c)) also contains the effect of the rotation of the Co magnetizations with the external magnetic field (H_{y}), which tends to align the spin polarization with H_{y}, restoring the R_{NL} signal to its zero-field value $R_{\mathrm{NL}}(0)$ for parallel Co magnetizations. When this effect is taken into account, R_{NL} can be expressed as [30]:

$$R_{\mathrm{NL}}^{\mathrm{P(AP)}}(H_{\mathrm{y}}, \delta) = \pm R_{\mathrm{NL}}^{\mathrm{P}}(H_{\mathrm{y}})\cos^2\delta + |R_{\mathrm{NL}}(0)|\sin^2\delta, \tag{6.5}$$

where $R_{\mathrm{NL}}^{\mathrm{P(AP)}}$ is the nonlocal resistance measured as a function of H_{y} when the two Co electrodes are parallel(antiparallel) and δ is the angle of the Co magnetization with respect to the easy axis of the electrode (x axis). Note that the sign " + " corresponds to the parallel curve, " − " to the antiparallel curve and that $R_{\mathrm{NL}}^{\mathrm{P}}(H_{\mathrm{y}}) = -R_{\mathrm{NL}}^{\mathrm{AP}}(H_{\mathrm{y}})$ for the pure spin precession and decoherence. By the proper combination of the measured parallel and antiparallel curves, we can obtain the rotation of the Co magnetization (Fig. 6.2(d)):

$$\sin^2\delta = \frac{R_{\mathrm{NL}}^{\mathrm{P}}(H_{\mathrm{y}}, \delta) + R_{\mathrm{NL}}^{\mathrm{AP}}(H_{\mathrm{y}}, \delta)}{2|R_{\mathrm{NL}}(0)|}, \tag{6.6}$$

and the pure spin precession and decoherence (Fig. 6.2(e)):

$$R_{\mathrm{NL}}^{\mathrm{P}}(H_{\mathrm{y}}) = |R_{\mathrm{NL}}(0)| \frac{R_{\mathrm{NL}}^{\mathrm{P}}(H_{\mathrm{y}}, \delta) - R_{\mathrm{NL}}^{\mathrm{AP}}(H_{\mathrm{y}}, \delta)}{2|R_{\mathrm{NL}}(0)| - R_{\mathrm{NL}}^{\mathrm{P}}(H_{\mathrm{y}}, \delta) - R_{\mathrm{NL}}^{\mathrm{AP}}(H_{\mathrm{y}}, \delta)}. \tag{6.7}$$

For the fitting of the pure spin precession and decoherence curve of the reference graphene LSV in Fig. 6.2(e), we assume the injecting and detecting electrodes have the same current spin polarization ($\alpha_{\mathrm{Co1}} = \alpha_{\mathrm{Co2}} \equiv \alpha_{\mathrm{Co}}$ and $\alpha_{\mathrm{ICo1}} = \alpha_{\mathrm{ICo2}} \equiv \alpha_{\mathrm{ICo}}$) and following Ref. [151], we assume an isotropic spin absorption, hence $G_{\mathrm{I}k}^{\uparrow,\downarrow} = 1/(2R_{\mathrm{I}k} + 2R_{\mathrm{s}}^{k})$. We fix the following experimental parameters: $\alpha_{\mathrm{Co}} = 0.12$ [119], R_{ICo1}=42 kΩ, R_{ICo2}=10 kΩ, L = 2.7 μm, w_{Gr} = 250 nm, w_{Co1} = 344 nm, w_{Co2} = 315 nm, $R_{\mathrm{Gr}}^{\blacksquare} = 1085\ \Omega$, ρ_{Co} = 19 μΩcm [119], λ_{Co} = 40 nm [152,153] and obtain $\alpha_{\mathrm{ICo}} = 0.068 \pm 0.001$, $D = 0.005\ \mathrm{m^2 s^{-1}}$, $\lambda_{\mathrm{s}}^{\mathrm{Gr}} = 1.20 \pm 0.02$ μm. Because the spin signal is constant across the temperature range from 10 K to 300 K, for the calculations in Section 6.4.4 we assume α_{ICo} and $\lambda_{\mathrm{s}}^{\mathrm{Gr}}$ are independent of temperature [139–142].

Results. Part II

The spin Hall effect and anomalous Hall effect in ferromagnets

Chapter 7

Relation between spin Hall effect and anomalous Hall effect in 3d ferromagnets

Ferromagnetic (FM) materials are relevant in the field of spintronics. Due to their intrinsic spin polarization, they have been traditionally exploited to inject and detect electrically spin currents in non-magnetic (NM) materials. NM materials with strong spin-orbit coupling (SOC) can also generate and detect spin currents by using the spin Hall effect (SHE) and the inverse spin Hall effect (ISHE) that occur in these elements, as we saw in Chapters 4, 5 and 6.

The SHE and ISHE also occur in ferromagnets due to the SOC that is present in this type of materials. When a charge current, I_c, is applied, spin-up and spin-down electrons are also deflected in opposite direction, see Fig. 7.1(a). The unbalanced spin population of ferromagnets (3 spin-up *vs.* 2 spin-down electrons in Fig. 7.1(a)), gives rise to both the anomalous Hall effect (AHE), which is linked to the transverse charge accumulation (the difference of the deflected electrons $3 - 2 = 1$ in Fig. 7.1(a)), and SHE, related to the transverse spin accumulation (proportional to the difference of spin direction $(3 - (-2) = 5$ in Fig. 7.1(a)). The AHE has been widely studied in different FM conductors [62] and, more recently, it has been experimentally verified that both ISHE [154–156] and the SHE [157–160] occur in these type of materials.

It has been commonly accepted that both the SHE and the AHE share the same origin and are driven by the same intrinsic and extrinsic mechanisms [49,76]. This would indicate that the phenomenological equations proposed by Tian *et al.* [67] (Eq. 1.9) and Hou *et al.* [71] (Eq. 1.11) for the anomalous Hall resistivity, ρ_{AH}, which consider the different mechanisms that contribute to the effect, are also valid for the spin Hall resistivity ρ_{SH}, see Sections 1.2.1 and 1.2.2. Indeed, this

has been confirmed in Chapters 4 and 5 for the case of Eq. 1.9 [67]. Furthermore, it was suggested that both effects were related by the current spin polarization of the ferromagnet, α_{FM} [155]:

$$\frac{\sigma_{\mathrm{AH}}}{\sigma_{\mathrm{SH}}} = \frac{\rho_{\mathrm{AH}}}{\rho_{\mathrm{SH}}} = \frac{\theta_{\mathrm{AH}}}{\theta_{\mathrm{SH}}} = \alpha_{\mathrm{FM}}, \tag{7.1}$$

where σ_{AH}, σ_{SH}, θ_{AH} and θ_{SH} are the anomalous Hall conductivity, spin Hall conductivity, anomalous Hall angle and spin Hall angle, respectively. Thus, for the case in Fig. 7.1(a), $\alpha_{\mathrm{FM}} = (3-2)/(3+2) = 1/5$. However, it has not been experimentally verified if this simple relation is general, and therefore valid for all the ferromagnets and all the mechanisms. From a theoretical viewpoint, such a relation might hold in the limit of diffusive transport*, but it is not expected to hold in general.

In this chapter, we study the relation between the AHE and SHE in different $3d$ FM metals: Fe, Co, Py ($Ni_{81}Fe_{19}$) and Ni. First, we extract the spin diffusion length, λ_{s}, of the ferromagnets using the spin absorption technique in lateral spin valves (LSVs). Then, we measure the AHE using Hall bars and the SHE using the spin absorption in LSVs, at different temperatures. We extract the weight of each mechanism for the AHE and SHE and verify that the aforementioned simple relation given by Eq. 7.1 is not generally fulfilled and valid for all the mechanisms. The skew-scattering mechanism in Py is the only one that satisfies the simple relation. The temperature dependence of the SHE in all the studied $3d$ FM metals shows an interesting common feature, but it is dramatically different from the temperature dependence obtained for the AHE. A possible scenario to explain the observed results is discussed. Some of the samples of this chapter were fabricated and measured in the laboratory of Prof. Otani, in the Institute of Solid State Physics of the University of Tokyo, and others in CIC nanoGUNE, which makes the study very robust.

7.1 Characteristics of the samples

LSVs were fabricated on 150 nm SiO_2/Si substrates with multiple-step e-beam lithography followed by metal deposition and lift-off, as detailed in Section 3.2.1 and Table 3.1. We first patterned two ∼100-nm-wide wires and deposited 30 nm of Py by e-beam evaporation. The two Py wires are separated by a length, L, of

*Within the semiclassical picture, σ_{AH} and σ_{SH} arising from scatterings are given by $\sigma_{\mathrm{AH}} = -\frac{e^2}{\hbar}\frac{1}{(2\pi)^3}\int_{\mathrm{FS}}\frac{v_x(\vec{k})\lambda_y(\vec{k})}{|\vec{v}(\vec{k})|}dS$ and $\sigma_{\mathrm{SH}} = -\frac{e^2}{\hbar}\frac{1}{(2\pi)^3}\int_{\mathrm{FS}} s_z(\vec{k})\frac{v_x(\vec{k})\lambda_y(\vec{k})}{|\vec{v}(\vec{k})|}dS$, respectively. Here, $v_i(\vec{k})$ are the Fermi velocities, $\lambda_i(\vec{k})$ is the mean-free path, $s_z(\vec{k})$ is the spin polarization and we integrate over the Fermi surface (FS). In the limit of diffusive transport with an isotropic spin polarization $s_z(\vec{k}) = \alpha_{\mathrm{FM}}$, we can take α_{FM} in front of the integral and we find $\sigma_{\mathrm{AH}} = \alpha_{\mathrm{FM}}\sigma_{\mathrm{SH}}$.

650 nm − 1 µm. One of the Py wires is used as a spin current injector, while the other is used as detector to estimate λ_s of our material to study (MS). In the second step, the MS, a 3*d* FM wire with the width of 200 nm was placed just in the middle of the two Py wires and a 5- to 30-nm-thick 3*d* FM metal (Fe, Co, Py or Ni) was deposited with e-beam evaporation.

In the third step, a 100-nm-wide and 100-nm-thick Cu strip was bridged on top of the three wires with a Joule heating evaporator. Before the Cu evaporation, an Ar-ion milling treatment was performed to achieve transparent interfaces. Transparent interfaces were confirmed by measuring the interface resistances using the configuration shown in Fig. 3.6(c). The AHE measurements were performed either in the same middle wire where the SHE was measured (see Fig. 7.1(b)), in a 20-µm-long and 3-µm-wide Hall bar or in a 780-µm-long and 100-µm-wide Hall bar. The latter was patterned in the same type of substrate with photolithography and the FM metal (5 to 30 nm in thickness) was deposited at the same time as the SHE devices were prepared, following the recipe of Section 3.2.3. The electric transport measurements were performed in a ^{4}He flow cryostat applying an external magnetic field, $\vec{H}$, and varying temperature, T. Some of the samples were measured using delta mode and others the equivalent lock-in technique, see Section 3.3.1.

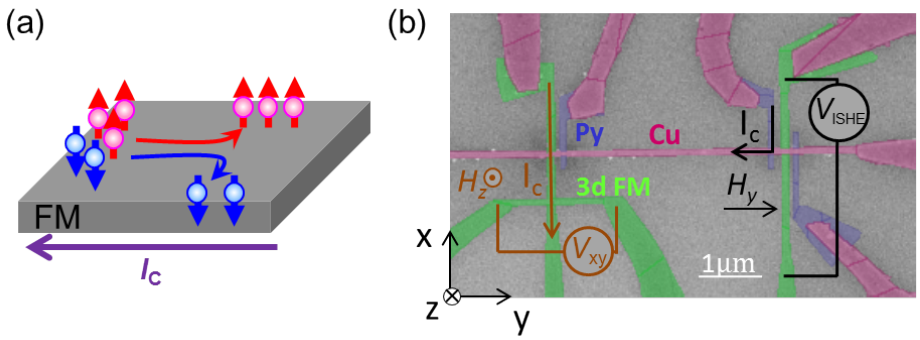

Figure 7.1: **Sketch and measurement configuration of the SHE and AHE occurring in a FM conductor.** (a) Intuitive sketch of the SHE and AHE occurring in a FM conductor. Spin and charge accumulations appear in the transverse direction with respect to the incident current I_c and are detected as the SHE and AHE, respectively. (b) Scanning electron microscopy (SEM) image of a sample where the AHE and SHE measurement configurations are shown (orange and black, respectively). Note that the AHE and SHE can be measured in the same FM nanowire.

7.2 Spin diffusion length of 3*d* FM metals

In order to achieve an accurate quantification of the spin Hall parameters, first λ_s should be extracted, as remarked in Chapter 4. Therefore, we start by characterizing this spin transport property of the different 3*d* ferromagnets.

7.2.1 Spin diffusion length of Py

The first MS will be Py. In Chapters 4 and 5, Py was used as electrical spin injector and detector and, in order to calculate its spin resistance, R_s^{Py}, the spin diffusion length of Py, λ_s^{Py}, was taken from Refs. [28, 133, 134]. Here, its value was estimated: for instance, in Ref. [28], it was assumed to be 5 nm at 10 K and considered a temperature dependence coming from the resistivity, ρ_{Py}, in the form $\lambda_s^{Py} = \text{const}/\rho_{Py}$. However, in this chapter, Py is not only employed as spin injector and detector, but also as spin Hall metal. In order to extract the precise spin Hall parameters of Py, λ_s^{Py} should be first accurately quantified.

We will employ the spin absorption technique using Py/Cu LSVs with Py middle wires to extract λ_s^{Py}. We fabricated 2 samples (Sample 1 and Sample 2) for this specific task, following the recipe described in the previous Section 7.1, that contained extra reference LSVs with different L. In these samples, both the middle wire and the FM metal for spin injection and detection are made of Py, so the calculation of λ_s^{Py} is slightly different compared to the procedure described in Section 2.1.2. This last procedure was followed with Pt and Ta in Chapters 4 and 5, respectively, and will also be used with the rest of 3*d* FM metals later.

Sample 1 consists of two types of devices, see a SEM image of this sample in Fig. 7.2(a). The first type of device consists of a Py/Cu LSV, where the Py injector and Py detector are connected by a Cu channel with the Py interelectrode distance L. The second type of device is a Py/Cu LSV that contains an additional 30-nm-thick Py nanowire in between the Py injector and detector, see the third LSV starting from the left in Fig. 7.2(a). The comparison of the nonlocal signals obtained in each of the devices allows us to study the spin relaxation in the middle Py wire.

We measure R_{NL} as a function of H_x in the devices without the middle Py wire with different interelectrode distances L and at different temperatures using the red measurement configuration in Fig. 7.2(a). Figure 7.2(b) shows the obtained results for the LSV with L =650 nm and Fig. 7.2(c) the obtained ΔR_{NL} as a function of L at 10 K. From the fitting of the data to Eq. 2.13, see red solid line in Fig. 7.2(c) for 10 K, we extract the spin diffusion length of Cu, λ_s^{Cu}, and the current spin polarization of Py, α_{Py}, which are plotted as a function of temperature in Figs. 7.2(d) and 7.2(e), respectively. In order to perform the fitting, we measure experimentally all the dimensions by SEM, thicknesses by X-ray reflection (XRR) and resistivities of the wires that form the device. The resistivities of Cu and Py wires, obtained by four-point resistance measurement shown in Fig. 3.6(a), are plotted as a function of temperature in the insets of Figs. 7.2(d) and 7.2(e), respectively. λ_s^{Py} was first assumed to be 5 nm at 10 K and considered a temperature dependence coming from the resistivity in the form

$\lambda_s^{Py} = \text{const}/\rho_{Py}$ [28].

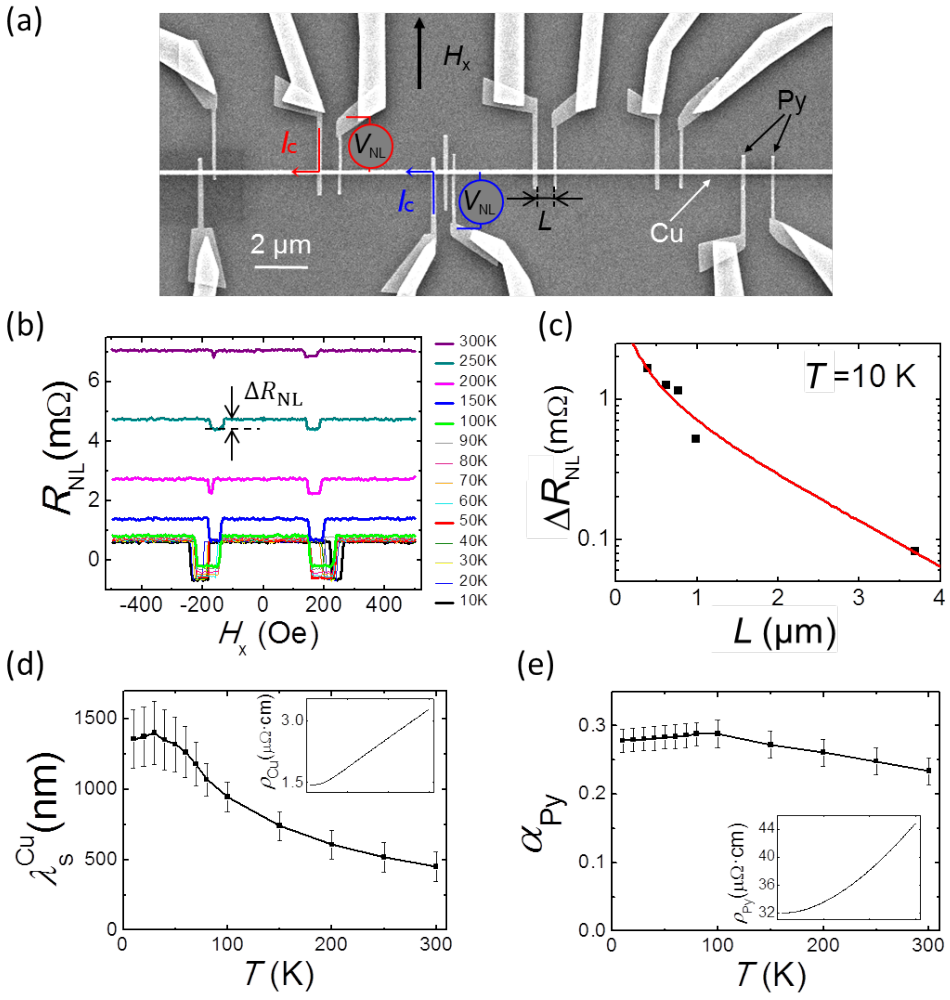

Figure 7.2: **Results of the nonlocal measurements in the reference Py/Cu LSVs in the first cycle.** (a) SEM image of Sample 1 containing six Py/Cu LSVs with different interelectrode distances L. One of them, the third LSV from the left side, has an additional Py wire in between the Py electrodes where the spin absorption will occur. The nonlocal measurement configuration and the direction of the applied magnetic field, H_x, are shown. (b) Nonlocal resistance as a function of the magnetic field measured at different temperatures in a reference LSV in Sample 1 where L=650 nm, using the configuration shown in (a) and applying I_c=100 μA. The spin signal ΔR_{NL} has been tagged. (c) ΔR_{NL} as a function of L measured in the different reference LSVs of Sample 1 at 10 K. The red solid line is the fitting of the experimental data, represented by black squares, to Eq. 2.13 from which we extract (d) the spin diffusion length of Cu and (e) the current spin polarization of Py as a function of the temperature. Insets in (d) and (e) correspond to the temperature dependence of the resistivity of Cu and Py, respectively. The scale in the horizontal axis of the insets is the same as in their respective main panel.

Next, we measure R_{NL} in the LSV with the middle Py wire (the third one from the left side in Fig. 7.2(a)). The inset in Fig. 7.3(a) shows R_{NL} as a function

of H_x for the reference LSV, red solid line, and the LSV with the middle Py wire, blue solid line, measured in the configuration shown in Fig. 7.2(a). The distance between the Py injector and detector in both LSVs is 650 nm.

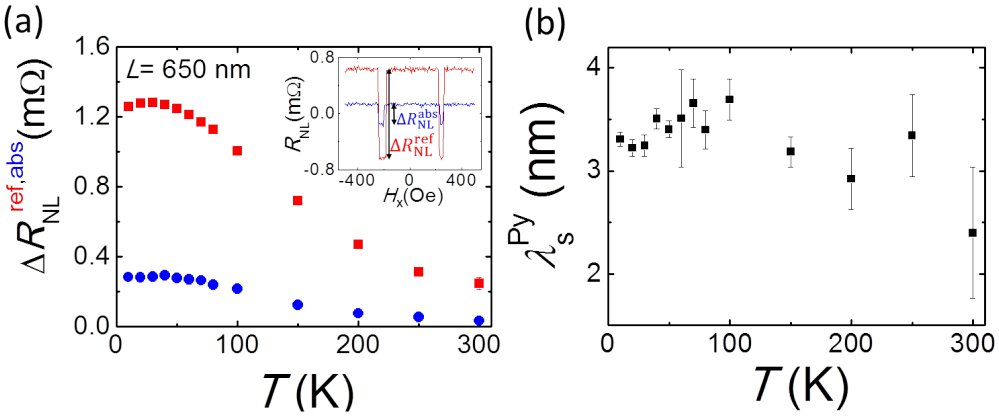

Figure 7.3: **Nonlocal measurements of reference and spin absorption LSVs and the extracted spin diffusion length of Py in the first cycle.** (a) Spin signal as a function of temperature for the reference Py/Cu LSV (red squares) and for Py/Cu LSV with a middle Py wire (blue circles), both in Sample 1, using I_c=100 μA. The distance between the injector and detector is the same in both devices. Inset: nonlocal resistance as a function of the applied magnetic field at 10 K for the reference Py/Cu LSV (red solid line) and the Py/Cu LSV with a middle Py wire (blue solid line). The reference spin signal (ΔR_{NL}^{ref}) and the spin signal with Py absorption (ΔR_{NL}^{abs}) are tagged. (b) Spin diffusion length of Py as a function of the temperature obtained from the data in (a) using Eq. 2.18.

The spin signal, ΔR_{NL}, obtained for each type of LSV at different temperatures is shown in Fig. 7.3(a). The middle Py wire absorbs part of the spins that are flowing in the Cu channel, reducing the spin signal in comparison to the reference LSV. From the ratio of both spin signals, given by Eq. 2.18 where the one-dimensional spin-diffusion model for transparent interfaces has been considered, λ_s^{Py} is extracted by substituting the value of the dimensions, resistivities and λ_s^{Cu} and α_{Py} obtained in the previous fitting. This procedure is repeated for all the studied temperatures and Fig. 7.3(b) shows the result of λ_s^{Py} as a function of temperature. The obtained λ_s^{Py} is different from the one originally assumed. With the new λ_s^{Py}, we can make another iteration with Eqs. 2.13 and 2.18 to recalculate λ_s^{Cu}, α_{Py}, and λ_s^{Py}. Iterations were performed until λ_s^{Cu}, α_{Py}, and λ_s^{Py} parameters converged in a self-consistent manner.

The results obtained in the second cycle are shown by blue solid lines in Fig. 7.4. Although the parameter λ_s^{Cu} barely changes from the first to the second cycle, α_{Py} varies quite significantly. In the third cycle, the convergence is attained for the three parameters, see the red solid line in Fig. 7.4. The obtained λ_s^{Cu}, α_{Py}, and λ_s^{Py} values are consistent with the values that are reported in the literature,

see Tables 7.1 and 7.2.

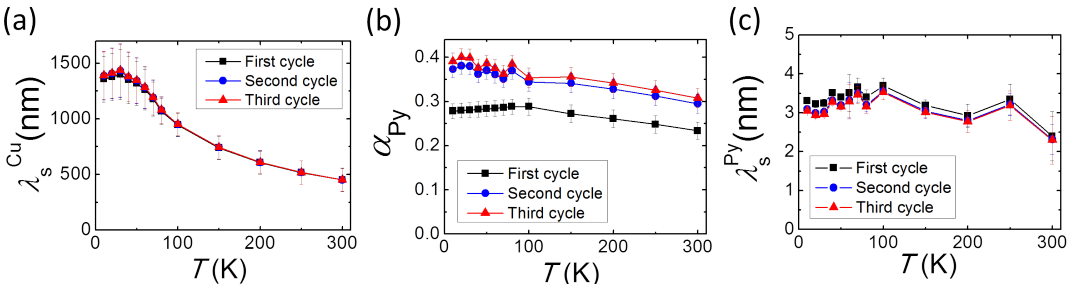

Figure 7.4: **Results of three self-consistent cycles.** (a) Spin diffusion length of Cu, (b) current spin polarization of Py and (c) spin diffusion length of Py as a function of temperature. First, second and third cycles are represented by black, blue and red solid lines, respectively. Data correspond to Sample 1.

We fabricate an additional Py/Cu LSV (Sample 2) with a thinner middle Py wire (9 nm) than in the previous one (Sample 1), in order to increase its resistivity. The dimensions and characteristics of the Cu channel and Py injector and detector in this new sample are the same as in the previous one. Therefore, from the previous analysis we know λ_s^{Py} and α_{Py} of the injector and detector and λ_s^{Cu}. We measure the spin signal from 10 K to 50 K and extract λ_s^{Py} of the middle Py wire by employing Eq. 2.18. The obtained results have been added in Table 7.2.

Table 7.1: **Spin diffusion length of Cu and current spin polarization of Py extracted from literature and this work.** The temperature and resistivity of Cu are included.

T (K)	ρ_{Cu} ($\mu\Omega$cm)	λ_s^{Cu} (nm)	α_{Py}	Ref.
10	0.69	1000	0.58	[134]
10	1.26	1020	0.40	[28]
10	1.2	770	0.39	[161]
10	1.44	1390 ± 200	0.39 ± 0.02	Sample 1
80	1.2	1300	0.35	[162]
250	2.4	380	0.34	[161]
290	2.35	400	0.49	[134]
300	2.08	500	0.25	[133]
300	2.90	410	0.34	[28]
300	2.90	410	0.34	[28]
300	3.30	450 ± 100	0.31 ± 0.02	Sample 1

Table 7.2: **Spin diffusion length and resistivity of Py extracted from literature and this work.** The temperature is included.

T (K)	ρ_{Py} (μΩcm)	λ_s^{Py} (nm)	Ref.
4.2	12	5.5 ± 1.0	[37, 163]
10	17.1	5	[134]
10	32	3.04 ± 0.06	Sample 1
10	80.2	1.4 ± 0.2	Sample 2
77	...	4.3 ± 1.0	[164]
290	23.1	4.5	[134]
300	...	2.5	[154]
300	26.8	3	[133]
300	44	2.30 ± 0.61	Sample 1

Figure 7.5(a) shows that the $\rho_{Py}\lambda_s^{Py}$ values vary slightly with temperature and are similar for Sample 1 and Sample 2. The obtained values are close to the one given in Ref. [165]. More generally, Fig. 7.5(b) demonstrates the linear dependence of λ_s^{Py} with the conductivity of Py, $\sigma_{Py} = 1/\rho_{Py}$, not only for our samples but also for the experimental data from the literature. We observe a general linear tendency that fits well to $\lambda_s^{Py} = (0.916 \pm 0.04)$ (fΩm^2)$/\rho_{Py}$. These plots indicate that the main spin relaxation mechanism in Py is Elliott-Yafet, see Section 1.1.2, which is consistent with the theoretical prediction of Berger [166].

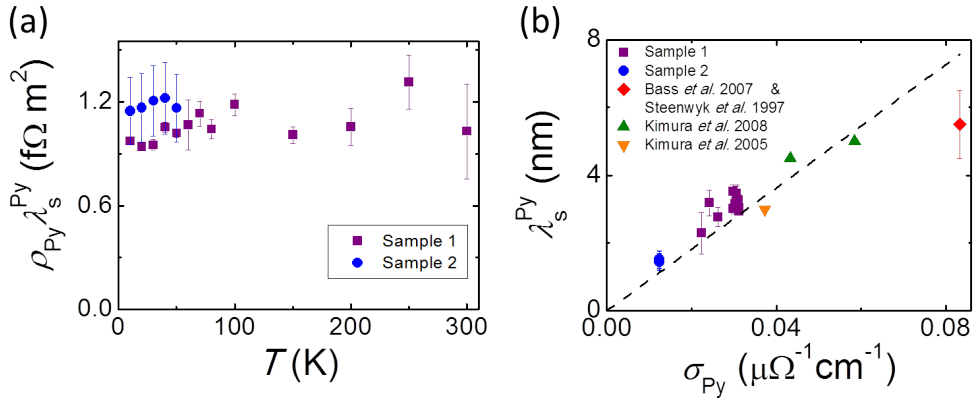

Figure 7.5: **Relation of the spin diffusion length of Py with resistivity, or conductivity, of Py.** (a) Product of the spin diffusion length and resistivity of Py as a function of temperature for Sample 1 and Sample 2. (b) Spin diffusion length of Py as a function of the conductivity. Literature values of λ_s^{Py} are also included for completing the data set from Refs. [37,133,134,163]. The black dashed line corresponds to the linear fit to all data.

7.2.2 Spin diffusion length of Fe, Co and Ni

In order to extract λ_s of Fe, Co and Ni, the middle wire of the Py/Cu LSV is made of these metals and we follow the procedure described in Section 2.1.2. These experiments were performed by our collaborator Dr. Y. Omori. He measured the spin absorption signal in LSVs with and without middle wire and extracted λ_s of these three ferromagnets as a function of temperature. For the calculation, the longitudinal resistivity measured in four-point configuration (see Fig. 3.6(a)), shown in Fig. 7.6(a), and the values of α_{FM} extracted from Refs. [29, 167] were considered. The obtained results are shown in Fig. 7.6(b).

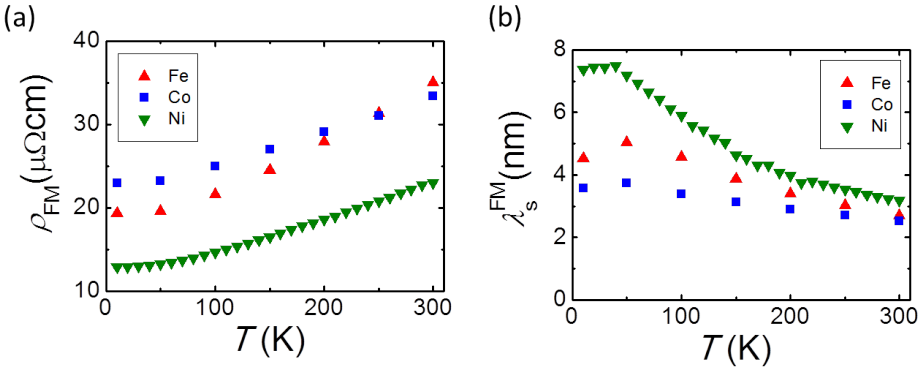

Figure 7.6: **Temperature dependence of the resistivity and spin diffusion length of Fe, Co and Ni.** (a) Temperature dependence of the resistivity of Fe (red triangles), Co (blue squares) and Ni (green inverted triangles) measured in four-point configuration. (b) Temperature dependence of the spin diffusion length of Fe (red triangles), Co (blue squares) and Ni (green inverted triangles) measured using the spin absorption technique.

7.3 SHE and AHE in 3*d* FM metals

Once the spin transport properties of the 3*d* FM metals are characterized, we measure the SHE using the spin absorption technique in LSVs and AHE employing Hall bars as described in Sections 2.1.3 and 2.2.1, respectively.

7.3.1 SHE and AHE in Py

Figure 7.7(a) shows the nonlocal resistance originated due to the ISHE, R_{ISHE}, in Py as a function of H_y, measured using the black configuration shown in Fig. 7.1(b). A positive ISHE signal, $2\Delta R_{ISHE} \sim 50$ μΩ, is obtained at 10 K for a 20-nm-thick Py middle wire with ρ_{Py} of 22 μΩcm. Using Eqs. 2.20 and 2.24, and substituting $2\Delta R_{ISHE}$, the geometrical factors measured by SEM, the

thicknesses measured by XRR, λ_s^{Cu}, λ_s^{Py} and α_{Py} that were accurately determined in the previous section and the shunting factor, $x_{Py,Cu}$, that was calculated by SPINFLOW 3D software [80] by Dr. Y. Omori (considering w_{Cu}, w_{Py}, ρ_{Cu} and ρ_{Py} values of the devices), we extract $\rho_{SH} \equiv \rho_{xy,SH}$. The obtained $-\rho_{SH}$, which corresponds to the ΔR_{ISHE} value in Fig. 7.7(a), is plotted by a black square in Fig. 7.7(c).

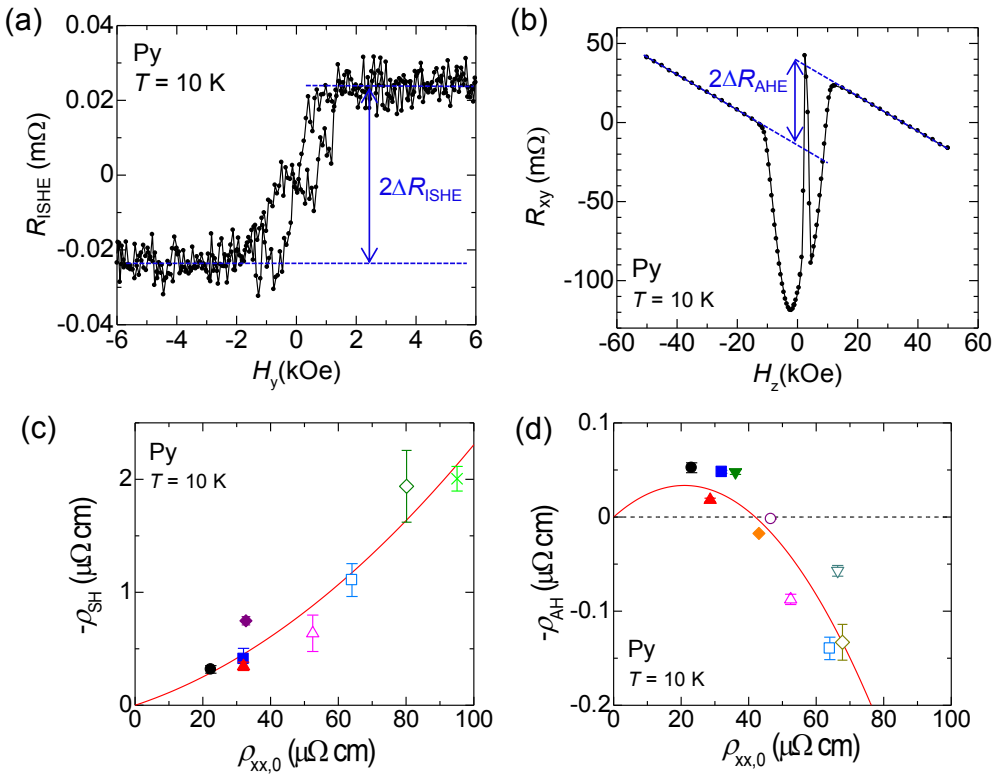

Figure 7.7: **SHE and AHE measurements and the obtained spin Hall and anomalous Hall resistivities at 10 K for Py.** (a) Inverse spin Hall resistance of the middle Py wire (20 nm in thickness) as a function of H_y at 10 K measured using the orange configuration shown in Fig. 7.1(b). The ISHE signal ($2\Delta R_{ISHE}$) is tagged. (b) Transverse resistance of Py as a function of H_z at 10 K measured using the black configuration shown in Fig. 7.1(b). The AHE signal ($2\Delta R_{AHE}$) is tagged. (c) Spin Hall resistivity in Py as a function of residual resistivity at 10 K. (d) Anomalous Hall resistivity in Py as a function of residual resistivity at 10 K. The dotted line indicates $-\rho_{AH}$=0. The red solid lines in (c) and (d) are the best fits to Eq. 7.2. The same symbol is used in (c) and (d) if the Py deposition is done at the same time for the SHE and AHE samples.

We next measure the AHE in a Hall bar, prepared at the same time as the SHE device. By applying an out-of-plane magnetic field, H_z, and flowing I_c in the longitudinal direction of the Hall bar, a transverse voltage drop, V is detected, as shown by the orange configuration in Fig. 7.1(b). Figure 7.7(b) shows a typical $R_{xy} = V/I_c$ *vs.* H_z curve for 20-nm-thick Py with ρ_{Py} of 22 μΩcm at 10 K. Although there are two backgrounds, namely, the ordinary Hall resistance and

planar Hall resistance in between ±10 kOe [168], a clear positive AHE signal, $2\Delta R_{\rm AHE} \sim 50$ mΩ, can be extracted extrapolating $R_{\rm xy}$ values at H_z=0 from the two linear curves at positive and negative H_z, as described in Section 2.2.1. From the measured $\Delta R_{\rm AHE}$ value, we obtain the corresponding $\rho_{\rm AH} \equiv \rho_{\rm xy,AH}$, using Eq. 2.27, which is plotted by a black solid square in Fig.7.7(d).

To determine the weight of each mechanism, the SHE and AHE of Py must be measured in a wide resistivity range. Hence, we fabricated different devices varying the thickness of the Py wire (from 5 to 30 nm) and the deposition rate (from 0.04 nm/s to 0.08 nm/s) in order to modify the residual resistivity, $\rho_{\rm xx,0}$. Figures 7.7(c) and 7.7(d) show the obtained $-\rho_{\rm SH}$ and $-\rho_{\rm AH}$ of Py at 10 K as a function of $\rho_{\rm xx,0}$, respectively. At low temperatures, where the phonon contribution is negligible, Eq. 1.11 that relates $-\rho_{\rm H}$ with $\rho_{\rm xx,0}$ can be written as:

$$-\rho_{\rm H} = \alpha_{\rm H}^{\rm ss}\rho_{\rm xx,0} + \beta_{\rm H}^{0}\rho_{\rm xx,0}^{2}, \tag{7.2}$$

where H refers to the SHE or AHE. By fitting $-\rho_{\rm SH}$ and $-\rho_{\rm AH}$ to Eq. 7.2 (see the red solid lines in Figs. 7.7(c) and 7.7(d)), the skew-scattering angle, $\alpha_{\rm H}^{\rm ss}$, and the combination of the side-jump and intrinsic contributions, $\beta_{\rm H}^{0}$, are obtained for the SHE and AHE:

$$\begin{aligned} \alpha_{\rm SH}^{\rm ss} &= 1.0 \pm 0.4\%, \quad \beta_{\rm SH}^{0} = 131 \pm 60(\hbar/e)\Omega^{-1}{\rm cm}^{-1} \\ \alpha_{\rm AH}^{\rm ss} &= 0.32 \pm 0.1\%, \quad \beta_{\rm AH}^{0} = -76 \pm 20(\hbar/e)\Omega^{-1}{\rm cm}^{-1}. \end{aligned}$$

$\alpha_{\rm AH}^{\rm ss}$ and $\beta_{\rm AH}^{0}$ are in good agreement with a previous report [168]. Strictly speaking, $\beta_{\rm AH}^{0}$ (and $\beta_{\rm AH}^{1}$ of Eq. 1.11) are different from b which is the coefficient of $\rho_{\rm Py}^{2}$ in Ref. [168]. In general, b should be closer to $\beta_{\rm AH}^{1}$, but in the case of Py, both $\beta_{\rm AH}^{0}$ and $\beta_{\rm AH}^{1}$ are comparable to b. Interestingly, the ratio of the AHE and SHE in Py for the skew-scattering contribution, $\alpha_{\rm AH}^{\rm ss}/\alpha_{\rm SH}^{\rm ss} = 0.32$, is a reasonable value for $\alpha_{\rm Py}$, see Table 7.1 or the third self-consistent cycle at Fig. 7.4(b). Therefore, for the skew scattering of Py, the relation between the AHE and SHE is given by Eq. 7.1. This can be understood because Py is a random alloy composed of Ni and Fe. The anisotropy on the Fermi surface should be suppressed and lead to more isotropic scattering properties. Thus, the Hall angle is essentially a spin-independent property averaged over all the contributing states. This supports the finding that the simplified relation holds for the skew scattering in Py, see the footnote in page 98.

7.3.2 SHE and AHE in Fe, Co and Ni

We now study the SHE and the AHE in other 3*d* FM metals using the same experimental technique. We show the obtained $\theta_{\rm SH}$ and $\theta_{\rm AH}$ at T = 10 K in Figs.

7.8(a) and 7.8(b), respectively. As in the case of the intrinsic SHE in 4*d* and 5*d* transition metals [74, 78, 169], θ_{SH} is expected to change the sign from negative to positive with increasing the number of electrons in the outer shell [156], due to the change in sign of the intrinsic spin Hall conductivity, see Fig. 1.9(a). Such a tendency can be seen clearly in θ_{SH} of the 3*d* FM metals in Fig. 7.8(a) and it is in good agreement with the work of Du *et al.* [156]. However, the sign of θ_{SH} is opposite to that of θ_{AH} for Fe, Co, and Ni. For instance, α_{Fe} is predicted to be positive [170,171], hence θ_{SH} and θ_{AH} should have the same sign according to Eq. 7.1. Even in the case of Py, θ_{AH} is negative when $\rho_{\mathrm{xx},0}$ is more than 40 μΩcm, see Fig. 7.7(d). This obviously shows that Eq. 7.1 is not general and the detailed band structure of the electron orbitals has to be considered.

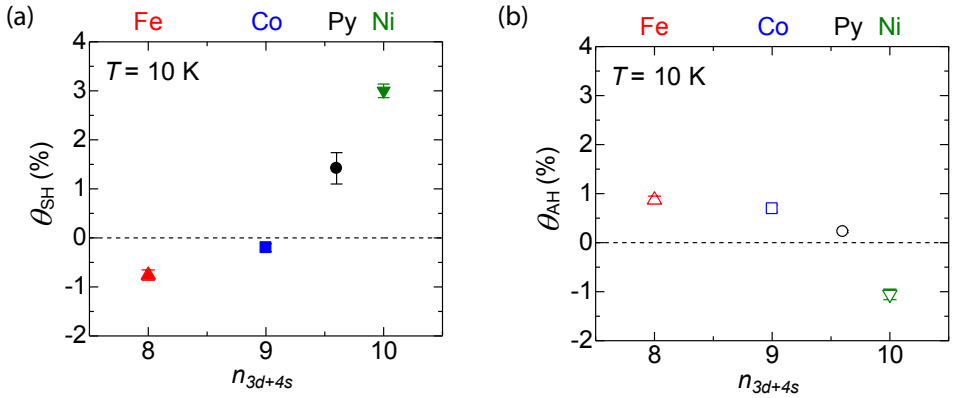

Figure 7.8: **Spin Hall and anomalous Hall angle of 3*d* FM metals at 10 K.** Number of electrons in the outermost shell dependence of the (a) spin Hall angle and (b) anomalous Hall angle in the 3*d* ferromagnets. The thickness of the four metals is 20 nm.

So far, we have focused on the low-temperature parts of the SHE and AHE. To address the effect of dynamic disorder, we next discuss the temperature dependencies of the SHE and AHE.

Temperature dependence of the SHE is much stronger than that of the AHE, as can be seen from the comparison of Figs. 7.9(a) and 7.9(b) for each ferromagnet. In case of the SHE, $-\rho_{\mathrm{SH}}$ remains fairly constant from 10 K up to $\sim$ 150 K and above this temperature, a strong temperature dependence takes place, which is a common feature for all the FM metals. Namely, for Fe, Py, and Ni, the sign of $-\rho_{\mathrm{SH}}$ changes at 200–250 K. However, such a sign change or strong temperature dependence is not observed for $-\rho_{\mathrm{AH}}$ in any of the FM elements. This result is a priori unexpected, if common mechanisms are shared between the SHE and AHE. Note that such strong temperature, or resistivity, dependence above a certain temperature is neither observed in $-\rho_{\mathrm{SH}}$ of Pt or Ta (see Figs. 4.4 and 5.4(c), respectively).

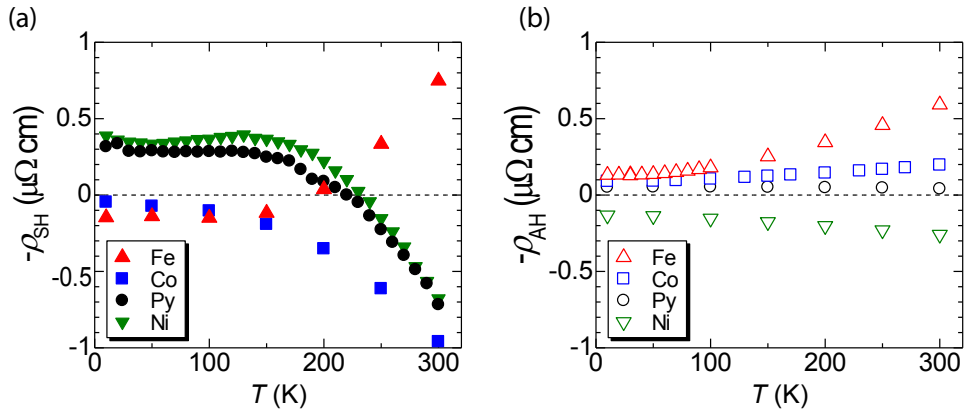

Figure 7.9: **Temperature dependence of the spin Hall and anomalous Hall resistivity in 3*d* FM metals.** Temperature dependence of (a) spin Hall resistivity and (b) anomalous Hall resistivity in four 3*d* ferromagnets. The thickness of the four metals is 20 nm.

To specify the reason for such temperature dependencies, we have individually fitted both $-\rho_{SH}$ and $-\rho_{AH}$ for each FM element as a function of $\rho_{xx,T}(= \rho_{xx} - \rho_{xx,0}$, where $\rho_{xx} = \rho_{FM})$ with Eq. 1.11, as shown in Fig. 7.10. This recent phenomenological equation considers an extra term (last term in the equivalent Eq. 1.12 written in terms of conductivities) that becomes relevant at intermediate T regime, precisely where we observe the main difference between the two effects.

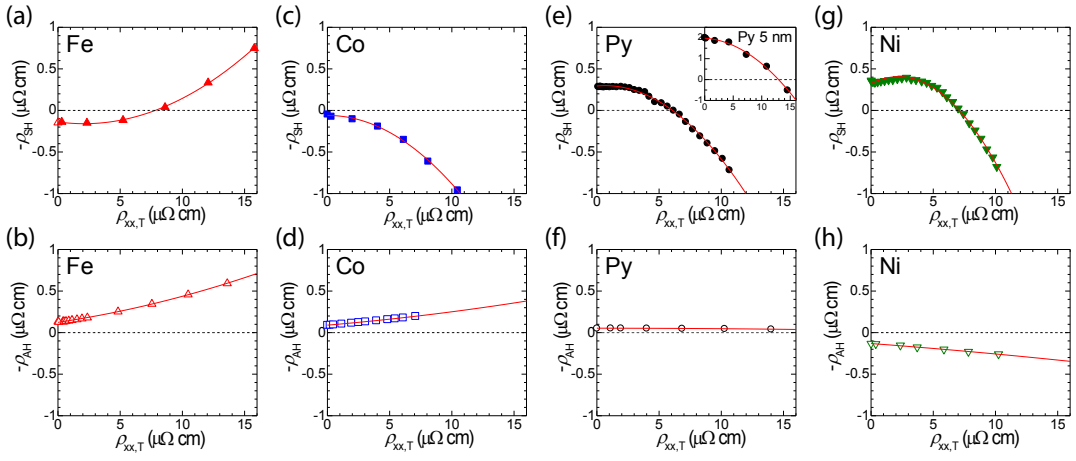

Figure 7.10: **Spin Hall and anomalous Hall resistivity in four FM metals at finite temperatures.** Spin Hall resistivity as a function of $\rho_{xx,T}$ in (a) Fe, (c) Co, (e) Py and (g) Ni. Anomalous Hall resistivity as a function of $\rho_{xx,T}$ in (b) Fe, (d) Co, (f) Py and (h) Ni. $\rho_{xx,T}$ varies by changing temperature from 10 K to 300 K. The solid lines are the best fits to the data to Eq. 1.11. The thickness of the four ferromagnets is 20 nm both for SHE and AHE measurements except for the inset in (e). The inset in (e) shows the spin Hall resistivity of 5-nm-thick Py wire. For the fitting with Eq. 1.11, the same parameter $\beta^1_{SH}= -10100\ \Omega^{-1}\text{cm}^{-1}$ was obtained within the error bars for both 20-nm and 5-nm-thick Py wires.

We obtain the values of β_{H}^{1} and γ_{H} as the quadratic and linear terms in Eq. 1.11, respectively, which are collected in Table 7.3. β_{H}^{0} and $\alpha_{\mathrm{H}}^{\mathrm{ss}}$, being both independent of ρ_{xxT}, are indistinguishable in this fitting. In case of Py, the obtained constant term is consistent with β_{H}^{0} and $\alpha_{\mathrm{H}}^{\mathrm{ss}}$ values extracted in the previous section. In addition, β_{SH}^{1} term extracted independently from the fits of 5-nm- and 20-nm-thick Py, see Fig. 7.10(e) and its inset, are compatible considering the error bar. We can draw the following conclusions from the obtained results:

- The obtained β_{AH}^{1} values, associated to the intrinsic mechanism, are in good agreement with the values obtained in previous experiments [168, 172–175] and tight-binding calculations [176].
- $|\beta_{\mathrm{SH}}^{1}|$ values, associated to the intrinsic mechanism, of the $3d$ FM metals range between 4900 and 17000 $(\hbar/e)\Omega^{-1}\mathrm{cm}^{-1}$.
  - The obtained β_{SH}^{1} are much larger than that of a typical SHE material, Pt (1600 $(\hbar/e)\Omega^{-1}\mathrm{cm}^{-1}$) or Ta (-820 $(\hbar/e)\Omega^{-1}\mathrm{cm}^{-1}$), obtained in Chapters 4 and 5, respectively.
  - The sign change of β_{SH}^{1} with the filling of the outermost shell is expected [156].
- $\beta_{\mathrm{SH}}^{1} \gg \beta_{\mathrm{AH}}^{1}$ for all the $3d$ ferromagnets. In particular, β_{SH}^{1} of Py is more than two orders of magnitude larger than β_{AH}^{1}. Therefore, even for Py, the relation between the SHE and AHE for β_{H}^{1}, and γ_{H} is not as simple as the skew-scattering term.
- The relation between γ_{SH} and γ_{AH} strongly varies with the $3d$ FM metal.

Table 7.3: **Spin Hall and anomalous Hall parameters of the 3d FM metals.** The coefficients β_{SH}^{1}, β_{AH}^{1}, γ_{SH} and γ_{AH} extracted from the fittings with Eq. 1.11 for each FM element. For comparison, we also show β_{AH}^{1} coefficient values from previous works (Refs. [168, 172–175]) in the table.

FM metal	Fe	Co	Py	Ni
β_{SH}^{1} $(\cdot 10^{3}(\hbar/e)\Omega^{-1}\mathrm{cm}^{-1})$	4.9 ± 0.2	-8.3 ± 0.5	-10.1 ± 0.3	-17.1 ± 0.5
β_{AH}^{1} $(\Omega^{-1}\mathrm{cm}^{-1})$	890 ± 40	340 ± 30	-56 ± 15	-140 ± 110
$\beta_{\mathrm{AH}}^{1}(\Omega^{-1}\mathrm{cm}^{-1})$ in literature	1100 [168] 820 [172]	200 [173] 730 [174]	-50 [168]	-(500∼1000) [175]
γ_{SH} $(\cdot 10^{3}(\hbar/e)\Omega^{-1}\mathrm{cm}^{-1})$	-1.1 ± 0.1	0.04 ± 0.24	0.57 ± 0.14	5.9 ± 0.4
γ_{AH} $(\Omega^{-1}\mathrm{cm}^{-1})$	1500 ± 30	970 ± 20	-2 ± 9	-890 ± 90

Much larger β^1_{SH} values than β^1_{AH} ones would originate from the stronger temperature dependence of the SHE in 3*d* FM metals. At the moment, we do not have a conclusive picture for the origin of this dependence. As mentioned above, β^1_{SH} values are surprisingly large, which makes us doubt whether it is the intrinsic mechanism the only responsible of the strong T dependence. One possible scenario is to have an additional contribution, only in the SHE of FM elements, originated from the electron-magnon interactions in these materials. In general, the spin transport can be mediated not only by conduction electrons, but also by magnons in ferromagnets [177, 178] and recently, a theoretical report claims that magnon spin current can be significant around room temperature in 3*d* FM elements [179]. The electron-magnon interactions would induce additional spin-flip processes and spin-dependent scattering. We note that such spin-flip processes are equivalent in magnitude for up-to-down and down-to-up spin channels even in FM systems [†].

In such a situation, some asymmetric scatterings which are spin dependent would contribute only to the SHE but not to the AHE, and thus would be associated with the fact that the strong temperature dependence is not present in the AHE of the 3*d* FM elements or the SHE of NM metals. However, there are some open questions: how large the asymmetric scatterings are quantitatively and whether any other mechanisms contribute to the observed spin Hall resistivity or not. These would be addressed in the future.

7.4 Conclusions

In conclusion, we experimentally investigated the relation between the SHE and AHE in four 3*d* FM metals: Fe, Co, Py, and Ni. In a typical FM alloy, Py, the skew-scattering contribution of the AHE is related to that of the SHE via the current spin polarization of Py, as can be understood intuitively. However, this relation does not hold for other mechanisms. This fact is highlighted by the temperature dependence of the SHE and AHE. For all the 3*d* FM metals, there is a strong temperature dependence of $-\rho_{\mathrm{SH}}$ above $\sim$ 150 K, including a sign change in most of the cases, which is a feature that is not present in $-\rho_{\mathrm{AH}}$ of any of the 3*d* FM elements or even in $-\rho_{\mathrm{SH}}$ of Pt or Ta. As a result, a much larger intrinsic mechanism term β^1_{SH} than β^1_{AH} or intrinsic spin Hall conductivity of Pt or Ta is obtained. A new mechanism in the SHE of 3*d* FM elements, based on asymmetric spin-dependent scatterings in the spin-flip processes induced by the

[†] The scattering probability related to the spin-flip process is defined as $P^{+-}_{kk'} \sim |\langle\psi^-_{k'}|\hat{T}|\psi^+_k\rangle|^2$ where $\psi^{+(-)}_{k(k')}$ is the wave function before (after) the scattering with the wave number $k(k')$ and spin-up + (spin-down −), and $\hat{T}$ is a matrix in spin space including SOC and magnetism. By defining $P^{-+}_{kk'}$ in an equivalent way and integrating k and k', we find that on average it holds $\tau^{-1}_{+-} = \tau^{-1}_{-+}$, with $\tau^{-1} = \int dk \int dk' P_{kk'}$, even in the magnetic case.

electron-magnon interactions, would be a possible explanation for the observed strong temperature dependence, in contrast to the AHE or SHE in NM metals.

We also obtained λ_s of the $3d$ FM metals using the spin absorption technique in LSVs. In case of Py, we observe a linear dependence between λ_s^{Py} and $1/\rho_{Py}$, which evidences that Elliott-Yafet is the dominating spin relaxation mechanism.

Chapter 8

Interfacial mechanism in the anomalous Hall effect of Co/Bi_2O_3

Spin-to-charge current conversions not only occur in bulk systems, but also at interfaces and surfaces. The Edelstein effect [51] is a good example of this, which takes place at Rashba interfaces, such as Bi/Ag [55], Bi/Cu [45], Bi_2O_3/Cu [102] and $LaAlO_3/SrTiO_3$ [103], and at the surface states of topological insulators, in α-Sn [104] and $(Bi_{1-x}Sb_x)_2Te_3$ [105], for instance. Furthermore, it has been theoretically predicted that the inversion symmetry breaking at the interface of different materials can generate giant spin-orbit coupling (SOC) that results in extra conversions between charge currents and spin currents in the bulk [180–182]. This prediction has been confirmed in the results of ab-initio calculations for Py/Pt [124] and Fe/Au [183] systems, which show a large enhancement of such a conversion, which is not confined to the interface between the two metals. In this framework, it is appealing to unveil whether the inversion symmetry breaking introduced when a ferromagnetic material is interfaced with a non-magnetic (NM) material, either metallic or insulating, can affect the anomalous Hall effect (AHE). Interestingly, the AHE has been observed to be modified in the presence of metallic interfaces, such as in Ni/Cu [184] and Py/Pt [185].

In this chapter, we study the AHE in Co/Bi_2O_3 bilayers for different Co thicknesses, unraveling the role that the interface between Co and Bi_2O_3 plays in the AHE of Co. We consider Bi_2O_3 an ideal material since (i) due to its insulating nature, we can discard additional effects such as extra magnetoresistances coming from the NM layer, and (ii) a large Rashba coefficient is expected in our Co/Bi_2O_3 system, as the work function of Co is similar to that of Cu [102, 186]. We observe an up to 37% variation in the AHE of Co by adding the Bi_2O_3 capping layer to the

Co. The temperature dependence of the AHE allows us to extract the weight of the intrinsic and extrinsic contributions. We show that the intrinsic contribution is insensitive to the Bi_2O_3 capping layer, which acts as a scattering source at the interface, with a contribution to the observed skew scattering that decays with the thickness of Co layer.

8.1 Characteristics of the samples

The Co (reference) and Co/Bi_2O_3 (bilayer) Hall bars used in this study are fabricated using the recipe described in Section 3.2.3 and Table 3.4. Firstly, Co and Co/Bi_2O_3 thin films were deposited *in situ* on top of doped-Si/SiO_2 (150 nm) substrates. Co was e-beam evaporated at 0.5 Å/s and $\sim 8 \times 10^{-7}$ Torr, and Bi_2O_3 was also e-beam evaporated at 0.1 Å/s and $\sim 2 \times 10^{-6}$ Torr. Later, 100-μm-wide and 780-μm-long Hall bars were patterned, keeping after the developing the H-shaped resist on top of the substrate and, subsequently, ion-milling was performed. The thickness of Bi_2O_3 is 20 nm for all the Co(t)/Bi_2O_3 bilayers and the thickness of Co(t) layer, t given in nm, varies from 10 to 160 nm. The grazing incidence X-ray diffraction (GI-XRD) spectrum shows, for all the samples, a broad and low peak at $\sim$ 44.5°that corresponds to (0002) hcp-Co, indicating that the films consist of small grains of hcp-Co with preferential orientation of the c-axis out of plane [187]. We cannot confirm whether other orientations are also present out of plane, as the corresponding peak might be unresolvable. All longitudinal and transverse magnetotransport measurements were carried out using a "dc reversal" technique, see Section 3.3.1, in a liquid-He cryostat, applying an external magnetic field, $\vec{H}$, and varying temperature, T.

8.2 Anomalous Hall effect in Co and Co/Bi_2O_3

There is an overlap between the longitudinal resistivity of the Co(t) reference layer and the one of Co(t)/Bi_2O_3 bilayer, ρ_{Co}, as a function of temperature, see Fig. 8.1(a) for 10-nm-thick Co, which has been measured using four-point configuration shown in the inset. This result is expected as Bi_2O_3 is an insulator. The transverse resistance, $R_{xy} = V_{xy}/I_c$, is measured in the Co(t) reference and Co(t)/Bi_2O_3 bilayer as a function of the external out-of-plane magnetic field, H_z, at different temperatures using the configuration shown in the inset of Fig. 8.1(b). Figure 8.1(b) shows the case for a Co thickness of 10 nm at 10 K. At $|H_z| \gtrsim 2{\times}10^4$ Oe, where the magnetization of Co is saturated out of plane, there is a linear dependence of R_{xy} with H_z in both systems, due to the ordinary Hall effect occurring in Co. Namely, the slopes are the same for Co(10) and Co(10)/Bi_2O_3, indicating that the current is flowing through Co in both systems and the density

of charge carriers does not change from the reference to the bilayer. At $|H_z| \lesssim 2\times10^4$ Oe, we evidence the magnetization rotation. Importantly, there is a jump of the transverse resistance from positive values to negative values, which is associated to the AHE. We quantified the AHE signal, ΔR_{AHE}, following the procedure described in Section 2.2.1. ΔR_{AHE} varies significantly from the Co reference sample to the sample with the Bi_2O_3 capping. For the case shown in Fig. 8.1(b), a remarkable 37% difference is observed. The large variation in the AHE cannot be attributed to a change in ρ_{Co}, which is very close for the two samples (see Fig. 8.1(a)), and, hence, the effect is arising from the presence of the Bi_2O_3 capping. This clearly indicates that, in Co(10)/Bi_2O_3, in addition to the regular AHE occurring in the bulk of Co, there is an extra contribution to the AHE.

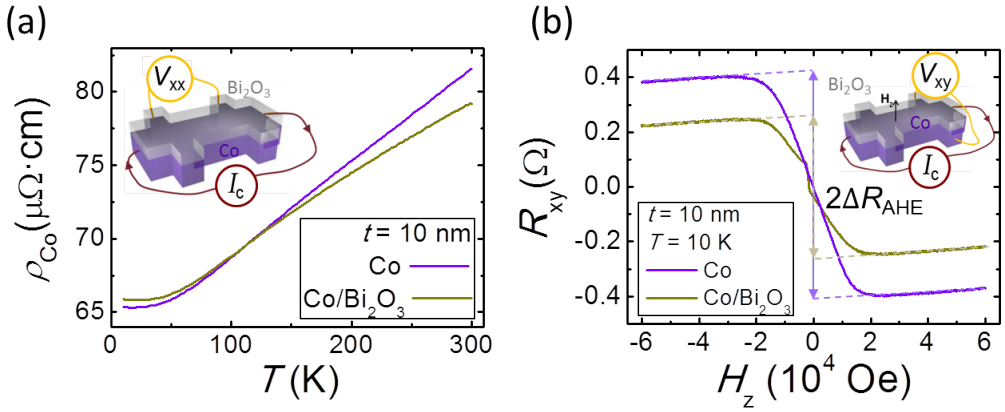

Figure 8.1: **Longitudinal resistivity and transverse resistance measurement in Co(10) and Co(10)/Bi_2O_3 bilayers.** (a) Temperature dependence of the longitudinal resistivity of Co(10) (purple line) and Co(10)/Bi_2O_3 (golden line). Inset: Measurement configuration of the longitudinal resistivity. (b) Transverse resistance measurement as a function of external out-of-plane magnetic field in Co(10) (purple line) and Co(10)/Bi_2O_3 (golden line) at 10 K. The curves have been shifted for clarity. The AHE signal ($2\Delta R_{\mathrm{AHE}}$) is tagged. Inset: Measurement configuration of the transverse resistance applying out-of-plane magnetic field. The applied current, I_c, is 1 μA in (a) and 10 μA in (b).

The transverse measurement is repeated at different temperatures in the range of 10-300 K, and each measurement is related to the corresponding ρ_{Co} using the results of Fig. 8.1(a). Anomalous Hall resistivity, $\rho_{\mathrm{AH}} \equiv \rho_{\mathrm{xy,AH}}$, is extracted for both systems using Eq. 2.27 and introducing the measured ΔR_{AHE} value. Repeating this procedure for all the studied temperatures, we can plot the obtained ρ_{AH} *vs.* ρ^2_{Co} as shown in Fig. 8.2. By following the phenomenological relation for the AHE proposed by Tian *et al.* [67] that considers both the extrinsic (skew scattering and side jump) and intrinsic contributions to the AHE of Co, see Section 1.2.1, we can write ρ_{AH} as:

$$-\rho_{\mathrm{AH}} = \sigma^{\mathrm{int}}_{\mathrm{AH}}\rho^2_{\mathrm{Co}} + \alpha^{\mathrm{ss}}_{\mathrm{AH}}\rho_{\mathrm{Co},0} + \sigma^{\mathrm{sj}}_{\mathrm{AH}}\rho^2_{\mathrm{Co},0}, \tag{8.1}$$

where σ_{AH}^{int} is the intrinsic anomalous Hall conductivity, α_{AH}^{ss} is the skew-scattering angle, σ_{AH}^{sj} is the anomalous Hall conductivity that corresponds to side-jump contribution and $\rho_{Co,0}$ is the residual resistivity of Co. The last two terms represent the extrinsic contribution:

$$-\rho_{AH}^{ext} = \alpha_{AH}^{ss}\rho_{Co,0} + \sigma_{AH}^{sj}\rho_{Co,0}^{2}. \tag{8.2}$$

Figure 8.2 shows $-\rho_{AH}$ as a function of $\rho_{Co,0}^2$ for the Co(10) reference sample and the Co(10)/Bi_2O_3 bilayer, where the experimental data have been fitted to Eq. 8.1, see the purple and gold solid lines. We clearly observe that the slopes of both curves are the same, $93.6 \pm 0.6\ \Omega^{-1}\text{cm}^{-1}$ and $94 \pm 1\ \Omega^{-1}\text{cm}^{-1}$, respectively, indicating that σ_{AH}^{int} is not affected by the Bi_2O_3 capping layer on top. However, we obtain a very different extrinsic contribution for each system. $-\rho_{AH}^{ext}$ in Co(10)/Bi_2O_3 ($-0.224 \pm 0.008\ \mu\Omega\text{cm}$) is almost four times larger than in Co(10)($-0.06 \pm 0.002\ \mu\Omega\text{cm}$), suggesting that the Co/Bi_2O_3 interface acts as an extra scattering source.

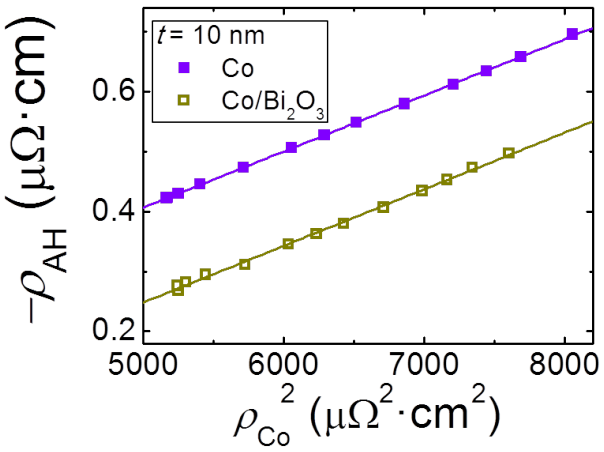

Figure 8.2: **Anomalous Hall resistivity in Co(10) and Co(10)/Bi_2O_3 bilayers.** Anomalous Hall resistivity as a function of the square of the longitudinal resistivity of Co (solid purple squares) and Co/Bi_2O_3 (open golden squares). Purple solid line (golden solid line) is the fitting of Co (Co/Bi_2O_3) data to Eq. 8.1.

In order to confirm the interfacial origin of the effect, we make the same measurements and extract ρ_{AH} in Co(t) reference and Co(t)/Bi_2O_3 bilayer samples with different Co thicknesses, t = 10, 13, 16, 23, 39, 74, 157 nm. ρ_{Co} for the Co(t) reference and Co(t)/Bi_2O_3 bilayer with the same t is the same, as shown in Fig. 8.3(a) at 10 K. We observe that $\rho_{Co,0}$ shows a t^{-1} dependence, following the Mayadas and Shatzkes model [188].

Figure 8.3(b) shows $-\rho_{AH}$ for all the samples with different Co thicknesses, with and without the Bi_2O_3 capping layer. Interestingly, the thinnest Co samples show a larger difference between the AHE signals with and without the Bi_2O_3

capping, further suggesting that the additional effect has an interfacial origin. We extract the weight of each mechanism by fitting each individual sample to Eq. 8.1 and extracting σ_{AH}^{int} and ρ_{AH}^{ext}, as we did previously with $t = 10$ nm in Fig. 8.2.

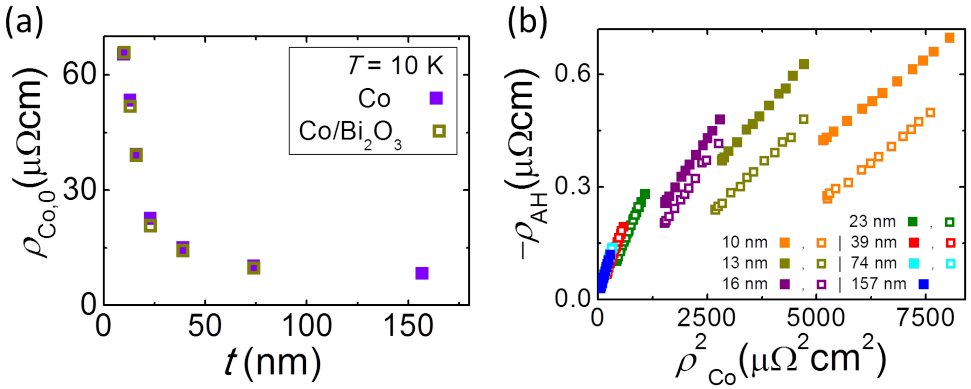

Figure 8.3: **Co thickness dependence of the residual resistivity and anomalous Hall resistivity.** (a) Residual resistivity of Co as a function of the thickness for the Co reference (solid purple squares) and the Co/Bi_2O_3 bilayers (open golden squares) at 10 K. (b) Anomalous Hall resistivity as a function of the square of the longitudinal resistivity of Co (solid squares) and Co/Bi_2O_3 (open squares) for different Co thicknesses. The applied currents range from 1 to 10 μA in (a) and from 10 to 100 μA in the measurements that gave the results shown in (b).

Figure 8.4(a) shows σ_{AH}^{int} obtained from the individual fitting for each sample, as a function of its $\rho_{Co,0}$. There is almost no difference between σ_{AH}^{int} obtained for $Co(t)/Bi_2O_3$ and $Co(t)$ samples, which is consistent with the result in Fig. 8.2. Therefore, we confirm that σ_{AH}^{int} in Co is independent of the presence of Bi_2O_3 capping layer on top. Taking into account that σ_{AH}^{int} is a property of the band structure of the material, this result indicates that the Bi_2O_3 capping layer is not modifying the band structure of Co.

Interestingly, the same results show that σ_{AH}^{int} is modified by $\rho_{Co,0}$, a feature in principle not expected. For instance, a constant σ_{AH}^{int} value of 205 $\Omega^{-1}cm^{-1}$ for hcp-Co is reported for a $\rho_{Co,0}$ range of 16-42 μΩcm [173], while the σ_{AH}^{int} value we obtain for that resistivity range (15-39 μΩcm) decays from 318 to 176 $\Omega^{-1}cm^{-1}$. However, our data is in good agreement with the tight-binding calculations performed by Naito *et al.* [176], which show a decay in σ_{AH}^{int} as the impurity concentration increases, even before entering the dirty limit. They report a value of 341 $\Omega^{-1}cm^{-1}$ for Co with a $\rho_{Co,0}$ of 5 μΩcm, which decreases to 148 $\Omega^{-1}cm^{-1}$ before entering the dirty limit [176]. In our case, we obtain 402 ± 4 $\Omega^{-1}cm^{-1}$ for 8.2 μΩcm, which decays to 113.0 ± 0.4 $\Omega^{-1}cm^{-1}$ when $\rho_{Co,0}$ increases to 65.3 μΩcm. This agreement suggests that we are experimentally observing the predicted decay of σ_{AH}^{int} as $\rho_{Co,0}$ increases in the intermediate (moderately dirty) regime of Co. An alternative explanation could be that the texture of the hcp

Co varies with the thickness of Co, going from a *c*-axis orientation of the grains to an *ab*-plane orientation. As reported by Roman *et al.*, $\sigma_{\mathrm{AH}}^{\mathrm{int}}$ for hcp Co in *c*-axis is 481 $\Omega^{-1}\mathrm{cm}^{-1}$ and in *ab*-plane is 116 $\Omega^{-1}\mathrm{cm}^{-1}$ [189], values that would be in agreement with our results. However, we cannot resolve any variation in the texture of our polycrystalline Co films from the GI-XRD measurements. Note that in the previous chapter we obtained $\beta_{\mathrm{AH}}^{1} = 340 \pm 30\ \Omega^{-1}\mathrm{cm}^{-1}$ (parameter where the intrinsic mechanism is most strongly reflected) for Co with $\rho_{\mathrm{Co},0} = 23$ μΩcm, and this value is quite close to what we expect for this $\rho_{\mathrm{Co},0}$ considering the curve in Fig. 8.4(a).

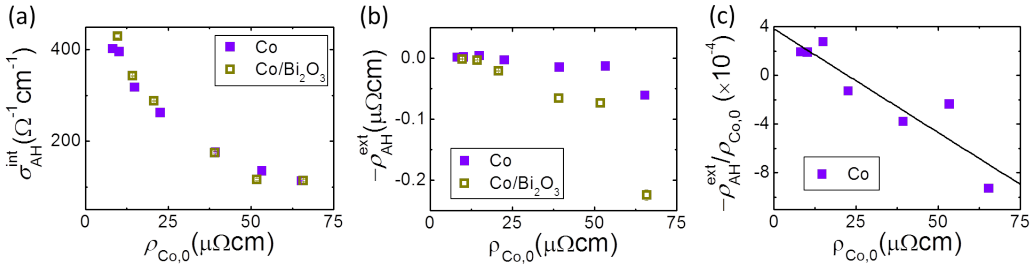

Figure 8.4: **Intrinsic and extrinsic mechanism terms of the AHE in Co and Co/Bi_2O_3.** (a) Residual resistivity dependence of the intrinsic anomalous Hall conductivity of Co for the Co reference layers (solid purple squares) and the Co/Bi_2O_3 bilayers (open golden squares). (b) Residual resistivity dependence of the anomalous Hall resistivity corresponding to the extrinsic contribution for the Co reference layers (solid purple squares) and the Co/Bi_2O_3 bilayers (open golden squares). (c) Ratio of the anomalous Hall resistivity corresponding to the extrinsic contribution and the residual resistivity of Co *vs.* the residual resistivity of Co in the reference Co(t) samples. Black solid line is the fit of the data following Eq. 8.2.

We now turn to the extrinsic contribution $\rho_{\mathrm{AH}}^{\mathrm{ext}}$, obtained from the individual fitting for each sample. $\rho_{\mathrm{AH}}^{\mathrm{ext}}$ differs significantly from the reference sample to the bilayer system in the thinnest (most resistive) Co samples, as shown in Fig. 8.4(b). We first analyze $\rho_{\mathrm{AH}}^{\mathrm{ext}}$ in the reference samples, which corresponds to the bulk of Co, in order to disentangle the skew scattering from the side-jump contribution. By plotting $\rho_{\mathrm{AH}}^{\mathrm{ext}}/\rho_{\mathrm{Co},0}$ as a function of $\rho_{\mathrm{Co},0}$, we can linearly fit the data following Eq. 8.2 in order to extract $\sigma_{\mathrm{AH}}^{\mathrm{sj}}$ from the slope and $\alpha_{\mathrm{AH}}^{\mathrm{ss}}$ from the intercept, see Fig. 8.4(c). We obtain: $\sigma_{\mathrm{AH}}^{\mathrm{sj}} = -17 \pm 3\ \Omega^{-1}\mathrm{cm}^{-1}$ and $\alpha_{\mathrm{AH}}^{\mathrm{ss}} = 0.04 \pm 0.01$ % for the Co reference samples.

The extrinsic contribution of the bulk of the Co layer should also be present in the bilayer system. Therefore, in order to isolate the additional extrinsic contribution that is present only in the bilayer system due to the interface, we subtract $\rho_{\mathrm{AH}}^{\mathrm{ext}}$ of the corresponding Co reference layer from $\rho_{\mathrm{AH}}^{\mathrm{ext}}$ of each bilayer, obtaining $\rho_{\mathrm{AH}}^{\mathrm{interface}}$. $\rho_{\mathrm{AH}}^{\mathrm{interface}}$ increases when the thickness of the Co layer decreases, as shown in Fig. 8.5(a), which confirms the interfacial origin of the effect. This interfacial extrinsic effect could modify either the skew scattering or the side

jump. In order to resolve this question, we plot the characteristic coefficients of each mechanism, $\rho_{AH}^{interface}/\rho_{Co,0}$ and $\rho_{AH}^{interface}/\rho_{Co,0}^2$ for skew scattering and side jump, respectively, as a function of t, see Figs. 8.5(b) and 8.5(c). Being the effect originated at the interface and the system diffusive, a t^{-1} dependence is expected for the coefficient that is influenced by the interface. Indeed, Fig. 8.5(b) shows that the ratio between $\rho_{AH}^{interface}$ and $\rho_{Co,0}$ follows a t^{-1} dependence, indicating that the interfacial contribution can be written as $\rho_{AH}^{interface}=\alpha_{AH}^{ss,interface}\cdot\rho_{Co,0}$ where $\alpha_{AH}^{ss,interface}$ shows a t^{-1} dependence. In contrast, the ratio between $\rho_{AH}^{interface}$ and $\rho_{Co,0}^2$ does not show any clear dependence with t (see Fig. 8.5(c)).

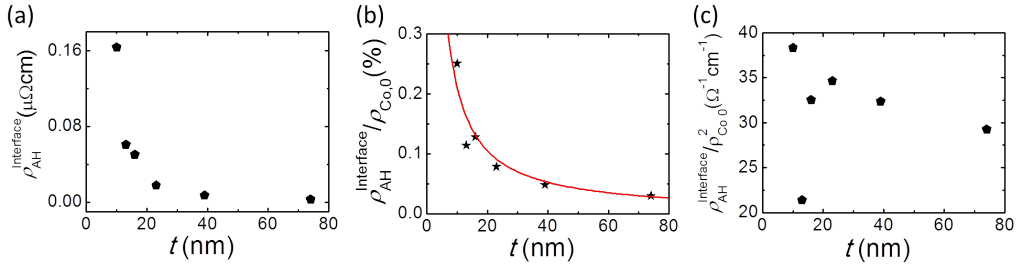

Figure 8.5: **Interfacial contribution that is only present in the Co/Bi_2O_3 bilayers.** (a) Thickness dependence of the interfacial anomalous Hall resistivity. (b) Thickness dependence of the ratio of the interfacial anomalous Hall resistivity and the residual resistivity of Co. Red solid line is a fit to t^{-1}. (c) Thickness dependence of the ratio of the interfacial anomalous Hall resistivity and the square of the residual resistivity of Co.

Therefore, we determine that the interface modification, by adding a Bi_2O_3 layer on top of Co, results on an interfacial skew-scattering contribution of the AHE in Co. Xu *et al.* reported an interfacial skew scattering in epitaxially grown Ni/Cu metallic bilayers, where $\alpha_{AH}^{ss,interface}$ is constant and does not depend on the thickness of Ni [184]. In contrast to our case, transport in their system is not in the diffusive regime along the thickness because their samples were grown epitaxially and the mean free path is longer than the thickness. A recently reported interface-induced anomalous Hall conductivity [190] is unlikely to be present in our system, given that our samples are polycrystalline.

8.3 Conclusions

We evidence a variation of up to 37% in the AHE of Co originated by interface modification. The addition of an insulating Bi_2O_3 layer on top of Co gives rise to interfacial skew scattering, where the skew-scattering angle follows a t^{-1} dependence, characteristic of an interfacial effect. We also observe that σ_{AH}^{int} of Co is insensitive to the presence of the Bi_2O_3 capping layer, demonstrating that no Rashba contribution modifies the intrinsic contribution. σ_{AH}^{int} decreases when

we increase $\rho_{\mathrm{Co},0}$, evidencing the influence of the impurities of the bulk of Co on the intrinsic mechanism when the system enters the dirty limit.

Chapter 9

Final conclusions and outlook

This thesis presents a comprehensive research work on the conversions between charge currents and spin currents that occur in different systems with spin-orbit coupling (SOC). Starting from unspoiled Si/SiO_2 substrates, spintronic devices, lateral spin valves (LSVs) and Hall bars (HBs), are fabricated by lithography and metal deposition processes, and electrical measurements are performed varying external magnetic fields and temperatures to experimentally study the spin Hall effect (SHE) and anomalous Hall effect (AHE) in metals with SOC. The main objective has been to unveil the mechanisms that give rise to these phenomena, with the final goal of showing the path to enhance the spin-to-charge current conversion (SCC) efficiency for plausible spin-orbit-based technological applications.

In the first part, we analyze the SHE in Pt and Ta, two heavy metals with strong SOC, using the spin absorption technique. Firstly, metallic Py ($Ni_{81}Fe_{19}$) /Cu LSVs with middle nanowires made of Pt or Ta are fabricated to measure, in the very same device, the spin diffusion length and the inverse spin Hall effect (ISHE) of the heavy metal. We highlight the relevance of the accurate quantification of the spin diffusion length in order to extract precise spin Hall parameters. Secondly, a graphene-based LSV is employed to study SCC signals in a Pt/graphene heterostructure.

- In Chapter 4, we are able to show a general scaling of the SHE in Pt. We evidence the crossover from the moderately dirty regime, where the intrinsic mechanism dominates the SHE, to the superclean metal regime, dominated by the skew scattering. Analogous crossover was reported in the AHE of different ferromagnetic (FM) materials, but it was never observed experimentally in a spin Hall system before. We are able to extract a constant intrinsic spin Hall conductivity of Pt, $\sigma_{SH}^{int} = 1600 \pm 150(\hbar/e)$

$\Omega^{-1}\text{cm}^{-1}$, for all the studied resistivity range ($\sim 7-70$ $\mu\Omega$cm), which is in good agreement with theoretical reports.

- In Chapter 5, we determine the intrinsic mechanism as the leading contribution of the SHE in β-Ta. We extract $\sigma_{\text{SH}}^{\text{int}} = -820 \pm 120(\hbar/e)$ $\Omega^{-1}\text{cm}^{-1}$ for Ta, which is constant in a broad range of resistivities ($\sim 300-648$ $\mu\Omega$cm).

- In both heavy metals, in the predominance of the intrinsic mechanism, we show that the efficiency of the SCC (given by the spin Hall angle, θ_{SH}), enhances linearly with the resistivity of the metal, ρ_{xx}: $\theta_{\text{SH}} = \sigma_{\text{SH}}^{\text{int}}\rho_{\text{xx}}$. The variation of ρ_{xx} among different groups is one of the reasons for the spread of θ_{SH} values in literature. The output signal, being proportional to θ_{SH}, is then expected to increase linearly with ρ_{xx}. However, we evidence that the shunting effect, originated from the smaller resistivity of the Cu spin channel in comparison to the heavy metal, prevents this enhancement of the output voltage.

- In Chapter 6, with the aim of overcoming the shunting effect, we replace the Cu spin channel by a graphene spin channel with larger resistance. We observe that, at room temperature, the SCC output signal in the Pt/graphene heterostructure increases almost two orders of magnitude as compared to the metallic counterparts. This result is a consequence of the temperature-independent long spin diffusion length of graphene, the enhancement of ρ_{xx} and θ_{SH} of Pt with temperature and the negligible shunting effect of the Pt/graphene system.

In these three chapters, we unravel the leading mechanisms of the SHE in Pt and Ta and show a clear path the enhance the SCC output signals. The knowledge extracted from this part can be applied in the spin-orbit-based devices that employ the SCCs for reading or writing operations of magnetic memories. For instance, for the writing task in the spin-orbit torque-based memory devices or for reading operations in the recently proposed magneto-electric spin-orbit (MESO) logic device by Manipatruni *et al.* from Intel Corporation [24]. Here, efficient SCCs are required for the reading of magnetic elements that will lead to logic operations.

In a next stage, LSVs could be substituted by local devices that consist of a FM nanowire which is in contact with a T-shaped heavy metal where the two perpendicular wires of the T merge. Transverse measurements can be carried out by injecting a spin-polarized current directly from the FM nanowire into the long wire of the heavy metal, where ISHE will occur, and measuring the resulting voltage drop in the other two contacts of the heavy metal. The measured ISHE

signal can be up to three orders of magnitude larger than the one measured in a LSV, since the injected spin current does not exponentially decay as it occurs in the Cu channel of the LSV, as recently shown in a collaboration between our group and Intel Corporation [191]. Therefore, the local device is a simpler platform from the fabrication point of view and very appealing to further study and implement SCCs. Moreover, the design of this device is inspired by the one proposed by Manipatruni *et al.* for the MESO logic device, thus it has the potential to be part of the building block that leads spin-orbit logic devices to the market!

In the second part, we study the SHE and anomalous Hall effect (AHE) in 3*d* FM metals using the spin absorption technique and Hall bars, respectively. Firstly, we focus on understanding the relation between the SHE and AHE in Fe, Co, Py and Ni, and secondly, we analyze the effect of a Bi_2O_3 capping layer in the AHE of Co.

- In Chapter 7, we evidence that the SHE and AHE in 3*d* FM metals are not related by the current spin polarization, and, therefore, this simple relation that sometimes is assumed is not generally fulfilled. We observe that only in Py, a typical FM alloy, the skew-scattering contribution of the AHE is related to that of the SHE via current spin polarization of Py. The temperature dependence of the spin Hall resistivity above $\sim$ 150 K is strong in all the ferromagnets and it includes a sign change in most of the cases. This common feature of the SHE for all the 3*d* FM metals is dramatically different from the temperature dependence obtained for both the anomalous Hall resistivity of any of the 3*d* FM metals and the spin Hall resistivity of Pt or Ta. The obtained intrinsic anomalous Hall conductivity, $\sigma_{\mathrm{AH}}^{\mathrm{int}}$, values for all the 3*d* ferromagnets are in good agreement with the results found in literature. However, $\sigma_{\mathrm{SH}}^{\mathrm{int}}$ values are unexpectedly large. The results lead us to suggest that an additional mechanism is present only in the SHE of 3*d* ferromagnets, and not in the AHE or the SHE of a non-magnetic material, which would be the responsible of the observed strong temperature dependence. A possible scenario is the asymmetric spin-dependent scattering in the spin-flip processes induced by the electron-magnon interactions.

- In Chapter 8, we observe an up to 37% variation in the AHE of Co when an insulating Bi_2O_3 capping layer is added to this ferromagnet. This interface modification, which leaves unaltered both the longitudinal resistivity and $\sigma_{\mathrm{AH}}^{\mathrm{int}}$ of Co, gives rise to an interfacial skew scattering.

In these two chapters, we study in depth the different mechanisms that contribute to the AHE and SHE in the 3*d* FM metals. As a future task, it remains to experimentally confirm the origin of the extra effect present in the SHE

of ferromagnets and find the complete expression or picture that links both phenomena.

It would be appealing to study the SHE and AHE in Gd, a $4f$ FM element, with the Curie temperature of $\sim$290 K. While below this temperature both phenomena should be non-zero, above this temperature the AHE should go to zero and it would be interesting to study what is obtained in the SHE. Such a system could help to further understand the link between the two phenomena. In addition, the demonstration of the tuning of the AHE by interface modification offers many possibilities to explore. Searching new combination of FM/insulator or FM/heavy metal bilayers with the potential to enhance the anomalous Hall angles will be possible, without altering the electronic properties of the FM material. The obtained results could also be useful to implement in the SHE.

Bibliography

[1] S. Blundell, *Magnetism in Condensed Matter* (Oxford University Press, 2001).

[2] S. Manipatruni, D. E. Nikonov, and I. A. Young, *Nature Physics* **14**, 338 (2018).

[3] H. Dery *et al.*, *Nature* **447**, 573 (2007).

[4] B. Behin-Aein, D. Datta, S. Salahuddin, and S. Datta, *Nature Nanotechnology* **5**, 266 (2010).

[5] M. Johnson and R. H. Silsbee, *Physical Review Letters* **55**, 1790 (1985).

[6] M. N. Baibich *et al.*, *Physical Review Letters* **61**, 2472 (1988).

[7] G. Binasch, P. Grünberg, F. Saurenbach, and W. Zinn, *Physical Review B* **39**, 4828 (1989).

[8] Y. Xu, D. D. Awschalom, and J. Nitta, *Handbook of Spintronics* (Springer, 2016).

[9] H. Ohno, M. Stiles and B. Dieny , https://electroiq.com/2017/09/advancements-in-spintronics/ .

[10] M. Julliere, *Physics Letters A* **54**, 225 (1975).

[11] D. Wang, C. Nordman, J. M. Daughton, Z. Qian, and J. Fink, *IEEE Transactions on Magnetics* **40**, 2269 (2004).

[12] S. Ikeda *et al.*, *Applied Physics Letters* **93**, 082508 (2008).

[13] S. Bhatti *et al.*, *Materials Today* **20**, 530 (2017).

[14] J. C. Slonczewski, *Journal of Magnetism and Magnetic Materials* **159**, L1 (1996).

[15] L. Berger, *Physical Review B* **54**, 9353 (1996).

[16] STT-MRAM: Introduction and market status, https://www.mram-info.com/stt-mram.

[17] Y. Zhang *et al.*, *Journal of Applied Physics* **101**, 103905 (2007).

[18] I. M. Miron *et al.*, *Nature* **476**, 189 (2011).

[19] Y. Ohsawa *et al.*, *IEEE Journal of the Electron Devices Society* **6**, 1233 (2018).

[20] B. Dieny *et al.*, *Handbook of Magnetic Materials* **19**, 107 (2011).

[21] V. Sverdlov, J. Weinbub, and S. Selberherr, *Informacije MIDEM* **47**, 195 (2015).

[22] S. Datta and B. Das, *Applied Physics Letters* **56**, 665 (1990).

[23] W. Yan *et al.*, *Nature Communications* **7**, 13372 (2016).

[24] S. Manipatruni *et al.*, *Nature* **565**, 35 (2019).

[25] R. M. Bozorth, *Ferromagnetism* (IEEE Press, Wiley, 1968).

[26] N. F. Mott, *Proceedings of the Royal Society of London A* **153**, 699 (1936).

[27] J. Gregg, I. Petej, E. Jouguelet, and C. Dennis, *Journal of Physics D: Applied Physics* **35**, R121 (2002).

[28] E. Villamor, M. Isasa, L. E. Hueso, and F. Casanova, *Physical Review B* **87**, 094417 (2013).

[29] F. J. Jedema, M. S. Nijboer, A. T. Filip, and B. J. van Wees, *Physical Review B* **67**, 085319 (2003).

[30] G. Mihajlović, J. Pearson, S. Bader, and A. Hoffmann, *Physical Review Letters* **104**, 237202 (2010).

[31] M. Isasa *et al.*, *Journal of Physics D: Applied Physics* **48**, 215003 (2015).

[32] H. Idzuchi, Y. Fukuma, L. Wang, and Y. Otani, *Applied Physics Letters* **101**, 022415 (2012).

[33] J. Ryu, M. Kohda, and J. Nitta, *Physical Review Letters* **116**, 256802 (2016).

[34] H. Gamou, J. Ryu, M. Kohda, and J. Nitta, *Applied Physics Express* **10**, 023003 (2017).

[35] M. D'yakonov and V. Y. Kachorovskii, *Sov. Phys. Semicond.* **20**, 110 (1986).

[36] J. Kikkawa and D. Awschalom, *Physical Review Letters* **80**, 4313 (1998).

[37] J. Bass and W. P. Pratt Jr, *Journal of Physics: Condensed Matter* **19**, 183201 (2007).

[38] H. Idzuchi, Y. Fukuma, and Y. Otani, *Physica E* **68**, 239 (2015).

[39] K. Ando, *Semiconductor Science and Technology* **29**, 043002 (2014).

[40] A. Slachter, F. L. Bakker, J.-P. Adam, and B. J. van Wees, *Nature Physics* **6**, 879 (2010).

[41] T. Kimura, Y. Otani, T. Sato, S. Takahashi, and S. Maekawa, *Physical Review Letters* **98**, 156601 (2007).

[42] H. Isshiki, P. Muduli, J. Kim, K. Kondou, and Y. Otani, *arXiv preprint arXiv:1901.03095* (2019).

[43] K. Ando *et al.*, *Physical Review Letters* **101**, 036601 (2008).

[44] J. Flipse, F. Bakker, A. Slachter, F. Dejene, and B. J. van Wees, *Nature Nanotechnology* **7**, 166 (2012).

[45] M. Isasa *et al.*, *Physical Review B* **93**, 014420 (2016).

[46] E. Saitoh, M. Ueda, H. Miyajima, and G. Tatara, *Applied Physics Letters* **88**, 182509 (2006).

[47] K. Uchida *et al.*, *Solid State Communications* **150**, 524 (2010).

[48] K. Uchida *et al.*, *Nature Materials* **9**, 894 (2010).

[49] J. Sinova, S. O. Valenzuela, J. Wunderlich, C. Back, and T. Jungwirth, *Reviews of Modern Physics* **87**, 1213 (2015).

[50] A. Hoffmann, *IEEE Transactions on Magnetics* **49**, 5172 (2013).

[51] V. M. Edelstein, *Solid State Communications* **73**, 233 (1990).

[52] L. Liu, T. Moriyama, D. Ralph, and R. Buhrman, *Physical Review Letters* **106**, 036601 (2011).

[53] U. H. Pi *et al.*, *Applied Physics Letters* **97**, 162507 (2010).

[54] J. Flipse *et al.*, *Physical Review Letters* **113**, 027601 (2014).

[55] J. C. Rojas-Sánchez *et al.*, *Nature Communications* **4**, 2944 (2013).

[56] S. Maekawa, S. O. Valenzuela, T. Kimura, and E. Saitoh, *Spin Current* (Oxford University Press, 2007).

[57] A. Soumyanarayanan, N. Reyren, A. Fert, and C. Panagopoulos, *Nature* **539**, 509 (2016).

[58] A. Manchon, H. C. Koo, J. Nitta, S. Frolov, and R. Duine, *Nature Materials* **14**, 871 (2015).

[59] E. H. Hall, *American Journal of Mathematics* **2**, 287 (1879).

[60] E. H. Hall, *The London, Edinburgh, and Dublin Philosophical Magazine and Journal of Science* **12**, 157 (1881).

[61] A. W. Smith and R. Sears, *Physical Review* **34**, 1466 (1929).

[62] N. Nagaosa, J. Sinova, S. Onoda, A. MacDonald, and N. Ong, *Reviews of Modern Physics* **82**, 1539 (2010).

[63] R. Karplus and J. Luttinger, *Physical Review* **95**, 1154 (1954).

[64] T. Jungwirth, Q. Niu, and A. MacDonald, *Physical Review Letters* **88**, 207208 (2002).

[65] J. Smit, *Physica* **24**, 39 (1958).

[66] L. Berger, *Physical Review B* **2**, 4559 (1970).

[67] Y. Tian, L. Ye, and X. Jin, *Physical Review Letters* **103**, 087206 (2009).

[68] S. Sangiao *et al.*, *Physical Review B* **79**, 014431 (2009).

[69] S. Onoda, N. Sugimoto, and N. Nagaosa, *Physical Review B* **77**, 165103 (2008).

[70] T. Miyasato *et al.*, *Physical Review Letters* **99**, 086602 (2007).

[71] D. Hou *et al.*, *Physical Review Letters* **114**, 217203 (2015).

[72] M. D'yakonov and V. Perel, *Soviet Journal of Experimental and Theoretical Physics Letters* **13**, 467 (1971).

[73] J. Hirsch, *Physical Review Letters* **83**, 1834 (1999).

[74] M. Morota *et al.*, *Physical Review B* **83**, 174405 (2011).

[75] C. Stamm *et al.*, *Physical Review Letters* **119**, 087203 (2017).

[76] B. Zimmermann *et al.*, *Physical Review B* **90**, 220403 (2014).

[77] M. Isasa, E. Villamor, L. E. Hueso, M. Gradhand, and F. Casanova, *Physical Review B* **91**, 024402 (2015).

[78] T. Tanaka *et al.*, *Physical Review B* **77**, 165117 (2008).

[79] M. Gradhand *et al.*, *SPIN* **2**, 1250010 (2012).

[80] Y. Niimi *et al.*, *Physical Review Letters* **109**, 156602 (2012).

[81] Y. Niimi *et al.*, *Physical Review Letters* **106**, 126601 (2011).

[82] G. Allen, S. Manipatruni, D. E. Nikonov, M. Doczy, and I. A. Young, *Physical Review B* **91**, 144412 (2015).

[83] L. Liu *et al.*, *Science* **336**, 555 (2012).

[84] J. Gómez *et al.*, *Physical Review B* **90**, 184401 (2014).

[85] D. Qu, S. Huang, G. Guo, and C. Chien, *Physical Review B* **97**, 024402 (2018).

[86] C. Hahn *et al.*, *Physical Review B* **87**, 174417 (2013).

[87] A. Kumar, R. Bansal, S. Chaudhary, and P. K. Muduli, *Physical Review B* **98**, 104403 (2018).

[88] R. Yu *et al.*, *Physical Review Materials* **2**, 074406 (2018).

[89] C.-F. Pai *et al.*, *Applied Physics Letters* **101**, 122404 (2012).

[90] L. Vila, T. Kimura, and Y. Otani, *Physical Review Letters* **99**, 226604 (2007).

[91] J.-C. Rojas-Sánchez *et al.*, *Physical Review Letters* **112**, 106602 (2014).

[92] M.-H. Nguyen, D. Ralph, and R. Buhrman, *Physical Review Letters* **116**, 126601 (2016).

[93] Y. Niimi *et al.*, *Physical Review B* **89**, 054401 (2014).

[94] R. Ramaswamy *et al.*, *Physical Review Applied* **8**, 024034 (2017).

[95] P. Laczkowski *et al.*, *Physical Review B* **96**, 140405 (2017).

[96] M. Obstbaum *et al.*, *Physical Review Letters* **117**, 167204 (2016).

[97] Y. K. Kato, R. C. Myers, A. C. Gossard, and D. D. Awschalom, *Science* **306**, 1910 (2004).

[98] S. O. Valenzuela and M. Tinkham, *Nature* **442**, 176 (2006).

[99] K. Garello *et al.*, *Nature Nanotechnology* **8**, 587 (2013).

[100] S. O. Valenzuela, *International Journal of Modern Physics B* **23**, 2413 (2009).

[101] Y. Niimi and Y. Otani, *Reports on Progress in Physics* **78**, 124501 (2015).

[102] S. Karube, K. Kondou, and Y. Otani, *Applied Physics Express* **9**, 033001 (2016).

[103] E. Lesne *et al.*, *Nature Materials* **15**, 1261 (2016).

[104] J.-C. Rojas-Sánchez *et al.*, *Physical Review Letters* **116**, 096602 (2016).

[105] K. Kondou *et al.*, *Nature Physics* **12**, 1027 (2016).

[106] F. Jedema, A. Filip, and B. J. van Wees, *Nature* **416**, 810 (2002).

[107] T. Valet and A. Fert, *Physical Review B* **48**, 7099 (1993).

[108] D. Gall, *Journal of Applied Physics* **119**, 085101 (2016).

[109] S. Takahashi and S. Maekawa, *Physical Review B* **67**, 052409 (2003).

[110] P. Laczkowski *et al.*, *Physical Review B* **92**, 214405 (2015).

[111] P. Jacquod, R. S. Whitney, J. Meair, and M. Büttiker, *Physical Review B* **86**, 155118 (2012).

[112] A. Burkov, *Physical Review B* **96**, 041110 (2017).

[113] K. Koshelev *et al.*, *Journal of Vacuum Science & Technology B* **29**, 06F306 (2011).

[114] G. Balonek, University of Rochester, Institute of Optics, http://www2.optics.rochester.edu/workgroups/cml/opt307/spr13/greg/.

[115] M. Swain, *Multilayer film deposition characterization by reflectometry techniques and their structure property correlation* (Homi Bhabha National Institute, 2015), http://hdl.handle.net/10603/79579.

[116] D. L. Smith, *Thin-film deposition: principles and practice* (McGraw-hill New York etc, 1995).

[117] A. Castellanos-Gomez *et al.*, *2D Materials* **1**, 011002 (2014).

[118] L. A. Giannuzzi and F. A. Stevie, *Micron* **30**, 197 (1999).

[119] E. Villamor, M. Isasa, L. E. Hueso, and F. Casanova, *Physical Review B* **88**, 184411 (2013).

[120] H. Y. T. Nguyen, W. P. Pratt Jr, and J. Bass, *Journal of Magnetism and Magnetic Materials* **361**, 30 (2014).

[121] Y. Liu *et al.*, *Physical Review B* **91**, 220405 (2015).

[122] A. Fert and P. M. Levy, *Physical Review Letters* **106**, 157208 (2011).

[123] S. Lowitzer *et al.*, *Physical Review Letters* **106**, 056601 (2011).

[124] L. Wang *et al.*, *Physical Review Letters* **116**, 196602 (2016).

[125] S. Onoda, N. Sugimoto, and N. Nagaosa, *Physical Review Letters* **97**, 126602 (2006).

[126] J. Narayan *et al.*, *Journal of Vacuum Science & Technology A* **24**, 1948 (2006).

[127] S. Lee, M. Doxbeck, J. Mueller, M. Cipollo, and P. Cote, *Surface and Coatings Technology* **177**, 44 (2004).

[128] L. Clevenger, A. Mutscheller, J. Harper, C. Cabral Jr, and K. Barmak, *Journal of Applied Physics* **72**, 4918 (1992).

[129] A. Jiang *et al.*, *Thin Solid Films* **437**, 116 (2003).

[130] J. Qiao, J. Zhou, Z. Yuan, and W. Zhao, *Physical Review B* **98**, 214402 (2018).

[131] L. J. van der Pauw, *Philips Res. Repts.* **13**, 1 (1958).

[132] K. W. Urban *et al.*, *Philosophical Transactions of the Royal Society A* **367**, 3735 (2009).

[133] T. Kimura, J. Hamrle, and Y. Otani, *Physical Review B* **72**, 014461 (2005).

[134] T. Kimura, T. Sato, and Y. Otani, *Physical Review Letters* **100**, 066602 (2008).

[135] X. Sui *et al.*, *Physical Review B* **96**, 241105 (2017).

[136] K. Fujiwara *et al.*, *Nature Communications* **4**, 2893 (2013).

[137] G. Schmidt, D. Ferrand, L. Molenkamp, A. Filip, and B. J. van Wees, *Physical Review B* **62**, R4790 (2000).

[138] E. Rashba, *Physical Review B* **62**, R16267 (2000).

[139] T. Maassen, F. Dejene, M. Guimaraes, C. Józsa, and B. J. van Wees, *Physical Review B* **83**, 115410 (2011).

[140] N. Tombros, C. Jozsa, M. Popinciuc, H. T. Jonkman, and B. J. van Wees, *Nature* **448**, 571 (2007).

[141] T.-Y. Yang *et al.*, *Physical Review Letters* **107**, 047206 (2011).

[142] C. Ertler, S. Konschuh, M. Gmitra, and J. Fabian, *Physical Review B* **80**, 041405 (2009).

[143] Y. Fukuma *et al.*, *Nature Materials* **10**, 527 (2011).

[144] P. Laczkowski *et al.*, *Applied Physics Letters* **104**, 142403 (2014).

[145] R. J. Pedersen and F. L. Vernon Jr, *Applied Physics Letters* **10**, 29 (1967).

[146] J. M. Pomeroy and H. Grube, *Journal of Applied Physics* **105**, 094503 (2009).

[147] M. Drögeler *et al.*, *Nano Letters* **16**, 3533 (2016).

[148] J. Ingla-Aynés, R. J. Meijerink, and B. J. van Wees, *Nano Letters* **16**, 4825 (2016).

[149] W. Savero-Torres *et al.*, *2D Materials* **4**, 041008 (2017).

[150] H. Dery *et al.*, *IEEE Transactions on Electron Devices* **59**, 259 (2012).

[151] H. Idzuchi, A. Fert, and Y. Otani, *Physical Review B* **91**, 241407 (2015).

[152] L. Piraux, S. Dubois, A. Fert, and L. Belliard, *The European Physical Journal B* **4**, 413 (1998).

[153] A. Reilly *et al.*, *IEEE Transactions on Magnetics* **34**, 939 (1998).

[154] B. Miao, S. Huang, D. Qu, and C. Chien, *Physical Review Letters* **111**, 066602 (2013).

[155] A. Tsukahara *et al.*, *Physical Review B* **89**, 235317 (2014).

[156] C. Du, H. Wang, F. Yang, and P. C. Hammel, *Physical Review B* **90**, 140407 (2014).

[157] K. S. Das, W. Y. Schoemaker, B. J. van Wees, and I. Vera-Marun, *Physical Review B* **96**, 220408 (2017).

[158] K. S. Das, J. Liu, B. J. van Wees, and I. J. Vera-Marun, *Nano Letters* **18**, 5633 (2018).

[159] J. D. Gibbons, D. MacNeill, R. A. Buhrman, and D. C. Ralph, *Physical Review Applied* **9**, 064033 (2018).

[160] C. Qin, S. Chen, Y. Cai, F. Kandaz, and Y. Ji, *Physical Review B* **96**, 134418 (2017).

[161] J. Batley *et al.*, *Physical Review B* **92**, 220420 (2015).

[162] T. Kimura, N. Hashimoto, S. Yamada, M. Miyao, and K. Hamaya, *NPG Asia Materials* **4**, e9 (2012).

[163] S. D. Steenwyk, S. Y. Hsu, R. Loloee, J. Bass, and W. P. Pratt Jr, *Journal of Magnetism and Magnetic Materials* **170**, L1 (1997).

[164] S. Dubois *et al.*, *Physical Review B* **60**, 477 (1999).

[165] L. OBrien *et al.*, *Physical Review B* **94**, 094431 (2016).

[166] L. Berger, *Physical Review B* **83**, 054410 (2011).

[167] J. M. Coey, *Magnetism and magnetic materials* (Cambridge University Press, 2010).

[168] Y. Zhang *et al.*, *Journal of Applied Physics* **114**, 163714 (2013).

[169] G.-Y. Guo, S. Murakami, T.-W. Chen, and N. Nagaosa, *Physical Review Letters* **100**, 096401 (2008).

[170] I. I. Mazin, *Physical Review Letters* **83**, 1427 (1999).

[171] B. Nadgorny *et al.*, *Physical Review B* **61**, R3788 (2000).

[172] L. Wu, Y. Li, J. Xu, D. Hou, and X. Jin, *Physical Review B* **87**, 155307 (2013).

[173] J. Kötzler and W. Gil, *Physical Review B* **72**, 060412 (2005).

[174] D. Hou *et al.*, *Journal of Physics: Condensed Matter* **24**, 482001 (2012).

[175] L. Ye, Y. Tian, X. Jin, and D. Xiao, *Physical Review B* **85**, 220403 (2012).

[176] T. Naito, D. Hirashima, and H. Kontani, *Physical Review B* **81**, 195111 (2010).

[177] J. Cramer *et al.*, *Nature Communications* **9**, 1089 (2018).

[178] L. Cornelissen, J. Liu, R. Duine, J. B. Youssef, and B. J. van Wees, *Nature Physics* **11**, 1022 (2015).

[179] Y. Cheng, K. Chen, and S. Zhang, *Physical Review B* **96**, 024449 (2017).

[180] I. Tokatly, E. Krasovskii, and G. Vignale, *Physical Review B* **91**, 035403 (2015).

[181] J. Borge and I. Tokatly, *Physical Review B* **96**, 115445 (2017).

[182] V. P. Amin and M. D. Stiles, *Physical Review B* **94**, 104419 (2016).

[183] S. Li, K. Shen, and K. Xia, *arXiv preprint arXiv:1807.03433* (2018).

[184] J. Xu, Y. Li, D. Hou, L. Ye, and X. Jin, *Applied Physics Letters* **102**, 162401 (2013).

[185] Y. Zhang, N. Sun, W. Che, R. Shan, and Z. Zhu, *AIP Advances* **6**, 025214 (2016).

[186] H. Tsai *et al.*, *Scientific Reports* **8**, 5564 (2018).

[187] L. Fallarino, O. Hovorka, and A. Berger, *Physical Review B* **94**, 064408 (2016).

[188] A. Mayadas and M. Shatzkes, *Physical Review B* **1**, 1382 (1970).

[189] E. Roman, Y. Mokrousov, and I. Souza, *Physical Review Letters* **103**, 097203 (2009).

[190] O. E. Parfenov *et al.*, *ACS Applied Materials & Interfaces* **10**, 35589 (2018).

[191] V. T. Pham *et al.*, (submitted).

List of acronyms and symbols

Acronyms

A	anisole
AHE	anomalous Hall effect
AMR	anisotropic magnetoresistance
CMOS	complementary metal-oxide-semiconductor
DL	double layer
DP	D'yakonov-Perel'
DUT	device under test
e	electron
ED	electron diffraction
EE	Edelstein effect
EY	Elliott-Yafet
FFT	fast Fourier transform
FIB	focused ion beam
FM	ferromagnetic
FMR	ferromagnetic resonance
GI-XRD	grazing incidence X-ray diffraction
GMR	giant magnetoresistance
HB	Hall bar
HR-TEM	high-resolution transmission electron microscopy
IEE	inverse Edelstein effect
ISHE	inverse spin Hall effect
ISO	International Organization for Standardization
LSSE	longitudinal spin Seebeck effect
LSV	lateral spin valve
MESO	magneto-electric spin-orbit
MO	magneto-optical
MOKE	magneto-optical Kerr effect
MRAM	magnetic random access memory
MS	material to study
MTJ	magnetic tunnel junction

NM	non-magnetic
OHE	ordinary Hall effect
PMMA	poly (methyl methacrylate)
PPMS	Physical Property Measurement System
Py	Permalloy
SA	spin absorption
SCC	spin-to-charge current conversion
SEM	scanning electron microscopy
SHE	spin Hall effect
SHM	spin Hall metal
SOC	spin-orbit coupling
SOT	spin-orbit torque
SP	spin pumping
ST-FMR	spin-torque ferromagnetic resonance
STT	spin-transfer torque
TCR	temperature coefficient of resistance
TEM	transmission electron microscopy
TI	topological insulator
TMR	tunnel magnetoresistance
UHV	ultra-high vacuum
UV	ultra-violet
WF	write field
XRD	X-ray diffraction
XRR	X-ray reflectivity
2D	two-dimensional

Symbols *

A	cross-sectional area
α_{FM}	current spin polarization of a FM material
α_{I}	spin polarization of the interface
α_{R}	Rashba coefficient
$\alpha_{\mathrm{AH}}^{\mathrm{ss}}$	skew-scattering angle of the AHE
$\alpha_{\mathrm{SH}}^{\mathrm{ss}}$	skew-scattering angle of the SHE
β_{AH}^{0}, β_{AH}^{1}	conductivity coefficients corresponding to AHE mechanisms
β_{SH}^{0}, β_{SH}^{1}	conductivity coefficients corresponding to SHE mechanisms
d	distance between adjacent atomic planes in a crystal
D	diffusion coefficient
δ	angle of magnetization of the FM electrode with respect to its easy axis
δs	spin density

*Symbols are not listed here if they occur only in the immediate context of a statement.

ΔR_{AHE}	AHE signal
ΔR_{NL}	nonlocal spin signal
$\Delta R_{\mathrm{NL}}^{\mathrm{abs}}$	spin absorption signal
$\Delta R_{\mathrm{NL}}^{\mathrm{ref}}$	reference spin signal
ΔR_{ISHE}	ISHE signal
ΔR_{SHE}	SHE signal
$\Delta\mu$	discontinuity of μ_{ECP} at NM/FM interface
e	electron charge
E_{ex}	exchange energy
E_{F}	Fermi energy
$\vec{E}$	Electric field
G	spin mixing conductance
γ_{AH}^{0}	conductivity coefficient corresponding to AHE mechanisms
γ_{SH}^{0}	conductivity coefficient corresponding to SHE mechanisms
$\hat{H}$	Hamiltonian
$\vec{H}$	external magnetic field
$\hbar$	reduced Planck constant
I, I_{c}	charge current
I_{beam}	current applied to the ion-beam in the ion miller
$I_{\mathrm{e\text{-}beam}}$	e-beam current applied to target in the e-beam evaporator
I_{s}	spin current
$\vec{j_{\mathrm{c}}}$	charge current density
$\vec{j_{\mathrm{s}}}$	spin current density
$\vec{k}$	wavenumber of carriers
l	distance between FM injector and MS in a LSV
L	FM interelectrode distance in a LSV, length of a Hall bar
λ	wavelength of X-rays
λ_{e}	mean free path
λ_{s}	spin diffusion length
$\vec{M}$	magnetization
μ	electrochemical potential
μ_{ch}	chemical potential
μ_{ECP}	average of spin-up and spin-down electron electrochemical potential
μ_{s}	spin accumulation
μ_0	vacuum permeability
n_{c}	carrier density
n_o	number of electrons in the outermost shell (o orbital)
$N(E_{\mathrm{F}})$	density of states at the Fermi energy
$\vec{p}$	momentum operator
P_{base}	base pressure
P_{dep}	deposition pressure
ϕ	angle between the sample plane and ion beam in the ion miller

φ	rotation angle of the spin around a magnetic field
ψ	rotation angle of $\vec{H}$ in plane with respect to y axis
R	resistance
R_{I}	interface resistance
R_{ISHE}	nonlocal resistance originated due to the ISHE
R_{NL}	nonlocal resistance
R_{s}	spin resistance
R_{SHE}	nonlocal resistance originated due to the SHE
R_{xx}	longitudinal resistance
R_{xy}	transverse resistance
$R^{\blacksquare}$	sheet resistance
R_0	Hall coefficient
R_1	anomalous Hall coefficient
ρ, ρ_{xx}	longitudinal resistivity
ρ_{AH}	anomalous Hall resistivity
$\rho_{\mathrm{AH}}^{\mathrm{ext}}$	extrinsic contribution of the anomalous Hall resistivity
$\rho_{\mathrm{AH}}^{\mathrm{interfacial}}$	interfacial contribution of the anomalous Hall resistivity
ρ_{SH}	spin Hall resistivity
$\rho_{\mathrm{xx,0}}$	residual resistivity
$\rho_{\mathrm{xx,T}}$	resistivity induced by phonons
ρ_{xy}	transverse resistivity
$\vec{s}$	spin polarization
σ, σ_{xx}	longitudinal conductivity
σ_{AH}	anomalous Hall conductivity
$\sigma_{\mathrm{AH}}^{\mathrm{int}}$	intrinsic anomalous Hall conductivity
$\sigma_{\mathrm{AH}}^{\mathrm{sj}}$	anomalous Hall conductivity related to side-jump contribution
σ_{SH}	spin Hall conductivity
$\sigma_{\mathrm{SH}}^{\mathrm{int}}$	intrinsic spin Hall conductivity
$\sigma_{\mathrm{SH}}^{\mathrm{sj}}$	spin Hall conductivity related to side-jump contribution
$\sigma_{\mathrm{xx,0}}$	residual conductivity
σ_{xy}	transverse conductivity
$\sigma_{\uparrow,\downarrow}$	conductivity of spin-up, spin-down electron
$\vec{\sigma}$	vector of Pauli matrices
t	thickness
T	temperature
τ	momentum relaxation time
τ_{s}	spin relaxation time
$\mathrm{\tau}$	time
θ	half of the angle between the incident X-rays and diffracted wave
θ_{AH}	anomalous Hall angle
θ_{SH}	spin Hall angle
$\theta_{\mathrm{SH}}^{\mathrm{int}}$	intrinsic contribution of the spin Hall angle

V	electric potential, voltage
V_{acc}	acceleration voltage of the ion-beam in the ion miller
V_{beam}	voltage applied to the ion-beam in the ion miller
$V_{\text{e-beam}}$	voltage applied to the e-beam in the e-beam evaporator
v_{F}	Fermi velocity
V_{I}	voltage associated to the interface resistance
V_{ISHE}	voltage originated due to the ISHE
V_{NL}	nonlocal voltage
V_{s}	voltage originated due to a spin accumulation
V_{SHE}	voltage originated due to the SHE
V_{xx}	voltage measured in a longitudinal configuration
V_{xy}	voltage measured in a transverse configuration
w	width
ω_{L}	Larmor frequency
$x_{\mathrm{MS,NM}}$	shunting factor between MS and NM
Z	atomic number

List of publications

This thesis is based on the following publications:

- *Tuning the spin Hall effect of Pt from the moderately dirty to the superclean regime*
  Edurne Sagasta*, Yasutomo Omori*, Miren Isasa*, Martin Gradhand, Luis E. Hueso, Yasuhiro Niimi, YoshiChika Otani and Fèlix Casanova,
  Phys. Rev. B **94**, 060412(R) (2016).

  (Chapter 4)

- *Unveiling the mechanisms of the spin Hall effect in Ta*
  Edurne Sagasta, Yasutomo Omori, Saül Vélez, Roger Llopis, Christopher Tollan, Andrey Chuvilin, Luis E. Hueso, Martin Gradhand, YoshiChika Otani and Fèlix Casanova,
  Phys. Rev. B **98**, 060410(R) (2018).

  (Chapter 5)

- *Large temperature spin-to-charge conversion signals in a graphene/Pt lateral heterostructure*
  Wenjing Yan*, Edurne Sagasta*, Mario Ribeiro, Yasuhiro Niimi, Luis E. Hueso and Fèlix Casanova,
  Nature Communications **8**, 661 (2017).

  (Chapter 6)

- *Spin diffusion length of Permalloy using spin absorption in lateral spin valves*
  Edurne Sagasta, Yasutomo Omori, Miren Isasa, YoshiChika Otani, Luis E. Hueso and Fèlix Casanova,
  Appl. Phys. Lett. **111**, 082407 (2017).

  (Chapter 7)

- *Relation between the spin Hall effect and the anomalous Hall effect in 3d ferromagnetic metals*

Yasutomo Omori*, Edurne Sagasta*, Yasuhiro Niimi, Martin Gradhand, Luis E. Hueso, Fèlix Casanova and YoshiChika Otani,
Phys. Rev. B **99**, 014403 (2019).

(Chapter 7)

- *Interfacial mechanism in the anomalous Hall effect of Co/Bi_2O_3 bilayers*
  Edurne Sagasta, Yasutomo Omori, Yasuhiro Niimi, Martin Gradhand, YoshiChika Otani, Luis E. Hueso and Fèlix Casanova,
  submitted.

  (Chapter 8)

Other publications:

- *Spin Hall Magnetoresistance as a Probe for Surface Magnetization in $Pt/CoFe_2O_4$ Bilayers*
  Miren Isasa, Saül Vélez, Edurne Sagasta, Amilcar Bedoya-Pinto, Nico Dix, Florencio Sánchez, Luis E. Hueso, Josep Fontcuberta and Fèlix Casanova,
  Phys. Rev. Applied **6**, 034007 (2016).

- *Hanle-induced Magnetoresistance in Pt thin films*
  Saül Vélez, Vitaly N. Golovach, Amilcar Bedoya-Pinto, Miren Isasa, Edurne Sagasta, Mikel Abadia, Celia Rogero, Luis E. Hueso, F. Sebastian Bergeret and Fèlix Casanova,
  Phys. Rev. Lett. **116**, 016603 (2016).

- *Spin doping using transition metal phthalocyanine molecules*
  Ainhoa Atxabal*, Mario Ribeiro*, Subir Parui, Leire Urreta, Edurne Sagasta, Xiagnan Sun, Roger Llopis, Fèlix Casanova and Luis E. Hueso,
  Nat. Commun. **7**, 13751 (2016).

* Equal contribution

Acknowledgements

I am very grateful to both Fèlix and Luis, first for giving me the chance to join their group and work as a researcher with all the possibilities and opportunities that a scientist can have. I really appreciate the trust I felt you placed on me. This was encouraging and a big challenge at the same time; in the end it was the seed from where it grew everything. In particular, I would like to thank Fèlix for all his effort, dedication and time inverted on discussing the physics behind the effects we were studying and the attention to the every single detail that makes the difference in your work. Thanks also to Luis for all the discussions, advice and support received from him that motivated me to realize the work as good as possible. I find the complementary ideas, perspectives, advices and support received from you are enriching for the group you lead.

I would like to show my gratitude to Prof. Txema Pitarke for the opportunity to develop my PhD project in CIC nanoGUNE. I would like to thank also Miguel Odriozola and Yurdana Castelruiz for all their help related to my grant and the organization of the trip to Japan. Thanks also to Itziar Otegui for encouraging the participation in different outreach activities. I take the chance to thank the Ministerio de Educación, Cultura y Deporte (MECD) for the FPU (Formación Profesorado Universitario) 14/03102 grant.

Many thanks to Prof. YoshiChika Otani and his entire group in the Institute of Solid State Physics in the University of Tokyo and RIKEN for their charming three months host and collaborations during the four years of my PhD. I am very grateful to all what I learnt there, apart from the spintronics point of view, about the nice and original Japanese culture. Let me write down all your names as your were the ones who made this internship very special: Yasutomo Omori, Hironari Isshiki, Jorge Puebla, Sei Takizawa, Prasanta Muduli, Yoko Kaneda, Michiko Ishinabe, Nobuto Narita, Kenta Matsumoto, Yusuke Uchida and Mingran Xu.

Special thanks to Martin Gradhand and Yasuhiro Niimi for all our discussions that help me understand the physics we were studying much better. Martin, thanks for all your detailed theoretical explanations and Yasu for all your hard work in our collaborations. I would also like to thank Juan Borge for all the

discussions we had about interfacial spin-orbit effects. Many thanks also to Andrey Chuvilin and Christopher Tollan for the high-resolution transmission electron microscope images and analysis, which helped to observe closely our devices and to complete the understanding of the spin-based effect that was taking place there. Thanks a lot to Yuichiro Ando for the interesting project we started to develop in the last year about the spin-to-charge conversions in topological insulators!

I would like to thank Ralph and Roger for all their support in the fabrication procedures, training of the equipments and all transmitted knowledge about the instruments. Together with this, all the moments we spent in the clean room or lab 13. Thanks for all your patience, persistence and effort, I witness that this is the secret to make the devices work!

Sincere thanks to all the Nanodevices group, former and present members. Starting with Miren, who was my first guide and pillar in this experimental world and from whom I learnt the concentrate and orderly way of fabricating the spintronic devices. Together with Miren, Oihana and Estitxu as they embraced me as the new member in their Angel´s club (Angels + 1). Oihana, badakizu asko apreziatzen zaitxudala zaren modukua izetiarren! Thanks to Wenjing for all the nice moments we spent working with graphene/Pt, together with Lingxi :) . And to Mario, Saül, Santi and Pablo, who were there since the very first moment I arrived to nanoGUNE. Last but not least, to the most recent Bomba de Humo group: Ainho for being always kind, happy and helpful there, Maider for the strong support I received from you, Betty for all your super-stories, Tuong for your permanent smile, CaRamba and EduRne moments. Safeer, Kaushik and Subir: I will not forget the goodbye party of Subir, where the Rashba chicken of Safeer and the dress of shark of Subir were the protagonist!! Pep for all the discussions but mostly for all the biscuits you offered me! Franz and Sara for the climbing moments! Maria, David, Isabel, Won Young for all the moments we shared these last months! Nerea for making me laugh so much with your funny comments, and all your offers to eat chips and biscuits. Inge for all and each interesting conversations that we had and clearly, for introducing me to playing volleyball!! Juanma, specially for your goodness and also for all the nice dinners in the kitchen. Josu, for your special humor, your way of expressing yourself and all the happiness you do transmit me and Francesco, italiano, for all your corrections to my pasta-based dishes, your great pizzas, and importantly, for learning all my Basque surnames!! Eva, Marta, Diogo for the last trip to Bardenas! I cannot finish this list without mentioning Patri, I am very grateful to all the moments we shared in the last eight years in the university and nanoGUNE!

Many thanks also to Luis Goitiandia for introducing me in the teaching world of the University. Giving lessons in the University has been enjoyable.

Etxera eta herrira bueltatuz, nire bizitzan hurbileneko direnak eskertu nahiko nituzke. Laurok osatzen dogun Sagasta-Urrutia familia; ama, aita eta Danel, nigan sinisten dozuela askotan erakutsi duztezuelako eta zuengandik jasotako indar ta babes danagatik. Baitxa Sagasta-Errasti eta Urrutia-Uribetxeberria parte garen danoi. Xa; zuri eta zure familixa danai, urte honeitan bizitako momentu eder danengatik, eta ni hain ondo zaindu eta apreziatziarren. Guruxunien osatzen dogun danoi; gure laguntasun horrek asko balixo dauelako eta eztaukolako preziorik beti zuekin elkartzeko aukera izetiak. Aspe, Li mendixen pasau ditxugun berriketaldi danengatik, Julen, zure baldintzabako babes eta alaitasun etengabia eskaintzearren eta Eid, elkar ederto ulertzen dogulako gure kontu horreitan. Elen, Lei urte honeitan Donostin, Atxabaltan eta bidien pasautako momentuengatik.

I feel that my bag is full of support that I have received from all of you, and also full of tools that I have developed these years. All this will help me to be a better professional and most importantly, more open-minded and conscious person. I am grateful to all the experienced moments that make you aware of the main principles one person should have.

Thanks for being there these years.

I feel with energy and eager to go on in this unique live.

Donostia, 2019ko maiatza.

Edurne